UNIVERSITY OF POTSDAM

DOCTORAL THESIS

Asian dust, monsoons and westerlies during the Eocene

Author:
Niels Meijer

A thesis submitted in fulfillment of the requirements for the degree of Doctor of Philosophy

in the

Faculty of Science

Institute of Geosciences

Submitted on:
June 17, 2020

Defended on:
November 5, 2020

Supervisors:
Dr. Guillaume Dupont-Nivet
Dr. Hemmo A. Abels

Reviewers:
Prof. Dr. Silke Voigt
Dr. Anu Kaakinen

Published online on the
Publication Server of the University of Potsdam:
https://doi.org/10.25932/publishup-48868
https://nbn-resolving.org/urn:nbn:de:kobv:517-opus4-488687

Abstract

Asian dust, monsoons and westerlies during the Eocene

The East Asian monsoons characterize the modern-day Asian climate, yet their geological history and driving mechanisms remain controversial. The southeasterly summer monsoon provides moisture, whereas the northwesterly winter monsoon sweeps up dust from the arid Asian interior to form the Chinese Loess Plateau. The onset of this loess accumulation, and therefore of the monsoons, was thought to be 8 million years ago (Ma). However, in recent years these loess records have been extended further back in time to the Eocene (56-34 Ma), a period characterized by significant changes in both the regional geography and global climate. Yet the extent to which these reconfigurations drive atmospheric circulation and whether the loess-like deposits are monsoonal remains debated. In this thesis, I study the terrestrial deposits of the Xining Basin previously identified as Eocene loess, to derive the paleoenvironmental evolution of the region and identify the geological processes that have shaped the Asian climate.

I review dust deposits in the geological record and conclude that these are commonly represented by a mix of both windblown and water-laid sediments, in contrast to the pure windblown material known as loess. Yet by using a combination of quartz surface morphologies, provenance characteristics and distinguishing grain-size distributions, windblown dust can be identified and quantified in a variety of settings. This has important implications for tracking aridification and dust-fluxes throughout the geological record.

Past reversals of Earth's magnetic field are recorded in the deposits of the Xining Basin and I use these together with a dated volcanic ash layer to accurately constrain the age to the Eocene period. A combination of pollen assemblages, low dust abundances and other geochemical data indicates that the early Eocene was relatively humid suggesting an intensified summer monsoon due to the warmer greenhouse climate at this time. A subsequent shift from predominantly freshwater to salt lakes reflects a long-term aridification trend possibly driven by global cooling and the continuous uplift of the Tibetan Plateau. Superimposed on this aridification are wetter intervals reflected in more abundant lake deposits which correlate with high-stands of the inland proto-Paratethys Sea. This sea covered the Eurasian continent and thereby provided additional moisture to the winter-time westerlies during the middle to late Eocene.

The long-term aridification culminated in an abrupt shift at 40 Ma reflected by the onset of windblown dust, an increase in steppe-desert pollen, the occurrence of high-latitude orbital cycles and northwesterly winds identified in deflated salt deposits. Together, these indicate the onset of a Siberian high atmospheric pressure system driving the East Asian winter monsoon as well as dust storms and was triggered by a major sea retreat from the Asian interior. These results therefore show that the proto-Paratethys Sea, though less well recognized than the Tibetan Plateau and global climate, has been a major driver in setting up the modern-day climate in Asia.

Contents

To my late grandfather Nico Hulshof for inspiring me with his passion for history, rocks and the Earth

Chapter 1

Introduction

1.1 Research context and relevance

Monsoons are arguably the most characteristic feature of Asian climate, yet their origin and geological history remain poorly understood. During summer, the Asian monsoons supply moisture from the southeast and thereby support the livelihoods of billions of people living in the region (e.g. An et al., 2015; Wang et al., 2020a). During winter, the atmospheric circulation reverses and dry northerly winds sweep up silt-sized dust, called loess, from the arid continental interior to central China (e.g. Sun, 2002). Over millions of years, this dust has accumulated to form the Chinese Loess Plateau (Fig. 1.1) and has provided an excellent geological record to study the history of the monsoons (e.g. An, 2014; Maher, 2016). Yet after decades of research, fundamental questions concerning the driving mechanisms of the monsoons remain unclear. Traditionally, the Asian monsoons are linked to uplift of the Tibetan Plateau (e.g. An et al., 2001; Molnar et al., 1993), a vast region of high elevation (>3000 m) formed by the continuous collision of India with the Asian continent (Fig. 1.1). This uplift affects sensible heating of high-altitude air and was thought to be crucial in establishing monsoonal circulation (Molnar et al., 1993; Prell and Kutzbach, 1992). More recent studies, however, indicate that the interactions between the Plateau and the monsoons are more complex and may have existed since the formation of a lower elevation proto-Plateau (Molnar et al., 2010).

The oldest loess on the central Chinese Loess Plateau is dated at 8 Ma, coeval with uplift of the northern Tibetan Plateau, and has been interpreted to mark the onset of the monsoons (An et al., 2001). A subsequent increase in loess accumulation at 2.6 Ma is linked to the coeval northern hemisphere glaciation resulting in aridification of the Asian interior and strengthening of the winter monsoon (An et al., 2001; Ding et al., 1995). These records suggest that uplift of the Tibetan Plateau and global cooling have been the key triggers in setting up the modern-day atmospheric circulation in Asia. In recent years, however, loess deposits have been reported with increasingly older ages of 22 Ma (Guo et al., 2002), 40 Ma (Licht et al., 2014) or even 50 Ma (Li et al., 2018a). These studies suggest that the Asian monsoons are considerably older than previously thought and may have existed since the Eocene (56-34 Ma), a period characterized by both climatic and regional tectonic reconfigurations. While this is supported by climate model simulations and proxy records (Caves Rugenstein and Chamberlain, 2018; Farnsworth et al., 2019; Huber and Goldner, 2012; Licht et al., 2014; Quan et al., 2012; Quan et al., 2014; Roe et al., 2016; Wang et al., 2013a; Xie et al., 2019; Xie et al., 2020; Zoura et al., 2019), other studies stress that the Eocene monsoonal circulation may have been significantly different than today (Herman et al., 2017; Li et al., 2018b; Spicer et al., 2016; Spicer et al., 2017; Tardif et al., 2019; Zhang et al., 2012; Zhang et al., 2018b).

Both tectonic and climatic Eocene features have been hypothesized as driving paleoenvironmental change and monsoons in Asia, yet the relative importance of each

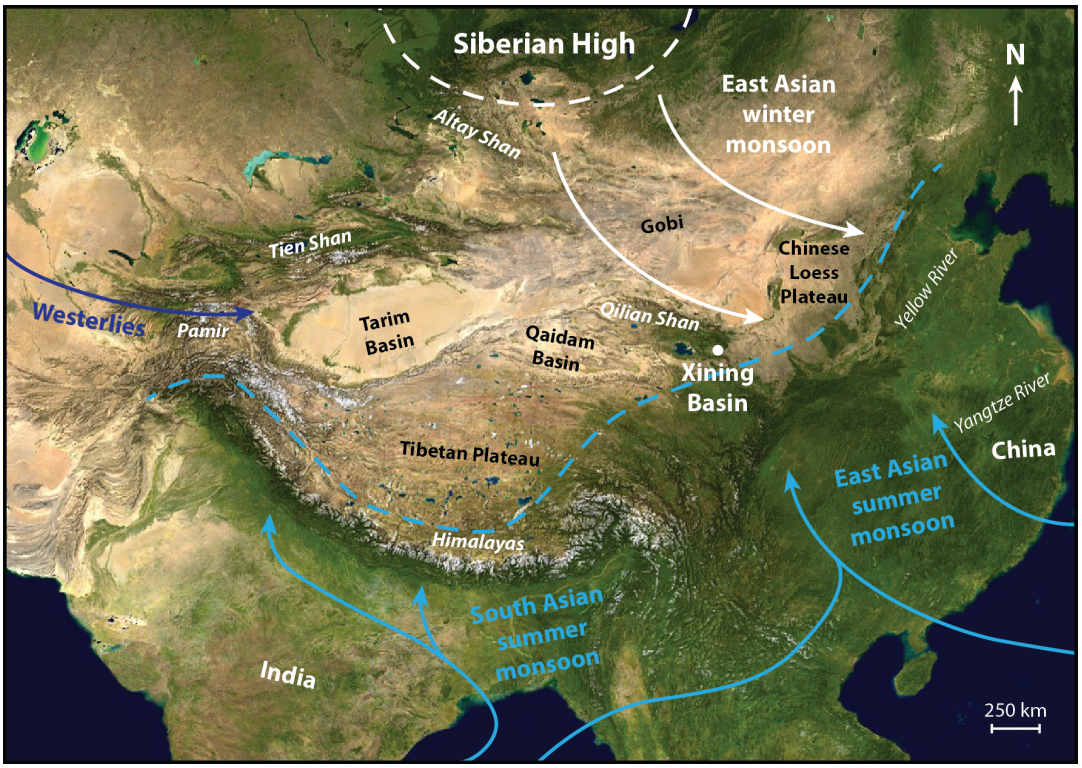

FIGURE 1.1: Satellite image of Asia (source: NASA) showing the main geographic features mentioned in this thesis and the modern-day atmospheric circulation patterns. The South and East Asian summer monsoons are indicated in light-blue arrows and their maximum extent by the dashed line. The wintertime low-level westerlies are indicated in dark-blue and the East Asian winter monsoon and Siberian High are indicated in white.

driver remains unclear. These driving mechanisms include uplift of the Tibetan Plateau shortly following the India-Asia collision at 60 Ma (e.g. Kapp and DeCelles, 2019) as well as global cooling resulting in a shift from warm greenhouse conditions to an icehouse state (e.g. Zachos et al., 2008). In addition, a vast inland sea, called the proto-Paratethys Sea, covered the Eurasian continent during the Eocene and subsequently retreated (e.g. Bosboom et al., 2011; Kaya et al., 2019). The resulting land-sea redistribution may have driven aridification of the continental interior and promoted monsoonal circulation (e.g. Ramstein et al., 1997; Guo et al., 2002). Recent studies have accurately constrained the timing of the Tibetan Plateau uplift (e.g. Kapp and DeCelles, 2019; Staisch et al., 2016; Wang et al., 2014b), global cooling (Anagnostou et al., 2016; Cramwinckel et al., 2018) and proto-Paratethys Sea retreat (Bosboom et al., 2011; Bosboom et al., 2014b; Bosboom et al., 2014c; Bosboom et al., 2017; Carrapa et al., 2015; Chapman et al., 2019; Kaya et al., 2019; Kaya et al., 2020) and therefore provide an excellent opportunity to study the origins of the Asian climate system. However, well-dated paleoenvironmental records from the Eocene are lacking.

In this thesis, I use various tools including stratigraphy, sedimentology, palynology and stable isotope geochemistry to present a detailed Eocene paleoenvironmental reconstruction of the Xining Basin in central China (Fig. 1.1). This basin is located at the boundary between the modern-day monsoonal domain and the dry continental interior and is therefore perfectly situated to study both the evolution of the monsoons and inland aridification. The age of the deposits can be accurately determined by applying magnetostratigraphy; the use of past reversals of Earth's magnetic field

as recorded by magnetic minerals in the sediments (e.g. Dai et al., 2006). Furthermore, the Eocene strata in this basin have been previously identified as loess (Licht et al., 2014; Licht et al., 2016b) and hence may be used to track monsoonal evolution. In the following section I will introduce in more detail the geological setting of the Xining Basin, the modern-day Asian climate configuration and its driving mechanisms over geological time. Then I will present the research questions and outline of this thesis.

1.2 Geological setting of the Xining Basin

The Xining Basin is located on the northeastern margin of the Tibetan Plateau and is bounded by the Laji Shan (shan = mountain range) in the south, the Qilian Shan (locally known as the Daban Shan) in the north and the Riyue Shan in the west (Fig. 1.2A). The basin is open towards the east and forms a sub-basin of the Cenozoic Longzhong Basin extending towards the Qinling Shan in the south and the Liupan Shan in the east (Fig. 1.2B; Horton et al., 2004). Other sub-basins include the Guide and Xunhua Basins south of the Laji Shan, and the Lanzhou and Linxia Basins in the east (Fig. 1.2B).

Cenozoic deposition in the Longzhong Basin initiated during the early to middle Eocene in the Xining and Lanzhou Basins (Dai et al., 2006; Wang et al., 2016a). The formation of the Longzhong Basin has variously been interpreted as post-rift thermal subsidence (Horton et al., 2004), a transtensional basin (Wang et al., 2016a; Zhang et al., 2016a), a foreland basin due to uplift of the Western Qinling Shan (Liu et al., 2007; Liu et al., 2013) or a NW-SE extensional basin (Wang et al., 2013b; Fan et al., 2019). The common occurrence of synsedimentary NE-SW trending normal faults in the Paleogene strata of the Xining Basin supports the latter and is hypothesized to be driven by slab rollback of the Pacific plate (Fan et al., 2019). During the late Oligocene, deposition in the Longzhong Basin expanded to the Xunhua (Lease et al., 2012), Linxia (Fang et al., 2003; Fang et al., 2016), Tianshui (Qiang et al., 2011) and Sikouzi Basins (Wang et al., 2011). This expansion is proposed to be driven by transtension and clockwise rotation of crustal blocks recorded in the magnetostratigraphy between 45 and 29 Ma (Dupont-Nivet et al., 2004; Dupont-Nivet et al., 2008b; Wang et al., 2013b; Zhang et al., 2016a). Alternatively, the Longzhong Basin may have transformed into a foreland basin due to flexural subsidence from the uplifting Qinling Shan (Fang et al., 2016; Wang et al., 2016a). During the Neogene, the Longzhong Basin was segmented into smaller sub-basins due to compressive deformation of the northward expanding Tibetan Plateau which resulted in the uplift of the Laji Shan starting at 22 Ma and the Jishi Shan at 13 Ma (Horton et al., 2004; Hough et al., 2014; Lease et al., 2011; Lease, 2014).

Cenozoic strata in the Xining Basin conformably (Zhai and Cai, 1984) or unconformably (QBGMR, 1985) overlie Mesozoic mudrocks, sandstones and conglomerates of the Lower Cretaceous Hekou Group and the Upper Cretaceous Minhe Formation (Fig. 1.2C; Dai et al., 2006; Horton et al., 2004). Deposition during the Cenozoic is quasi-continuous and extends from the Eocene to the Pliocene epoch (Fang et al., 2019a). The deposits include mudrocks, sandstones and evaporites of the Paleogene Qijiachuan, Honggou, Mahalagou and Xiejia Formations as well as mudrocks, sandstones and conglomerates of the Neogene Chetougou, Guanjishan and Mojiazhuang Formations (Fig. 1.2C; sensu Fang et al., 2019a; Dai et al., 2006; Horton et al., 2004). Subsequent fluvial incision resulted in terraces which are capped by up to 200 meters

of Quaternary loess constituting the westernmost part of the Chinese Loess Plateau (Fig. 1.1B; Fang et al., 2019a; Zhang et al., 2017).

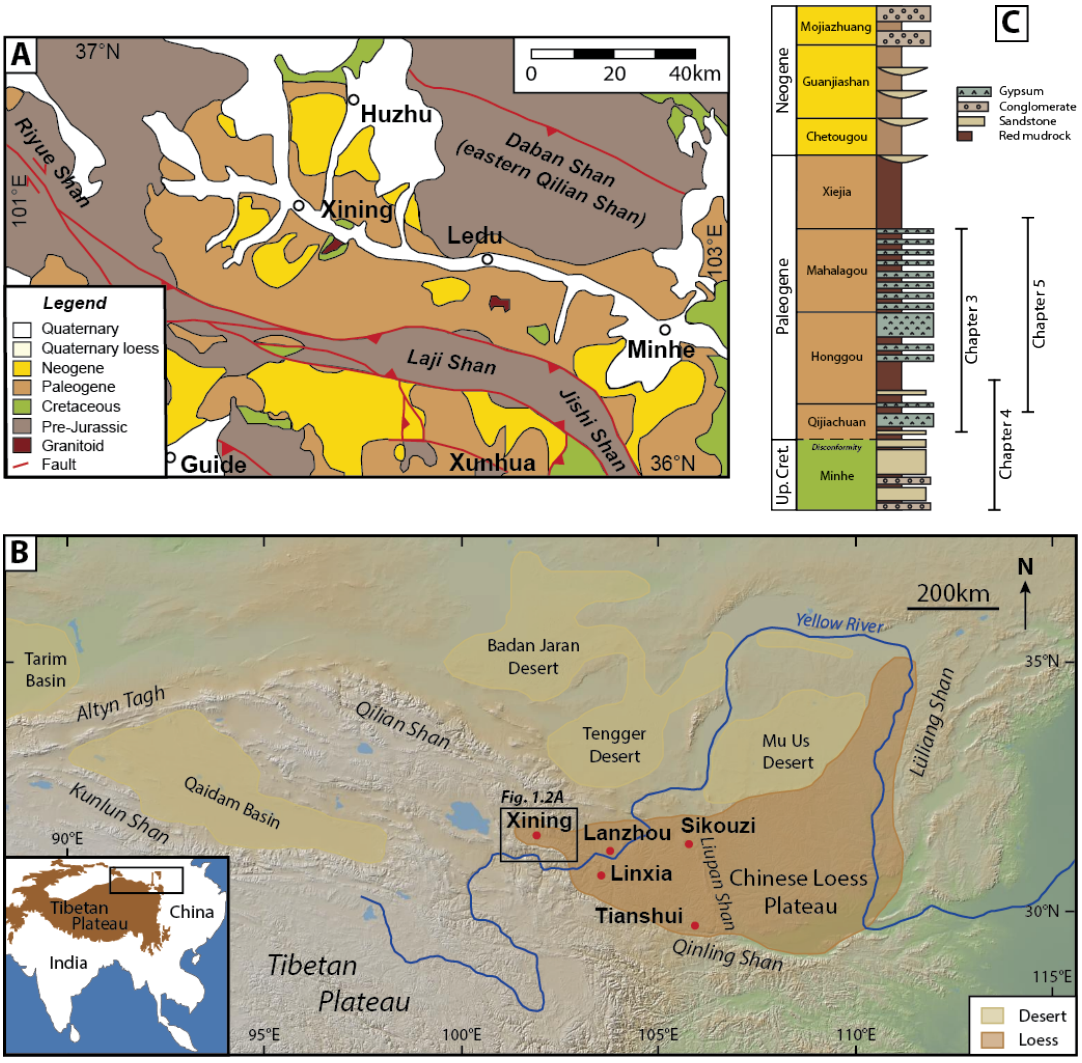

FIGURE 1.2: (A) Geological map of the Xining Basin (modified from Fan et al., 2019). (B) Modern-day topographic map (http://www.geomapapp.org) of the northeastern Tibetan Plateau showing the occurrences of Quaternary loess and deserts as well as the various sub-basins of the Cenozoic Longzhong Basin. C) Lithostratigraphy listing the formations of the Xining Basin adapted from Horton et al. (2004) and updated following Fang et al. (2019a). Stratigraphic intervals covered by the chapters of this thesis are indicated as well.

1.3 Asian monsoons and westerlies

Monsoonal circulation is characterized by the distinction between a rainy and a dry season due to the reversal of wind directions. This reversal is driven by the seasonal shift in insolation and modified by topography and the varying heat capacities of the land-sea distribution (e.g. An et al., 2015). Traditionally, monsoons are described as a giant sea breeze (Halley, 1686) with summer heating of the land resulting in low atmospheric pressures and moist air from the ocean transported inland. During winter, cooling of the land surface reverses this circulation resulting in a dry continental wind. However, recent studies show that surface heating is only of minor

importance and that instead topography is essential for insulating moist air and deflecting air flow resulting in moist convergence (Boos and Kuang, 2010; Gadgil, 2018; Molnar et al., 2010; Roe et al., 2016; Son et al., 2019).

In Asia, the summer monsoon can be subdivided in the South Asian summer monsoon over India and Indochina, and the East Asian summer monsoon over China, Japan and the Korean peninsula (Fig. 1.1; e.g. Molnar et al., 2010). Although these monsoonal systems interact, they are to a large extent independent and driven by separate mechanisms (Ding et al., 2005). The South Asian monsoon is a tropical monsoon linked to the migration of the Intertropical convergence zone (ITCZ) resulting in peak precipitation along the southern flank of the Himalayas during summer, before moving southward during winter (Fig. 1.1; Gadgil, 2018). In contrast, the East Asian summer monsoon is an extratropical monsoon associated with frontal systems and the subtropical jet stream (Molnar et al., 2010; Chiang et al., 2015; Sampe and Xie, 2010). During spring, persistent weak rainfall derived from the Bay of Bengal and the South China Sea occurs in southern China when the jet stream is south of the Tibetan Plateau. As northern hemisphere warming continues, the jet stream moves northwards and flows around the northern edge of the Tibetan Plateau in June (Schiemann et al., 2009). Downstream of the Plateau, the jet stream separates the warm moist air over southern China from the dry cooler air in the north and promotes frontal convection resulting in a band of rainfall that extends east-northeast from central China to Japan, termed the Meiyu Front (Chiang et al., 2015; Ding et al., 2005; Molnar et al., 2010; Sampe and Xie, 2010). In July, the jet stream weakens and the Meiyu front disintegrates allowing moisture transport to northern China (north of 35°N), while southern and central China become relatively dry (Chiang et al., 2015). The shifts between these different stages of the East Asian monsoon occur relatively abruptly, in contrast to the more smooth transitions observed in tropical monsoons such as the South Asian monsoon (Chiang et al., 2015; Ding et al., 2005).

The monsoonal regions border the dry continental interior of Asia, which is characterized by vast sand and stony deserts such as the Taklimakan in the Tarim Basin and the Gobi in Mongolia and northern China (Fig. 1.1). These arid regions receive only limited amounts of precipitation, predominantly derived from the low-level westerlies during winter. These westerlies transport moisture from the Mediterranean and Atlantic Ocean that has been recycled over the Eurasian continent (Fig. 1.1; Caves et al., 2015). Mountain ranges such as the Pamir and Tien Shan (Fig. 1.1) block westerly moisture and thereby promote aridity in western China. In addition, cooling of the Asian interior during winter causes a high atmospheric pressure system to develop over southern Siberia and Mongolia (Fig. 1.1; Chang et al., 2006). The formation of this so-called Siberian High is promoted by snow cover in Eurasia and the extent of sea ice in the Bering Sea (Chang et al., 2006; Roe, 2009). The Siberian High drives the strong northwesterly surface winds of the East Asian winter monsoon bringing cold and dry air towards the south (Fig. 1.1; Chang et al., 2006). During spring, the cold air of the Siberian High creates a strong meridional temperature gradient with the warming air in the south resulting in frequent dust storms in northern and central China (Roe, 2009). Over time, this dust has accumulated to form the Chinese Loess Plateau (e.g. An, 2014; Liu and Ding, 1998; Maher, 2016).

1.4 Driving mechanisms of Asian climate

As aforementioned, the uplift of the Tibetan Plateau, proto-Paratethys Sea retreat and global climate have all been proposed to drive the Asian atmospheric circulation during the Eocene (Fig. 1.3). In the following, I will introduce the background of these driving mechanisms in more detail and discuss their climatic impacts.

1.4.1 Tibetan Plateau

Uplift of the Tibetan Plateau, driven by the continental collision between India and Asia, began at 60 Ma (Kapp and DeCelles, 2019). However, the geological history of the Plateau is more complex and consists of an amalgamation of various Gondwanan terranes that accreted mostly during Mesozoic times in subduction zones at the southern margin of the Asian continent (e.g. Kapp and DeCelles, 2019; Molnar et al., 2010; Spicer et al., 2020). These accretions resulted in an Andean-style margin with a proto-Plateau which subsequently rose and expanded northwards after the India-Asia collision (e.g. Molnar et al., 2010). Various aspects of the Tibetan Plateau uplift remain fiercely debated such as the maximum elevations attained (Botsyun et al., 2019; Valdes et al., 2019) and the existence of low-elevation valley systems within the Plateau (e.g. Spicer et al., 2020). The timing and northward movement of deformation is however well constrained by thermochronologic and structural data (Rohrmann et al., 2012; Wang et al., 2014b; Staisch et al., 2016).

The Tibetan Plateau and other mountain belts located north of the Plateau affect the regional climate in various ways. First, as mentioned above, the mountain ranges such as the Himalayas, Pamir and Tien Shan block atmospheric moisture transported from the south and west. Stable isotope records suggest that the Tibetan proto-Plateau has been blocking southerly moisture since at least the early Eocene (Caves et al., 2015; Caves Rugenstein and Chamberlain, 2018). Sedimentological and stable isotope data show that the Neogene uplift of the Tien Shan and Pamir has resulted in aridification of western China (Bougeois et al., 2018; Heermance et al., 2018; Wang et al., 2020b; Zheng et al., 2015). In addition to blocking moisture, the Himalayas are proposed to drive the South Asian summer monsoon by insulating the warm and moist tropical air over India from the cold and dry extratropical air (Boos and Kuang, 2010; Molnar et al., 2010). Furthermore, the deflection of westerly airflow by the Asian orographies results in stationary waves in the upper atmosphere driving subsidence and aridity upstream of the Plateau, while promoting moist convergence downstream (Manabe and Broccoli, 1990). The latter plays an important role in driving the Meiyu front of the East Asian summer monsoon (Chiang et al., 2015; Molnar et al., 2010; Sampe and Xie, 2010; Son et al., 2019) as long as the Plateau is high enough (at least 3000 meters) to interact with the upper atmosphere (Zoura et al., 2020). Climate model simulations have shown that the northward growth of the Tibetan Plateau continuously strengthens both the South and East Asian monsoons (Yu et al., 2018) as long as the Plateau is located in the subtropical latitudes, and not in the tropics (Zhang et al., 2018b). In addition, uplift of the Tibetan Plateau as well as the Mongolian mountains enhances the atmospheric pressures in the Siberian High thereby strengthening the East Asian winter monsoons (Sha et al., 2015; Zhang et al., 2015b). Furthermore, the topography in Mongolia and northern China promotes lee cyclogenesis and the formation of dust storms (Roe, 2009).

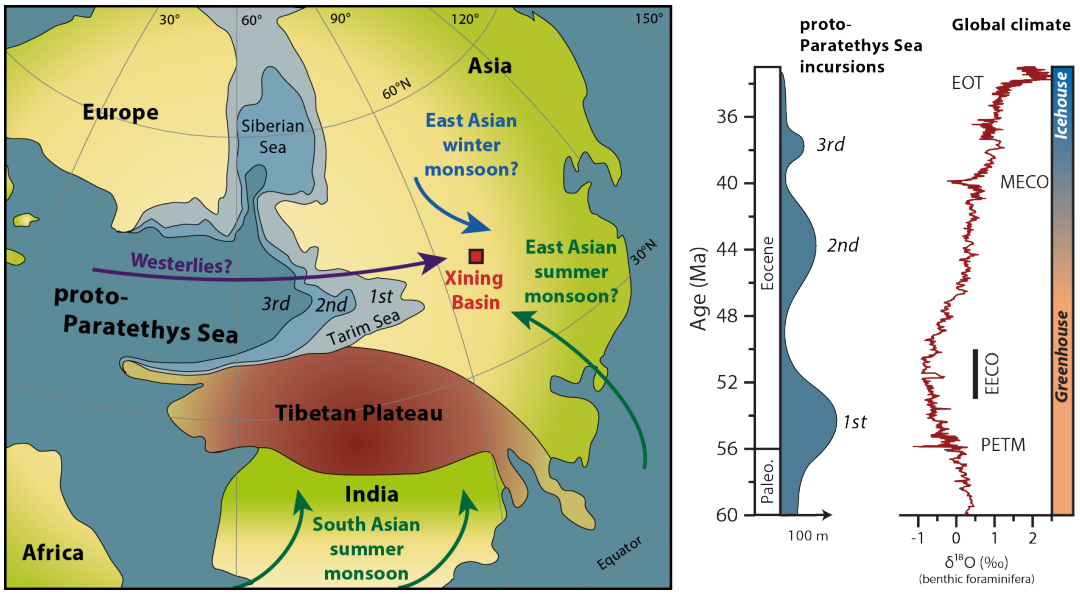

FIGURE 1.3: Eocene paleogeographic map (modified from Bosboom et al., 2011) showing the Xining Basin, the Tibetan Plateau, the maximum extent of the proto-Paratethys during the three Paleogene highstands (derived from Kaya et al., 2019) and the hypothesized atmospheric configurations. Inset figure shows the timing of the proto-Paratethys highstands (Kaya et al., 2019). Trends in global climate are shown on the right by the 5-point moving average of the benthic foraminifera $\delta^{18}O$ record of Cramer et al. (2009). The Paleocene-Eocene Thermal Maximum (PETM), Early Eocene Climatic Optimum (EECO), Middle Eocene Climatic Optimum (MECO) and Eocene-Oligocene Transition (EOT) are indicated as well.

1.4.2 Proto-Paratethys Sea

The proto-Paratethys Sea was an epicontinental sea that extended from the Mediterranean to western China since the Cretaceous until the Paleogene period (Fig. 1.3; e.g. Bosboom et al., 2011; Kaya et al., 2020). At times, the sea was connected with the Arctic Ocean via the Turgai Strait and the Siberian Sea (1.3; e.g. Kaya et al., 2019). A combination of eustatic sea-level fluctuations and regional tectonics resulted in five major sea incursions into Central Asia; two during the Cretaceous and three during the Paleogene (1.3; Bosboom et al., 2011; Bosboom et al., 2014b; Bosboom et al., 2014c; Bosboom et al., 2017; Carrapa et al., 2015; Chapman et al., 2019; Kaya et al., 2019; Kaya et al., 2020; Wang et al., 2019b). These were followed by a drastic late Eocene sea retreat and isolation of the sea during the Oligocene and Miocene resulting in the formation of the Paratethys Sea (e.g. Popov et al., 2004).

Climate model simulations of the proto-Paratethys Sea retreat suggest that the resulting land-sea redistribution played a major role in driving the Asian monsoonal circulation (Ramstein et al., 1997; Fluteau et al., 1999). However, more recent proxy and climate model studies have suggested that the sea would have been too shallow to significantly affect the land-sea contrast and the summer monsoons (Bougeois et al., 2014; Bougeois et al., 2018; Roe et al., 2016). Instead, the sea incursions may have played a role by supplying atmospheric moisture to the wintertime westerlies (Bougeois et al., 2018; Zhang et al., 2012). Furthermore, the sea retreat from Siberia is shown to promote the development of the Siberian High and strengthen the East Asian winter monsoon (Zhang et al., 2007).

1.4.3 Global climate

The Eocene period marks the transition from a warm and mostly ice-free greenhouse world to colder icehouse conditions with stable ice sheets on Antarctica (Fig. 1.3; e.g. Zachos et al., 2001; Zachos et al., 2008). This cooling trend has been linked to reconfigurations in ocean circulation (e.g. Bijl et al., 2013; Kennett, 1977), but more recent proxy records suggest that a decrease in atmospheric CO_2 concentrations was the dominant driver instead (Anagnostou et al., 2016; Cramwinckel et al., 2018). Peak warmth occurred during the Early Eocene Climatic Optimum (EECO) from 52 to 49 Ma, followed by a long-term drop in global temperatures (Cramer et al., 2009; Cramwinckel et al., 2018; Mudelsee et al., 2014; Westerhold et al., 2018; Zachos et al., 2001; Zachos et al., 2008). Various mechanisms have been proposed to explain this long-term decrease in atmospheric CO_2 concentrations, including increased organic carbon burial (France-Lanord and Derry, 1997), a decrease in CO_2 release from volcanic outgassing (Brune et al., 2017; Zachos et al., 2008) and an increase in the silicate weathering feedback (Caves et al., 2016). This change in feedback may have been driven by uplift of the Tibetan Plateau (Raymo and Ruddiman, 1992), the low-latitude obduction of island arcs (Macdonald et al., 2019) or changes in ocean circulation affecting precipitation and chemical weathering (Elsworth et al., 2017).

The early Eocene is characterized by transient (40-200 kyrs) hyperthermal events with elevated temperatures and depleted $\delta^{13}C$ excursions. Of these, the Paleocene-Eocene Thermal Maximum (PETM) at 56 Ma is the largest in magnitude (e.g. Kennett and Stott, 1991; McInerney and Wing, 2011) and is followed by multiple orbitally-forced smaller hyperthermals throughout the early Eocene (Cramer et al., 2003; Kirtland-Turner et al., 2014; Littler et al., 2014; Sexton et al., 2011; Westerhold et al., 2018). These are thought to be driven by periodic perturbations of exogenic carbon pools (e.g. Dickens, 2001), but become less frequent in the middle to late Eocene. The Middle Eocene Climatic Optimum (MECO) at 40 Ma, is a transient warming event which, in contrast to the previous hyperthermals, has a longer duration (400 kyrs) and an asynchronous $\delta^{13}C$ excursion (Sluijs et al., 2013). This event is proposed to reflect a reorganization of internal carbon reservoirs (Sluijs et al., 2013; Henehan et al., 2020), possibly triggered by orbital forcing (Westerhold and Röhl, 2013) or a decrease in the silicate weathering feedback (van der Ploeg et al., 2018). Subsequent long-term cooling culminated in the Eocene-Oligocene Transition (EOT) at 34 Ma, triggered by both orbital forcing and the crossing of a critical threshold in atmospheric CO_2 which resulted in the formation of continental-scale ice sheets on Antarctica and a corresponding sea-level drop (Coxall et al., 2005; DeConto and Pollard, 2003; Ladant et al., 2014; Pearson et al., 2009). Geological evidence indicates that substantial ice volumes already existed on Antarctica before the major glaciation of the continent (Carter et al., 2017; Gulick et al., 2017), but were likely highly dynamic (e.g. Scher et al., 2014) and sensitive to orbital forcing as shown by climate model simulations (DeConto and Pollard, 2003; Ladant et al., 2014).

The global climate directly affects atmospheric temperatures and therefore Asian paleoenvironments but also indirectly the hydrological cycle (e.g. Lu et al., 2010) possibly through additional interactions with ocean circulation (e.g. Sun et al., 2012). The role of warming in the hydrological cycle can be separated in dynamic effects, involving atmospheric circulation, and thermodynamic effects (Wang et al., 2020a). The latter is well-constrained and includes the exponential dependence of humidity on temperature resulting in an intensification of the hydrological cycle with increasing temperatures (e.g. Chou et al., 2009; Wang et al., 2020a). However, the dynamic

effects on large-scale atmospheric circulation due to warming remain poorly understood, with climate model simulations often disagreeing (Wang et al., 2020a). Most simulations tend to predict a "wet-get-wetter response" with enhanced precipitation in regions with already strong moist convergence while arid regions under subsiding air tend to get drier (Chou et al., 2009; Held and Soden, 2006; Wang et al., 2020a). In addition, the differential heating of land and oceans with increasing temperatures may promote monsoonal circulation, but is counteracted by the differential heating of the upper and lower troposphere which stabilizes the atmosphere and prevents deep convection (Wang et al., 2020a).

Licht et al. (2014) proposed that the warmer Eocene period would have enabled Asian monsoonal circulation, but other climate model studies show only limited effects of CO_2 on the monsoons (Farnsworth et al., 2019; Roe et al., 2016; Zoura et al., 2019). Instead, it has been suggested that warmer climates may have driven a more northward movement of the ITCZ (Schneider et al., 2014; Pettke et al., 2002; Rea et al., 2000), which could explain the occurrence of Eocene Asian monsoons in southern China (Spicer et al., 2017). Alternatively, a warmer climate is also shown to drive a more northward movement of the subtropical jet stream (Grise and Polvani, 2014), which may affect the East Asian summer monsoon (Chiang et al., 2015). In conclusion, the effect of the warmer Eocene on the monsoons and possible interactions with the ITCZ and jet stream remain poorly understood.

Global cooling and positive feedbacks with Eurasian snow cover and Arctic sea ice strengthen the East Asian winter monsoon and the Siberian High (Chang et al., 2006; Roe, 2009). Consequently, the long-term cooling during the Cenozoic has been suggested to drive the aridification of the Asian interior by weakening the hydrological cycle, lowering sea-level due to growing ice sheets and by strengthening of the Siberian High during winter (Lu et al., 2010; Miao et al., 2012). In addition, climate models suggest that global cooling enhances the seasonality in precipitation in eastern China and may have played a role in the establishment of the modern-like East Asian monsoons (Zhang et al., 2018c).

1.5 Research questions

In this thesis I aim to study and date the Eocene stratigraphic records in the Xining Basin to answer the following research questions:

- What is the depositional origin of 'loess-like' siltstones and to what extent do these reflect the evolution of dust accumulation, aridification and the East Asian winter monsoon? (**Chapters 2 and 5**)
- What was the role of the wintertime westerlies in supplying atmospheric moisture and driving the regional climate in Asia during the Eocene? (**Chapter 3**)
- How did the East Asian summer and winter monsoons evolve during the Eocene and which mechanisms drove them: Tibetan Plateau uplift, global climate or the proto-Paratethys Sea retreat? (**Chapter 4 and 5**)

1.6 Thesis outline and author contributions

Chapter 2 reviews dust deposits in general and presents methods for reliable identification and quantification of windblown dust in the geological record. Pre-Quaternary

records are shown to reflect a mix of both eolian and alluvial deposits in contrast to Quaternary loess which is almost entirely composed of windblown sediments. Yet the dust component can be distinguished from other components in mixed depositional environments by using a combination of quartz surface morphology, provenance and grain-size-shape end-member analyses. These methods have important implications for reconstructing aridification and eolian dust fluxes in the past.

This chapter is published in **Earth-Science Reviews**.

N.M. designed the study and wrote the manuscript. G.D-N., A.L., J.T.-A., S.B. and H.A.A. helped with interpretations, references, discussions and contributed to writing the manuscript.

Chapter 3 presents the litho- and magnetostratigraphy of the early to middle Eocene strata of the Xining Basin. In addition, U-Pb radiometric ages of zircons from a tuff layer are reported constraining the age model at 50.0 ± 0.4 Ma. Transient intervals of lacustrine mudrocks and evaporites are shown to correlate with highstands of the proto-Paratethys Sea and interpreted as periods of increased westerly moisture.

This chapter is published in **Earth and Planetary Science Letters**.

N.M., G.D.-N. and H.A.A. designed the study. N.M., G.D.-N., H.A.A., M.Y.K., A.L., M.X., Y.Z., Z.L. and Z.G. performed or facilitated field work and sample collection. N.M., G.D.-N., H.A.A. and P.R. performed magnetostratigraphic analyses. N.M., M.Y.K. and M.P. performed radiometric dating. N.M. and G.D.-N. wrote the manuscript with contributions from the other authors.

Chapter 4 shows the litho- and magnetostratigraphy of the early Eocene strata of the Xining Basin constraining the age to an unconformity at 50.9 Ma (magnetochron C23n). High sediment accumulation rates, increased organic carbon burial, pollen assemblages and stable isotopes of pedogenic carbonates and bulk organic carbon are interpreted to reflect an intensified hydrological cycle during peak greenhouse warmth at the Early Eocene Climatic Optimum (EECO) between 50.4 and 49.8 Ma.

N.M., G.D.-N. and A.L. designed the study. N.M., G.D.-N., A.L., A.W., N.B., A.R. and A.S. performed field work and sample collection. N.M., P.R. and N.N. performed magnetostratigraphic and rock magnetic analyses. N.M., A.L. and H.M. performed stable isotope sample preparation and measurements. A.W., N.B. and C.H. performed the palynological study. N.M. wrote the manuscript with contributions from the other authors.

Chapter 5 presents the grain-size record of the early to late Eocene strata in the Xining Basin revealing the appearance of windblown dust at 40 Ma as well as a change to steppe-desert taxa observed in the palynological record and a shift in the dominant cyclicity from 405 kyr eccentricity to 41 kyr obliquity cycles. In addition, sedimentological analysis reveals prevailing northwesterly winds after 40 Ma. These shifts are interpreted to reflect the onset of the Siberian High driving winter monsoons and dust storms due to the retreat of the proto-Paratethys Sea from the Siberian Sea.

This chapter has been submitted to **Paleoceanography and Paleoclimatology**.

N.M., G.D.-N., A.L. and H.A.A. designed the study. N.M., G.D.-N., N.B., A.W., A.R., Y.Z., X.J.L., A.L. and H.A.A. performed field work and sample collection. N.B., A.W.

and C.H. performed the palynological study. N.M., and N.N. performed magnetostratigraphic analyses. N.M. and R.T. performed XRF and color analyses and cyclostratigraphy. N.M., C.A. and M.D. performed the grain-size analyses. N.M. and G.D.-N. wrote the manuscript with contributions from the other authors.

Chapter 2

Identifying eolian dust in the geological record

Niels Meijer, Guillaume Dupont-Nivet, Alexis Licht, João P. Trabucho-Alexandre, Sylvie Bourquin, Hemmo A. Abels

Abstract

Recognition of terrestrial dust in geological records is essential for reconstructing paleoenvironments and quantifying dust fluxes in the past. However, in contrast to eolian sands, silt-sized dust is difficult to recognize in pre-Quaternary records due to a lack of macroscopic features indicating eolian transport and mixing with alluvial sediments. Windblown dust deposits are commonly identified by comparing their sedimentological and petrological features with Quaternary examples of dust known as loess. Here, we review the characteristics of terrestrial dust deposits and conclude that most of these features are not exclusively windblown and may be formed by alluvial deposits as well. We therefore synthesize a set of criteria which enable a reliable identification and quantification of dust while acknowledging potential contributions of alluvial components. These methods include quartz-grain surface morphology analysis to distinguish eolian and alluvial transport modes, provenance studies to identify local and extrabasinal sources, grain-size-shape end-member modelling to quantify the various sedimentary contributions to the record, and a basin-scale stratigraphic approach to derive regional patterns and avoid interpretation of local phenomena. We reassess the Eocene to Pliocene records of the Chinese Loess Plateau and conclude that these strata represent both alluvial and eolian sediments deposited in extensive mudflat systems. Quaternary loess, by contrast, is almost exclusively composed of windblown dust. The early Pleistocene shift from mudflat to loess deposits is associated with a significant increase in accumulation rates, likely due to increased dust production upwind, overwhelming and blanketing the local mudflat systems in central China.

2.1 Introduction

Mineral dust is a fundamental component of the Earth system by driving various physical, chemical and biological processes including radiation scattering, cloud nucleation and ocean fertilization (e.g. An, 2014; Jickells et al., 2005; Knippertz and Stuut, 2014; Pye, 1987). Geological records of mineral dust enable the reconstruction of dust fluxes in the past and are therefore key to assess its impact on the Earth system. Furthermore, dust deposits provide valuable clues on paleoenvironmental settings such as continental aridity, glacial conditions and dominant wind directions (e.g. An, 2014; Soreghan et al., 2002; Soreghan et al., 2008; Soreghan et al., 2014) and may provide analogues for the desertification due to the ongoing global warming

(e.g. D'Odorico et al., 2013). However, these studies are all limited by the reliability of recognizing and quantifying windblown dust in the geological record. As a result, the role of dust forcing remains poorly understood and constitutes one of the largest uncertainties in climate model simulations (Heavens et al., 2012; Lee et al., 2016; Schwartz and Andreae, 1996).

Dust is atmospherically transported in suspension and generally contains particles not bigger than ∼100 µm (Pye, 1987; Újvári et al., 2016). After settling, these particles form structureless deposits with no sedimentary features diagnostic of eolian transport. This is in contrast to coarser-grained eolian sediments that may form dune cross-bedding and wind ripple laminations after deposition by wind or ventifacts indicating eolian transport (e.g. Hunter, 1977; Durand and Bourquin, 2013). The lack of diagnostic eolian features in silt complicates recognizing dust deposits, especially in pre-Quaternary records where paleowind directions are unknown and geographic relationships between the source and dust bodies are difficult to assess. Yet pre-Quaternary dust has been identified in various records (Fig. 2.1) including Precambrian siltstones in northern Norway and Svalbard (Edwards, 1979), Triassic mudrocks in England and the North Sea (Jefferson et al., 2002; Wilkins et al., 2018; Wilson et al., 2020), Cenozoic siltstones in Argentina (Bellosi, 2010; Selkin et al., 2015), both Paleozoic and Cenozoic siltstones in western North America (Johnson, 1989; Soreghan et al., 2008; Fan et al., 2020), as well as Permian, Cretaceous and Cenozoic deposits in Central Asia (Carrapa et al., 2015; Chen et al., 2019; Obrist-Farner and Yang, 2016; Sun and Windley, 2015; Wasiljeff et al., 2020).

To overcome the lack of diagnostic eolian features, these studies use a variety of petrological, geochemical and grain-size characteristics and compare them with well-known dust deposits from the Quaternary period, termed loess, to infer an eolian origin. However, in recent years, these methods have been challenged. Several studies have shown that deposits previously considered to be formed almost entirely by windblown dust derived from deserts, are instead predominantly water-laid (alluvial) and derived from local mountain ranges (Alonso-Zarza et al., 2009; Cheng et al., 2018; Liu et al., 2019). Here, we aim to solve these controversies by first reviewing the depositional environments of dust and critically assessing the traditional methods used to identify an eolian origin. Then, we present a clear set of methods which, when combined, will improve the recognition of dust in the geological record. Finally, we use the insights of our review to reinterpret the pre-Quaternary records of the Chinese Loess Plateau, which are considered as the longest and most continuous dust records in the world spanning the Neogene and arguably the Paleogene periods (e.g. An, 2014). Our review is limited to mineral dust in terrestrial records and excludes the marine realm. For a more detailed review on identifying dust from the Quaternary period, we refer to Muhs (2013), which includes lakes, marine records and ice cores.

2.2 Depositional environments of dust

In the following, we review the characteristics of loess, loessites and dust deposits in general.

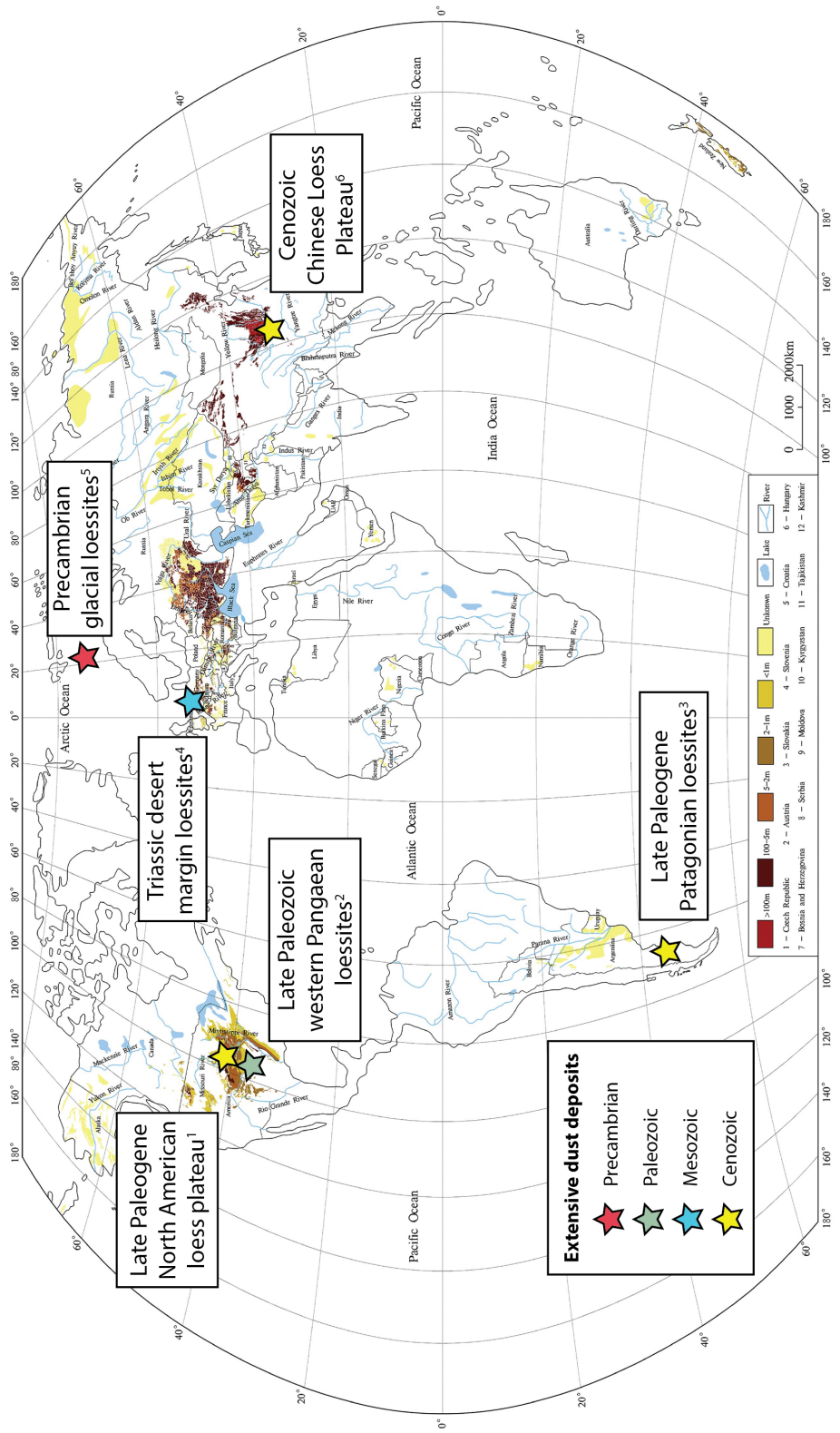

FIGURE 2.1: Map of the global distribution of Quaternary loess deposits and thicknesses (modified from Li et al., 2020 and references therein). Stars indicate examples of extensive dust deposits from the pre-Quaternary: 1) Fan et al. (2020); 2) Johnson (1989); Soreghan et al. (2008); 3) Bellosi (2010); Selkin et al. (2015); 4) Jefferson et al. (2002); Wilkins et al. (2018); Wilson et al. (2020); 5) Edwards (1979); 6) An, (2014); Guo et al., (2008).

2.2.1 Dust production, transport and deposition

The silt particles that constitute dust are generated by a wide variety of mechanisms including: abrasion of larger particles (by wind, in streams or by glaciers), chemical weathering, frost weathering in cold environments, salt weathering and aggregation of clay minerals in arid settings, biological production (e.g. diatoms, radiolaria, phytoliths and pollen) or inheritance from fine-grained parent rocks such as older mudrocks or metamorphic schists and phyllites (Potter et al., 2005; Pye, 1987; Muhs and Bettis, 2003; Wright, 2007). Glacial grinding has been proposed as an efficient silt producer during glacial periods (Smalley, 1966b; Smalley and Vita-Finzi, 1968), whereas desert processes such as salt weathering and abrasion by ephemeral streams or wind may dominate in arid environments (Crouvi et al., 2010; Pye, 1987; Tsoar and Pye, 1987; Whalley et al., 1982; Wright, 2001b). However, the efficiency of these desert processes is debated due to the lack of extensive dust deposits near vast deserts such as the Sahara and the Australian interior (Fig. 2.1; Smalley and Krinsley, 1978; Smalley, 1995). In addition, orogenies may play a major role in generating silt by: 1) fracturing minerals during exhumation, 2) the steep gradients resulting in high energy transport and abrasion, and 3) the high altitude climate promoting frost and salt weathering (Assallay et al., 1998; Pye, 1995; Smalley and Krinsley, 1978; Smalley, 1995; Sun, 2002; Wright, 2001a). The relative importance of these processes in producing large quantities of silt over various timescales remains unclear (Potter et al., 2005).

After production, the dust particles are entrained in the lower atmosphere by turbulent surface winds during storms and may remain suspended until the wind speed and turbulence decrease and the dust settles (Fig. 2.2; Pye, 1987; Roe, 2009; Újvári et al., 2016). In general, grains finer than ~20 µm can remain suspended for longer and may travel thousands of kilometers when lifted up to the jet stream in the upper atmosphere (Fig. 2.2; Pye and Zhou, 1989; Sun, 2002; Sun et al., 2004; Vandenberghe et al., 2006). In addition, 'giant' mineral dust particles of >75 µm in diameter have been found to be transported over long distances as well, though the physical mechanisms underlying this transport remain unclear (van der Does et al., 2018). Dust transport via long-term suspension plays an important role in fertilizing the oceans with iron and thereby affecting the carbon cycle (Jickells et al., 2005; Martin, 1990).

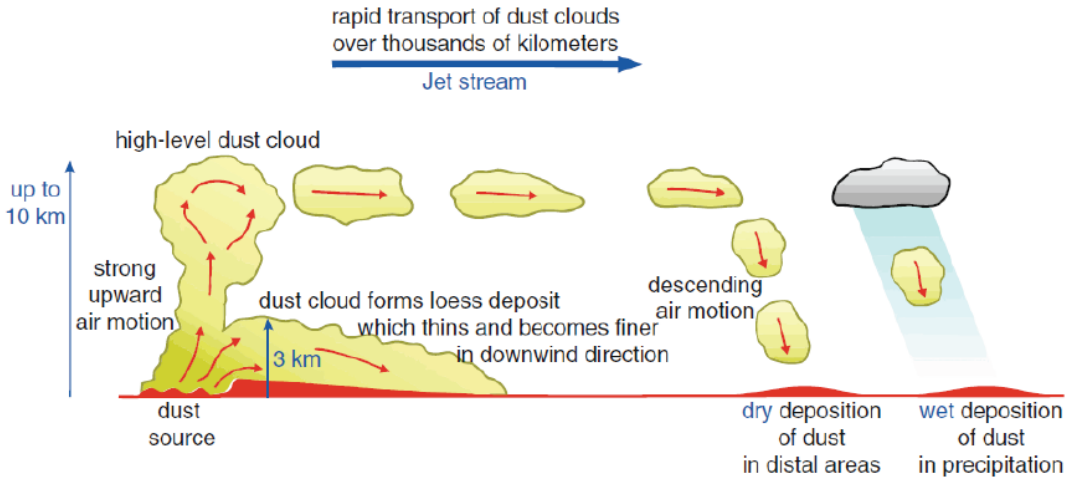

FIGURE 2.2: Schematic diagram showing atmospheric low- and high-level dust transport. Figure redrawn from Pye and Zhou (1989) by Knippertz and Stuut (2014).

Atmospherically transported dust particles may settle in a wide variety of both marine and terrestrial depositional environments, but need to be trapped to prevent subsequent deflation and to accumulate in the geological record. Efficient trapping mechanisms include surface obstacles such as vegetation and topography as well as wet surfaces such as lakes, oceans, ice caps, swamps and salt pans (Pye, 1995). After deposition, the dust particles may be reworked by water or significantly altered by pedogenesis, which obscures their eolian origin (e.g. Smalley, 1972; Smalley et al., 2009; Vandenberghe, 2013; Vandenberghe et al., 2018). Furthermore, the silt particles may have experienced a complex sedimentological history involving multiple steps of transport, deposition and reworking before being transported by dust storms (Li et al., 2020; Licht et al., 2016a; Muhs and Bettis, 2003; Pye, 1995; Smalley, 1966b; Wright, 2001a; Zheng, 2016).

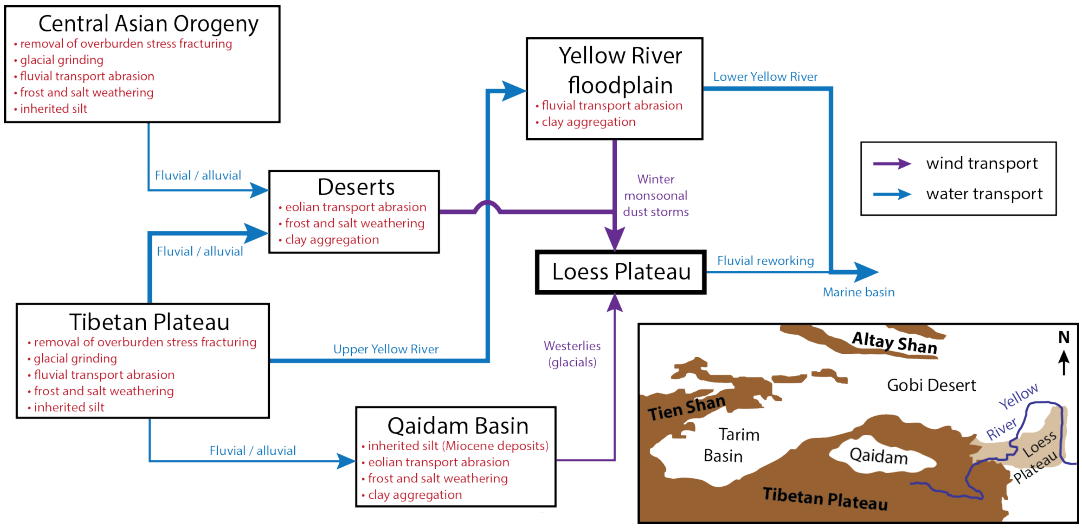

FIGURE 2.3: Schematic overview of predominant transport pathways that result in the deposition and reworking of the Chinese Loess Plateau. Silt producing mechanisms are indicated in red, transport by water in blue and transport by wind in purple. Note that the transport of fine-grained dust by the upper-level westerly jet stream is not included in this diagram. Inset map shows the main geographic features of the northeastern Tibetan Plateau region.

This is exemplified by the dust deposits of the Chinese Loess Plateau where provenance studies have revealed a complex network of transport pathways ultimately resulting in the deposition of dust on the Plateau (Fig. 2.3). This dust was traditionally thought to originate from the interior deserts, but recent provenance studies show that the silt is mainly derived from the northern Tibetan Plateau with some additional contributions from the Central Asian orogeny (including the Tien Shan and the Gobi-Altay; see review in Sun et al., 2020). In this view, the deserts draining these mountain ranges are acting as a transient storage for the alluvial mountain silt to be reworked as loess, rather than a significant source of silt (Assallay et al., 1998; Li et al., 2020; Smalley, 1995; Sun, 2002). Accordingly, Derbyshire et al. (1998) noted that the alluvial fans north of the Tibetan Plateau provide an important source of silt for modern-day dust storms in central China. The Yellow River is also shown to be of major importance in transporting material from the Tibetan Plateau to floodplains in the north, where the silt can subsequently be reworked by dust storms (Fig. 2.3; Bird et al., 2015; Stevens et al., 2013; Licht et al., 2016a; Nie et al., 2015). Some of these studies recognized an additional input of deflated material from the Qaidam Basin during colder glacial periods due to a stronger influence of the low-level westerlies (Fig. 2.3; Kapp et al., 2011; Licht et al., 2016a; Pullen et al., 2011). These studies

demonstrate that the deposition of dust may be only the latest step in a complex history of sediment transport, which has important implications for the petrological and geochemical characteristics of the dust deposits.

2.2.2 Loess and loessites

Dust particles bigger than ~20 µm start to settle as the turbulence in the lower atmosphere decreases, forming blankets of dust which are fining and thinning away from the source due to selective transport (Fig. 2.2; Pye, 1987; Pye and Zhou, 1989). These bodies composed entirely of terrestrial dust are termed loess (Pye, 1995) and are well known from the Quaternary period covering substantial portions of the Earth's surface (Fig. 2.1; Li et al., 2020). Loess can be recognized as buff colored deposits of loosely-packed silt-sized grains forming steep vertical outcrops (Fig. 2.4A). The sedimentary structure is massive, but may contain burrows and fractures. Primary structures such as vague horizontal- or cross-laminations are observed only in rare cases (e.g. Muhs, 2013). Other characteristic features of the Quaternary loess are the interbedded fossil soils (paleosols), which can be readily identified in the field as laterally extensive, reddish-brown layers (Fig. 2.4B). These paleosols are enriched in fine-grained phyllosilicates occurring as clay coatings due to chemical weathering (e.g. Maher, 2016; Muhs and Bettis, 2003).

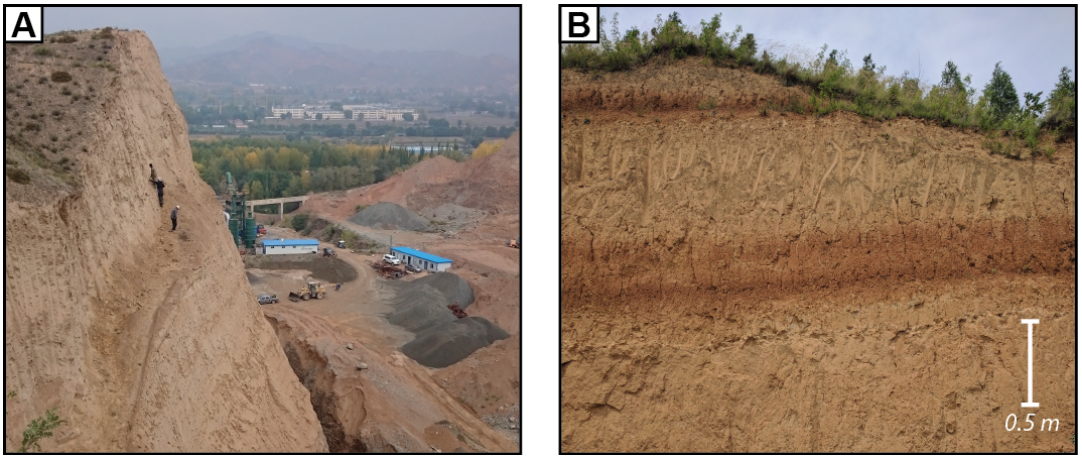

FIGURE 2.4: Pictures of Quaternary loess from: (A) Ledu (Xining Basin) in the westernmost Chinese Loess Plateau, person at outcrop for scale. (B) Xi'an in the south-central Chinese Loess Plateau.

The lack of primary sedimentary structures in loess resulted in controversies dating back to the nineteenth century regarding the origin of these deposits (Pye, 1987; Smalley et al., 2001; Richthofen, 1882). Massive silt beds are common in various depositional environments including alluvial, lacustrine, eolian and marine settings. Additionally, it has been proposed that loess may have formed by in-situ weathering of the underlying material (e.g. Pécsi, 1990). Richthofen was one of the early proponents arguing for an eolian origin and listed numerous observations from the Chinese Loess Plateau to support his case (Smalley et al., 2001; Richthofen, 1882). These include the common occurrence of rootlets, land snails and mammal fossils indicating a terrestrial environment. Furthermore, the distinctly different composition of loess compared to the underlying bedrock suggests transport from elsewhere, rather than in-situ weathering. The most convincing evidence for an eolian nature of this transport is the sheet-like draping of loess bodies covering the underlying topography and resulting in undulating surfaces found over a wide altitudinal range (Muhs,

2013; Pye, 1987; Richthofen, 1882). Pye (1987) adds that the loose packing and associated high porosity of loess is an additional characteristic for eolian silt. Furthermore, the geographic relationship between the pathways of modern-day storm tracks and the fining and thinning of loess bodies further corroborates their eolian origin (Pye, 1987). However, these observations are of limited use when studying older geological records, because burial diagenesis affects porosity, the paleo-topography is rarely preserved and ancient atmospheric pathways are unknown.

Nevertheless, lithified pre-Quaternary deposits sharing the characteristics of Quaternary loess have been observed and interpreted as dust-blown deposits. These strata are termed loessites (Pye, 1995) and have been identified using the following criteria: 1) massive sedimentary structure showing no evidence of alluvial or lacustrine deposition (e.g. Ding et al., 1998b; Guo et al., 2002; Johnson, 1989; Wilkins et al., 2018), 2) homogeneous silt-sized grain-size distributions due to selective transport (e.g. Carrapa et al., 2015; Fan et al., 2020; Guo et al., 2001; Guo et al., 2002; Li et al., 2018a; Licht et al., 2014; Lu et al., 2001; Sun et al., 2010; Wang et al., 2016b; Wasiljeff et al., 2020; Yang and Ding, 2004; Zheng et al., 2015), 3) angular shapes of the quartz grains, as well as other surface morphology features indicating eolian transport (e.g. Carrapa et al., 2015; Edwards, 1979; Fan et al., 2020; Guo et al., 2001; Guo et al., 2002; Li et al., 2018a; Liu et al., 2006; Licht et al., 2014; Wang et al., 2016b, 4) provenance signals similar to the Quaternary loess including major, minor and rare earth elemental compositions, as well as Nd isotopes and detrital zircon U-Pb (e.g. Garzione et al., 2005; Guo et al., 2002; Li et al., 2018a; Licht et al., 2016b; Jiang and Ding, 2010; Sun et al., 2010; Sun and Windley, 2015; Wang et al., 2014a; Wang et al., 2016b), 5) magnetic fabric similar to Quaternary loess (Liu et al., 1988), 6) geographic relationships between the supposed source of the dust and the dust bodies as observed in grain-size and thickness of the deposits (Miao et al., 2004; Yang and Ding, 2004), 7) low accumulation rates (Ding et al., 1998a; Garzione et al., 2005; Sun et al., 1998b) and 8) the occurrence of land snail fossils (Li et al., 2006a).

Another commonly used argument in identifying loessites is the absence of alternative depositional models to explain the occurrence of massive silt-sized deposits in the terrestrial realm (e.g. Johnson, 1989). However, several studies have proposed a distal mudflat/floodplain involving predominantly alluvial deposition as an alternative to exclusively windblown deposits (Alonso-Zarza et al., 2009; Alonso-Zarza et al., 2010; Flynn et al., 2011; Li et al., 2006b; Liu et al., 2019; Zhang et al., 2013). In the following, we will present this mudflat depositional model.

2.2.3 Mudflat depositional model

Deposition on terrestrial mudflats involves predominantly alluvial transport in a low-relief basin, which would enable extensive suspension settling of fine-grained material in a fluvio-lacustrine environment (Fig. 2.5; Donselaar et al., 2013; Smoot and Lowenstein, 1991; Talbot et al., 1994; van Toorenenburg et al., 2018). This is especially common in arid to semi-arid settings and endorheic basins where downstream evapotranspiration and percolation may result in the subaerial termination of rivers on the floodplain rather than in lacustrine delta's (Donselaar et al., 2013). Modern analogues for these sedimentary systems include the Altiplano Basin in Bolivia (Donselaar et al., 2013; van Toorenenburg et al., 2018) and the continental interior of Australia (Talbot et al., 1994).

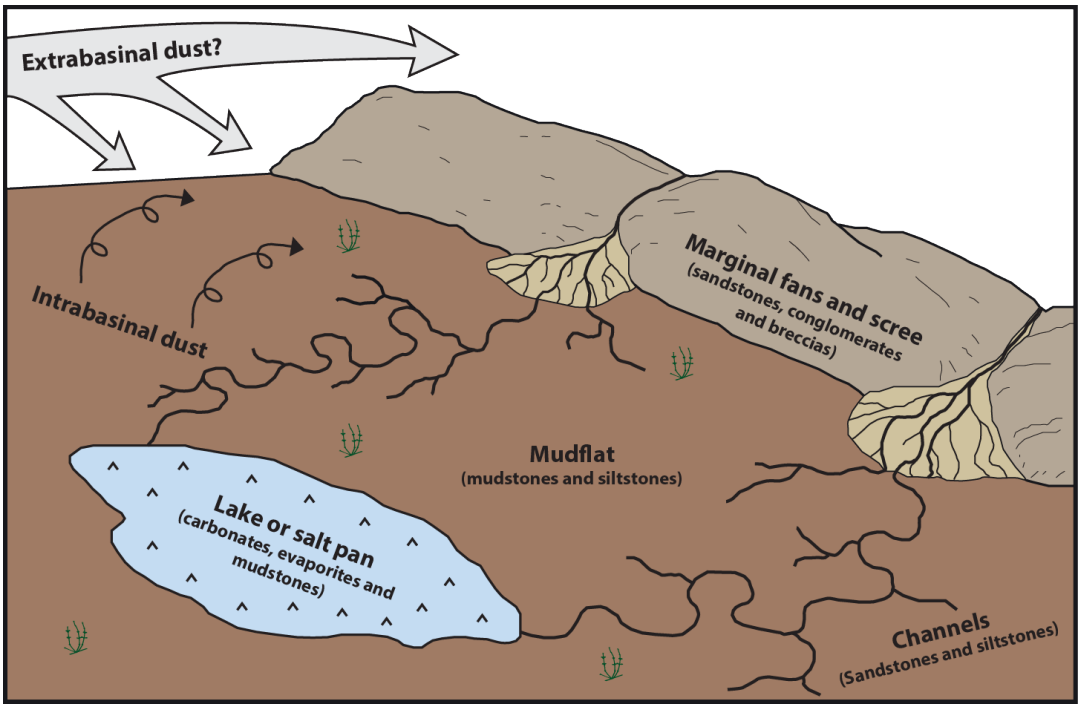

FIGURE 2.5: Alternative depositional model for loessites involving a low-relief basin resulting in alluvial deposition on an extensive mudflat. In addition, eolian deposition may occur by reworking local sediments or atmospheric transport of extrabasinal dust. Redrawn from Chapter 5 and Talbot et al. (1994).

Most of the sediments in this setting are derived from the local mountain ranges forming proximal alluvial fans and scree deposits containing breccias, conglomerates and sandstones. Fluvial channels, either ephemeral or perennial, transport the sediment to the more distal regions of the basin where the finer material is deposited on extensive mudflats via terminal fans, crevasse splays and overbank suspension settling during episodic floods. These flooding events are able to inundate vast areas due to the low gradient of the basin and lakes or salt pans may be found at the distal ends of this sedimentary system. The transition from proximal to distal sediments may occur rapidly. For example, the proximal sands in the Australian interior are observed to extend only one kilometer from the valley mouth into the basin and subsequently grade to open plains consisting predominantly of mud (Talbot et al., 1994). An additional input of windblown dust to the mudflat may occur as well, either from an extrabasinal source or by deflation and redeposition of local sediments. The latter is especially prevalent because most mudflats occur in arid to semi-arid environments and provide ample loose silt for eolian reworking. Fine-grained material entering mudflat systems can alternate multiple times between fluvial transport and eolian transport (Hardie et al., 1978), which makes the identification of "true" dust deposits difficult.

This mudflat model involves alluvial, fluvial and lacustrine deposits and thereby provides an explanation for the co-occurrence of lacustrine siltstones and fluvial sandstones, which are observed to interbed the loess-like siltstones in numerous locations (e.g. Alonso-Zarza et al., 2009; Alonso-Zarza et al., 2010; Flynn et al., 2011; Guo et al., 2010; Liu et al., 2019). Yet massive terrestrial siltstones are commonly interpreted as loessites or loess-like which implies deposition almost exclusively by wind. In the following, we will show that the loess-like features listed in section 2.2

may also occur via other modes of deposition on a terrestrial mudflat and therefore cannot be unambiguously linked to dust deposition alone.

2.2.4 Alluvial origin for massive terrestrial siltstones

The massive sedimentary structure observed in siltstones is often cited as characteristic for eolian deposition and is indeed similar to the Quaternary loess. However, it can be formed by different mechanisms as well. Modern observations show that clay and silt may aggregate to form sand-sized particles that are transported as bedload in fluvial systems or by wind to form lunettes (Rust and Nanson, 1989; Smoot and Lowenstein, 1991; Talbot et al., 1994; Wright and Marriott, 2007). Subsequent burial disaggregates these particles resulting in a massive sedimentary structure. In addition, post-depositional processes such as bioturbation, mud-cracking or pedogenesis may occur on subaerially exposed mudflats and rework the original sedimentary structures resulting in massive mud- and siltstones with only vaguely recognizable laminations (Smoot and Olsen, 1988; Talbot et al., 1994).

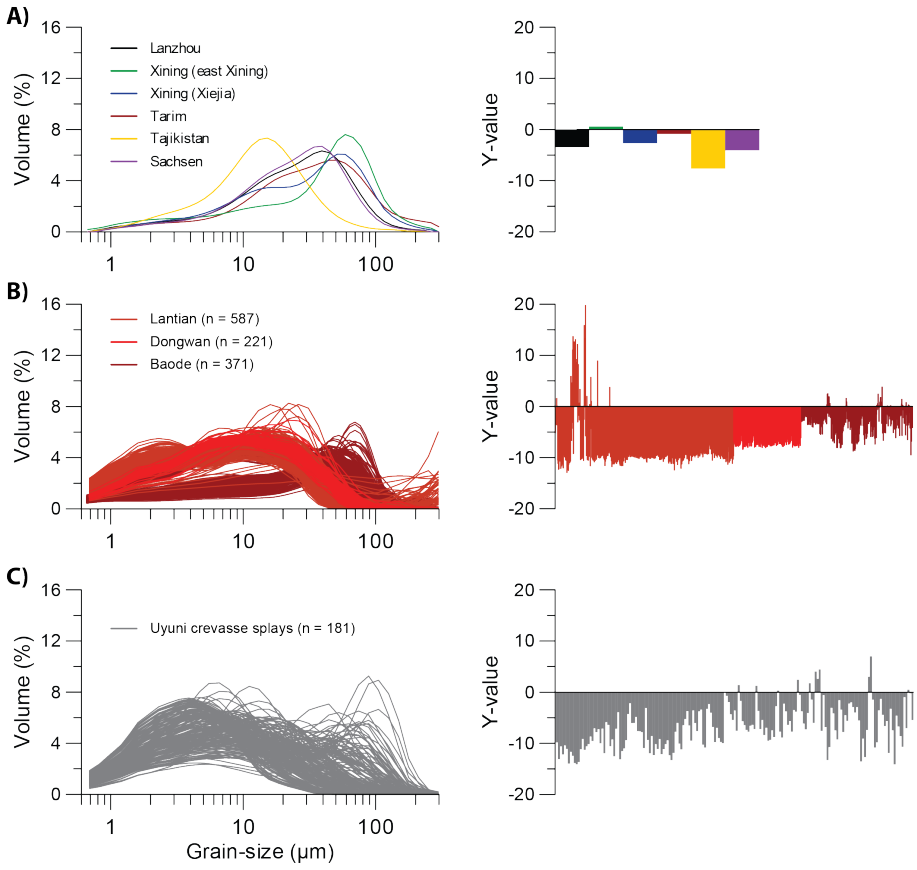

FIGURE 2.6: Grain-size distributions and Y-values calculated using the mean, sorting, skewness and kurtosis derived using the logarithmic moment method as implemented in Gradistat (Blott and Pye, 2001) and the Y-value equation of Lu et al. (2001) of: (A) Quaternary loess from a variety of locations (measured using the same methods as in Chapter 5; (B) Mio-Pliocene Red Clay from the southern (Lantian), western (Dongwan) and northeastern (Baode) Chinese Loess Plateau (Shang et al., 2016); (C) Crevasse splay deposits from the modern-day Altiplano Basin mudflat (van Toorenenburg et al., 2018). Note that the grain-size distributions shown here are derived from various studies using different pre-treatments, laser diffractors and optical parameters that may incur slight variations (Varga et al., 2019b).

Another indicator for dust is the uniform loess-like grain-size distribution. However, even the Quaternary loess shows a wide variety of poorly-sorted grain-sizes

depending on the source, distance to the source and pedogenic overprint (Fig. 2.6A; Pye, 1995; Újvári et al., 2016; Vandenberghe, 2013; Vandenberghe et al., 2018). A commonly accepted example of pre-Quaternary loess deposits are the Red Clay strata of central China (e.g. An et al., 2001; An, 2014). However, the grain-size distributions of the Red Clay are finer than Quaternary loess (Fig. 2.6B and C) and more similar to those found on the alluvial mudflat of the Altiplano Basin (Fig. 2.6D; van Toorenenburg et al., 2018). This shows that the grain-size distributions alone are not a good indicator for eolian transport. Lu et al. (2001) used the empirical Y-value, which is based on various grain-size characteristics including the mean, sorting, kurtosis and skewness, to distinguish eolian deposits with a negative Y-value from alluvial deposits which have a positive Y-value. However, most of the alluvial mudflat grain-size distributions shown here have negative Y-values as well, which indicates that this is not a reliable tool for identifying eolian deposits (Fig. 2.6).

The angular shape of the silt-sized quartz grains is proposed to be evidence of loess and is commonly linked to eolian transport. Newly weathered quartz grains derived from granites tend to form sand-sized particles due to crystallographic constraints (Smalley, 1966a). To create silt-sized quartz, these grains need to be broken and the resulting angular shape is therefore due to abrasional processes rather than an indication of eolian transport (Pye, 1987). Furthermore, the conchoidal fractures commonly observed on the surface of the quartz grains (e.g. Liu et al., 2006) may be found in a variety of depositional environments and alone are not diagnostic of eolian transport (Vos et al., 2014).

Geochemical provenance signatures showing similarities with the overlying Quaternary loess have been used as evidence for windblown transport, but also to derive paleowind directions, especially when linked to extrabasinal sources. However, as shown in section 2.2, dust deposits commonly experience a complex sedimentological history including both alluvial and eolian reworking (Fig. 2.3). The geochemical properties can thus be expected to be similar for both the eolian and alluvial sediments and are not necessarily diagnostic for either one. Furthermore, the REE patterns which are often cited as evidence for eolian transport are merely an indication of a multi-recycled and well-mixed sediment (Gallet et al., 1998) rather than eolian dust. Interestingly, Wang et al. (2014a) show a loess-like geochemistry for the siltstones interbedding the fluvial sandstones that underlie the Chinese Loess Plateau. They use this as evidence to propose that these silts should be regarded as dust as well, but alternatively it could indicate that both alluvial and eolian siltstones have a similar geochemistry, especially because both are ultimately derived from the Tibetan Plateau (Fig. 2.3). Furthermore, it should be noted that most bulk geochemistry studies only explore similarities with the Quaternary loess in order to imply long-range extrabasinal dust transport while failing to assess the influence of intrabasinal sources. More recent provenance studies using U-Pb signatures from detrital zircons and heavy mineral assemblages show significant contributions from local mountain ranges. The zircon age distributions of the Dongwan and Chaona Red Clay sections show strong similarities with the neighboring Liupan Shan (Nie et al., 2014; Shang et al., 2016), whereas the Lantian and various sections in Tianshui Basin indicate the neighboring Qinling Shan as the predominant source (Liu et al., 2019; Zhang et al., 2018a). This may indicate that local alluvial transport plays a major role rather than large-scale extrabasinal dust fluxes (Liu et al., 2019).

Liu et al. (1988) used the magnetic fabric to distinguish eolian from alluvial strata.

But this method is of limited use because the magnetic mineral assemblage and tectonic strain varies through time which would alter the magnetic fabric (Borradaile and Henry, 1997). Other studies have used basin-scale correlations between records to identify trends in grain-size and thickness. However, whether these can be linked to proposed dust sources or alluvial material derived from local mountain ranges remains debated (Ding et al., 2000; Liu et al., 2019; Miao et al., 2004; Yang and Ding, 2004). Furthermore, both the low accumulation rates and the occurrence of terrestrial snails are not diagnostic of eolian transport and can be observed on alluvial mudflats as well.

In conclusion, the evidence used to identify loess in pre-Quaternary records cannot exclude alternative interpretations involving alluvial deposition of silt on extensive low-gradient mudflats. This is supported by the co-occurrence of massive terrestrial siltstones with fluvial sandstones and lacustrine mudstones which would suggest various modes of deposition, in contrast to the almost exclusively windblown bodies of loess observed in the Quaternary period. Dust deposition may occur on these mudflats as well, but should be regarded among other alluvial sediment contributions (Fig. 2.5).

2.3 Methods to identify dust in the geological record

We synthesize here a set of existing methods which, when combined, enable a reliable identification of dust in the geological record while acknowledging additional alluvial components. First, quartz surface morphology analysis enables the identification of transport modes for the various grains and distinguishes eolian from alluvial components. Second, detailed provenance analysis enables to distinguish local reworked sediments from extrabasinal components which, in the case of dust, may aid in reconstructing atmospheric pathways and dust fluxes. Third, end-member analysis of grain-size and -shape distributions enables to quantify the various sedimentary contributions in the records. And finally, additional paleoenvironmental and basin analyses may be used to strengthen the interpretations regarding an eolian origin.

2.3.1 Quartz surface morphology

Particle collisions during transport result in characteristic nm- to µm-scale features on the grain surfaces. These features are largely dependent on the fluid viscosity of the transporting medium and can therefore be used to distinguish sediment transport in wind and water. The analysis of these surface morphologies has been applied to quartz grains in particular, because of their high abundance (e.g. Krinsley and Takahashi, 1962; Vos et al., 2014). Consequently, quartz surface morphologies have been extensively described using a scanning electron microscope (SEM) on quartz grains from a variety of both modern and ancient sedimentary environments, as well as on artificially-produced quartz particles subjected to various transport conditions in the lab (e.g. Costa et al., 2013; Keiser et al., 2015; Krinsley and Takahashi, 1962; Nieter and Krinsley, 1976; Vos et al., 2014). For a more detailed review on the sample preparation, SEM handling and surface morphology descriptions we refer to Vos et al. (2014) and references therein.

In general, the impacts by wind are of higher energy than subaqueous collisions which are cushioned by the surrounding water. The latter are therefore characterized

by µm-scale, v-shaped percussion marks, whereas eolian impacts result in larger conchoidal fractures separated by meandering ridges, crescentic percussion marks and dish-shaped depressions (Fig. 2.7). Furthermore, the higher energy eolian collisions result in the shattering of the quartz crystal lattice and create a highly reactive surface of amorphous silica with adhering nm-scale particles and thin parallel upturned plates, both composed of silica (Fig. 2.7; e.g. Krinsley and Trusty, 1985; Vos et al., 2014). Identification of these features therefore enables to distinguish between an alluvial or eolian mode of transport and can be applied to identify dust in the geological record (e.g. Licht et al., 2014; Fan et al., 2020). Careful quantification of these surface morphological features may even indicate the relative importance of various transport mechanisms for grains that have experienced multiple modes of transport. In addition, the identification of overprinting relations between these morphological features may help to derive the sequential order of the various transport modes (Vos et al., 2014), which is especially useful for loess-like materials characterized by both alluvial and eolian deposition and reworking (Fig. 2.5).

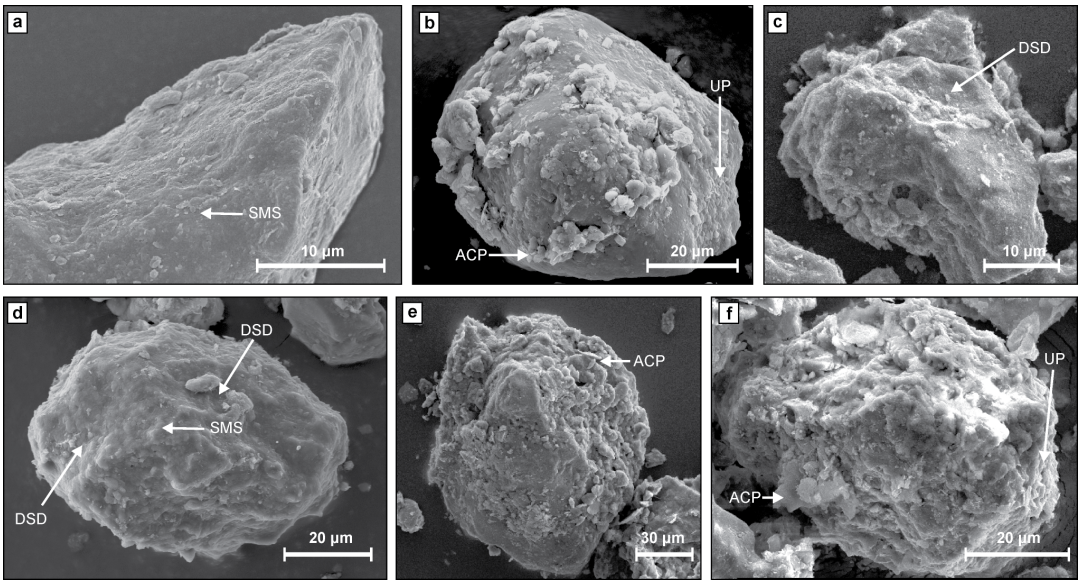

FIGURE 2.7: SEM images of quartz grains from the late Eocene strata of the Xining Basin showing morphological features resulting from high impact collisions and indicating eolian transport. These features include dish-shaped depressions (DSD), smooth surfaces (SMS), adhering clay-sized particles (ACP). Figure is reproduced from Licht et al. (2014).

However, it should be noted that most of the eolian surface morphologies described above have been identified on sand-sized quartz grains which are transported by saltation and creep, whereas silt-sized dust of <50 µm is transported in suspension (e.g. Újvári et al., 2016). Furthermore, silt-sized grains may not have enough momentum for the high energy impacts needed to create the typical eolian surface morphologies. So far, only few studies have focused on the surface morphologies of silt-sized quartz grains. Krinsley and McCoy (1977) note that most silt-sized quartz grains are fragments of broken sand-sized grains. They suggest that even though the silt-sized material may not create characteristic surface morphologies, the silt may still record useful surface textures on the surfaces of the original sand-sized grain preserved on some of the silt particles after fragmentation. Other studies have noted significant differences between the quartz morphologies of loess and eolian sand. The shape of the latter is commonly rounded and characterized by bulbous edges (e.g. Krinsley and Trusty, 1985; Vos et al., 2014), whereas silt-sized quartz

from loess deposits is subangular to subrounded with sharp edges and flat cleavage surfaces (Krinsley and Smalley, 1973; Nieter and Krinsley, 1976; Pye, 1987). Other more delicate features such as polygonal cracks formed by salt weathering are more common on silt-sized particles and rarely observed on sand-sized grains because the cracks are easily abraded by the higher energy impacts of saltation compared to transport in suspension (Pye, 1987; Vos et al., 2014). Adhering nm-scale particles are commonly observed in loess as well (Pye, 1987) and may be a diagnostic feature, because wind tunnel experiments show that wind-transported silt creates adhering silica particles due to abrasion (Nieter and Krinsley, 1976). However, Pye (1987) notes that the composition of the adhering particles in loess consist of illite, kaolinite and calcite of pedogenic origin as well as silica and therefore careful compositional analysis is required before interpreting the adhering particles as eolian features.

Quartz surface morphology analysis provides a strong tool to derive transport modes and identify dust in the geological record. Diagenetic overprinting may hamper the analysis for deposits older than the Mesozoic, but can be easily recognized as crystal overgrowths (Vos et al., 2014). Furthermore, the method may be biased by the expertise of the user in recognizing characteristic surface features but recent image analysis tools may aid in automating this process (Říha et al., 2019). However, extensive data is required for training these algorithms, but has been lacking for the silt-sized domain. Future work should therefore focus on describing quartz silt from a variety of sedimentary transport processes to bring the current surface morphology knowledge up to date with the sand-sized grains.

2.3.2 Provenance

Provenance studies play an important role in deriving the source regions of the dust and in assessing the intra- and extrabasinal contributions. In addition, these studies are widely used to derive atmospheric transport pathways (e.g. Soreghan et al., 2002; Soreghan et al., 2014). However, it should be emphasized that the provenance signal itself is no evidence for eolian deposition and should be used together with other data. Only when a clear extrabasinal source is identified in the absence of a fluvial connection to the deposits, can the provenance signal be used as proof for eolian transport. Still, it would remain unclear whether this mode of transport was the last step of sediment transport because the material could have been subsequently reworked. On the other hand, a local provenance is not exclusive to alluvial deposits and may result from local wind erosion of nearby outcrops (e.g. Kapp et al., 2015)

Sun et al. (2020) provide an extensive review of provenance tools which have been used on the Chinese Loess Plateau but are also applicable to other dust records and will be summarized in the following. These tools can be subdivided in tracers of single minerals or mineral assemblages. Single-mineral tracers include the various characteristics of quartz minerals such as $\delta^{18}O$, Electron Spin Resonance (ESR) and Crystallinity Index (CI), which are controlled by the age and temperature at the formation of the minerals. Another widely used single-mineral tracer is the U-Pb age spectra of detrital zircon grains. Mineral-assemblage tracers include elemental ratios, isotopic signatures of Sr-Nd-Pb-U, Hf-Th and Re-Os, magnetic minerals and heavy mineral composition. Preferably, multiple tracers should be used to identify the provenance more accurately.

Elemental ratios and isotopic signatures are generally measured on bulk samples,

which has the advantage of considering the entire range of grain-sizes in the material (Bird et al., 2020). On the other hand, these bulk mineral and geochemistry signatures perform poorly in sediments with mixed sources because the provenance signatures average out. To overcome this limitation, the signatures should be characterized for grain-size fractions or individual grains representing the various sources and modes of sediment transport. One of these methods applied to individual grains is measuring the U-Pb age spectra of zircons, which accurately distinguishes mixtures of various sources if a large enough number of grains are measured (Licht et al., 2016a). In addition, robust minerals such as zircons and quartz are less affected by post-depositional weathering and are therefore preferred over other minerals or bulk analyses. In the future, the use of other minerals such as titanite and rutile may be explored for U-Pb age spectra as well.

Provenance methods measuring the isotopic ratios of individual grains are limited to relatively large grains of often >40 µm due to the amount of material required via laser ablation. Neglecting the smaller grain-sizes introduces a size bias (e.g. Bird et al., 2015), but future technical developments may improve these limitations. This would enable characterizing the elemental and isotopic signatures of individual grains, rather than bulk measurements and would significantly improve the recognition of various source regions in mixed sediments.

2.3.3 End-member analysis of grain-size distributions

Uniform grain-size distributions in the silt domain are used to identify dust in geological records. However, these are of limited use due to the wide variety of overlapping grain-sizes occurring in both dust and other alluvial environments (Fig. 2.6). Furthermore, these distributions are rarely unimodal, but rather contain a multimodal mix representing grain-size fractions derived from various sources and sorted by distinct transport mechanisms. Unmixing these grain-size distributions enables the quantification of the various components within the sedimentary record (Fig. 2.8). This is especially useful for studying sedimentary environments with multiple depositional modes such as a low-relief terrestrial mudflat (Fig. 2.5).

Various methods can be used to unmix grain-size data including parametric curve-fitting and end-member modelling (Varga et al., 2019a). Parametric curve-fitting uses predefined functions of distributions and fits these with the measured grain-size distributions in the sedimentary record to quantify their relative abundance (Paterson and Heslop, 2015; Sun et al., 2002; Wu et al., 2020). The accuracy of this analysis depends on the predefinition of the fitting functions and is especially useful for modern and recent geological records, in which the potential sources are well constrained. However, on longer geological timescales, knowledge of the grain-sizes in the various sources is usually limited. In these cases, non-parametric end-member modelling is a more appropriate method (Weltje and Prins, 2007). End-member modelling uses an algorithm that considers the entire grain-size dataset of the record to construct multiple end-member distributions in which the dataset can be optimally decomposed (Fig. 2.8). In recent years, various end-member algorithms have been developed and shown to perform well using both artificial and natural datasets (Dietze and Dietze, 2019; Paterson and Heslop, 2015; van Hateren et al., 2018; Varga et al., 2019a).

End-member modelling has been successfully applied to distinguish eolian and alluvial contributions in marine cores (Weltje and Prins, 2003) and lacustrine records

(Dietze et al., 2014; Rits et al., 2016) as well as various dust components in Quaternary loess (Nottebaum et al., 2015; Prins et al., 2007) and Neogene Red Clay (Shang et al., 2016; Xu et al., 2018). However, it should be noted that the end-member grain-sizes themselves provide limited sedimentary information and should be combined with other data such as quartz surface morphology and provenance to interpret their sedimentary origin. After interpreting the origin of the end-members, their contributions can be quantified throughout the studied records.

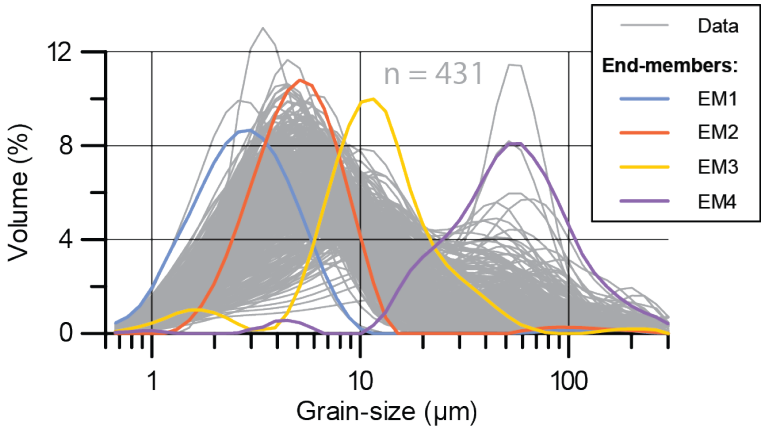

FIGURE 2.8: End-member analysis of grain-size distributions from Eocene mudflat deposits in the Xining Basin. Data and methods are reported in Chapter 5. EM4 is interpreted as dust based on quartz surface morphologies (Licht et al., 2014) and provenance (Licht et al., 2016b).

Various techniques can be used to measure grain-size distributions, but laser diffraction is the most widely applied for silt-sized sediments because of the high reproducibility and measurement speed (Goossens, 2008). This technique measures the grain-size distribution indirectly by converting the diffraction pattern of a laser beam passing through the suspended particles. The accuracy of the measurements depends on the optical parameters used for the conversion and may vary between different laser diffractors (Varga et al., 2019b). A more direct but time consuming measurement of the grain-size distributions can be obtained by using dynamic image analysis, which simultaneously provides additional data on the grain-shapes (Shang et al., 2018; van Hateren et al., 2020; Varga et al., 2018). These combined size and shape characteristics may aid to better define the end-members (van Hateren et al., 2019). Furthermore, a Raman spectroscope can be coupled to the optical microscope to determine the mineral properties of the studied particles (Szalai et al., 2019). Since sediment transport is controlled by the size, shape and density (and therefore mineralogy) of the particles, constraining these three parameters in one single analysis will benefit the characterization of both dust and other components in the sedimentary record.

2.3.4 Stratigraphic and basinal analysis

For significant dust deposition to occur, an effective source, sink and transport mechanism are needed (Pye, 1995). The source should provide ample of loose, silt-sized material available for transport and the sink should contain a trap, such as vegetation, a wetted surface or topographic obstacle to preserve the dust. Additional sedimentological, stratigraphic and biological data may therefore be used to assess the capacities of both the source and sink (e.g. Vandenberghe et al., 2018). In settings where the sink has a different bedrock lithology than the dust source, it is especially convenient to recognize allogenic dust components (e.g. Muhs, 2013). Quaternary

examples include the identification of quartz grains in the basaltic soils on Hawaii (Begét et al., 1993) and in a volcanic maar in Japan (Xiao et al., 1997). In settings involving chemically- or biologically-formed sediments it is similarly convenient to recognize and quantify siliciclastic dust components. For example, Permian dust accumulation rates have been derived from coal beds by measuring the titanium content as a proxy for dust (Large and Marshall, 2015; Marshall et al., 2016).

Furthermore, it should be noted that individual geological records reflect only the depositional environment of a specific location. This environment is partly constrained by the basin configuration and surrounding topography. Records located near the basin margin may contain abundant alluvial material derived from the neighboring mountain ranges, whereas windblown dust may accumulate in records located in a more distal setting. Individual records may be hindered by local autogenic variability related to splays, storms, events, and channels moving, eroding and/or redepositing sediments (e.g. Hajek and Straub, 2017). As such, a single record is limited for a robust evaluation of dust deposition and a basin-scale analysis is required instead. The use of multiple records to derive a regional or even global imprint of paleo-records is common practice in marine studies. Long-term stable carbon and oxygen isotopes series have been stacked to reduce the local noise and disturbances since considerable time (e.g. Hays et al., 1976; Lisiecki and Raymo, 2005). Similar methods have been applied to Quaternary loess records, but should be used for pre-Quaternary dust records as well.

2.4 The geological record of the Chinese Loess Plateau

Using the considerations discussed above, we reassess the geological record of the Chinese Loess Plateau located in north-central China where dust has accumulated for millions of years (Fig. 2.9). The Loess Plateau has therefore provided an invaluable record for studying paleoenvironmental changes in the terrestrial realm, especially during the Quaternary period (see reviews in: An, 2014; Liu and Ding, 1998; Maher, 2016; Porter, 2001). In recent years, this dust record has been expanded to include the underlying siltstones of increasingly older ages (Fig. 2.9). These strata cover the Pliocene-Miocene epochs in the eastern Loess Plateau (An et al., 2001; Ao et al., 2016; Qiang et al., 2001; Sun et al., 1998b; Sun et al., 1998a; Wang et al., 2014a; Xu et al., 2009), the Miocene-Oligocene in the west (Guo et al., 2002; Qiang et al., 2011), and the Eocene in the westernmost part of the Loess Plateau (Chapter 5; Licht et al., 2014). In the following, we will review the nature of these deposits and challenge the exclusively eolian origin of the pre-Quaternary strata.

2.4.1 Quaternary loess

The Chinese Loess Plateau covers a wide area of $\sim$4.4 $\times$ 105 km^2 with Quaternary dust ranging from several tens of meters to up to 450 meters in thickness (Fig. 2.1 and 2.9; see reviews in: An, 2014; Liu and Ding, 1998). This loess is composed of silt-sized grains containing predominantly quartz, but also significant amounts of feldspar, mica, a varying carbonate content and minor components of clay-sized phyllosilicates (mostly illite, but also smectite, chlorite, kaolinite and vermiculite) as well as iron oxides (Jeong et al., 2011). The loess is interbedded with reddish paleosols due to weathering and oxidation forming nanoscale hematite and other fine-grained phyllosilicates (Fig. 2.4B; Bronger and Heinkele, 1989; Chen et al., 2010; Jeong et al., 2011; Rutter et al., 1991; Rutter and Ding, 1993; Maher, 2016). Pedogenic

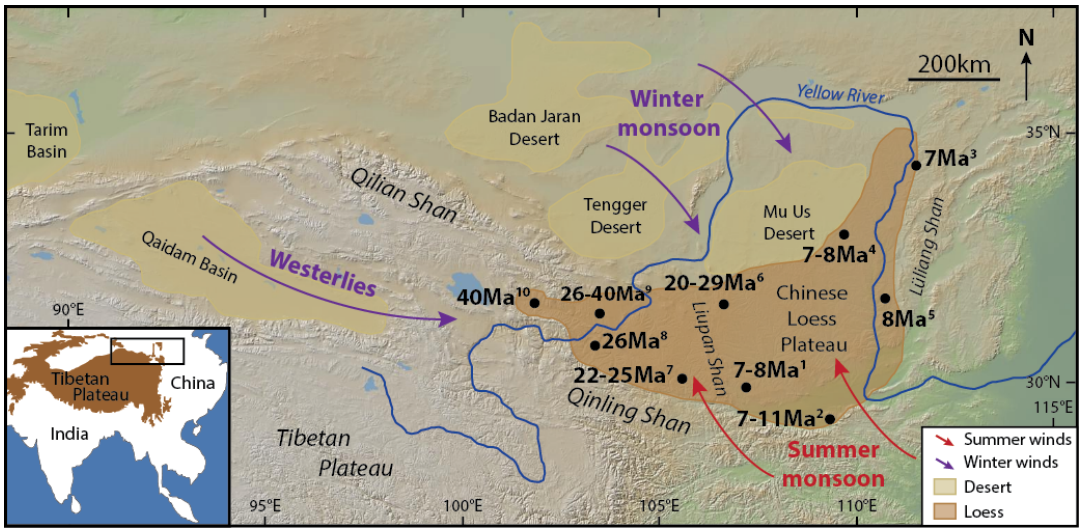

FIGURE 2.9: (A) Map of the Chinese Loess Plateau (modified from Chapter 5) showing the dominant atmospheric pathways and the various basal ages reported for the onset of loess: 1) central Loess Plateau: Ding et al., 2001; Song et al., 2001; Sun et al., 1997; Sun et al., 1998b; Sun et al., 1998a; 2) southern Loess Plateau: Sun et al., 1997; Wang et al., 2014a; Zheng et al., 1992; 3) Baode: Zhu et al., 2008; 4) Jiaxian: Ding et al., 1998a; Qiang et al., 2001; 5) Shilou: Xu et al., 2009; age reinterpreted by Ao et al., 2016; 6) Sikouzi: Jiang and Ding, 2010; age reinterpreted by Wang et al., 2011; 7) Tianshui Basin: Guo et al., 2002; record extended by Qiang et al., 2011; 8) Linxia Basin: Garzione et al., 2005; 9) Lanzhou Basin: Zhang et al., 2014; age reinterpreted by Wang et al., 2016a; 10) Xining Basin: Chapter 5; Licht et al., 2014. Modern-day topographic map is from http://www.geomapapp.org.

magnetite is observed in the paleosols as well and is responsible for higher magnetic susceptibilities than in the primary loess and commonly used as a proxy for pedogenesis (Ahmed and Maher, 2018; Maher and Thompson, 1991; Zhou et al., 1990). The detrital carbonate grains in the paleosols are leached and precipitated as root casts or carbonate concretions (Bronger and Heinkele, 1989; Rutter et al., 1991; Rutter and Ding, 1993).

Dating of the Chinese loess records revealed a temporal correlation between the loess-paleosol sequences and the glacial-interglacial cycles of the Quaternary period (Fig. 2.10; Bloemendal et al., 1995; Ding et al., 1995; Ding et al., 2002; Heller and Liu, 1984; Kukla et al., 1988). The dustier glacial periods are characterized by higher loess accumulation rates and coarser grain-sizes whereas the interglacials correlate with lower accumulation rates, finer grain-sizes and pedogenesis. In terms of atmospheric circulation (Fig. 2.9), the glacial periods are thought to be dominated by dust storms linked to the low-level westerlies (Kapp et al., 2011; Pullen et al., 2011) and the northwesterly East Asian winter monsoon transporting silt from the arid inlands of the Asian interior (An et al., 1990; Pye and Zhou, 1989; Roe, 2009; Sun et al., 2001; Sun, 2002). The interglacial periods reflect the predominance of the southeasterly East Asian summer monsoon, reducing dust accumulation, bringing moisture and promoting soil formation (An et al., 1990). The interplay between these atmospheric configurations is observed on the Chinese Loess Plateau as a gradient of decreasing grain-size and loess thickness going from the dry winter monsoonal northwest to the wetter summer monsoonal southeast (Ding et al., 1999a; Ding et al., 2005; Porter, 2001). In addition, the deposits are increasingly weathered going from the northwest to the southeast (Jeong et al., 2011).

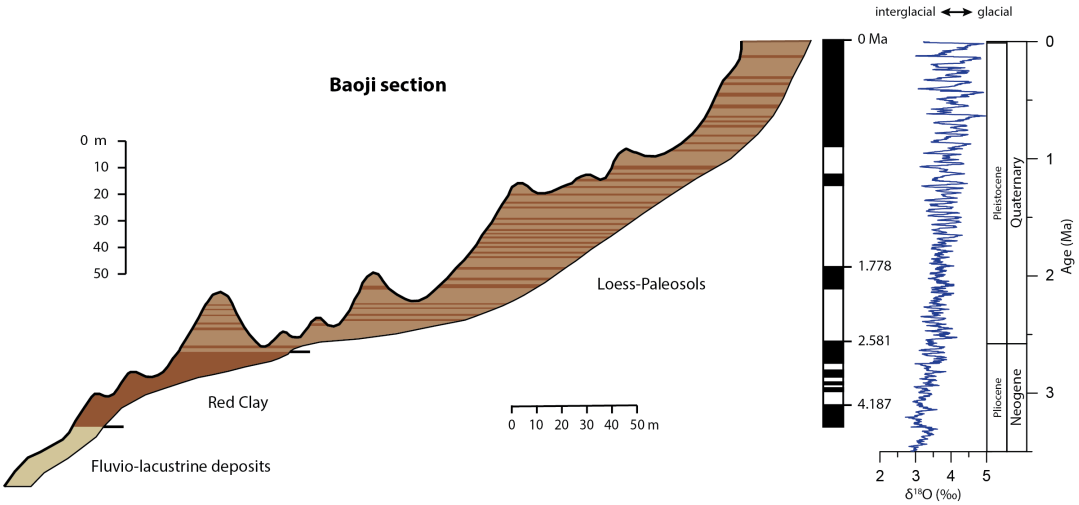

FIGURE 2.10: Stratigraphy at Baoji (central Chinese Loess Plateau) showing fluvio-lacustrine and Red Clay strata underlying the Quaternary loess-paleosol alternations (redrawn from Ding et al., 1994). Magnetostratigraphy is from Evans et al. (1991) with ages recalibrated to the GTS16 (Ogg et al., 2016). Benthic foraminifera $\delta^{18}O$ are shown on the right (5-point moving average through the compilation of Zachos et al., 2008) to reflect the glacial-interglacial cycles.

2.4.2 Pre-Quaternary 'loess'

The Quaternary loess is underlain by Neogene strata that have been proposed to be formed by predominantly dust deposition as well. These strata are commonly referred to as Red Earth, Red Clay or sometimes Hipparion Red Clay after the eponymous fossils found in these deposits (Fig. 2.10; Mo and Derbyshire, 1991; Flynn et al., 2011; Kaakinen et al., 2013). However, other than the name suggests, most of these deposits consist of fine silt rather than clay (Ding et al., 1998b; Flynn et al., 2011; Guo et al., 2001; Han et al., 2002; Lu et al., 2001; Shang et al., 2016; Yang and Ding, 2004). The beds have a pronounced reddish color and the sedimentary structure is massive with occasional sub-horizontal laminations (Ding et al., 1998b; Mo and Derbyshire, 1991).

The Red Clay was originally suggested to be fluvio-lacustrine (Kukla, 1987), however Mo and Derbyshire (1991) noted that the microfabric is different than both alluvial and lacustrine sediments and proposed that the Red Clay is formed by weathering on hillslopes and transported over relatively short distances by creep, rainwash and possibly wind. Subsequent studies showed that the fabric of the Red Clay is characterized by pedogenic features including horizonated clay coatings and accumulations of carbonate nodules (Ding et al., 1998b; Guo et al., 2001; Han et al., 2002). These carbonate concretions form laterally extensive horizons that can be readily identified in the field and are comparable to the Quaternary loess-paleosol alternations (Fig. 2.11; Guo et al., 2001). Zheng et al. (1992) therefore suggested that these pedogenic variations might reflect a similar climatic origin as loess and subsequent studies interpreted the Red Clay as sequences of stacked paleosols (Ding et al., 1997; Ding et al., 1998b; Guo et al., 2001; Han et al., 2002). It should be noted that these pedogenic features indicate subaerial exposure but not a particular mode of sediment transport.

Liu et al. (1988) observed that the magnetic fabric (anisotropy of magnetic susceptibility) is similar to the overlying Quaternary loess and different than loess reworked by water. Furthermore, the mineral content of the Red Clay is similar to loess and

FIGURE 2.11: Picture of the Mio-Pliocene Red Clay at the Shilou section in the eastern Chinese Loess Plateau (photograph courtesy of Hong Ao).

consists predominantly of angular quartz grains, feldspars and mica's (Guo et al., 2001) as well as clay minerals including mostly illite and some kaolinite, chlorite and smectite (Han et al., 2002; Wang et al., 2019a). The geochemical signature of the major and trace elements as well as rare earth element (REE) abundances are also comparable with loess (Ding et al., 1998a; Guo et al., 2001; Han et al., 2002). Because of these similarities in mineral content, geochemistry and the massive sedimentary structure, it has been proposed that the Red Clay is formed by the accumulation of eolian dust that subsequently underwent pedogenesis (Ding et al., 1997; Ding et al., 1998b; Ding et al., 1998a; Ding et al., 1999b; Guo et al., 2001; Guo et al., 2004; Liu et al., 1988; Zheng et al., 1992). However, as discussed in section 2.4, none these features are diagnostic for eolian transport alone and may reflect alluvial mudflat deposition as well.

This is corroborated by the numerous fluvial sandstone and gravel beds that are observed to interbed the Red Clay especially in the Miocene strata and contain important localities for mammal fossils (Mo and Derbyshire, 1991; Flynn et al., 2011). In the central Chinese Loess Plateau, east of the Liupan Shan, these sandstone beds are increasing towards the base where they conformably or unconformably overlie Miocene fluvio-lacustrine sand- and siltstones (Fig. 2.11; Guo et al., 2001; Kaakinen and Lunkka, 2003; Qiang et al., 2001; Sun et al., 1997; Sun et al., 1998b; Sun et al., 1998a; Wang et al., 2014a; Zhu et al., 2008) or older sedimentary strata (An et al., 1999; Jiang and Ding, 2010; Song et al., 2001; Xu et al., 2009). Furthermore, there are notable differences between the Red Clay and the Quaternary loess. The accumulation rates in the Red Clay based on magnetostratigraphy are $\sim$3 cm/kyr, which is lower compared to the $\sim$6 cm/kyr in loess and $\sim$4 cm/kyr in paleosols (Ding et al., 1998a; Sun et al., 1998b; Sun et al., 1998a). In addition, the grain-size is finer with median grain-sizes of $\sim$5-15 µm and the grain-size distributions are more symmetric compared to the loess which has a median grain-size of $\sim$20-50 µm and a distinct tail of finer grain-sizes (Ding et al., 1998b; Guo et al., 2001; Han et al., 2002; Lu et al., 2001; Shang et al., 2016; Yang and Ding, 2004).

Several hypotheses have been proposed to explain these differences. One of these includes more intense pedogenesis because the grain-size distributions of the Red Clay strata are similar to the Quaternary paleosols (Ding et al., 1999b; Guo et al., 2001; Han et al., 2002). Sun et al. (2006) attempted to remove this pedogenic overprint by chemically isolating the quartz grains, which are more stable and unaffected by pedogenesis. Grain-size analysis of this quartz fraction revealed that the grain-size distributions are identical to the primary loess with a coarser median grain-size at ∼10-50 µm. They therefore suggested that the coarse component in the Red Clay is derived from winter monsoonal dust storms similar to the Quaternary but more strongly overprinted by pedogenesis due to the warmer and possibly wetter climate of the Miocene and Pliocene epochs (Ding et al., 1997; Ding et al., 1998b; Guo et al., 2004; Han et al., 2002; Lu et al., 2001; Miao et al., 2004; Sun et al., 2006; Yang and Ding, 2004). Lower accumulation rates during the Mio-Pliocene would have promoted pedogenesis and thereby enhanced the fine-grained components (Han et al., 2002; Sun et al., 2006). Alternatively, it has been suggested that the fine-grained component in the Red Clay is derived from the upper-level westerly jet stream which may have been the dominant dust transporter during the Neogene (Ding et al., 2000; Vandenberghe et al., 2006; Li et al., 2020). Based on the recent provenance studies indicating significant sediment contributions from local mountain-ranges (Liu et al., 2019; Nie et al., 2014; Shang et al., 2016; Zhang et al., 2018a) and fluvial strata interbedding some of the Red Clay sections (Mo and Derbyshire, 1991; Flynn et al., 2011), we propose that a local alluvial contribution should be considered as well and may explain the fine-grained components observed in the Red Clay thereby reflecting a terrestrial mudflat as described in section 2.3.

Another distinctly different feature of the Red Clay is the magnetic susceptibility, which is less than half of the susceptibility measured in the overlying loess-paleosols (Ding et al., 1997; Hao et al., 2008; Liu et al., 2003). This suggests a reduction in soil-formed magnetite, even though the pedogenic microfabrics in the Red Clay are more prominent (Ding et al., 1999b; Liu et al., 2003). The reason for these lower magnetic susceptibilities remains debated but possibilities include different soil conditions resulting in the dissolution and oxidation of iron oxides in the Red Clay or a shift in provenance of the primary minerals (Ding et al., 1999b; Liu et al., 2003; Nie et al., 2016; Yang and Ding, 2010). Several provenance studies using a variety of tools such as isotopic signatures have indeed reported a change between the Red Clay and the overlying Quaternary Loess (Li et al., 2020; Nie et al., 2014; Nie et al., 2018; Sun, 2005; Sun and Zhu, 2010; Sun et al., 2020; Yan et al., 2017). However, other studies do not find such a provenance shift (Bird et al., 2015; Peng et al., 2016; Wang et al., 2007) and argue that the isotopic variation is due to the higher degree of chemical weathering in the Red Clay (Bird et al., 2020). An alternative explanation for these inconsistencies is that the provenance signal of the Red Clay may be spatially heterogeneous (Sun et al., 2020) possibly due to significant local sediment contributions.

Older records have been identified as loess in the western part of the Chinese Loess Plateau, west of the Liupan Shan (Fig. 2.9). Guo et al. (2002) identified massive siltstones showing laterally extensive paleosols near Qinan spanning from 22 to 6.2 Ma based on magneto- and biostratigraphy. This record was subsequently extended with a drill-core to cover the late Oligocene with a basal age of 25 Ma (Qiang et al., 2011). Evidence used to argue for an eolian origin of these strata includes again grain-size distributions and geochemical properties, which are similar to Quaternary loess (Guo et al., 2002; Guo et al., 2008; Hao and Guo, 2004; Liu et al., 2006;

Qiang et al., 2011; Qiao et al., 2006). Furthermore, the quartz grains have an angular shape and show conchoidal fractures (Liu et al., 2006) and terrestrial land snail fossils similar to those found in the Quaternary loess have been identified in the Miocene siltstones (Li et al., 2006a). However, as discussed above, none of these features are diagnostic of eolian transport and more recent sedimentological, stratigraphic and provenance studies argue for predominantly alluvial deposition instead (Alonso-Zarza et al., 2009; Alonso-Zarza et al., 2010; Liu et al., 2019).

Subsequent studies have identified eolian dust, often along with other alluvial components, in even older Paleogene deposits spanning the western Chinese Loess Plateau (Fig. 2.9). Jiang and Ding (2010) use grain-size distributions and REE patterns to identify dust in the Sikouzi section spanning from ∼0.1 to ∼20 Ma based on magnetostratigraphy. However, the age of this section was subsequently reinterpreted to cover ∼0.5 to ∼29 Ma based on magneto- and biostratigraphy (Wang et al., 2011). The siltstones in the Linxia Basin with a basal age of ∼26 Ma are interpreted as dust based on the provenance signals (Nd and REE) and the low accumulation rates in the basin, which are comparable to the Red Clay and Quaternary loess (Garzione et al., 2005). Zhang et al. (2014) identified a dominant dust component along with alluvial contributions in the grain-size record of the Lanzhou Basin after ∼26 Ma, but a subsequent magnetostratigraphic study reinterpreted this age to ∼40 Ma (Wang et al., 2016a). Similarly, an eolian dust component is identified in the mudflat deposits of the Xining Basin after ∼40 Ma based on quartz surface morphologies and the provenance signal in detrital zircons (Chapter 5; Licht et al., 2014; Licht et al., 2016b).

We suggest that the Red Clay and similar massive terrestrial siltstones are different than the Quaternary loess and more adequately reflect a terrestrial mudflat instead of being entirely composed of eolian dust. This is corroborated by the abundance of closed geomorphic basins throughout Central Asia (Carroll et al., 2010), which would have promoted the development of low-relief mudflats surrounded by active mountain ranges. Although not loess-like, these mudflat deposits provide invaluable terrestrial records of pedogenesis and other paleoclimate proxies for reconstructing the monsoonal evolution in the past. Furthermore, both extrabasinal and intrabasinal dust components may be tracked and used to reconstruct paleoenvironmental conditions. An increase in extrabasinal dust may reflect aridification of distal source areas or an intensification of large-scale atmospheric dust transport, whereas intrabasinal dust may indicate local aridity in the basin.

The geological record of the Chinese Loess Plateau is unique because it records the transition between the Red Clay strata and the overlying Quaternary loess, and therefore from a mudflat environment to predominantly dust deposition. This transition is conformable in most locations showing a gradual shift to more loess-like beds (Ding et al., 1997; Kukla, 1987; Yang and Ding, 2010) associated with a 2- to 3-fold increase in accumulation rate (Ding et al., 1997; Lu et al., 2010). The mudflat-loess transition could therefore reflect a strengthening of the dust storms or an increase in dust production upwind which would have resulted in more dust accumulation and overwhelmed local mudflat deposition. Local environmental shifts on the Loess Plateau could have promoted the efficiency of dust trapping by creating wetted surfaces or increasing the vegetation cover. Magnetostratigraphic studies have dated the Red Clay to loess transition at 2.8-2.6 Ma, coeval with the Plio-Pleistocene boundary and the onset of northern hemisphere glaciation (Fig. 2.10; Ding et al., 1997; Han et al., 2002; Yang and Ding, 2010; Guo et al., 2020). This confirms the tight

coupling between the glacial climate and dust accumulation on the Loess Plateau (An et al., 1999; Ding et al., 1997; Ding et al., 2000).

2.5 Conclusion

Terrestrial dust deposits are well-known from the Quaternary period as bodies of loess draping the underlying topography, but increasingly difficult to recognize in older geological records due to a lack of diagnostic eolian features. Yet numerous siltstones have been interpreted as loessites being formed almost entirely by windblown dust. However, these interpretations are often based on ambiguous criteria, such as massive sedimentary structures, uniform grain-size distributions and angular-shaped quartz grains. Here, we show that such features are not exclusively windblown and may occur as well by alluvial deposition on low-gradient terrestrial mudflats. Such a depositional setting may better explain the provenance signatures of local mountain ranges and the fluvial sandstones observed to interbed supposed loessites.

Eolian dust may settle and accumulate on these mudflats along with other alluvial components and can be reliably quantified in sedimentary records by: 1) quartz surface morphology analysis to identify the modes transport and distinguish eolian from fluvial components, 2) provenance analysis to derive an extrabasinal or local origin, 3) end-member analysis of grain-size and -shape distributions to quantify the various sediment contributions throughout the record, 4) basin-scale analyses to remove local sedimentary features. Acknowledging and unmixing the various eolian and alluvial components in the record will enable a more reliable and robust estimation of dust in the geological record. This would have important implications for paleoclimate reconstructions and constraints on dust fluxes in the past.

The geological record of the Chinese Loess Plateau is continuous throughout the Neogene and reveals a marked shift from Red Clay strata, interpreted to have formed on a terrestrial mudflat by both alluvial and eolian deposition, to loess, composed almost entirely of windblown dust. The Red Clay-loess transition occurs at the boundary to the Quaternary period and is coeval with the onset of Northern Hemisphere glaciation which may have promoted dust production, mobilization and / or transport (e.g. Ding et al., 1997). This climatic shift would have overwhelmed local mudflat deposition on the Chinese Loess Plateau as evidenced by the abrupt increase in sedimentation rate (e.g. Ding et al., 1997; Lu et al., 2010). This suggests that loess deposits in the geological record may be found only during periods with extensive glaciation such as the Quaternary. Alternatively, exclusively windblown dust deposits may occur during the pre-Quaternary as well but are likely difficult to preserve due to the draping nature of loess bodies on the pre-existing landscape. Over longer geological timescales these loess bodies would be reworked as is occurring today on the Chinese Loess Plateau (Kapp et al., 2015; Licht et al., 2016a) before being preserved in the low-lying basins thereby biasing the geological record towards alluvial mudflat deposits. This is exemplified by the Quaternary sediments of the Weihe Basin at the southern margin of the Chinese Loess Plateau which contain predominantly of fluvio-lacustrine deposition of reworked loess and only rare occurrences of primary loess deposition (Rits et al., 2016).

Chapter 3

Central Asian moisture modulated by proto-Paratethys Sea incursions since the early Eocene

Niels Meijer, Guillaume Dupont-Nivet, Hemmo A. Abels, Mustafa Y. Kaya, Alexis Licht, Meimei Xiao, Yang Zhang, Pierrick Roperch, Marc Poujol, Zhongpai Lai, Zhaojie Guo

Abstract

The establishment and evolution of the Asian monsoons and arid interior have been linked to uplift of the Tibetan Plateau, retreat of the inland proto-Paratethys Sea and global cooling during the Cenozoic. However, the respective role of these driving mechanisms remains poorly constrained. This is partly due to a lack of continental records covering the key Eocene epoch marked by the onset of Tibetan Plateau uplift, proto-Paratethys Sea incursions and long-term global cooling. In this study, we reconstruct paleoenvironments in the Xining Basin, NE Tibet, to show a long-term drying of the Asian continental interior from the early Eocene to the Oligocene. Superimposed on this trend are three alternations between arid mudflat and wetter saline lake intervals, which are interpreted to reflect atmospheric moisture fluctuations in the basin. We date these fluctuations using magnetostratigraphy and the radiometric age of an intercalated tuff layer. The first saline lake interval is tentatively constrained to the late Paleocene-early Eocene. The other two are firmly dated between ∼46 Ma (top magnetochron C21n) and ∼41 Ma (base C18r) and between ∼40 Ma (base C18n) and ∼37 Ma (top C17n). Remarkably, these phases correlate in time with highstands of the proto-Paratethys Sea. This strongly suggests that these sea incursions enhanced westerly moisture supply as far inland as the Xining Basin. We conclude that the proto-Paratethys Sea constituted a key driver of Asian climate and should be considered in model and proxy interpretations.

3.1 Introduction

Asia's modern-day climate is characterized by monsoons and inland deserts, but the timing and mechanism of their origin remains controversial. Both have been linked to the uplift of the Tibetan Plateau, the retreat of the proto-Paratethys Sea from Eurasia and the cooling of global climate (e.g. Dupont-Nivet et al., 2007; Ramstein et al., 1997; Zhang et al., 2007). Uplift of the Plateau would create orographic barriers and intensify monsoonal circulation by increasing thermal contrasts and insulating southern moist air (e.g. Molnar et al., 2010). Retreat of the proto-Paratethys Sea would remove a significant source of moisture from the Asian interior (Bosboom et al., 2014a; Bosboom et al., 2014c; Bougeois et al., 2018; Ramstein et al., 1997;

Zhang et al., 2007) and may have strengthened the monsoons by increasing land-sea thermal contrasts (Ramstein et al., 1997; Roe et al., 2016; Zhang et al., 2007). The long-term global cooling during the Cenozoic (e.g. Cramer et al., 2009) could have induced the sea retreat by lowering the global sea level (Bosboom et al., 2014b; Bosboom et al., 2014c; Dupont-Nivet et al., 2007). Alternatively, the cooling may have caused aridification directly by weakening the hydrological cycle and the monsoons (Dupont-Nivet et al., 2007; Li et al., 2018c; Licht et al., 2014).

The Paleogene greenhouse period is key to understand the origin and mechanisms of Asian climate before significant Plateau uplift, sea retreat and global cooling had occurred. Early studies proposed that East Asia during this period was dominated by a subtropical arid belt with no monsoonal circulation (e.g. Guo et al., 2008). More recent studies show that the large-scale Asian atmospheric features were similar as today and that monsoons already existed during the Paleogene (Caves et al., 2015; Huber and Goldner, 2012; Licht et al., 2014; Licht et al., 2016b; Quan et al., 2014; Roe et al., 2016). However, others suggest that these monsoons were only tropical and restricted to South Asia, while quasi-absent in East and Central Asia (Li et al., 2018b; Spicer et al., 2017).

Today, the low-level westerlies are the main source for atmospheric moisture in the region north of the Tibetan Plateau, which is shielded from the southerly monsoons. Stable isotopes reveal that the westerlies have dominated this region since at least the late Paleocene (Bougeois et al., 2018; Caves et al., 2015), when a proto-Tibetan Plateau already created an orographic barrier from the south (e.g. Molnar et al., 2010). During the Paleogene, the westerlies may have carried additional moisture from the proto-Paratethys Sea (Bougeois et al., 2018; Roe et al., 2016; Zhang et al., 2007), which extended from the Mediterranean up to western China at this time (e.g. Bosboom et al., 2014b; Bosboom et al., 2014c). The extent of this sea fluctuated with three progressively smaller sea incursions that are superimposed on a long-term retreat. These are now well-constrained in time and space by new paleogeographic analyses (Bosboom et al., 2014b; Bosboom et al., 2014c; Kaya et al., 2019). During highstands, the sea extended far into the Tarim Basin of western China, whereas during lowstands it retreated entirely beyond Tajikistan (Bosboom et al., 2014b; Bosboom et al., 2014c; Kaya et al., 2019). These incursions may have modulated the moisture carried by the westerlies and affected precipitation in western China (Bosboom et al., 2014b; Bosboom et al., 2014c; Bougeois et al., 2018).

The Xining Basin, located on the northeastern margin of the Tibetan Plateau (3.1), provides an exceptional sedimentary record to understand Asian atmospheric circulation during the Paleogene. It contains quasi-continuous terrestrial mudrocks throughout the Cenozoic, which can be dated using magnetostratigraphy (e.g. Dai et al., 2006). Sedimentological and palynological studies show that these deposits reflect atmospheric moisture variations which are interpreted as the interplay between East Asian monsoons and westerlies (Abels et al., 2011; Bosboom et al., 2014a; Dupont-Nivet et al., 2007; Dupont-Nivet et al., 2008a). However, the Xining record has not been accurately dated and described before the late Eocene ($\sim$40-34 Ma). Therefore, the climatic effects of the India-Asia collision, the earlier proto-Paratethys Sea incursions and the onset of global cooling, all occurring during the early to middle Eocene ($\sim$56-40 Ma), remain unknown.

In this study, we extend the litho- and magnetostratigraphy of the upper Eocene - Miocene deposits in the Xining Basin (Abels et al., 2011; Bosboom et al., 2014a; Xiao et al., 2012) to the lower Eocene where the magnetostratigraphy remained unreliable

so far (Dai et al., 2006; Horton et al., 2004). We analyzed three laterally equivalent sections for magnetostratigraphy and complemented our correlations of the polarity zones with the radiometric age of a tuff layer. Furthermore, we interpret the evolution of atmospheric moisture and its driving mechanisms throughout the early Eocene to Oligocene epochs using our detailed lithostratigraphic descriptions and previous records from the Xining Basin.

3.2 Geological setting

The Xining Basin forms the western part of the Cenozoic Longzhong Basin, which subsequently segmented into smaller sub-basins during deformation in the Miocene (Horton et al., 2004). The origin of the basin during the Paleogene is unclear and is hypothesized to be an extensional basin either due to thermal subsidence (Horton et al., 2004) or differential clockwise-rotation of crustal blocks (Zhang et al., 2016a). Alternatively, the basin may have formed as a foreland basin of the Western Qinling Shan, a mountain range located $\sim$80 km to the south (Clark et al., 2010).

The Paleogene strata of the Xining Basin are composed of red gypsiferous mudrocks and gypsum beds and include the Qijiachuan, Honggou and Mahalagou Formations (Fig. 3.1; QBGMR, 1985). The depositional environment is interpreted as a distal arid mudflat based on the lack of fluvial channels, the widespread occurrence of evaporites and the massive structure of the mudrocks resulting from subaerial reworking (Abels et al., 2011; Dupont-Nivet et al., 2007; Smoot and Lowenstein, 1991; Talbot et al., 1994). Provenance analysis shows that the fluvio-lacustrine deposits were mostly derived from distal highlands such as the Western Qinling Shan in the south and the Qilian Shan in the north (Zhang et al., 2016a). The rest of the sediments were transported as eolian dust from reworked fluvial deposits and, to a minor extent, from the Qaidam Basin in the west (Licht et al., 2014; Licht et al., 2016b).

Gypsum is formed by evaporating surface- or groundwater and accumulates to form gypsum beds when groundwater tables are sufficiently close to the surface to replenish the brine with the necessary solutes (Abels et al., 2011; Dupont-Nivet et al., 2007; Rosen, 1994). In well-drained settings with a deeper groundwater table, the evaporites are unlikely to be preserved (Rosen, 1994) and subaerially oxidized mudrocks accumulate instead (Abels et al., 2011; Dupont-Nivet et al., 2007). Basin-wide alternations between red mudrocks and saline lake evaporites therefore indicate changes in the groundwater table and are interpreted to reflect variations in atmospheric moisture in the catchment (Abels et al., 2011; Dupont-Nivet et al., 2007).

3.3 Methods

3.3.1 Sections

We resampled and analyzed at higher resolution the previously published East Xining (36°34′50"N, 101°53′42"E) and Xiejia (36°31′20"N, 101°52′20"E) sections (Dai et al., 2006; Horton et al., 2004) and added the newly sampled Caijia section (36°36′55"N, 101°59′3"E). Stratigraphic thicknesses were measured using a Jacob's staff and detailed lithological logs were made in the field.

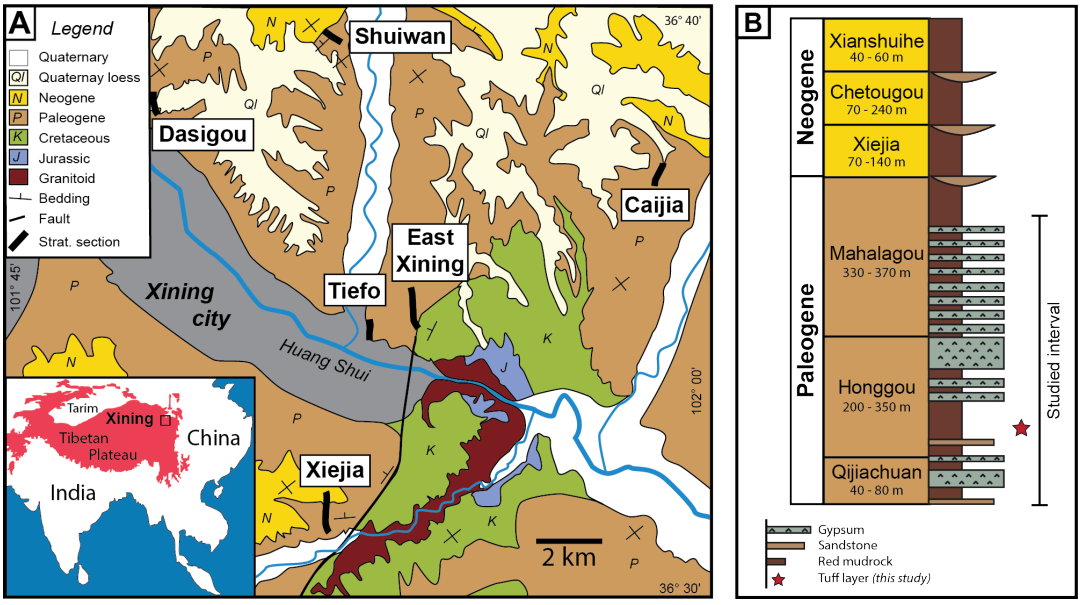

FIGURE 3.1: (A) Regional geological map (QBGMR, 1985) showing the locations of the sections examined here and in previous studies. Inset map shows the location of the Xining Basin along the margin of the northeastern Tibetan Plateau. (B) Generalized stratigraphic column modified from Horton et al. (2004), listing formations, thicknesses and lithologies.

3.3.2 U-Pb dating of a tuff

A tuff layer from the Xiejia section was processed for U-Pb radiometric dating. After crushing and grinding, the powder was separated using magnetic and heavy liquid separation. The zircon crystals were handpicked under a binocular microscope, mounted on a 25mm ring of epoxy, grinded, polished and imaged using cathodoluminescence. In total, 31 zircon crystals were collected from the tuff sample and U-Pb dating was conducted by in-situ laser ablation inductively coupled plasma mass spectrometry (LA-ICPMS) at Géosciences Rennes, France. Detailed analytical procedures and individual data are reported in the supplementary material (Appendix A). Additionally, three tuff samples were crushed and melted to make tablets for X-Ray Fluorescence (XRF) analysis to identify the chemical composition. The XRF analysis was performed using a PANalytical AXIOS Advanced at the German Research Center for Geosciences (GFZ), Potsdam, Germany.

3.3.3 Magnetostratigraphy

Paleomagnetic samples were collected at the sections with a resolution of ∼0.5 to 1 meter where possible. Sampling was conducted using a portable electric drill and a compass mounted on an orientation stage. The paleomagnetic samples were thermally demagnetized with 10-15 temperature steps up to 680 °C. Samples from the Caijia section, and the lower 105 meters of the Xiejia section were analyzed at Géosciences Rennes, France. Samples from the East Xining section and the upper 91 meters of the Xiejia section were analyzed at the Paleomagnetic Laboratory 'Fort Hoofddijk' of the Faculty of Geosciences at Utrecht University, the Netherlands.

3.4 Lithostratigraphy

The measured sections (Fig. 3.2) are subdivided in formations and members following the classification of the Qinghai Bureau of Geology and Mineral Resources (QBGMR, 1985). In the following, these formations are described and interpreted in terms of depositional environment. Detailed logs are provided in the supplementary material (Fig. A.1).

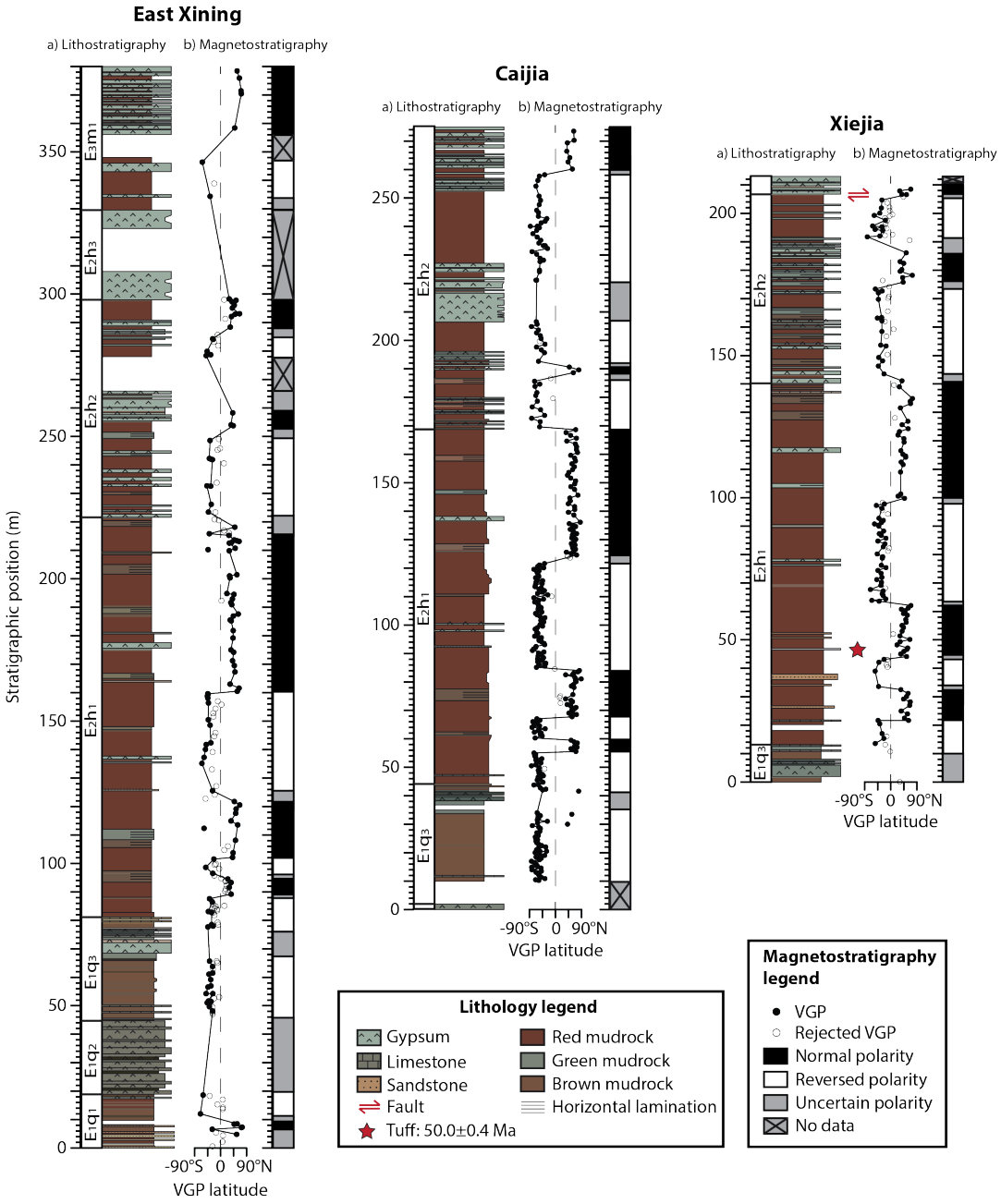

FIGURE 3.2: The East Xining, Caijia and Xiejia sections showing (A) the lithostratigraphy and (B) the magnetostratigraphy with Virtual Geomagnetic Pole (VGP) latitudes and corresponding polarity zones.

3.4.1 Lower Qijiachuan Formation (E_1q_1)

Description

The lower part of the Qijiachuan Formation (∼20 meters thick) consists of massive red mudrocks (2.5YR 4/4) interbedded with a few massive sandstone beds. Occasionally, the mudrocks contain slickensides and centimeter-scale horizons of grey (5GY 5/1) mottling. The sandstone beds are up to a few decimeters thick, fine- to coarse-grained and laterally extensive.

Interpretation

The dominance of massive, oxidized mudrocks indicates deposition on a subaerially exposed mudflat (Abels et al., 2011; Dupont-Nivet et al., 2007; Smoot and Lowenstein, 1991). The lateral extent and massive structure of the sandstone beds suggests deposition by unconfined fluvial flows (North and Davidson, 2012).

3.4.2 Middle Qijiachuan Formation (E_1q_2)

Description

The middle Qijiachuan Formation (∼30 meters thick) is characterized by a laterally extensive package of gypsum beds. The beds are decimeters thick and alternate between light gray (10Y 5/1), indurated intervals and dark grey (N 3/1), less indurated, organic-rich (TOC=∼0.7-1.7%) intervals (Fig. 3.3A). The gypsiferous beds are nodular, but reveal centimeter-scale horizontal lamination in fresh, unweathered outcrops (Fig. 3.3A).

Interpretation

The gypsum and horizontal lamination indicate deposition in a saline lake (Abels et al., 2011; Dupont-Nivet et al., 2007; Smoot and Lowenstein, 1991). The alternations between gypsiferous and carbonaceous beds may reflect fluctuating salinity and/or productivity (Potter et al., 2005).

3.4.3 Upper Qijiachuan Formation (E_1q_3)

Description

The upper Qijiachuan Formation (∼30 meters thick) consists of massive mudrocks with a characteristic liver-brown color (5YR 4/2, Fig. 3.3B). The mudrocks contain specks of organic debris, abundant slickensides and are commonly interbedded with centimeter-scale beds of coarse silt with ripple laminations. Centimeter-scale carbonate beds composed of micrite occur in the lower part. The top of the Qijiachuan Formation consists of a ∼5 meters-thick interval containing green (5GY 5/1) gypsiferous mudrocks and decimeter-scale beds of massive gypsum. The mudrocks are interbedded with centimeter-scale beds of micritic carbonate.

Interpretation

The lack of horizontal lamination and abundance of slickensides in the mudrocks indicate deposition on a subaerially exposed mudflat (Abels et al., 2011; Dupont-Nivet et al., 2007; Smoot and Lowenstein, 1991). The organic debris admixed with red regolith results in the characteristic liver-brown color (Potter et al., 2005). The

rippled beds of coarse siltstones are interpreted to be deposited in episodic events of surface flow (North and Davidson, 2012). The carbonates may represent deposition in local, relatively freshwater ponds (Smoot and Lowenstein, 1991). The gypsum beds at the top indicate deposition in a saline lake (Abels et al., 2011; Smoot and Lowenstein, 1991).

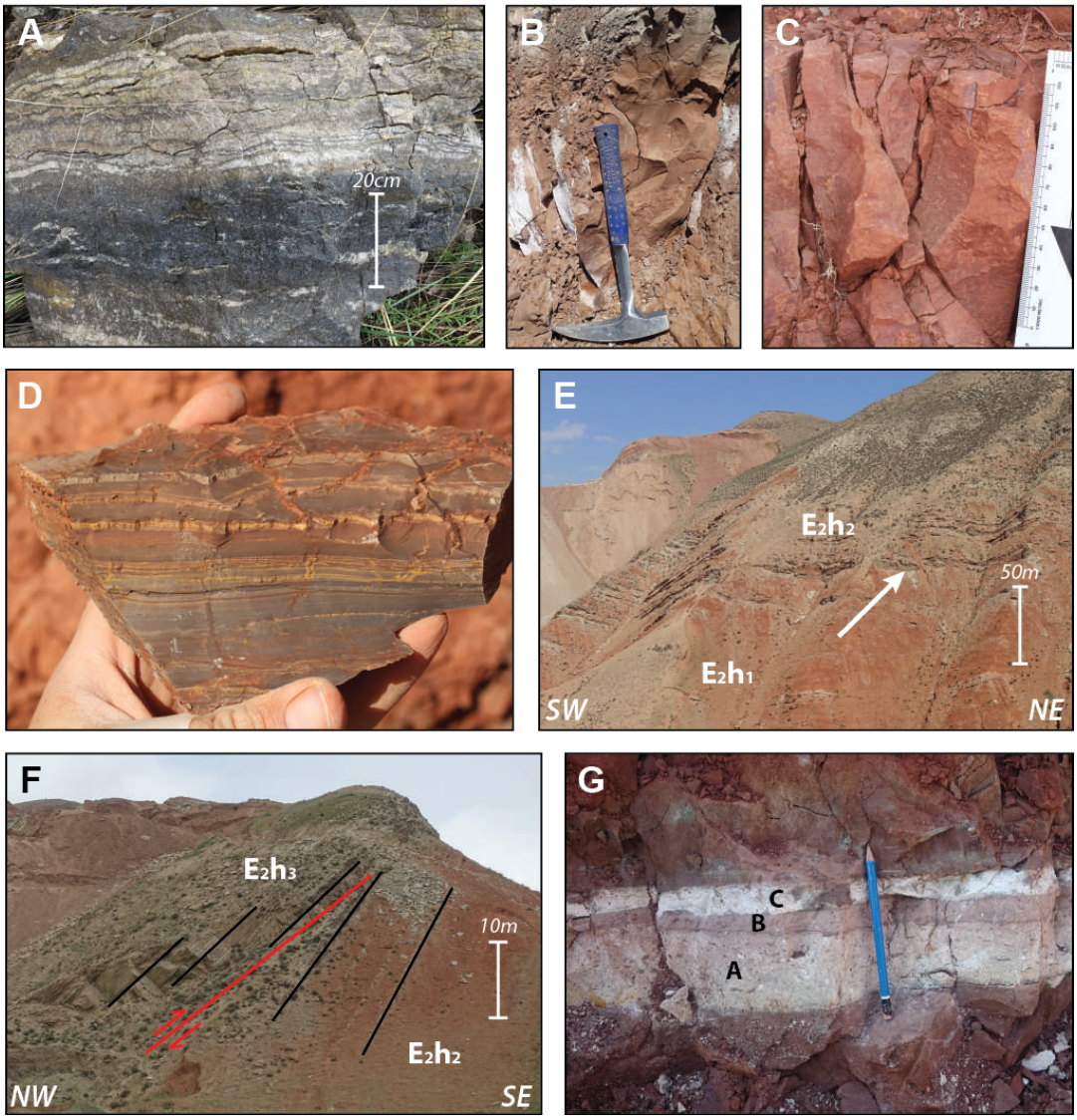

FIGURE 3.3: Field photos showing: (A) an alternation between carbonaceous and gypsiferous beds in the middle Qijiachuan Formation. Note the horizontal laminations in the upper part. (B) Massive liver-brown mudrock in the upper Qijiachuan Formation. Hammer for scale.(C) Massive brick-red mudrock in the lower Honggou Formation showing mm-scale burrows. Scale-bar on the right. (D) Finely laminated brown mudrock in the lower Honggou Formation showing mud-cracks and micrite laminae. (E) Overview of the Xiejia section showing the Honggou Formation. Arrow indicates the transition from the lower to middle Honggou Formation at the 140 meter-level. Scale-bar on the right. (F) Overview of the top of the Xiejia section showing a fault at the base of the upper Honggou Formation. Scale-bar on the right. (G) A tuff bed in the Xiejia section at the 46.3 meter-level showing the three different layers that were geochemically analyzed (A, B and C). Pencil for scale.

3.4.4 Lower Honggou Formation (E_2h_1)

Description

The lower Honggou Formation (∼130 meters thick) is characterized by brick-red (2.5 YR 4/6) massive mudrocks (Fig. 3.3C). The mudrocks are commonly interbedded with centimeter-scale beds of rippled coarse siltstones. Rare cross-bedded sandstones occur as decimeter-scale beds in the lower part of the more proximal Xiejia section. The red mudrocks of the Honggou Formation contain abundant millimeter-scale interstitial gypsum nodules. Millimeter-scale burrows, slickensides, blocky peds and grey (10GY 7/1) mottling are common, but millimeter-scale carbonate nodules are rare. The red mudrocks occasionally contain <5 meters-thick intervals of brown (5YR 4/2) mudrocks with millimeter-scale lamination (Fig. 3.3D). These intervals contain specks of organic debris, slickensides, desiccation cracks and centimeter-scale beds of micritic carbonate and gypsum. The red mudrocks are rarely interbedded with green (10GY 6/1), decimeter-scale beds of gypsum with either a nodular structure or centimeter-scale horizontal lamination.

Interpretation

The dominance of gypsiferous red mudrocks indicates deposition on a subaerially exposed arid mudflat (Abels et al., 2011; Dupont-Nivet et al., 2007; Smoot and Lowenstein, 1991), with occasional fluvial events evidenced by the coarse silt- and sandstone beds (North and Davidson, 2012). The laminated brown mudrock intervals are interpreted as lacustrine deposits. However, the observed desiccation cracks and slickensides suggest that these lakes were shallow and occasionally exposed to drying. The gypsum beds are interpreted as saline lake deposits (Abels et al., 2011; Dupont-Nivet et al., 2007; Smoot and Lowenstein, 1991).

3.4.5 Middle Honggou Formation (E_2h_2)

Description

A sudden increase in gypsum beds and mudrocks with fine horizontal laminations marks the transition (Fig. 3.3E) to the middle Honggou Formation (∼80 meters thick). The laminated mudrocks range in color from brown (5YR 4/3) to green (10GY 6/1). Massive red mudrocks occur as well, but are less abundant than in the lower Honggou Formation. The gypsum beds are green (10GY 6/1), laminated or nodular, and range in thickness from decimeter- to meter-scale. The middle Honggou Formation can be traced regionally as a more gypsiferous interval. However, individual beds are laterally discontinuous between sections spaced up to 14.5 kilometers.

Interpretation

The massive red mudrocks, laminated mudrocks and gypsum beds are interpreted to be deposits of subaerially exposed mudflat, lake and saline lake environments respectively (Abels et al., 2011; Dupont-Nivet et al., 2007; Smoot and Lowenstein, 1991). The lateral discontinuity of the beds suggests that the lacustrine mudrocks and evaporites accumulated in local topographic depressions whereas oxidized mudflats formed on local highs. The nodular character of the gypsum beds is likely due to weathering because it is absent in fresh outcrops (Abels et al., 2011).

3.4.6 Upper Honggou Formation (E_2h_3)

Description

The upper Honggou Formation consists of a ∼10 - 30 meters-thick gypsum package containing decimeter-scale beds of massive to nodular gypsum as well as macro-crystalline gypsum and glauberite (Bosboom et al., 2014a). A minor fault observed at the base of the gypsum package in the Xiejia section may have resulted in a hiatus (Fig. 3.3F). Locally, the gypsum package can be replaced by fluvial sandstone beds, as observed in the Dasigou section, north of Xining (Fig. 3.1A; Bosboom et al., 2014a).

Interpretation

The thick accumulation of gypsum beds indicates prolonged deposition in a saline lake (Abels et al., 2011; Bosboom et al., 2014a; Smoot and Lowenstein, 1991). The beds containing euhedral macro-crystals suggest that the lake was perennial at times (Bosboom et al., 2014a; Smoot and Lowenstein, 1991). Although the thickness of the gypsum package varies, the upper Honggou Formation is characteristic and can be correlated across the basin (Horton et al., 2004).

3.4.7 Lower Mahalagou Formation (E_3m_1)

Description

The lower Mahalagou Formation (∼70 meters thick) is characterized by meter-scale alternations between red mudrocks and gypsum beds that can be correlated between the studied sections (Abels et al., 2011; Bosboom et al., 2014a; Dupont-Nivet et al., 2007). The mudrocks have a massive structure, whereas the gypsum beds vary between a massive, laminated or nodular structure (Abels et al., 2011). An interval of reddish brown (5YR 4/3) mudrocks with a thickness of ∼20 meters occurs at the base.

Interpretation

The Mahalagou Formation has been described extensively in previous studies and is interpreted as deposits of astronomically forced cycles between subaerial mudflats and saline lakes (Abels et al., 2011; Bosboom et al., 2014a; Dupont-Nivet et al., 2007).

3.4.8 Summary

Throughout the studied interval, we observe several trends in the depositional environments (Fig. 3.4). A decrease in organic matter indicates a long-term aridification in the record. Organic-rich deposits are abundant in the Qijiachuan Formation, occur sporadically throughout the overlying Honggou Formation and disappear in the lower Mahalagou Formation along with carbonate beds (Bosboom et al., 2014a). Superimposed on this long-term drying we observe shorter term alternations between mudflat deposits and evaporites (Fig. 3.4). The middle Qijiachuan Formation is dominated by saline lake deposits and is overlain by organic-rich mudflat deposits of the upper Qijiachuan Formation and red mudrocks of the lower Honggou Formation. These mudflat deposits are followed by a shift to lacustrine mudrocks

and evaporites in the overlying middle to upper Honggou Formation. This is followed by a ∼20 meters-thick interval of mudflat deposits at the base of the overlying Mahalagou Formation, after which this formation is dominated by characteristic mudrock-evaporite cycles.

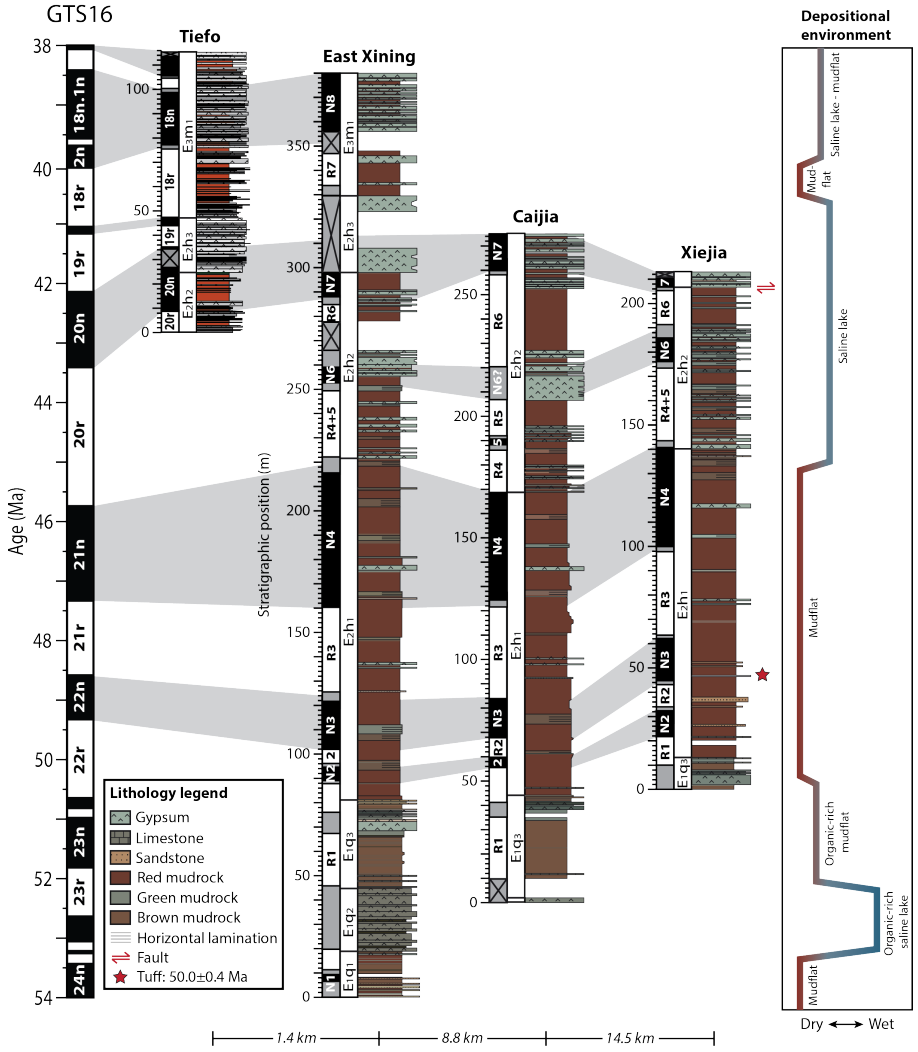

FIGURE 3.4: Magnetostratigraphic correlations between the three studied sections and the Tiefo section (Bosboom et al., 2014a). The chrons are correlated to the GTS16 (Ogg et al., 2016). Trends in the dominant depositional environment are shown on the right.

3.5 U-Pb radiometric dating of a volcanic tuff

A volcanic tuff with a thickness of 12 centimeters was identified in the Xiejia section at the 46.3 meter-level (Fig. 3.3G) and is used to constrain the age of the deposits. The tuff is composed of three different layers and consists predominantly of vitreous matrix. The layers have similar chemical compositions (Table A.1) and are classified, on an anhydrous basis, as trachyte (Fig. A.2) according to the classification of Le Maitre et al. (1989). However, the relatively high concentration of volatiles (LOI = ∼8%) indicates that this tuff may have been altered.

Of the 31 zircon crystals that were analyzed, 19 analyses plot in a concordant to sub-concordant position (99 to 80%, Fig. 3.5A), indicating the presence of a slight amount of common Pb in some of the zircon grains and/or a very small Pb loss.

Their weighted average $^{206}Pb/^{238}U$ age (Fig. 3.5B) is well defined at 50.2 ± 0.4 Ma (MSWD=1.9). This mean age is equivalent within error with the lower intercept date of 50.0 ± 0.4 Ma (Fig. 3.5A) if the discordia is forced to a $^{207}Pb/^{206}Pb$ value of 0.839 ± 0.01 calculated (at 50 ± 10 Ma) following the Pb evolution model of Stacey and Kramers (1975). This is also similar to the Tuffzirc age (Ludwig and Mundil, 2002) of 50.15 +0.65/-0.45 Ma. We therefore conclude that this tuff was deposited at 50.0 ± 0.4 Ma.

The remaining 12 crystals produced apparent ages ranging from 237 to 2450 Ma and are interpreted as xenocrystic in origin. The Eocene volcanic belt throughout the northern Qiangtang terrane provides a possible source for the tuff, since multiple ages reported here fit well within the error range of our tuff sample (Chapman and Kapp, 2017).

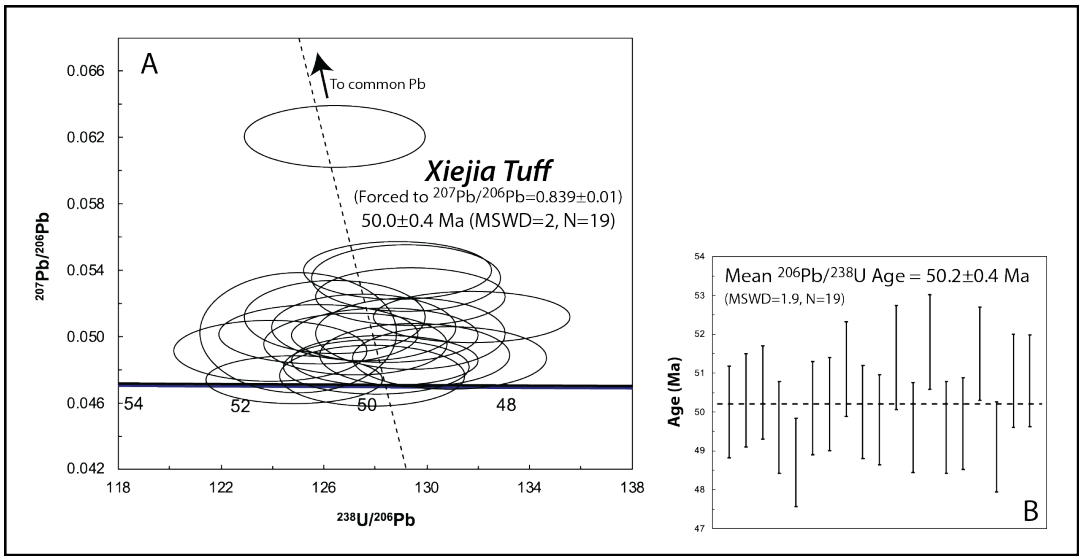

FIGURE 3.5: (A) Tera-Wasserburg diagram for the youngest group of zircons. (B) Weighted average $^{206}Pb/^{238}U$ Age for the same 19 zircon grains. All ellipses and apparent $^{206}Pb/^{238}U$ ages are plotted at 2σ.

3.6 Magnetostratigraphy

Paleomagnetic analysis is used to identify reversals and further constrain the age of the deposits.

3.6.1 Thermal demagnetization

Demagnetization of the red mudrock samples up to 200-300 °C resulted in the removal of a secondary normal overprint and is followed by a linear decay towards the origin (Fig. A.3). A drop in magnetization is observed between 550-680 °C indicating a combination of hematite and magnetite as the dominant ferromagnetic carriers (Fig. A.3). Samples from the gypsum beds have a lower magnetization and showed erratic directions that could not be interpreted. The magnetic behavior is similar as observed in previous studies in the Xining Basin (Abels et al., 2011; Bosboom et al., 2014a; Dai et al., 2006; Dupont-Nivet et al., 2007; Dupont-Nivet et al., 2008b; Xiao et al., 2012).

3.6.2 ChRM directions

Characteristic remanent magnetization (ChRM) directions of the samples were calculated by eigenvector principal component analysis (Kirschvink, 1980) on at least four temperature steps showing a linear decay between 300-600 °C. Maximum angular deviations (MAD) were estimated for all calculated ChRM directions. All samples have a MAD <30° and most are <10°.

Virtual geomagnetic poles (VGPs) were calculated from the ChRM directions and the VGP latitudes are shown in Fig. 3.2 and Fig. A.1. The VGPs show two clusters of either normal (positive latitude) or reversed (negative latitude) polarity. Samples with a VGP of more than 45° from the mean normal or reversed VGP are considered outliers and removed from further analysis (open symbols in Fig. 3.2 and Fig. A.1, red symbols in Fig. A.4).

The means for both the normal and reversed ChRM directions were calculated for each section (Fig. A.4) using Fisher statistics (Fisher, 1953). Reversals tests (McFadden and McElhinny, 1990) performed on the mean directions of the sections are negative indicating that the angle between the mean normal and reversed polarities is larger than the critical angle. These negative reversals tests are due to an unresolved normal overprint as observed in previous studies in the Xining Basin (Bosboom et al., 2014a; Dupont-Nivet et al., 2008b; Xiao et al., 2012). This is especially evident in the Xiejia and East Xining sections (Fig. A.4), which are more tilted (dip of $\sim$50°) compared to the Caijia section (dip of $\sim$7°). The normal overprint would preclude the use of these datasets for tectonic rotation analysis but it does not affect the reliability of the magnetostratigraphy used in this study as discussed further below.

3.6.3 Correlation to the GTS

Polarity zones are identified by at least two successive samples of the same polarity and are labeled N1 to N8 and R1 to R7 (Fig. 3.4). The magnetostratigraphy is laterally similar and can be readily correlated between the studied sections. However, normal zone N5 is only observed in the Caijia section. This zone with a thickness of only 2 - 4 meters is probably missed in the other sections due to a lower resolution of reliable VGP's. Zone N6 is lacking in the Caijia section because no magnetic signal is recorded in the gypsum beds of this interval.

In the following, the polarity zones are correlated to chrons (Fig. 3.4) in the geological timescale (GTS16, Ogg et al., 2016). The tuff, located at the base of normal polarity zone N3, provides a tie point for our correlation. The only normal chron with a basal age near 50±0.4 Ma is C22n, which has a basal age of 49.3 Ma in the GTS16, but was recently tuned to 49.7 Ma (Westerhold et al., 2017). The latter age fits well within the error range of the tuff. Zone N3 is therefore correlated to C22n. The overlying zones R3 and N4 are then correlated to C21r and C21n respectively. C21n is followed by a relatively long reversed and a long normal chron (C20r and C20n) in the timescale that were both identified at the base of the Tiefo section (Bosboom et al., 2014a). It follows that polarity zone N7 can be correlated to C20n by using the characteristic gypsum package of the upper Honggou Formation (E_2h_3) as a marker bed. Zones R7 and N8 in the East Xining section are subsequently correlated to C18r and C18n by using the gypsum cycles of the Mahalagou Formation as marker beds. Following the above, zones R4 to R6 are unequivocally correlated to C20r. The resulting age model shows stable accumulation rates of $\sim$3 cm/kyr in the Honggou Formation (Fig. A.5), which is similar to rates observed in the overlying

sections (Abels et al., 2011; Bosboom et al., 2014a; Xiao et al., 2012). This suggests an absence of major hiatuses and further supports our correlation.

However, the short normal zones N5 and N6 (with thicknesses of 5 to 10 meters) remain uncorrelated in our interpretation. No such zones are observed in C20r of the geological timescale. Zone N2, located just below N3, is uncorrelated as well because a correlation to C23n would result in an unusually low accumulation rate of ∼0.6 cm/kyr in both R2 (when correlated to C22r) and N2 (when correlated to C23n). To our knowledge, short normal chrons that could relate to N2, N5 and N6 have not been reported in any published marine or terrestrial records of this interval (e.g. Fig. 6 in Turtù et al., 2017 and references therein). Bouligand et al. (2006) record nine cryptochrons in C20r and three in C22r based on stacked marine magnetic anomaly profiles. Most of these cryptochrons have a short duration of less than 8 kyrs, but three have relatively long durations of 12 to 14 kyrs (C20r-5, C20r-6 and C22r-1). These three longer cryptochrons could fit with the stratigraphic positions of the short normal zones in the Xining Basin. However, this would imply anomalously high accumulation rates of at least ∼35 cm/kyr for these cryptochrons to be recorded in the observed >5 meters-thick normal zones. Therefore, a more probable hypothesis is that these zones result from secondary magnetizations occurring in stratigraphic intervals prone to remagnetization. However, we found no clear differences in lithologies (Fig. 3.2 and Fig. A.1), magnetic behavior (Fig. A.3) and ChRM directions (Fig. A.4) compared to the other polarity zones. Nevertheless, the pervasive secondary normal overprint evidenced by the failed reversals tests suggests that some stratigraphic intervals may have been overprinted.

The age of the Qijiachuan Formation cannot be constrained due to the low resolution of reliable VGP latitudes in the gypsum interval of the middle Qijiachuan Formation. This hinders the record of the expected polarity zones below the radiometric age of the tuff (50.0±0.4 Ma) and thus prevents a reliable downward extension of the magnetostratigraphic correlation.

3.7 Discussion

Our magnetostratigraphic correlations indicate that the Honggou Formation spans from ∼50 Ma (C22r) to ∼41 Ma (top of C19n). This extends the dated stratigraphic record to cover the early Eocene to Oligocene epochs (Fig. 3.6; Abels et al., 2011; Bosboom et al., 2014a; Xiao et al., 2012). Our age model agrees broadly with the preferred correlations reported in Dai et al. (2006), except for two notable differences: (1) our record shows that N22 in Dai et al. (2006) consists of two separate normal zones. The upper of these is correlated to C22n, which is now further constrained by the age of the tuff. The lower is interpreted here as a remagnetized normal zone. (2) N23 in Dai et al. (2006) is not observed in this study and is likely a result of remagnetized samples from this gypsiferous interval. Therefore, the previously proposed correlation of the base of the Xiejia section to ∼52 Ma (Dai et al., 2006) is revised by our results to ∼50 Ma.

Our paleoenvironmental record shows a long-term drying trend from ∼50 to 40 Ma (Fig. 3.4 and Fig. 3.6), which is corroborated by previous rock magnetic analyses in the basin (Fang et al., 2015). This drying trend persists in the overlying deposits, where the disappearance of organic-rich deposits and carbonate beds in the Mahalagou Formation is synchronous with an aridification step in the pollen record between 40.6 and 39.4 Ma (Bosboom et al., 2014a). Successive aridification steps are

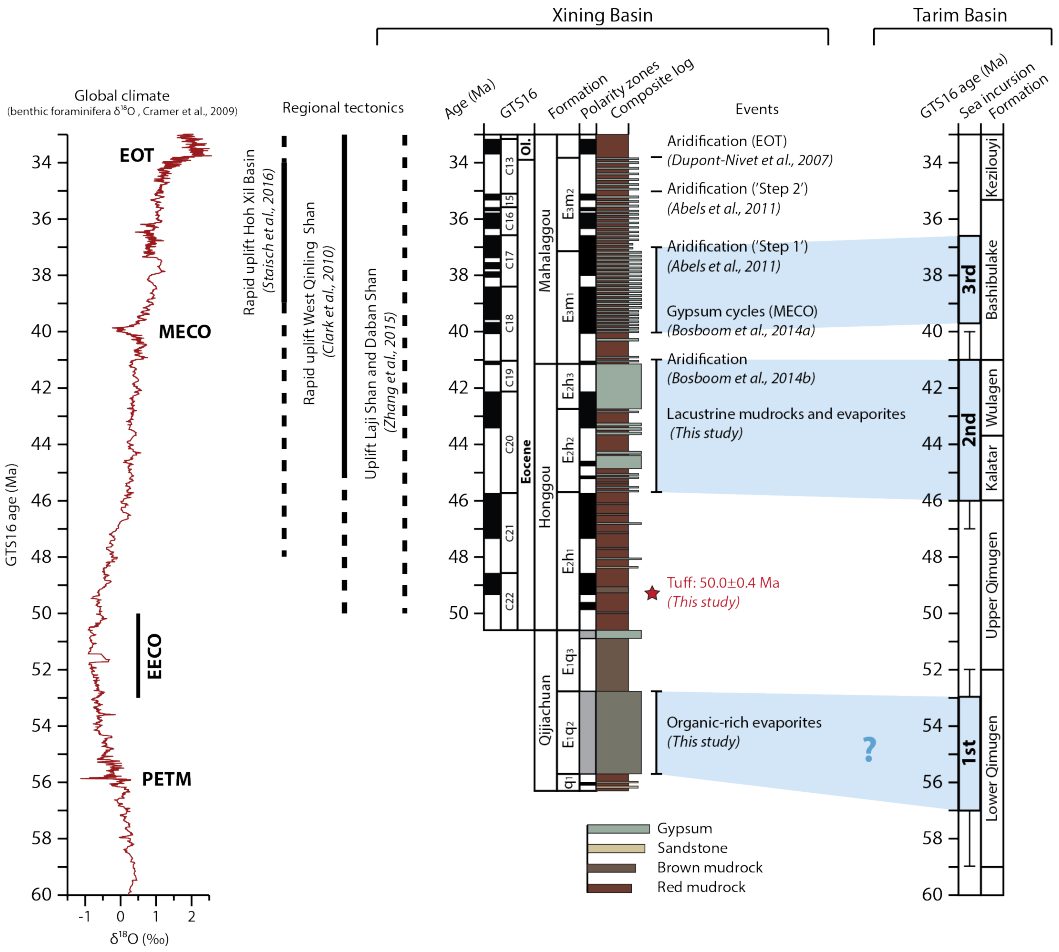

FIGURE 3.6: Composite lithostratigraphy of the East Xining, Tiefo (Bosboom et al., 2014a) and Shuiwan (Abels et al., 2011) sections. Global climate is represented by a 9-point moving average through the benthic foraminifera $\delta^{18}O$ record of Cramer et al. (2009). Regional tectonic events and climatic events observed in the basin are indicated, as well as the proto-Paratethys Sea incursions observed in the Tarim Basin (Kaya et al., 2019).

then recorded by a decrease in gypsum beds at ~37 Ma ('Step 1', Abels et al., 2011), an increase in accumulation rate at ~35 Ma ('Step' 2, Abels et al., 2011) and the final disappearance of saline lakes at the Eocene-Oligocene Transition (EOT; Dupont-Nivet et al., 2007). This long-term aridification of the Xining Basin has been linked to Tibetan Plateau uplift (Li et al., 2018c), long-term proto-Paratethys Sea retreat (Abels et al., 2011; Bosboom et al., 2014b; Bosboom et al., 2014c; Dupont-Nivet et al., 2007) and global cooling (Abels et al., 2011; Bosboom et al., 2014a; Dupont-Nivet et al., 2007; Fang et al., 2015; Li et al., 2018c) and is likely the result of a combination of these mechanisms.

Within this long-term 50-34 Ma drying trend, we observed shorter term alternations between mudflat and saline lake deposits (Fig. 3.6). Based on previous interpretations in the Xining Basin, we interpret these alternations to represent fluctuations in atmospheric moisture (Abels et al., 2011; Dupont-Nivet et al., 2007). A first wet phase is expressed in the middle Qijiachuan Formation by organic-rich evaporites. The age can only be approximated to late Paleocene - early Eocene based on existing pollen, ostracod and charophyte assemblages (Horton et al., 2004 and references therein) and by extending the average accumulation rate of the overlying deposits

downwards. A second wet phase, is recognized as a shift to more lacustrine mudrocks and evaporites in the middle to upper Honggou Formation. This phase can now be dated from ∼46 Ma (top C21n) to the top of the upper Honggou evaporites as previously recognized at ∼41 Ma (base of C18r; Bosboom et al., 2014b; Bosboom et al., 2014a). A third wet phase is observed to start at ∼40 Ma (base C18n) with the onset of regular gypsum/mudrock cycles (Bosboom et al., 2014a) and end at a decrease in gypsum beds at ∼37 Ma (top C17n.1n, 'Step 1' in Abels et al., 2011). This last phase was likely less intense, more fluctuating and drier, as indicated by the absence of organic-rich layers or carbonate beds and the presence of numerous interfingering layers of red mudrocks. These saline lake phases are laterally continuous throughout the basin suggesting an external control rather than an expression of autogenic basin infill. To identify potential driving mechanisms for the observed moisture fluctuations, we review constraints on tectonic uplift, proto-Paratethys Sea incursions and global climate trends (Fig. 3.6).

The influence of local tectonic uplift on moisture variations is considered unlikely because accumulation rates are continuously low (∼3 cm/kyr, Fig. A.5), no coarsening trends are observed and exhumation of the local mountain ranges (the Laji Shan and Daban Shan) occurred mainly in the Miocene (e.g. Lease et al., 2011). A loosely dated Eocene phase of exhumation is observed bordering the Xining Basin (Zhang et al., 2015a) and more regionally in both the northern Tibetan Plateau (Western Qinling Shan; Clark et al., 2010) and the central Plateau (Hoh Xil Basin; Staisch et al., 2016). Although this Eocene growth of the Tibetan Plateau may explain the long-term drying trend (Li et al., 2018c), the observed shorter term shifts appear too abrupt (Fig. 3.3G) to be caused by the slow tectonic uplift of the Plateau. Furthermore, the continuously growing Plateau cannot explain the episodic occurrence of wetter lithofacies which are separated by intervals of dry mudflats.

Previous studies have temporally linked the Xining aridification steps to the stepwise retreating proto-Paratethys Sea (Abels et al., 2011; Bosboom et al., 2014b; Bosboom et al., 2014c; Dupont-Nivet et al., 2007). During the Paleogene, the long-term sea retreat is superimposed by three progressively smaller incursions each dated by bio- and magnetostratigraphic studies (Fig. 3.6 and Fig. 3.7; Bosboom et al., 2014b; Bosboom et al., 2014c; Kaya et al., 2019). A recent reappraisal of these incursions in the Tarim Basin (Kaya et al., 2019) provides the following age constraints. The first and most extensive incursion lasted from ∼59-57 Ma to ∼53-52 Ma; the second incursion from ∼47-46 Ma to ∼41-40 Ma and the third and smallest sea incursion is more precisely dated from 39.8 Ma to 36.7 Ma (Fig. 3.6 and Fig. 3.7). These incursions fit well with the three wetter intervals recognized in the Xining Basin (Fig. 3.6). Our study therefore shows a temporal link between the proto-Paratethys highstands and increased moisture in the Xining Basin.

This moisture could have been derived either from the winter-time westerlies or the summer monsoon (Fig. 3.7). Climate models suggest that Asian summer monsoons may be weakened by the proto-Paratethys Sea due to reduced land-sea contrasts (Ramstein et al., 1997; Roe et al., 2016; Zhang et al., 2007). Other studies indicate that the sea was too shallow to affect monsoonal circulation, even during highstands (Bougeois et al., 2018; Licht et al., 2014). Either way, it seems unlikely that an extensive proto-Paratethys Sea was associated with increased monsoonal activity. Instead, the highstands would increase the amount of water available for evaporation along the westerly pathway (Bosboom et al., 2014b; Bosboom et al., 2014c; Bougeois et al., 2018). This would result in more winter precipitation and provides an explanation

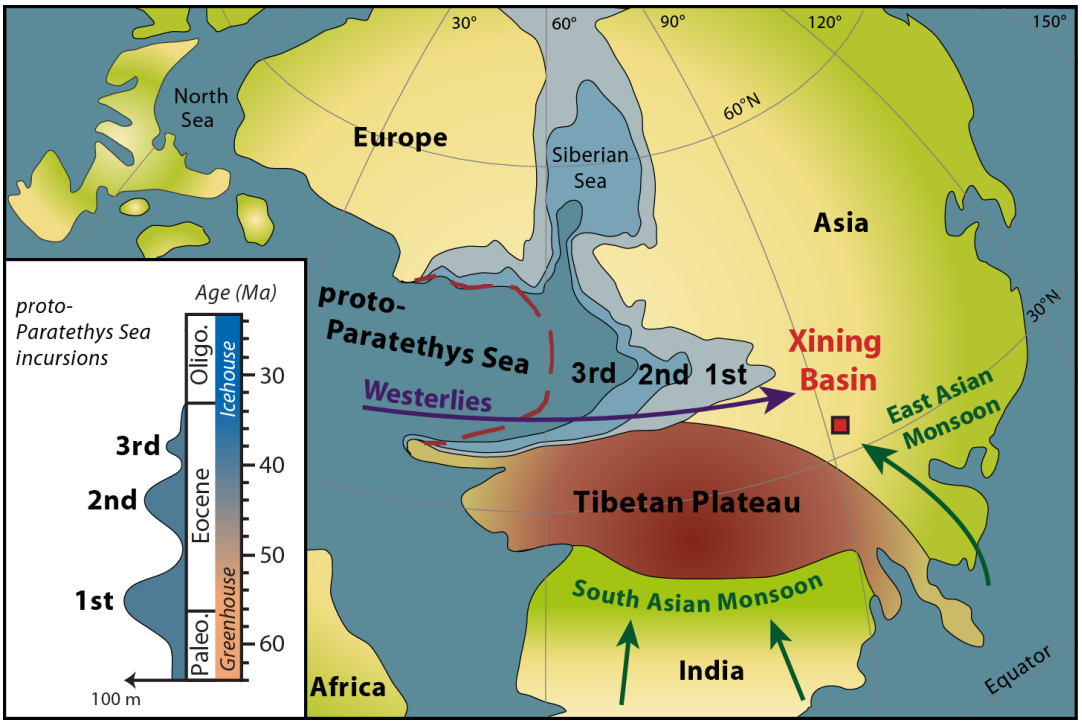

FIGURE 3.7: Generalized paleogeography of Eurasia during the Paleogene, modified from Bosboom et al., 2014b. The maximum spatial extent of the three proto-Paratethys Sea incursions are indicated on the map and in time on the left. The approximate extent of the regressions in between the incursions is indicated with a red dashed line. Atmospheric moisture sources are shown with arrows.

for the wetter lithofacies in Xining coeval with the sea incursions. This interpretation is in line with previous studies showing that Central Asian climate and coeval deposits were strongly influenced by the westerlies at this time (Bougeois et al., 2018; Caves et al., 2015).

Previous studies also suggested that global climate might have played a role in the Xining record (Fig. 3.6). Temperatures generally decreased during the studied interval but are superimposed by hyperthermal events and periods of incipient ice sheet formation (Fig. 3.6; e.g. Cramer et al., 2009). The onset of obliquity cycles after ~40 Ma has been associated with ice sheet dynamics after the MECO (Middle Eocene Climatic Optimum, Abels et al., 2011; Bosboom et al., 2014a) and the aridification at ~34 Ma has been linked to global cooling at the EOT (Dupont-Nivet et al., 2007). The latter may have resulted from either a weaker hydrological cycle in a colder climate (Licht et al., 2014; Li et al., 2018c), or from the proto-Paratethys Sea retreat induced by the growth of the Antarctic ice sheet (Bosboom et al., 2014b; Dupont-Nivet et al., 2007). However, the short-term moisture shifts observed in this study do not correspond with global climate events (Fig. 3.6). Instead, they systematically fit with the proto-Paratethys Sea incursions and retreats, some of which are thought to be driven by tectonics and others by eustasy (Bosboom et al., 2014b; Bosboom et al., 2014c; Kaya et al., 2019). Therefore, we suggest that the sea itself was a direct driver of precipitation in the region via the westerlies.

3.8 Conclusion

Our results extend the Xining record down to the early Eocene (∼50 Ma) by using magnetostratigraphy and tuff dating. This extended time frame shows a long-term drying trend in the lithostratigraphy with superimposed wetter periods that correlate in time with highstands of the proto-Paratethys Sea. These correlations suggest that moisture in the region was governed by the westerlies and modulated by the Paleogene sea incursions. The overall aridification of the Xining Basin may be explained by the long-term retreat of the proto-Paratethys Sea as well as the effects of the Tibetan uplift and global cooling.

Our results stress that, beyond the traditionally invoked Tibetan uplift and global climate as drivers of Asian climate, sea-driven moisture fluctuations should be taken into account as well. These results might influence both the assessment of model and proxy data constraining Eurasian weathering and dust production (Licht et al., 2016b) as well as paleobiogeographic reconstructions (e.g. Favre et al., 2015). Building upon these results, a better understanding of the interplay between the westerlies and monsoons at tectonic, orbital and seasonal timescales may be obtained by further work focused on the identification and quantification of the moisture sources in the Xining Basin as well as in other regional records.

Chapter 4

Intensification of the hydrological cycle during the Early Eocene Climatic Optimum (EECO) recorded in the Xining Basin

Niels Meijer, Guillaume Dupont-Nivet, Alexis Licht, Pierrick Roperch, Amber Woutersen, Carina Hoorn, Natasha Barbolini, Alexander Rohrmann, Aijun Sun, Hanno Meyer, Norbert Nowaczyk

Abstract

The evolution of Asian climate during the Cenozoic is traditionally linked to shifts in paleogeography such as uplift of the Tibetan Plateau driving monsoonal circulation and the proto-Paratethys Sea incursions modulating westerly moisture. In contrast, the role of global climate in the Asian hydrological cycle remains unclear. Here, we present a new stratigraphic record from the terrestrial mudflat deposits of the Xining Basin in central China, which covers the Early Eocene Climatic Optimum (EECO), a period characterized by long-term global warmth and elevated atmospheric CO_2 levels. The record is dated using magnetostratigraphy and extends the previously studied Paleogene strata down to an unconformity recognized in the rock magnetic properties at 50.9 Ma (chron C23n). Palynological assemblages and depleted $\delta^{13}C$ values of pedogenic carbonates reveal a relatively humid environment during the early Eocene with peak wet conditions identified by pedogenic $\delta^{18}O$ values, increased sedimentation rates and higher organic carbon preservation between 50.4 and 49.8 Ma during the EECO. This stratigraphic interval is in stark contrast to the arid red beds, evaporites and the pollen of xerophytic plants observed in the underlying Cretaceous–Paleocene strata and overlying middle–late Eocene deposits. The peak global warmth of the EECO is thus clearly linked to an intensified Asian hydrological cycle, suggesting a major driving role for global climate.

4.1 Introduction

The Early Eocene Climatic Optimum (EECO), driven by elevated atmospheric CO_2 concentrations (Anagnostou et al., 2016; Cramwinckel et al., 2018) and occurring between 53 and 49 Ma (Westerhold et al., 2018), was the warmest period in the past 100 million years. The EECO is regarded as an analogue for global warming in the near-future (2150 CE; Burke et al., 2018; Lunt et al., 2020), yet geological records of the terrestrial response during this period remain scarce, especially in Asia (Hollis et al., 2019). One record in the Qaidam Basin on the northeastern Tibetan Plateau suggests a monsoonal climate during the EECO (Song et al., 2018), but the age constraints are

debated (Wang et al., 2017). Some climate model simulations also suggest intensified Eocene monsoons (Licht et al., 2014), but others show only weak monsoons which intensify afterwards due to the progressive uplift of the Tibetan Plateau during the Cenozoic, rather than driven by global climate (Farnsworth et al., 2019).

To resolve these discrepancies, we studied the terrestrial deposits of the Xining Basin, located in central China. These strata have been accurately dated using magnetostratigraphy to cover the Pliocene to Eocene epochs (e.g. Fang et al., 2019a), however the early Eocene age model remains debated and the onset of Cenozoic deposition is inconsistently reported between 54 and 52 Ma (Dai et al., 2006; Fang et al., 2019a; Yang et al., 2019). Here, we present a detailed study of the early Eocene strata in the Xining Basin using five new magnetostratigraphic sections constrained by the U-Pb radiometric age of a lacustrine carbonate bed. Furthermore, we use lithostratigraphy, pedogenic and bulk organic stable isotopic compositions (following the study of Licht et al., 2020), palynology and rock magnetic properties to study the paleoenvironmental evolution of the basin and identify an intensification of the hydrological cycle during the EECO.

4.2 Geological setting

The modern-day Xining Basin is located on the northeastern margin of the Tibetan Plateau and is bounded by the Riyue Shan in the west, the Daban Shan (eastern Qilian Shan) in the north and the Laji Shan in the south (Fig. 4.1A). During the Mesozoic, the basin was part of the extensional Xining-Minhe Basin which stretched towards Lanzhou in the east and to Guide in the south (Horton et al., 2004). Mesozoic strata include Middle Jurassic mudrocks and sandstones interlayered with coal beds, which are exposed only in the center of the Xining Basin (Fig. 4.1B; QBGMR, 1985). These are unconformably overlain by the Early Cretaceous Hekou Group and the Late Cretaceous Minhe Formation (Fig. 4.1C). Both consist of red mudrocks, sandstones and conglomerates and are observed to coarsen towards the south (Horton et al., 2004; QBGMR, 1985).

During the Cenozoic, the Xining Basin formed the western part of the Longzhong Basin which extended towards the Liupan Shan in the east and the Western Qinling Shan in the south (Horton et al., 2004). The basin is proposed to have formed as either a foreland basin of the Western Qinling Shan (Liu et al., 2013), a transtensional basin due to the clockwise rotation of crustal blocks (Zhang et al., 2016a) or as an extensional basin related to slab rollback of the Pacific plate (Fan et al., 2019). Paleogene strata include red mudrocks, sandstones and gypsum beds of the Qijiachuan, Honggou, Mahalagou and Xiejia Formations (sensu Fang et al., 2019a; Fig. 4.1C). The boundary between the Cretaceous and Paleogene strata is reported as conformable in some locations (Zhai and Cai, 1984) and unconformable in others (QBGMR, 1985). Subsequent Neogene compressive deformation resulted in uplift of the Laji Shan, which segmented the Longzhong Basin into smaller sub-basins (Horton et al., 2004). Neogene strata in the Xining Basin include mudrocks, sandstones and conglomerates of the Chetougou, Guanjishan and Mojiazhuang Formations (sensu Fang et al., 2019a; Fig. 4.1C).

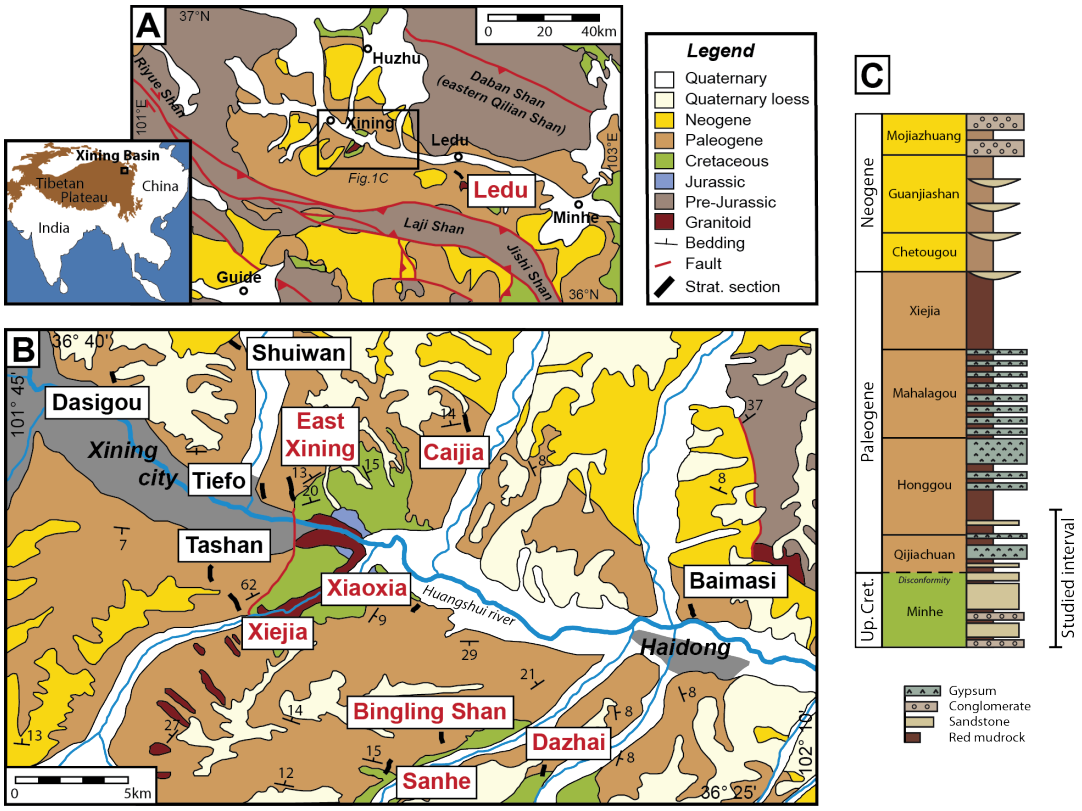

FIGURE 4.1: (A) Geological map of the Xining Basin (modified from Fan et al., 2019) showing the Ledu section. Inset map shows the location of the Xining Basin. (B) Detailed geological map (modified from BGMRQP, 1965 and QBGMR, 1985 showing the sections near Xining city. Sections sampled in this study are indicated in red. (C) Generalized lithostratigraphic column of the Xining Basin (based on QBGMR, 1985; Horton et al., 2004; Fang et al., 2019a).

4.3 Methods

4.3.1 Sections and sampling

We studied the litho- and magnetostratigraphy of the Ledu section, 36°25'48"N, 102°22'45"E, located in the eastern part of the Xining Basin (Fig. 4.1A) and the following sections in the western part near Xining city (Fig. 4.1B): Xiaoxia, 36°31'41"N, 101°57'7"E, Bingling Shan (Dai et al., 2006), 36°27'13"N, 101°58'51"E, Sanhe (Zhang et al., 2016a), 36°26'15"N, 101°56'54"E and Dazhai (Horton et al., 2004; Zhang et al., 2016a), 36°26'10"N, 102°1'21"E. The lithostratigraphy was described in the field and paleomagnetic samples were collected at ~0.5 to 2 meter-resolution using an electric hand drill. The orientations of the paleomagnetic samples were measured using a compass mounted on an orientation stage. In addition, hand-sized rock samples were collected for rock magnetic, total organic carbon content (TOC) and stable isotope analyses at Ledu, Binglang Shan, Sanhe and the previously studied Caijia section (Chapter 3) with a resolution of ~2 to 5 meters. Palynological samples were collected from the Dazhai section and the East Xining, Caijia and Xiejia sections reported in Chapter 3.

4.3.2 U-Pb dating of lacustrine carbonates

Fifteen lacustrine carbonates were collected throughout the sections for radiometric dating. The samples were cut to expose fresh surfaces and then incorporated into

a 1-inch epoxy mount for in situ U-Pb dating. The mounts were then manually polished, first with coarse then fine (5 µm grit size) sandpaper.

U-Pb dating was conducted by laser ablation inductively coupled plasma mass spectrometry (LA-ICPMS) at the TraceLab laboratory of the University of Washington; details about the LA-ICPMS hardware can be found in Licht et al. (2019). The analyses were performed by ablation with an Analyte G2 excimer laser using a spot diameter of 50 mm, 20 Hz pulse repetition rate and an energy fluence of 2.94 J cm^{-2}. The ablated material was carried in helium and mixed with nitrogen into the plasma source of an iCAP RQ Quadrupole ICP-MS. Our data acquisition procedure is described in Cong et al. (in preparation) and follows the one of Drost et al. (2018). Samples were ablated along parallel linear scans of 5 to 20 mm length at 10 µm.s^{-1}. Linear scans are arranged in successive order, with no overlaps or gaps between line scans, covering areas of 5x5 to 20x20 mm^2. Analyzed masses include ^{238}U, ^{235}U, ^{232}Th, ^{207}Pb, ^{206}Pb, ^{204}Pb, ^{24}Mg and ^{40}Ca, with a total combined dwell time of $\sim$0.4 s. Analyses of the linear scans of the calcite standard WC-1 (Roberts et al., 2017) and synthetic glass NIST 612 reference materials are used to bracket analyses of unknowns.

Data reduction follows the procedure of Parrish et al. (2018) and is conducted with Iolite, using the *Geochron* data reduction scheme without downhole fractionation correction to get U/Pb isotopic ratios (Paton et al., 2010). NIST 612 standard glass is used as the primary reference material for calibration of both reduction schemes. We then manually select >20 portions of scan per sample in Iolite by monitoring individual data channels, covering a broad range of $^{238}U/^{206}Pb$ values and making sure that every portion is at least 2 s long and has no jump in $^{238}U/^{206}Pb$, $^{207}Pb/^{206}Pb$, and $^{24}Mg/^{40}Ca$ ratios. The isotopic results from these portions of scan make individual analyses that are loaded into an MS Excel spreadsheet with a macro for matrix-dependent U-Pb fractionation correction from Parrish et al. (2018), based on 612-normalized WC-1 carbonate data. The additional uncertainty related to WC-1 final normalization (1–4% 2SE) is quadratically added to all individual analysis uncertainties. A linear regression of the individual analysis in Tera-Wasserburg space is then undertaken for each sample to obtain its initial $^{207}Pb/^{206}Pb$ ratio, the lower intercept date, and their associated uncertainties using IsoplotR (Vermeesch, 2018). Out of the fifteen carbonate samples only one sample (CJC07) yielded enough Uranium for dating; U-Pb data are reported in Table B.1.

4.3.3 Magnetostratigraphy and rock magnetism

The paleomagnetic samples of the Xiaoxia, Bingling Shan and Sanhe sections were analyzed at the Archeo-Paleomagnetic laboratory of Géosciences Rennes, France, the Dazhai section at the Paleomagnetic Laboratory 'Fort Hoofddijk' of the Faculty of Geosciences at Utrecht University, the Netherlands and the Ledu section at the Laboratory of Rock- and Paleomagnetism at the German Research Center for Geosciences (GFZ) in Potsdam. After measuring magnetic susceptibility, the samples were thermally demagnetized by stepwise heating up to 650 °C . The Natural Remanent Magnetization (NRM) was measured after every step. The magnetic susceptibilities of the samples were measured before the thermal demagnetization using a Bartington MS2 for the samples measured at Géosciences Rennes, and an AGICO Multifunction Kappabridge MFK-1A for the samples measured at the GFZ.

In addition, S-ratios were measured to characterize the magnetic components throughout the record. The hand samples of the Ledu and Caijia sections were carefully ground using a mortar and pestle and packed in cubic plastic boxes of 6 cm^3. Isothermal Remanent Magnetizations (IRM) were imparted using a 2G Enterprises 660 pulse magnetizer and subsequently measured using a Molyneux spinner magnometer. The IRM intensity acquired at 1.5 T is defined here as the saturation IRM (SIRM) and, together with the IRM intensity acquired at a reversed field of 0.2 T, is used to define the S-ratio as: $0.5 \times (1 - [IRM_{-0.2T} / SIRM_{1.5T}])$. Detailed IRM acquisition curves were measured for selected samples using a 4" Princeton Measurements Corporation 'Micromag' alternating gradient magnometer (AGM).

4.3.4 TOC and stable isotopes

To measure the total organic content (TOC), rock samples of the Caijia, Bingling Shan and Ledu sections were ground using a mortar and pestle and aliquots of 5-10 µg were weighed into silver capsules. These were treated with HCl to dissolve carbonates and TOC was measured using an Elementary Analysator EA3000 from EuroVector at the University of Potsdam.

For stable isotope analysis, samples of carbonate-bearing mudrocks were collected from the Ledu, Sanhe and Caijia sections. Samples from the Ledu section were analyzed at the University of Washington in Seattle and the samples from the Sanhe and Caijia sections were analyzed at the Goethe University-Senckenberg BiK-F Stable Isotope Facility in Frankfurt. A detailed diagenetic screening and study on the origin of the carbonates in these mudrocks was performed by Page et al. (2019). They concluded that the carbonates are vadose-grown, pedogenic cements showing no evidence for subsequent diagenetic alteration. Pedogenic vadose-grown cements precipitate from soil water and commonly display the same oxygen and carbon isotope ratios as pedogenic nodules (Quade and Roe, 1999; Fan et al., 2018). In addition, gypsum samples were collected from the Bingling Shan section for stable isotope analysis of the bulk organic matter. These samples were analyzed at the Alfred-Wegener Institute Isotope Laboratory (AWI) in Potsdam.

The gypsum samples and half of every mudrock sample were decarbonated with 6N HCl twice and washed with 18 M-ohm water several times for acid removal; Carbon content and organic matter $\delta^{13}C$ values were then measured with a Costech elemental analyzer coupled to a Thermo MAT253 gas source isotope ratio mass spectrometer (University of Washington) or with a Flash Elemental Analyzer 1112 connected to a Thermo MAT253 gas source isotope ratio mass spectrometer (Goethe University-Senckenberg), or with a Delta V Advantage (AWI). Measured carbon isotopic compositions were corrected using in-house reference materials. International reference materials USGS 24 and IAEA-CH-7 were analyzed along with the samples to check for accuracy. The other half of every mudrock sample was reacted with 105 % orthophosphoric acid; carbonate $\delta^{18}O$ and $\delta^{13}C$ values were measured with a Kiel III Carbonate Device coupled to a Thermo Finnigan Delta Plus gas source isotope ratio mass spectrometer (University of Washington) or with Thermo GasBench II interfaced with a Thermo MAT 253 gas source isotope ratio mass spectrometer (Goethe University-Senckenberg). Measured carbon content, carbon and oxygen isotope compositions were corrected using in-house reference materials as well as NBS18 and NBS19 carbonate reference materials. All $\delta^{13}C$ and $\delta^{18}O$ values are expressed relative to VPDB. Standard error for isotopic analyses is <0.15 ‰ at AWI

and is <0.01 ‰ at the University of Washington and Goethe-University Senckenberg.

4.3.5 Palynology

Productive palynological samples were collected from gypsum beds and laminated mudrocks in the East Xining, Xiejia, Caija and Dazhai sections. The samples were prepared either by Palynological Laboratory Services (Anglesey, UK) using standard palynological techniques (HCL, HF, sieving at 10µm), at the University of Amsterdam (Amsterdam, the Netherlands; HCL, sieving at 212µm, 20% pyrophosphate, acetolysis, bromoform treatment) or at the Sediment Laboratory of the Vrije Universiteit (Amsterdam, the Netherlands; following methods of Horowitz, 1992 and described in Dupont-Nivet et al., 2008a). Nine samples were productive; six from the middle and three from the upper Qijiachuan Formation. These samples are combined with the one sample from the lower Honggou Formation reported in Chapter 5. An exploratory study was done, meaning that palynomorphs were classified into one of the following six vegetation groups: xerophytic herbs, broad-leaved forest, temperate forest, conifers, ferns and others, and were not always identified to genus level. Palynomorphs were identified using the Genera File of Fossil Pollen and Spores (Jansonius and Hills, 1976 and recent updates), Song et al. (1999) and the Chinese palynological literature. Plant Functional Types (PFTs) were assigned using the Nearest Living Relatives (NLR) approach applied by Hoorn et al., 2012.

4.4 Lithostratigraphy

The lithostratigraphy is subdivided in formations and members following QBGMR (1985) and is presented in Figure 4.2. The lithofacies are described and interpreted below.

4.4.1 Upper Minhe Formation (K_2m_3)

Description

The upper Minhe Formation consists of dm- to m-scale beds of sandstone and conglomerate (Fig. 4.3A-C). Some m-scale channels are observed in the sandstones (Fig. 4.3C). The conglomerates are both clast- and matrix-supported and are composed of poorly sorted, subangular to subrounded polymictic pebbles (Fig. 4.3D). The sandstones are medium- to coarse-grained and poorly sorted containing subrounded granules and pebbles (Fig. 4.3D). The sedimentary structure is predominantly massive, but trough cross-bedding and horizontal bedding are observed occasionally as well. The sandstones and conglomerates are interbedded with rare dm-scale beds of massive red mudrocks. These mudrocks become more abundant towards the north (Fig. 4.3E).

Interpretation

The matrix-supported conglomerates in the upper Minhe Formation are interpreted as debris flow deposits and the clast-supported conglomerates and sandstones as braided river channel-fills (Smoot and Lowenstein, 1991). Consequently, the depositional environment of the upper Minhe Formation is interpreted as a proximal

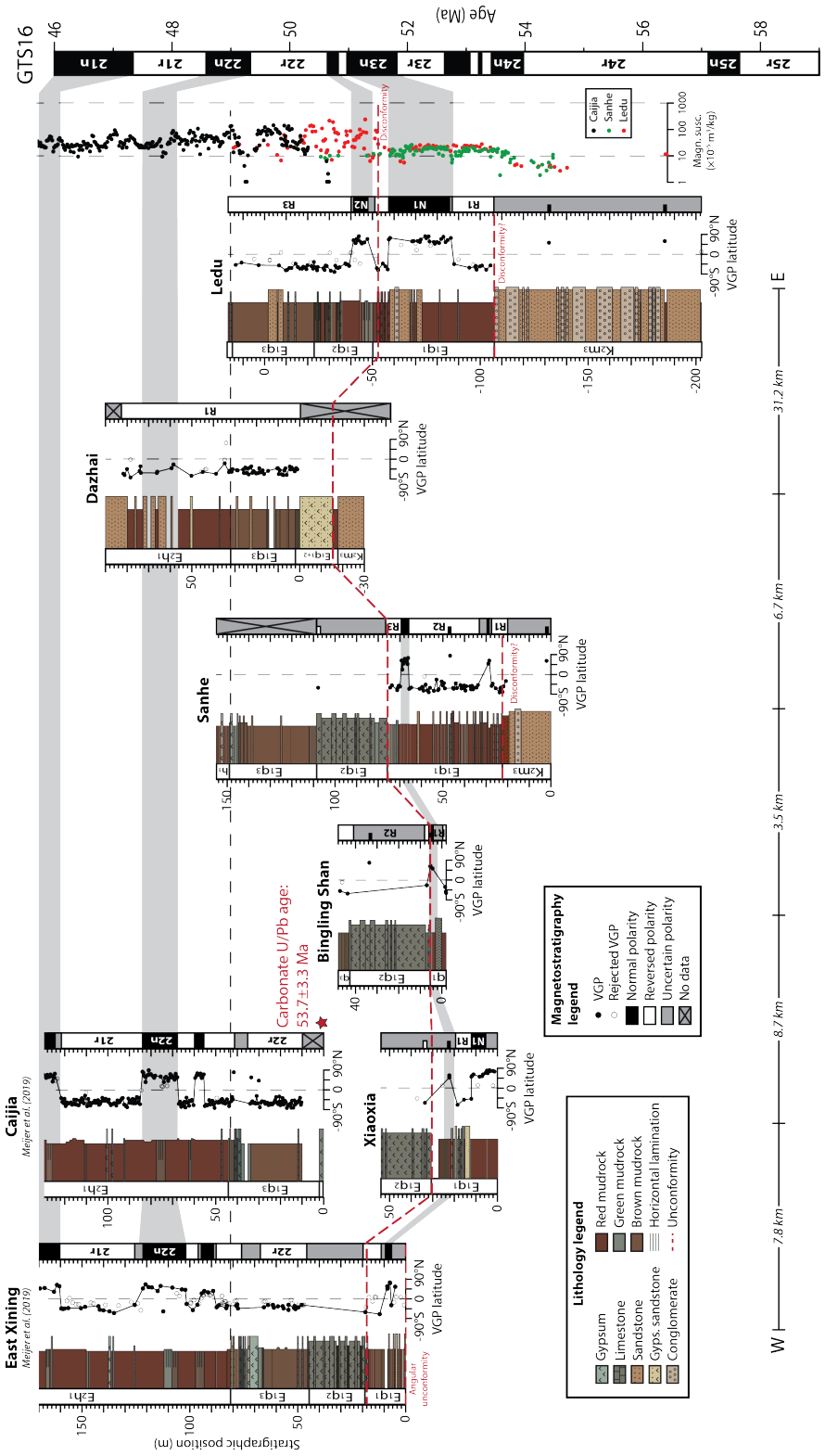

FIGURE 4.2: Litho- and magnetostratigraphy of the studied sections. The East Xining and Caijia sections are from Chapter 3. The polarity zones are correlated with the GTS16 (Ogg et al., 2016). The red dashed line indicates an unconformity and the black dashed indicates the 0-level for the composite stratigraphy presented in Fig. 4.7.

alluvial fan. The material is likely transported from the south as the upper Minhe Formation is fining towards the north (QBGMR, 1985).

4.4.2 Lower Qijiachuan Formation (E_1q_1)

Description

The Minhe Formation is overlain by the Qijiachuan Formation. At most locations this boundary is represented by a disconformity (Fig. 4.3A and B). However, an angular unconformity is observed at the East Xining section (Fig. 4.3E). The lithofacies of the lower Qijiachuan Formation consist predominantly of massive red mudrocks containing slickensides. Occasionally, these mudrocks contain cm- to dm-scale horizons of mottling (Fig. 4.3F) in red (2.5YR 4/4), purplish (7.5R 4/3), yellow (2.5Y 5/4), grey (10GY 5/1) and dark grey (10B 3/1). The mudrocks are commonly interbedded with laterally extensive dm- to m-scale sandstone beds. These sandstones are medium- to coarse-grained, contain granules and have a massive, horizontally bedded or trough cross-bedded structure. Occasionally, the mudrocks and sandstones are interbedded with cm-scale micritic carbonates containing a horizontally laminated or massive structure.

Interpretation

The fine-grained deposits in the lower Qijiachuan Formation indicate low energy suspension settling and we interpret the depositional environment as a distal alluvial mudflat (Abels et al., 2011; Dupont-Nivet et al., 2007; Smoot and Lowenstein, 1991; Talbot et al., 1994). The mottled horizons suggest that the mudrocks have been subjected to pedogenesis. The sandstones are interpreted as unconfined fluvial flows based on their lateral extent (North and Davidson, 2012). The carbonates may have formed in a lacustrine setting resulting in horizontal laminations or due to spring water as they are often observed to overlie the more porous sandstone beds (Smoot and Lowenstein, 1991).

4.4.3 Middle Qijiachuan Formation (E_1q_2)

Description

The middle Qijiachuan Formation is characterized by a ∼30 meters-thick package of organic-rich gypsum beds in the western part of the Xining Basin (Fig. 4.3A and G) and previously described in Chapter 3. These beds have a massive to nodular structure and alternate on a dm-scale between light grey and darker grey beds due to a varying content in gypsum and TOC (∼0.1-1.7%). The top ∼2 meters of this package consists of horizontally laminated gypsum interbedded with cm-scale micritic carbonates. Towards the east, the lithofacies of the middle Qijiachuan Formation vary considerably. At the Dazhai section, the lithofacies consist of ∼15 meters of gypsiferous, medium-grained sandstones with a massive structure (Fig. 4.3B). This is overlain by ∼3 meters of organic-rich gypsiferous mudrocks. At the Ledu section, located ∼30 km further towards the east, the characteristic gypsum beds are lacking completely. Instead, the lithofacies consist of red and grey massive mudrocks alternated with meter-scale intervals of dark grey, horizontally laminated mudrocks with a relatively high TOC (0.4%) and interbedded with cm-scale beds of nodular gypsum and micritic carbonate.

Interpretation

Based on the abundance of evaporites, we interpret the depositional environment of the middle Qijiachuan in the western part of the Xining Basin as a saline lake with

the TOC and gypsum content reflecting variations in salinity and/or productivity (Chapter 3). The abundance of sandstones at the Dazhai section indicates fluvial deposition, which is proposed to be local because it is not observed in other nearby sections. The massive mudrocks at the Ledu section are interpreted as a distal alluvial mudflat alternated with intervals of lacustrine deposition as indicated by the horizontally laminated mudrocks (Chapter 3; Abels et al., 2011; Dupont-Nivet et al., 2007; Smoot and Lowenstein, 1991). The lack of evaporites and the occurrence of carbonates suggest that these lakes were alkaline compared to the saline lakes observed in the western part of the basin.

4.4.4 Upper Qijiachuan Formation (E_1q_3)

Description

The boundary to the upper Qijiachuan Formation can be identified by a shift to liver-brown colored mudrocks (Fig. 4.3A, B and H), previously described in Chapter 3. The mudrocks are massive and contain slickensides, carbonate nodules and are interbedded with cm-scale cross-laminated siltstones and dm-scale cross-bedded sandstones. The mudrocks have relatively high TOC values varying between 0.2-0.6%. The top of the upper Qijiachuan Formation is characterized by dm-scale massive gypsum beds and green mudrocks alternated with cm-scale micritic carbonate beds (Fig. 4.3H).

Interpretation

The depositional environment is interpreted as an organic-rich distal alluvial mudflat (Chapter 3). The organic material results in the characteristic liver-color of the mudrocks. The slickensides and carbonate nodules indicate subaerial exposure and pedogenesis. The silt- and sandstones indicate episodic fluvial activity by unconfined flows (North and Davidson, 2012). The top of the formation is interpreted as lacustrine deposits in a saline to alkaline environment (Chapter 3).

4.4.5 Lower Honggou Formation (E_2h_1)

Description

The transition to the lower Honggou Formation is marked by a shift to brick-red colored mudrocks with a massive structure (Fig. 4.3A, B and H). The Honggou Formation has been described previously in Chapter 3 and will be summarized here. The red mudrocks are interbedded with m-scale intervals brown-colored, horizontally laminated mudrocks, cm-scale carbonate beds and occasional dm-scale sandstone and gypsum beds. At the Dazhai section, we observe abundant dm- to m-scale sandstone beds, which are laterally extensive, medium- to coarse-grained and have a massive or trough cross-bedded structure.

Interpretation

The depositional environment of the red mudrocks is interpreted as an alluvial mudflat alternated with alkaline to saline lacustrine conditions and occasional fluvial deposits (Chapter 3). The Dazhai section is interpreted as a more proximal setting as evidenced by the more abundant fluvial sandstones.

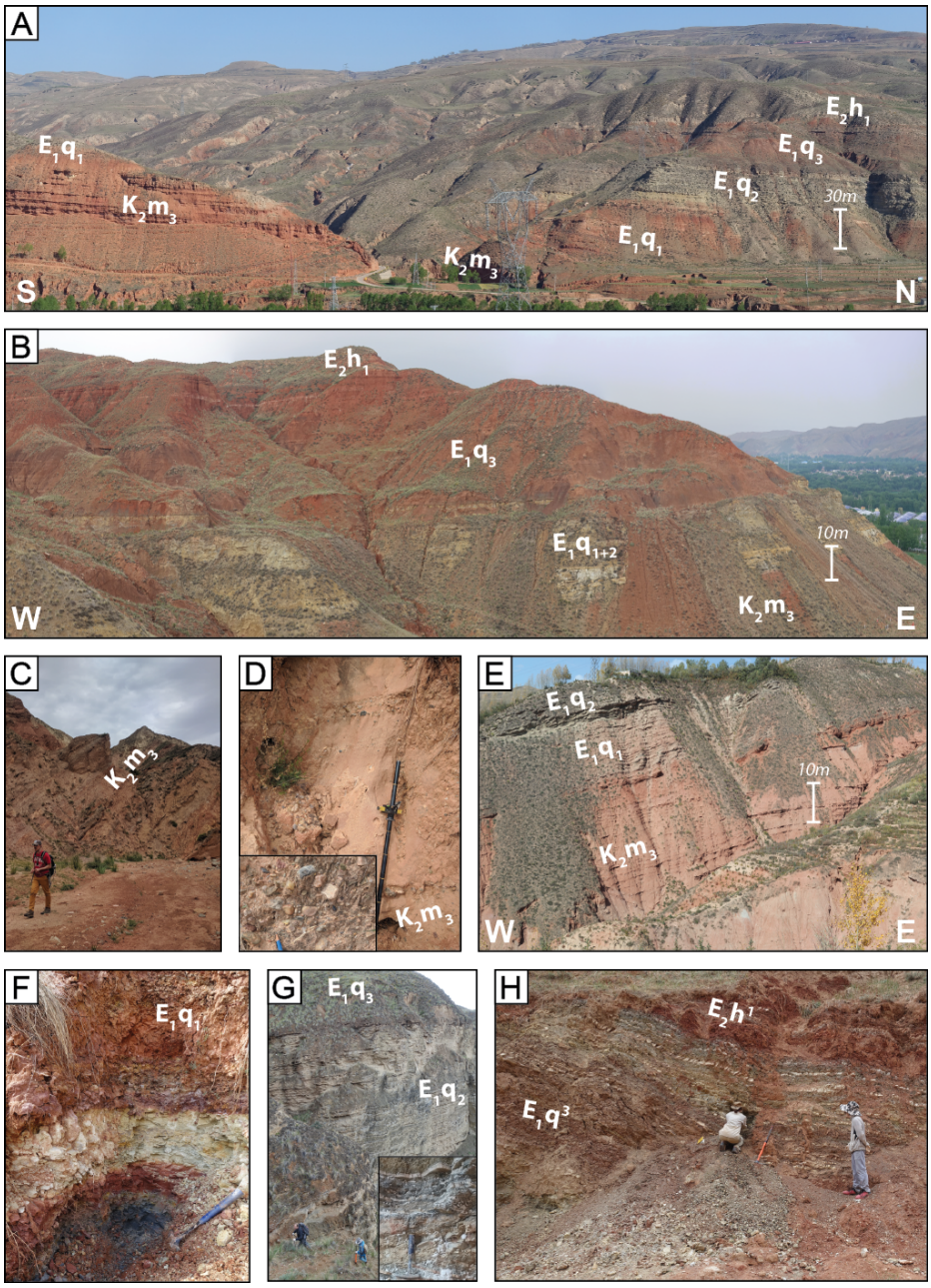

FIGURE 4.3: Pictures of the studied sections and lithofacies. (A) Overview of the Sanhe section. (B) Overview of the Dazhai section. (C) Conglomerates and sandstones of the Minhe Formation at the Ledu section. Person for scale. (D) Sandstone of the Minhe Formation at the Ledu section. Jacob's staff for scale. Inset shows the polymictic composition of the clasts. Pencil for scale. (E) Overview of the base of the East Xining section showing an angular unconformity between the Minhe and Qijiachuan Formations. (F) Yellow-white siltstone and variegated mudrocks at the 47-meter level of the Sanhe section. Hammer for scale. (G) Overview of the Bingling Shan section showing the middle Qijiachuan Formation. People for scale. Inset shows alternations between light gray and darker grey gypsiferous mudrocks and gypsum beds. Hammer for scale. (H) Transition from the Qijiachuan to the Honggou Formation at the Xiejia section. People for scale.

4.5 Radiometric dating and magnetostratigraphy

4.5.1 U-Pb radiometric age

The only carbonate bed which provided a radiometric age, CJC07, is located at the top of the middle Qijiachuan Formation in the Caijia section (1.3-meter level). The

age of this sample was determined from the lower intercept on Tera-Wasserburg plot (Fig. B.1). The resulting age is 53.7 ± 3.3 Ma with a low mean standard weighted deviation (0.4).

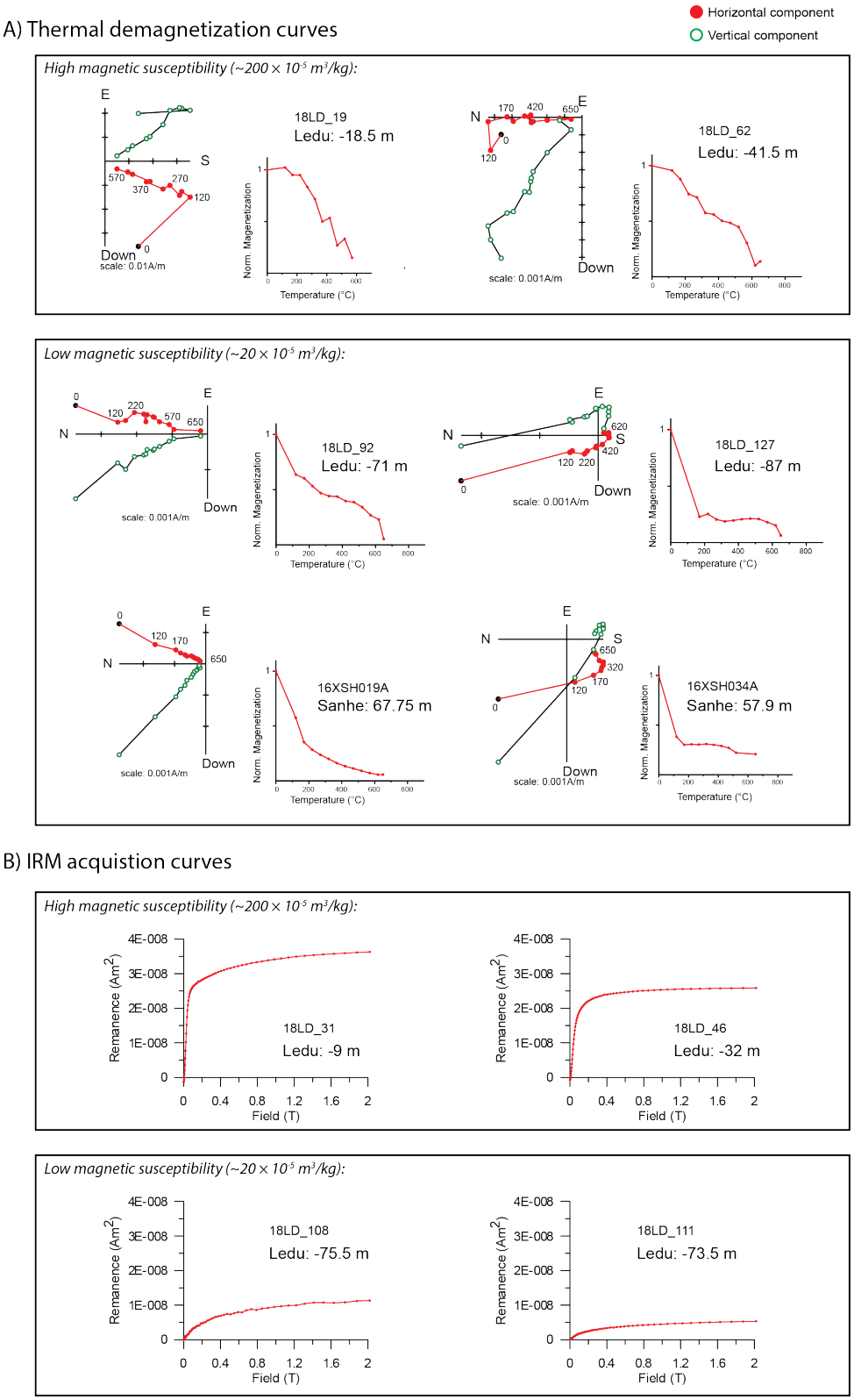

FIGURE 4.4: (A) Vector end-point diagrams (tilt corrected) and remanent magnetization during thermal demagnetization of representative samples. (B) IRM acquisition curves of representative samples.

4.5.2 Rock magnetism

The studied mudrocks show an abrupt shift in rock magnetic behavior occurring at the transition between the lower and middle Qijiachuan mudrocks. This shift can be clearly identified in the magnetic susceptibilities which increase abruptly from ~20 $\times 10^{-5}$ to ~200 $\times 10^{-5}$ m^3/kg (Fig. 4.2). Magnetic susceptibilities remain relatively high throughout the upper Qijiachuan Formation and gradually decrease down to ~20 $\times 10^{-5}$ m^3/kg in the Honggou Formation. Thermal demagnetization results in the removal of a viscous normal overprint up to ~200 °C resulting in a drop in the NRM (Fig. 4.4). High-susceptibility samples show a subsequent drop in NRM at ~580 °C indicating the presence of magnetite. Samples with both high and low magnetic susceptibilities require temperatures beyond 650 °C to completely demagnetize, which indicates the ubiquitous presence of hematite throughout the record. Measured S-ratios also show a shift at the transition from the lower to the middle Qijiachuan mudrocks (Fig. 4.7). S-ratios below the transition are <0.5 and indicate that coercive magnetic minerals such as hematite and goethite are predominantly carrying the NRM. Above the transition, the S-ratios are >0.5 indicating that magnetite is the dominant magnetic carrier. The NRM of the sandstone, conglomerate and gypsum beds is too low to determine the ChRMs. This hampers reconstructing the magnetostratigraphy of the Minhe Formation and the middle Qijiachuan Formation in the western part of the Xining Basin.

4.5.3 ChRM directions

Characteristic Remanent Magnetization (ChRM) directions were calculated for each sample using eigenvector principal component analysis on at least four temperature steps showing a linear decay between ~300-650 °C (Fig. 4.4; Kirschvink, 1980). The ChRMs were anchored to the origin and the directions resulting in a Maximum Angular Deviation (MAD) of >30° were rejected. However, most samples have a MAD of <10°.

The ChRMs show two clusters with either normal or reversed directions (Fig. 4.5). Mean directions were calculated using Fisher statistics (Fisher, 1953) and directions with an angle of more than 45° from the mean were rejected from further analysis (open symbols in Fig. 4.2 and red symbols in Fig. 4.5). We performed a reversals test (McFadden and McElhinny, 1990) on the mean directions of the sections to check the reliability of our dataset. The test succeeded for the Sanhe section with classification C, but is indeterminate for the Xiaoxia section and failed for the Ledu and Bingling Shan sections. The poor performance of the reversals tests is due to an unresolved normal overprint which has been observed in previous magnetostratigraphic studies in the Xining Basin (Chapter 3). This would exclude our dataset for the analysis of tectonic rotations, but does not affect the reliability of the reversals used in our magnetostratigraphy. Only in the Xiaoxia section we observe a cluster of normal directions similar to the modern-day field, suggesting that these may have been completely remagnetized (blue symbols in Fig. 4.5). These samples are from a weathered interval at the base of the section and are not considered as a polarity zone in the magnetostratigraphy (Fig. 4.2). Virtual Geomagnetic Poles (VGPs) were calculated from the ChRMs and are shown in Fig. 4.2. Polarity zones are defined by at least two samples of the same polarity.

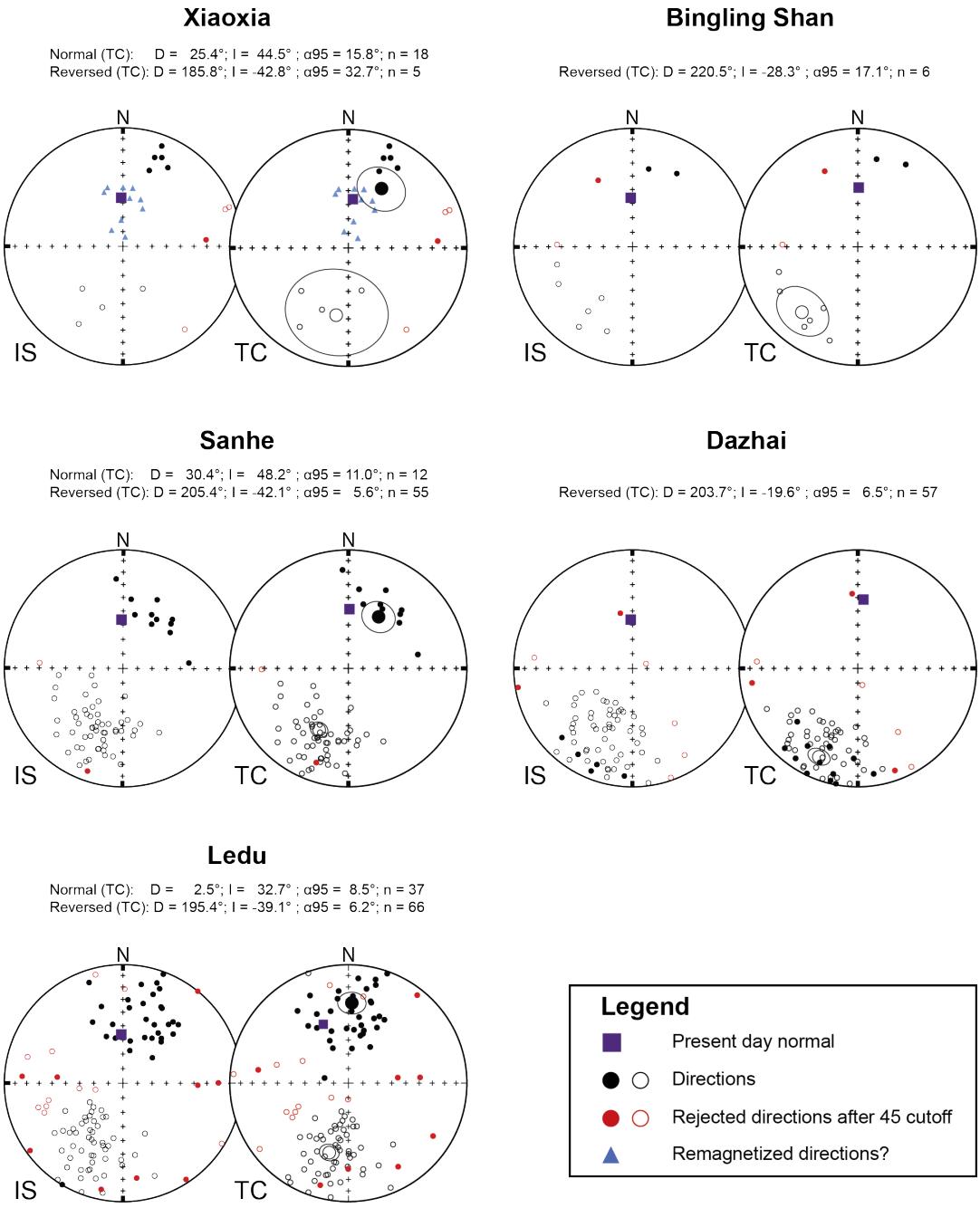

FIGURE 4.5: Equal-area stereographic projections of calculated ChRM directions of the studied sections both in situ (IS) and tilt corrected (TC).

4.5.4 Correlations to the GTS

In the following we correlate the observed polarity zones between the different sections and with the geological timescale (GTS16; Ogg et al., 2016) using correlations of previously studied sections (Chapter 3) and the tie point provided by the radiometric age of the carbonates (Fig. 4.2). The upper Qijiachuan mudrocks are characterized by a reversed polarity zone (R1 in Dazhai and R3 in Ledu), previously correlated with the C22r at the East Xining and Caijia sections and constrained by the radiometric age of a tuff (Chapter 3). The overlying C22n is lacking in the Dazhai section, possibly due to the abundance of fluvial sandstones in this interval resulting in the poor quality of the magnetic samples. At the Ledu section, C22r is underlain

by a short normal and reversed zone, followed by a longer normal and reversed zone (N2 to R1). This fits with the expected pattern of C23. However, these polarity zones are not observed at the Sanhe section in the western part of the Xining Basin. Here, the paleomagnetic signal is hampered due to the diamagnetic behavior of the evaporites. Furthermore, the lower Qijiachuan mudrocks show a different magnetostratigraphic pattern which is characterized by a long reversed zone, punctuated by two normal zones with small thicknesses of ∼2 and ∼5 meters. The upper of these normal zones is also recognized in the Bingling Shan, Xiaoxia and East Xining sections.

We identify an unconformity at the transition between the lower to middle Qijiachuan Formation based on the abrupt shift observed in the rock magnetic properties (Fig. 4.2, 4.4 and Fig. 4.7) and the inconsistent polarity zones between sections observed below this transition (Fig. 4.2). Ostracods and palynomorphs suggest a Paleocene to early Eocene age for the lower Qijiachuan Formation (Horton et al., 2004), which offers multiple possibilities of correlating the observed polarity zones and therefore we refrain from interpreting these. The base of N2 at the Ledu section occurs at the transition to the middle Qijiachuan Formation just above the unconformity. The boundary can therefore be confidently correlated with the base of C23n.1n with an age of 50.9 Ma. Furthermore, we linearly interpolate the duration of C22r to constrain the ages of the middle to upper Qijiachuan transition and the Qijiachuan to Honggou transition at 50.4 and 49.8 Ma respectively. Our age model results in accumulation rates of ∼5-7 cm/kyr for the middle-upper Qijiachuan Formation (Fig. 4.6), which is a doubling compared to the accumulation rate of ∼3 cm/kyr observed in the overlying Honggou Formation (Chapter 3).

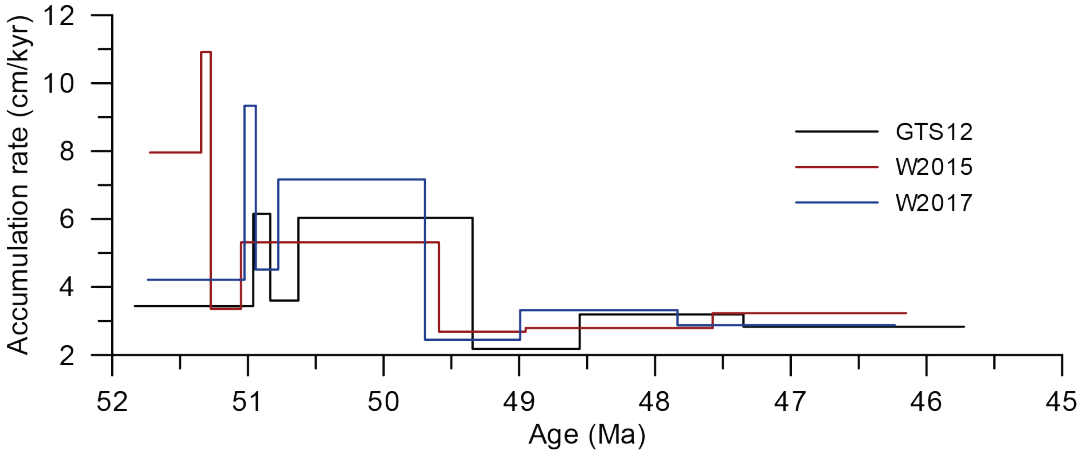

FIGURE 4.6: Accumulation rates using the magnetostratigraphic correlations presented in this study and various astronomically tuned age models for the chron boundary ages (Gradstein et al., 2012; Westerhold et al., 2015; Westerhold et al., 2017). Note that the GTS16 ages are the same as the W2015 ages for this interval.

4.6 Stable isotopes

The stable isotope records of the vadose-grown carbonates and bulk organic matter reveal several shifts that fit with the lithological boundaries between the lower, middle and upper Qijiachuan Formation (Fig. 4.7). The most pronounced of these shifts are recognized in the $\delta^{13}C$ values of the bulk organic material. These vary between -24 to -22‰ in the lower Qijiachuan Formation, slightly increase to -22 to -19‰ in

the middle Qijiachuan Formation, but are then followed by an abrupt excursion to ∼-28‰ at the transition to the upper Qijiachuan Formation. This is then followed by a gradual recovery to -24 to -22‰ during the transition to the Honggou Formation. These shifts can be explained by several mechanisms which will be explored in the discussion.

In contrast to the bulk organic carbon stable isotopes, the $\delta^{13}C$ values of the pedogenic carbonates remain low in the entire interval from the middle Qijiachuan to the Honggou Formation with values between -12 to -8‰. Only the lower Qijiachuan Formation is characterized by higher values varying between -6 to 0‰, which is similar to the values recognized in the middle to upper Eocene strata of the Xining Basin and linked to lower soil respiration rates (Fig. B.2; Licht et al., 2020). Values of $\delta^{18}O$ are variable throughout the record suggesting a significant influence of evaporation of soil water on the isotopic compositions (e.g. Horton et al., 2016). Only in the upper Qijiachuan Formation are these values stable at ∼-8‰.

4.7 Palynology

The palynological record of the middle Qijiachuan Formation is dominated by steppe-desert vegetation between ∼50.9 and 50.4 Ma, with temperate forest elements and conifers present in lower amounts (Fig. 4.7). This interval is mainly composed of *Ephedripites* pollen, which represent the xerophytic shrub *Ephedra* common in many Paleocene–Eocene assemblages in Central Asia (e.g., Wang, 1990; Sun and Wang, 2005). The conifer assemblage (e.g. *Podocarpidites*, *Vitreisporites* and *Abietineapollenites*) does not contain the typical highland species (e.g. nearest living relatives of *Picea*, Pinaceae), and could be derived from lower montane slopes instead. Ferns are observed as well in samples between ∼50.6 and 50.4 Ma. At ∼50.4 Ma, a palynological shift is revealed by a decrease in steppe-desert pollen in the upper Qijiachuan Formation. After this shift, the vegetation is composed of predominantly temperate forest and ferns, indicating a wetter environment. This assemblage lasts until at least ∼49.8 Ma, but may continue further into the overlying Honggou Formation. Unfortunately, the red mudrocks of this formation are not conducive to palynomorph preservation thereby limiting the record and our understanding of the vegetation in this interval (Fig. 4.7). Overlying strata reveal a subsequent increase in steppe-desert vegetation with *Ephedripites* comprising over 50% of the total pollen sum by the middle Eocene (Chapter 3; Bosboom et al., 2014a; Dupont-Nivet et al., 2008a; Hoorn et al., 2012).

4.8 Discussion

The magnetostratigraphy presented here extends the age model of the Eocene strata in the Xining Basin down to ∼50.9 Ma. This age is marked by an unconformity evidenced by the abrupt shift in rock magnetic properties and the inconsistent polarity zones in the underlying strata. Another angular unconformity is observed between the Minhe and Qijiachuan Formations at the base of the East Xining section and reported elsewhere (QBGMR, 1985). There is no evidence for significant tectonic activity in the region at this time, except for a poorly constrained phase of exhumation recorded in the Southern Qilian Shan located ∼500 km toward the west (He et al., 2018; Qi et al., 2016) and the activation of a thrust fault in the Western Qinling Shan located ∼80 km towards the south. This fault activation is dated at

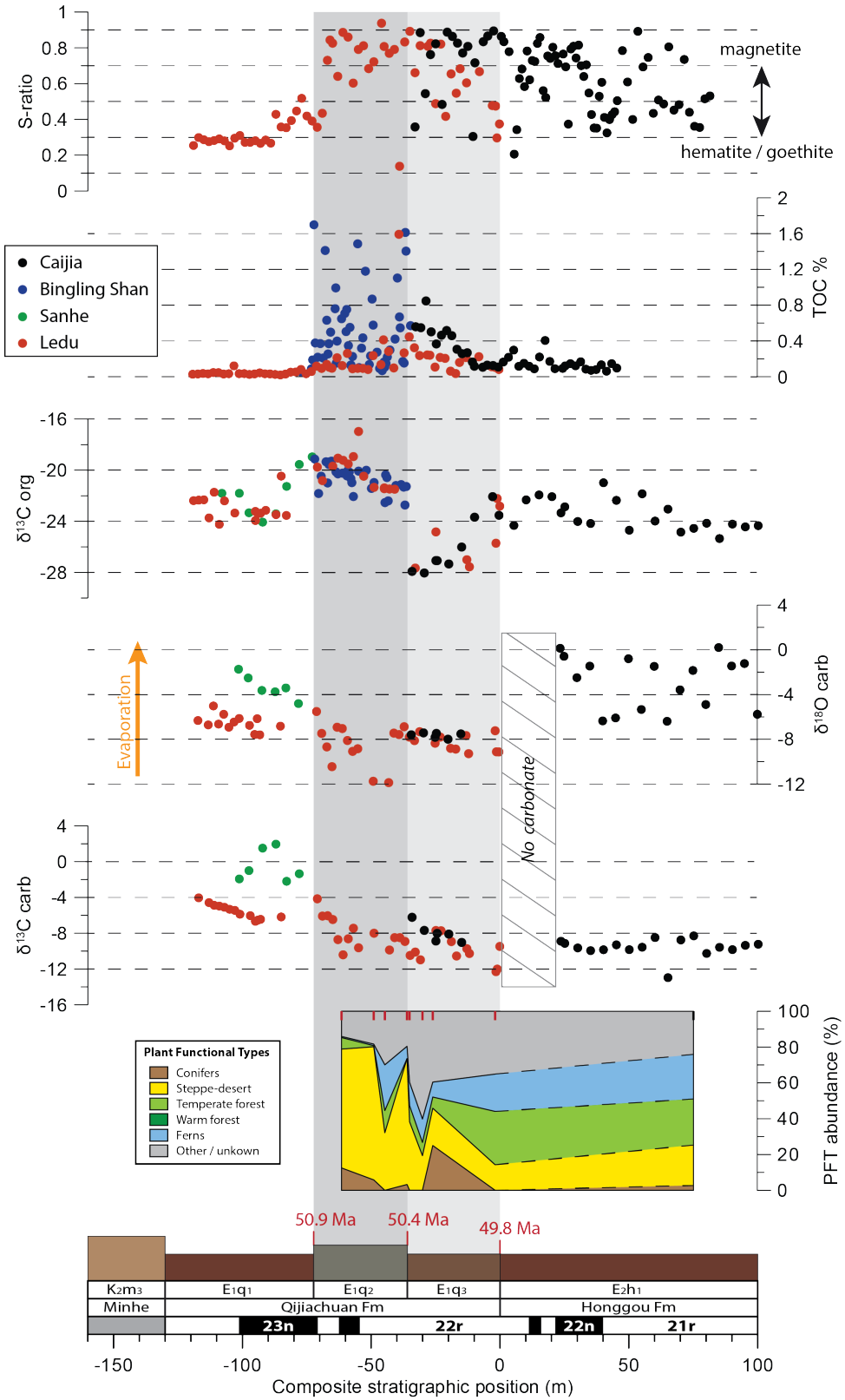

FIGURE 4.7: Composite of the studied sections constructed by aligning the distinct transition between the Qijiachuan and Honggou Formations (0-meter level). The composite record shows the S-ratios, TOC, $\delta^{13}C$ of organic matter, $\delta^{18}O$ and $\delta^{13}C$ of soil carbonate and the Plant Functional Type (PFT) abundances derived from the palynological record. A generalized illustration of the stratigraphy is shown below with ages based on linear interpolation between chron boundaries.

$\sim$50 ± 8 Ma (Duvall et al., 2011) and may be linked to the unconformities. Nevertheless, the overlying strata appear continuous and suitable for paleoenvironmental reconstructions.

4.8.1 Intensification of the hydrological cycle during the early Eocene

The palynological assemblages, consisting of steppe-desert pollen as well as temperate forest elements together with conifers and ferns, and the low $\delta^{13}C$ values of the pedogenic carbonates suggest that the early Eocene (represented by the middle Qijiachuan to lower Honggou Formations) was relatively humid compared to both the underlying and overlying strata (Hoorn et al., 2012; Horton et al., 2004; Licht et al., 2020). The pedogenic $\delta^{13}C$ values are driven by the isotopic compositions of atmospheric and soil respired CO_2 as well as a number of other processes including soil respiration rate, depth of carbonate formation in the soil (Cerling, 1984), plant water-stress (Kohn, 2010; Schlanser et al., 2020) and early diagenesis of soil organic matter (Wynn, 2007). Although these individual processes are difficult to constrain, together they drive the $\delta^{13}C$ composition towards higher values as aridity increases and therefore may be used as a crude proxy for aridification (Caves Rugenstein and Chamberlain, 2018). A regional compilation of Eocene pedogenic carbonates reveals a gradient with lower $\delta^{13}C$ values (-9 to -8‰) occurring in eastern China and interpreted as monsoonal influence, while higher values (-5 to -2‰) occur in the arid Asian interior (Caves Rugenstein and Chamberlain, 2018). The low $\delta^{13}C$ values recorded in the Xining Basin therefore suggest that it belonged to the humid monsoonal domain during the early Eocene, but is followed by a shift to higher values in the middle Eocene to Oligocene strata (Fig. B.2; Licht et al., 2020). This aridification is linked to global cooling and Tibetan Plateau uplift and was previously recognized in rock magnetic properties (Fang et al., 2015) and clay minerals (Fang et al., 2019b) in the Xining Basin as well as in the regional compilation of the pedogenic stable isotopes (Caves Rugenstein and Chamberlain, 2018).

Pedogenic $\delta^{18}O$ values are stable and unaffected by evaporation in the upper Qijiachuan Formation, which is in contrast to the overlying and underlying deposits showing variable values in $\delta^{18}O$. This suggests that peak humid conditions occurred during this liver-brown mudrock interval, which is recognized throughout the basin. Increased atmospheric moisture and runoff may explain the higher sediment accumulation rates; especially in the absence of other tectonic drivers on these short timescales, and because the underlying evaporites suggest that the basin was underfilled and therefore susceptible to changes in sediment input (Carroll and Bohacs, 1999). Wetter environmental conditions may also explain first, the higher abundance of magnetite, either through improved preservation or increased pedogenic production (e.g. Ahmed and Maher, 2018; Maher, 2016), and second, the higher organic carbon content of these deposits, either through increased burial or higher primary productivity. In addition, the $\delta^{13}C$ values of the bulk organic matter show an excursion of $\sim$-6‰ in this interval which can be interpreted in various ways. First, it may reflect a shift in the isotopic composition of atmospheric CO_2 such as an injection of isotopically-light carbon during hyperthermal events (e.g. Kirtland-Turner et al., 2014). However, the duration of the upper Qijiachuan interval is too long for hyperthermals which last $\sim$40–200 kyrs. Second, the excursion may reflect a shift in plant fractionation due to reduced water stress (Kohn, 2010; Schlanser et al., 2020) or third, better preservation of organic material in the soil (Wynn, 2007). Both would

indicate wetter conditions, also confirmed by the reduction in the steppe-desert vegetation observed at ∼50.4, and we therefore interpret the upper Qijiachuan Formation, spanning from 50.4 to 49.8 Ma, to reflect an intensified hydrological cycle resulting in a more humid and organic-rich mudflat as opposed to the evaporites and the dry mudflat deposits found elsewhere in the record. The underlying middle Qijiachuan Formation is characterized by organic-rich beds as well but with enriched bulk organic $\delta^{13}C$ values and interbedded with evaporites. This interval is therefore interpreted to reflect variable climatic conditions alternating between both arid and humid periods, which correlates well with the prevalence of both xerophytic vegetation and moisture loving-ferns documented by the palynological record. The meter-scale alternations of the beds (Fig. 4.3G) suggest an orbital timescale for these fluctuations.

4.8.2 Driving mechanisms

Uplift of the Tibetan Plateau, sea incursions of the proto-Paratethys Sea and global climate are all hypothesized to have driven the Asian paleoclimate during the Eocene (e.g. Chapter 3; Caves Rugenstein and Chamberlain, 2018; Licht et al., 2014). In the following, we discuss which of these mechanisms may be responsible for the intensified hydrological cycle observed in our study. The Tibetan Plateau shows a long-term trend of progressive northward growth since the India-Asia collision at ∼60 Ma (Kapp and DeCelles, 2019; Rohrmann et al., 2012) and therefore cannot explain the transient and relatively short period of increased atmospheric moisture in the Xining Basin. Furthermore, the proto-Paratethys Sea was experiencing a lowstand (Kaya et al., 2019) and would have supplied less westerly moisture at this time. The regional gradient in pedogenic $\delta^{13}C$ values also suggests that the atmospheric moisture was derived from the east rather than the west (Caves Rugenstein and Chamberlain, 2018).

The humid interval in the Xining Basin correlates with the Early Eocene Climatic Optimum (EECO), a long-term period of peak greenhouse warmth between 53 and 49 Ma (Westerhold et al., 2018). The warmer climate at this time is driven by elevated atmospheric CO_2 concentrations (Anagnostou et al., 2016; Cramwinckel et al., 2018). However, these concentrations alone would result in more enriched $\delta^{13}C$ values in the soil carbonates and therefore need to be counteracted by other mechanisms such as increased atmospheric moisture to explain the depleted values observed in the Xining Basin. The greenhouse warmth could have driven an intensified hydrological cycle and possibly promoted monsoonal circulation as suggested by some climate model simulations (Licht et al., 2014; Zoura et al., 2019), but not by others (Farnsworth et al., 2019). Intensified monsoonal circulation is supported by clay minerals recorded during the EECO in the paleosols of the Qaidam Basin, western China (Song et al., 2018) and a coeval shift from semi-arid evaporites to subhumid carbonates during the early Eocene in the Jianghan Basin, central China (Teng et al., 2019). Globally, precipitation is observed to increase during the EECO in several midlatitude terrestrial records in both the northern and southern hemisphere (Hyland and Sheldon, 2013; Hyland et al., 2017).

Detailed marine records reveal high-amplitude climate fluctuations between 51.5 and 50.5 Ma, which are interpreted to reflect a climate system approaching a critical tipping point (Lauretano et al., 2018; Westerhold et al., 2018). This highly-sensitive climatic state may explain the variable paleoenvironmental setting inferred for the

middle Qijiachuan Formation in the Xining Basin. However, the abrupt shift observed between the Qijiachuan and the overlying Honggou Formation at 49.8 Ma is not represented by the marine records (Westerhold et al., 2018). Instead, these records show a gradual long-term cooling but may have triggered an abrupt nonlinear response in the terrestrial environment.

4.9 Conclusion

Pedogenic stable isotopes and fossil palynomorphs reveal a transient period of increased atmospheric moisture during the early Eocene in the Xining Basin. Peak humid conditions are identified between ~50.4 and 49.8 Ma and reflected by increased sedimentation rates, higher organic carbon preservation and shifts in pedogenic and bulk organic stable isotope compositions. These results are in stark contrast to the semi-arid and arid environments of the Cretaceous and most of the Cenozoic period as evidenced by abundant redbeds, eolian dunes, evaporites and the pollen of xerophytic plants reported in the region (Guo et al., 2008; Hasegawa et al., 2012; Sun and Wang, 2005).

This indicates a significant reconfiguration of the hydrological cycle and possibly intensification of monsoonal circulation. The increase in atmospheric moisture is linked to the peak greenhouse warmth of the EECO and is therefore driven by atmospheric CO_2 forcing as opposed to recent climate model simulations stating that paleogeography and not CO_2 is the dominant control on the Asian monsoons (Farnsworth et al., 2019). This mismatch between model and proxy data highlights that the role of global warming in driving atmospheric moisture remains poorly understood, especially in terms of the dynamic effects governing moist convergence and monsoonal circulation (e.g. Chou et al., 2009; Wang et al., 2020a). Better understanding of the hydrological cycle during past greenhouse climates may therefore hold major implications regarding current and future global warming.

Chapter 5

Asian dust appearance at 40 Ma

Niels Meijer, Guillaume Dupont-Nivet, Natasha Barbolini, Amber Woutersen, Yang Zhang, Xiang-Jun Liu, Alexis Licht, Hemmo A. Abels, Carina Hoorn, Rik Tjallingii, Christoff Andermann, Michael Dietze, Norbert Nowaczyk

Abstract

Asian mineral dust has been studied extensively for its role in affecting regional- to global-scale climate and for its deposits, which enable reconstructing Asian atmospheric circulation in the past. However, the timing and origin of the dust deposits remain debated. Numerous dust records have been reported across the Asian continent and are linked to various mechanisms including global cooling, Tibetan Plateau uplift and retreat of the inland proto-Paratethys Sea. Here, we study the terrestrial mudrocks of the Xining Basin in central China and identify a dust component appearing in the grain-size record at 40 Ma. This is coeval with the onset of high-latitude orbital cycles and a shift to predominant steppe-desert vegetation in our record. Furthermore, wind directions derived from eolian dunes suggest northwesterly winds, similar to the modern-day winter monsoon which is driven by an atmospheric high pressure system developing over Siberia. We propose that the observed shifts at 40 Ma reflect the onset of the Siberian High interacting with westerly-derived moisture at orbital timescales and driving dust storms and aridification in central China. The timing suggests that the onset was triggered by increased continentality due to the retreating proto-Paratethys Sea rather than by uplift or atmospheric cooling. This suggests that the large-scale Asian atmospheric circulation is resilient and should be considered in climate modelling studies and proxy records covering the past 40 million years.

5.1 Introduction

During wintertime, the Asian continent is characterized by a high atmospheric pressure system developing over southern Siberia and Mongolia. This so-called Siberian High drives the strong northwesterly winds of the modern-day East Asian winter monsoon bringing cold and dry air from the Asian interior (Chang et al., 2006). During springtime, the Siberian High creates a strong meridional temperature contrast between cold air in the north and warmer air in the lower mid-latitudes resulting in frequent dust storms (Roe, 2009). These storms transport silt-sized material (20-60 µm) from the arid upwind areas to form the Chinese Loess Plateau (Sun, 2002) providing a unique record for studying the history of Asian aridification and atmospheric circulation (Maher, 2016). Furthermore, the transported mineral dust plays an important role in the climate system by scattering solar radiation, promoting

cloud formation and providing nutrients to the Pacific Ocean (Jickells et al., 2005; Martin, 1990; Shaffer and Lambert, 2018).

Identifying the onset of the Chinese dust deposits is key to better understand the origin of the East Asian atmospheric circulation and the role of mineral dust in the evolution of regional- to global-scale climate. However, various ages for the onset of dust records (Fig. 5.1A) have been reported so far (Ao et al., 2016; Ding et al., 1998a; Ding et al., 2001; Garzione et al., 2005; Guo et al., 2002; Jiang and Ding, 2010; Li et al., 2018a; Licht et al., 2014; Qiang et al., 2011; Song et al., 2001; Sun et al., 1997; Sun et al., 1998b; Sun et al., 1998a; Xu et al., 2009; Zhang et al., 2014; Zheng et al., 1992; Zhu et al., 2008). The classic sequence of Quaternary loess initiated at ∼2.6 Ma and is linked to the coeval glaciation of the northern hemisphere (Ding et al., 1997; Lu et al., 2010). These loess deposits are interbedded with finer-grained (10-30 µm) reddish paleosols formed during interglacials, which are interpreted to have formed under a wetter East Asian summer monsoon (Maher, 2016). Conformably underlying the Quaternary loess is the Red Clay, which, despite the name, consists mostly of silt-sized material similar to the paleosols in the Quaternary loess. These are therefore interpreted to reflect the atmospheric circulation during the warmer and wetter Miocene-Pliocene epochs (Maher, 2016). In the central Chinese Loess Plateau, east of the Liupan Shan, ages of the Red Clay are ∼7-11 Ma (Ao et al., 2016; Ding et al., 1998a; Ding et al., 2001; Wang et al., 2014a; Song et al., 2001; Sun et al., 1997; Sun et al., 1998b; Sun et al., 1998a; Xu et al., 2009; Zheng et al., 1992; Zhu et al., 2008). The onset of these dust deposits is interpreted as the set-up of winter monsoonal circulation and inland aridification both linked to the uplift of the Tibetan Plateau (An et al., 2001). However, older loess-like deposits extending up to ∼20-29 Ma were identified west of the Liupan Shan (Garzione et al., 2005; Guo et al., 2002; Qiang et al., 2011; Zhang et al., 2014) and to the north of the Loess Plateau (Jiang and Ding, 2010). These records suggest that the monsoonal circulation is much older and proposed to be driven by the combined effect of an earlier phase of Tibetan Plateau uplift and the retreat of the inland Paratethys Sea that covered the Eurasian continent during the Paleogene (Guo et al., 2002). In recent years, even older dust deposits have been identified in Eocene strata (Li et al., 2018a; Licht et al., 2014), suggesting that the Asian atmospheric circulation may have been driven by the India-Asia collision, greenhouse to icehouse cooling or proto-Paratethys Sea incursions, all occurring during the Eocene epoch.

The Eocene mudrocks in the Xining Basin have been previously identified as some of the oldest loess-like deposits in the region (Fig. 5.1) based on grain-size distributions, quartz surface morphologies and a provenance signal derived from U-Pb age spectra (Licht et al., 2014; Licht et al., 2016b). This record is shown to extend from 34 Ma to 40 Ma and has been used as an indicator for aridity and winter monsoonal circulation. However, it remains unclear when dust deposition started in the basin which has important implications for the origin of Asian dust and associated atmospheric circulation. Moreover, recent sedimentological and provenance studies show that the pre-Quarternary dust records in the region contain significant contributions from local alluvial sources which obscures the dust signal (Alonso-Zarza et al., 2009; Nie et al., 2014; Liu et al., 2019; Zhang et al., 2014; Zhang et al., 2018a).

Here, we reassess and extend the record of Licht et al. (2014) to ∼50.5 Ma using sections in the Xining Basin (Fig. 5.1B) previously dated by magnetostratigraphic correlations (Chapter 3; Abels et al., 2011; Bosboom et al., 2014a; Dupont-Nivet et al., 2007) and construct a composite record of grain-size distributions (GSDs) to identify

windblown dust. The measured GSDs of the mudrocks represent a mix of the different alluvial and eolian components operating in the basin (Paterson and Heslop, 2015; van Hateren et al., 2018; Varga et al., 2019a). These are subsequently unmixed using a non-parametric end-member analysis to quantify the relative contributions of eolian dust. End-member modelling of GSDs is widely used (see appendix I in van Hateren et al., 2018) and has been successfully applied to distinguish eolian and fluvial contributions in marine cores (e.g. Weltje and Prins, 2003) and lacustrine records (e.g. Dietze et al., 2014). In addition, the end-member models have been extensively tested and shown to perform well using both artificial and natural datasets (Dietze and Dietze, 2019; Paterson and Heslop, 2015; van Hateren et al., 2018; Varga et al., 2019a). In addition, we use the composite record to study the cyclostratigraphy as well as palynology and study a new sedimentary section (Baimasi), containing eolian sedimentary structures to derive paleowind directions.

5.2 Geological setting and lithostratigraphy

The modern-day Xining Basin is bounded by the eastern Qilian Shan in the north, the Laji Shan in the south and the Riyue Shan in the west. The basin constitutes the westernmost part of the Cenozoic Longzhong Basin, which stretches towards the Liupan Shan in the east (Horton et al., 2004). Various tectonic settings have been proposed for the Paleogene Xining Basin, including a foreland basin of the western Qinling Shan (Liu et al., 2013), a strike-slip basin due to differential rotation of crustal blocks (Zhang et al., 2016a) or an extensional basin due to the far-field effect of the subducting Pacific plate (Fan et al., 2019). During the Neogene, the Longzhong Basin was segmented into smaller sub-basins due to deformation of the northeastern Tibetan Plateau (Horton et al., 2004).

Cenozoic deposition commenced during the early Eocene and unconformably overlies Cretaceous strata or older basement rocks (Fan et al., 2019; Fang et al., 2019a). Paleogene deposits include the Qijiachuan, Honggou, Mahalagou and Xiejia Formations (Dai et al., 2006; Horton et al., 2004; BGMRQP, 1965; QBGMR, 1985 and Fig. 5.1C). The Qijiachuan Formation consists of organic-rich evaporites and fluviolacustrine mudrocks (Chapter 3; Fang et al., 2019a). These are followed by brick-red, massive mudrocks of the Honggou Formation alternated with occasional lacustrine mudrocks containing carbonate beds and evaporites. Fluvial sandstones are found occasionally in the lower part, but decrease upwards. The Honggou Formation successions are interpreted mainly as a dry mudflat in a distal alluvial environment based on the occurrence of evaporites and the massive structure of the mudrocks resulting from subaerial reworking (Chapter 3). The overlying Mahalagou Formation is characterized by orbitally-forced alternations between massive red mudrocks and gypsum beds (Fig. 5.2A; Abels et al., 2011; Dupont-Nivet et al., 2007; Xiao et al., 2010). The gypsum beds in the Xining Basin disappear after the Eocene-Oligocene Transition (EOT) due to regional aridification (Dupont-Nivet et al., 2007). The uppermost gypsum bed at the EOT is used as a stratigraphic marker for the boundary to the Oligocene Xiejia Formation composed predominantly of brownish-red mudrocks (Fang et al., 2019a). The mudrocks of the Mahalagou Formation have been interpreted as eolian dust similar to the Quaternary Chinese loess (Licht et al., 2014; Licht et al., 2016b).

Neogene formations include the brownish-yellow alluvial mudrocks and fluvial sandstones of the Chetougou and Guanjiashan Formations and the conglomerates of the

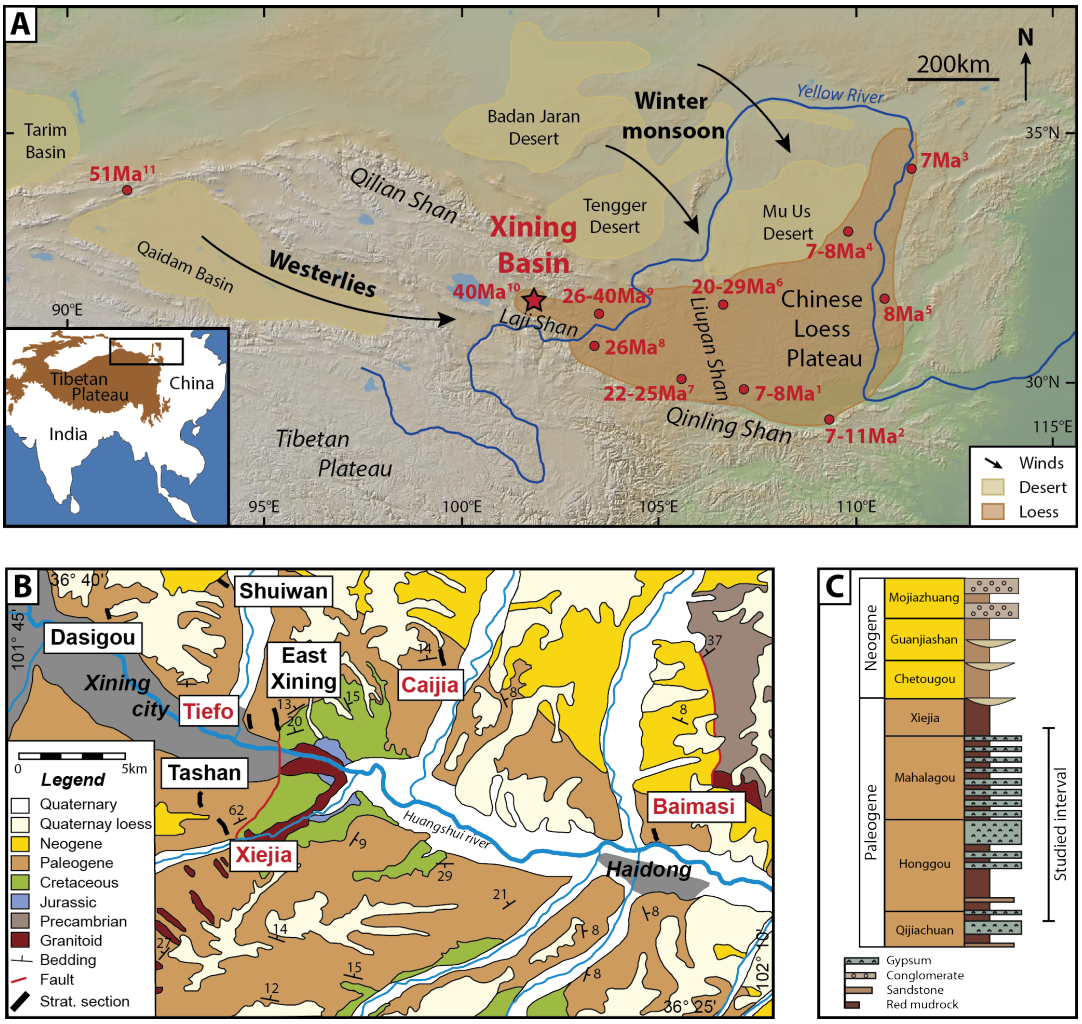

FIGURE 5.1: (A) Modern-day topographic map (http://www.geomapapp.org) of the northeastern Tibetan Plateau showing various reported ages for the onset of loess-like deposits: 1) central Loess Plateau: Ding et al., 2001; Song et al., 2001; Sun et al., 1997; Sun et al., 1998b; Sun et al., 1998a; 2) southern Loess Plateau: Sun et al., 1997; Wang et al., 2014a; Zheng et al., 1992; 3) Baode: Zhu et al., 2008; 4) Jiaxian: Ding et al., 1998a; Qiang et al., 2001; 5) Shilou: Xu et al., 2009; age reinterpreted by Ao et al., 2016; 6) Sikouzi: Jiang and Ding, 2010; age reinterpreted by Wang et al., 2011; 7) Tianshui Basin: Guo et al., 2002; record extended by Qiang et al., 2011; 8) Linxia Basin: Garzione et al., 2005; 9) Lanzhou Basin: Zhang et al., 2014; age reinterpreted by Wang et al., 2016a; 10) Xining Basin: Licht et al., 2014; 11) Xorkol Basin (Li et al., 2018a). The Xining Basin is indicated with a star.(B) Geological map of the Xining Basin based on BGMRQP (1965), QBGMR (1985) and Dai et al. (2006) showing the locations of the sections. Sections sampled in this study are indicated in red. (C) Lithostratigraphy listing the formations of the Xining Basin adapted from Horton et al. (2004) and updated following Fang et al. (2019a).

Mojiazhuang Formation (Fang et al., 2019a; Yang et al., 2017; Zhang et al., 2017). The Neogene deposits are coarsening upwards due to increased uplift of the eastern Qilian Shan, located north of the Xining Basin (Fang et al., 2019a; Yang et al., 2017), and of the Laji Shan located to the south (Xiao et al., 2012). Subsequent incision of the Huangshui River resulted in fluvial terraces which are capped by up to 200 meters of Pliocene Red Clay and Quaternary loess (Fang et al., 2019a; Zhang et al., 2017).

5.3 Materials and methods

5.3.1 Sections

We sampled previously dated sections (Fig. 5.1B) for grain-size analysis and fossil pollen to create a composite record covering the early to late Eocene. These sections include the Tiefo section, 36°34′37″N, 101°52′50″E (Bosboom et al., 2014a), and a freshly excavated quarry at the Xiejia section, 36°31′20″N, 101°52′20″E (Chapter 3; Dupont-Nivet et al., 2007), both covering the upper Honggou to lower Mahalagou Formations. We also sampled the Caijia section, 36°36′55″N, 101°59′03″E (Chapter 3), covering the Qijiachuan to Honggou Formations. In addition to grain-size analysis and pollen, this section was sampled for X-Ray Fluorescence (XRF) scanning and color to construct time series for cyclostratigraphic analysis. The Baimasi section, 36°31′6″N, 102°6′14″E (Zhang et al., 2016a), was logged and sampled for magnetostratigraphy and grain-size analysis. Additionally, we collected 10 grain-size samples from a 12-meter profile of the Oligocene deposits north of the Shuiwan section, 36°39′43″N, 101°52′11″E (Abels et al., 2011; Dupont-Nivet et al., 2007), and 10 grain-size samples from a 1-meter loess profile near the Xiejia section, 36°31′12″N, 101°52′17″E, for comparison with the Eocene grain-size distributions (GSDs).

5.3.2 Magnetostratigraphy

Paleomagnetic samples were taken at the Baimasi section at $\sim$1 meter resolution where possible, using a portable electric drill and a compass mounted on an orientation stage. The samples were analyzed in the laboratory of paleo- and rock magnetism at the German Research Centre for Geosciences (GFZ) in Potsdam. After cutting, the samples were thermally demagnetized in 12 temperature steps. A viscous normal overprint was removed during demagnetization up to 200 °C. Subsequent heating up to 650 °C resulted in a linear demagnetization towards the origin. The magnetic behavior is similar to previous paleomagnetic studies in the Xining Basin and indicates that magnetite and hematite are the dominant magnetic carriers (Dai et al., 2006).

5.3.3 Grain-size analysis

Mudrocks of the studied sections were sampled at $\sim$1 meter resolution where possible and grain-size analysis was performed in the sediment laboratory (Sedlab) of section 4.6 Geomorphology at the GFZ in Potsdam. Beds of evaporites and carbonates were not sampled. The samples were pretreated in several steps to remove organic matter, carbonate and gypsum and to disperse the grains. First, the samples were carefully ground using a mortar and pestle. Second, 2.5 ml of 30% hydrogen peroxide (H_2O_2) was added to remove the organic matter. The samples were left to react on a shaking table for at least six days until the reaction stopped. Third, 2.5 ml of 10% hydrochloric acid (HCl) was added and the samples were left on a shaking table for two days to dissolve the carbonate. Fourth, 50 ml of deionized water was added and the samples were left in an overhead shaker for three days to dissolve the gypsum. The deionized water was refreshed every day. Fifth, 0.1 g of sodium pyrophosphate ($Na_4P_2O_7{*}10H_2O$) in a 2.5 ml solution was added and the samples were left in an overhead shaker for at least 12 hours to disaggregate the grains.

The samples were measured in suspension using a Horiba Partica LA-950 v2 laser diffraction particle sizer. The diffraction data were converted to GSDs using the Mie

optical model, which is recommended for particle sizes below 30 µm (Varga et al., 2019b). However, the Mie model requires the refractive index and the absorption coefficient of the measured particles as input. These are difficult to constrain because the samples are composed of an unknown mix of minerals. Therefore, we tested a wide range of refractive indices (1.4-2.45) and absorption coefficients (0-1) and compared the GSDs (Fig. C.1). Artificial peaks appear in the submicron-range when the absorption coefficient approaches zero, as is reported in previous studies (Sperazza et al., 2004; Varga et al., 2019b). Otherwise, the GSDs are consistent and show only minor variations. Hereafter, we used a refractive index of 1.55 and an absorption coefficient of 1. GSDs are given in 92 size bins logarithmically distributed between 0.011 and 2500 µm.

To unmix the GSDs, we used the non-parametric end-member analysis implemented in the AnalySize software package (Paterson and Heslop, 2015). Although this analysis is non-parametric and therefore requires no predefined function of the end-members, the number of end-members needs to be prescribed. Tests with synthetic mixtures have shown that the use of an incorrect number of end-members leads to unreliable results (van Hateren et al., 2018). We ran the analysis using 1 to 10 end-members and found that four end-members are necessary to account for most (98.6%) of the variance in the dataset (R^2 = 0.986). Increasing the number of end-members does not significantly improve the quality of fit (Fig. C.2). The median grain-size, end-member abundances and sample-wise R^2 of the individual sections are shown in Fig. C.3. A composite grain-size record was created by linear interpolation of the samples between correlated polarity zone boundaries in the various sections.

5.3.4 Cyclostratigraphy

We constructed time series of the Caijia section by measuring XRF scanning and color at 0.5 meter resolution. Samples were carefully ground, assembled in 32 mm cups, covered by a 4 µm polypropylene film and measured using an ITRAX XRF core scanner. XRF intensities (in counts per second) were obtained for the 13 elements Al, Si, S, Cl, K, Ca, Ti, V, Mn, Fe, Rb, Sr and Zr. All statistical analyses were performed on element intensity records after log-ratio or centered-log-ratio transformation. We used principal component (PC) analysis as implemented in the ItraXelerate software (Weltje et al., 2015) to examine the covariance between the individual elements in our dataset. The results are presented in a biplot of PC1 and 2, which reveals three groups of elements (Fig. C.4). Lithogenic elements (Fe, Ti, K, Si, Al and Rb) are positively correlated and clearly separated from the authigenic elements (Ca, S, and Sr) by PC1, which explains 72.7% of the variance. The authigenic elements can be subsequently separated into carbonates (Ca) and gypsum (S and Sr) along PC2 explaining another 12.7% of the variance. We construct time series by using the dominant elements of these three groups (Ti, Ca and S). Hence, relative variations of lithogenics, carbonates and gypsum are represented by log-ratios of Ti/Ca, S/Ti and S/Ca, which provide the most easily interpretable signals of relative changes in the chemical composition (Weltje and Tjallingii, 2008).

RGB-values were extracted from high-resolution photographs produced by the corescanner to construct a color record. The average values of ten representative pixels were used and converted to CIELAB color space for interpretation purposes. These

values include: L^* (lightness), a^* (red over green) and b^* (yellow over blue). However, note that these values are not calibrated and should only be used to study relative changes throughout our record. Spectral analysis was performed using Redfit (Schulz and Mudelsee, 2002) as implemented in the Past software (Hammer et al., 2001) with no segmentation, no oversampling and a Welch window. The time series were bandpass filtered using the AnalySeries software (Paillard et al., 1996).

5.3.5 Palynology

Productive palynological samples were collected from gypsum beds and laminated mudrocks in the Tiefo, Xiejia and Caijia sections. Samples collected from red beds in these sections were barren of palynomorphs. The samples were prepared by Palynological Laboratory Services (Anglesey, UK) using standard palynological techniques (HCL, HF, sieving at 10µm) and examined at the University of Amsterdam, The Netherlands. Ten samples were productive; nine from the Mahalagou Formation, but only one from the Honggou Formation. These samples were added to the previously studied palynological record of the Xining Basin (Fig. C.5; Bosboom et al., 2014a; Dupont-Nivet et al., 2008a; Hoorn et al., 2012; Page et al., 2019). Palynomorphs were identified using the Genera File of Fossil Pollen and Spores (Jansonius and Hills, 1976 and recent updates), Song et al. (1999) and the Chinese palynological literature. Plant Functional Types (PFTs) were assigned using the Nearest Living Relatives (NLR) approach applied by (Hoorn et al., 2012).

5.4 Baimasi section

The late Eocene deposits in the Xining Basin are characterized by mudrocks alternated with gypsum beds (Fig. 5.2A) formed in saline lakes (Abels et al., 2011; Bosboom et al., 2011; Dupont-Nivet et al., 2007). The newly studied Baimasi section is located on the eastern margin of these saline lake deposits and is described in the following. The section is subsequently dated and correlated with the other sections by using magnetostratigraphy and marker beds.

5.4.1 Lithostratigraphy

Description

The lithostratigraphy of the Baimasi section consists of red gypsiferous mudrocks and gypsarenites (Fig. 5.2B and C). The mudrocks have a horizontally laminated or massive structure. The gypsarenites are horizontally bedded and contain dm-scale sets of planar cross-bedding and laterally extensive horizontal bounding surfaces (Fig. 5.2B and C). The foresets have a tangential base and a maximum dip of $\sim$20°. Measured paleocurrent directions are to the south (Fig. 5.3). The gypsarenites are well-sorted and consist of rounded to well-rounded grains of gypsum (Fig. 5.2D). Rare cm-scale beds of very fine sandstone containing ripple and climbing ripple cross-lamination are observed at the $\sim$30 meter-level. Dm-scale beds of green horizontally laminated gypsum are observed at the base and the top of the section and can be correlated with saline lake deposits in the center of the basin. Regular $\sim$3 meter alternations between red mudrocks and gypsum beds are observed on top of the section, followed by a shift to brownish-red mudrocks (Fig. 5.2E).

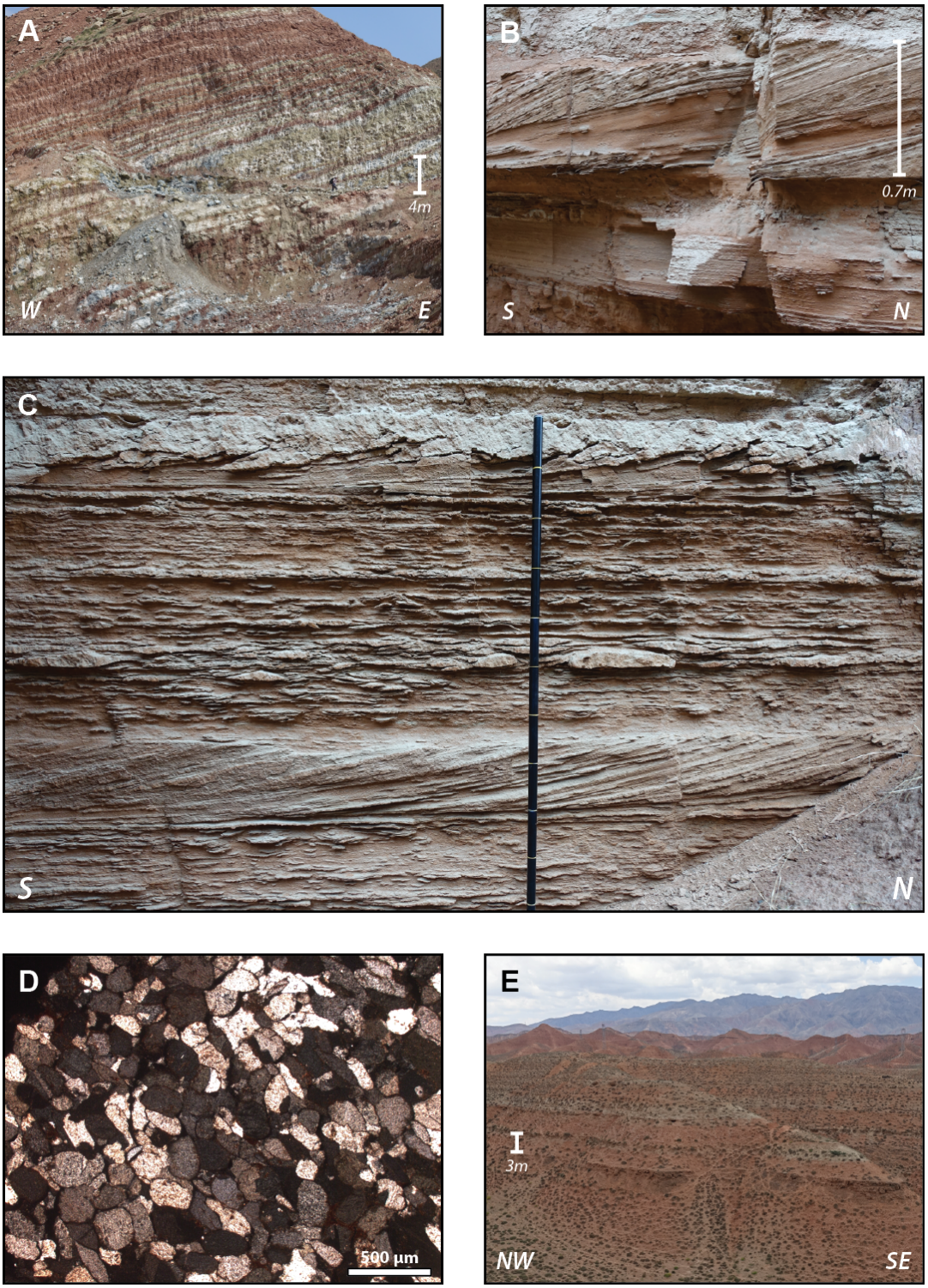

FIGURE 5.2: Pictures showing: (A) alternations between red mudrocks and gypsum beds at the Xiejia section; (B) gypsarenite showing planar cross-bedding and horizontal bedding at the Baimasi section at the 27 meter-level and (C) at the 20 meter-level with 10 cm markings on the staff for scale; (D) thin section under plain-polarized light of the cross-bedded gypsarenite at Baimasi section at the 27 meter-level showing rounded and well-sorted grains of gypsum; (E) top of the Baimasi section showing regular ∼3 m alternations between gypsum beds and red mudrocks followed by brownish-red mudrocks.

Interpretation

The depositional environment of the gypsiferous mudrocks is interpreted as a dry mudflat and as a saline lake for the gypsum beds (Abels et al., 2011; Dupont-Nivet et

al., 2007; Smoot and Lowenstein, 1991; Talbot et al., 1994). The sandstone beds with climbing ripples suggest rapid deposition by unconfined fluvial flows (North and Davidson, 2012). Gypsarenites are rare and almost always associated with eolian transport of gypsum grains deflated from nearby salt pans (Smoot and Lowenstein, 1991). Especially since extensive subaqueous reworking would result in the complete dissolution of the salt grains. The cross-bedded gypsarenites are thus interpreted as eolian dunes following Zhang et al. (2016a) and the horizontally-bedded gypsarenites as eolian sand sheets. However, we note that the cross-beds observed here are thin with more gentle foresets than is common for eolian sands (e.g. McKee, 1966). We argue that is may be due to the low accumulation rates observed in the Xining Basin (∼3 cm/kyrs; Chapter 3; Abels et al., 2011) resulting in only the more gently steeping base of the dunes being preserved.

The measured paleocurrent directions of the gypsarenites are corrected (red arrows in Fig. 5.3) for the clockwise 20° vertical axis rotation of the Xining Basin during the late Paleogene as reported in previous paleomagnetic studies (Dupont-Nivet et al., 2008b). Although only four beds of cross-bedding are preserved, the paleocurrent directions of these beds are consistently to the south and southeast. This suggests that north to northwesterly winds prevailed during the Eocene, which would be similar to the modern-day winter monsoon (Fig. 5.1). However, we note that the Eocene wind directions may be affected by local topography which is poorly constrained.

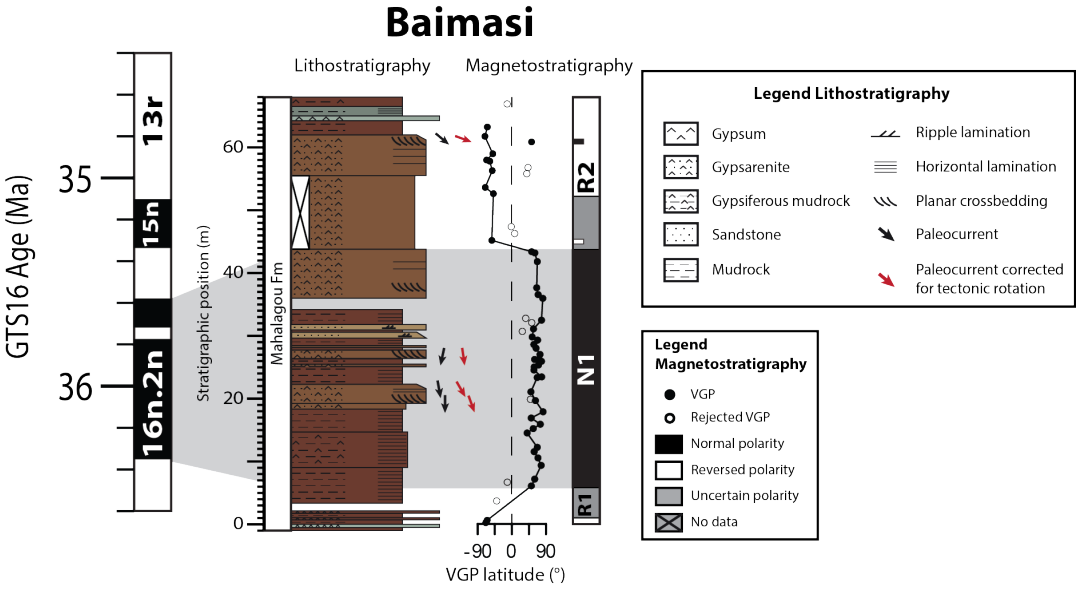

FIGURE 5.3: Litho- and magnetostratigraphy of the Baimasi section.

5.4.2 Magnetostratigraphy

ChRM directions

The Characteristic Remanent Magnetization (ChRM) directions were calculated using eigenvector principal component analysis (Kirschvink, 1980) on at least 4 temperature steps. The resulting directions reveal two clusters of either normal or reversed polarity (Fig. C.6). The means of these clusters were calculated using Fisher statistics (Fisher, 1953) and samples with an angle of more than 45° from the mean were rejected from further analysis (open symbols in Fig. 5.3). The reversals test was performed using the means of the two clusters (McFadden and McElhinny, 1990),

but failed due to an unresolved normal overprint as observed in previous studies in the Xining Basin (Chapter 3; Dupont-Nivet et al., 2008b). This would make our dataset unsuitable for rotational analysis, but does not affect the reliability of the magnetostratigraphy. The Virtual Geomagnetic Poles (VGP) were calculated and polarity zones are defined on at least two successive samples with the same polarity.

Correlation to the GTS

The Baimasi section contains a reversed polarity zone at the base (R1), followed by a ∼40 meters-thick normal polarity zone (N1) and a ∼20 meters-thick reversed polarity zone at the top (R2). The Baimasi section is mapped as the Mahalagou Formation (Fig. 5.1A; Dai et al., 2006; QBGMR, 1985) and is observed to grade upwards into the brownish-red mudrocks of the Xiejia Formation (Fig. 5.2E). Furthermore, the characteristic meter-scale gypsum beds of the Mahalagou Formation are observed both at the top and base of the section (Fig. 5.2E and 5.3). These observations confidently constrain the age of the Baimasi section to the Mahalagou Formation, which serves as a starting point for our magnetostratigraphic correlations. The chrons observed in the Mahalagou Formation include: (Fig. C.7): C13 to C18 (Abels et al., 2011). The only long reversed chron in this interval is C13r and we therefore correlate it with R2. C13r is preceded by a short normal and reversed chron (C15n and C15r), which are not observed in the Baimasi section, possibly because this interval is poorly exposed (Fig. 5.3). Below C15r is a long normal chron, C16n, which we correlate with N1 and R1 is correlated with C16r. This suggests the Baimasi section covers the 36.5-35 Ma interval but our interpretation is limited by the missing reversals of C15n and C15r. Nevertheless, we argue that based on the lithological observations listed above, we can confidently correlate the Baimasi section with the Mahalagou Formation spanning from 40 to 34 Ma.

5.5 Cyclostratigraphy

The characteristic meter-scale gypsum-mudrock cycles (Fig. 5.2A) observed in the center of the basin (at the Dasigou, Shuiwan, Tiefo, East Xining, Tashan and Xiejia sections; Fig 5.1B) have been studied in detail and are proposed to be driven by the 41-kyr obliquity cycle and to a minor extent by the 100-kyr eccentricity cycle (Abels et al., 2011; Dupont-Nivet et al., 2007; Xiao et al., 2010; Huang and Hinnov, 2019). The gypsum beds are interpreted as wet periods with an elevated groundwater level, whereas the red mudrocks reflect a dry mudflat. The cycles are observed to start at ∼40 Ma (Bosboom et al., 2014a) and end with the disappearance of gypsum beds at ∼34 Ma due to regional aridification (Dupont-Nivet et al., 2007). In the following, we examine whether the record in the Xining Basin is orbitally forced before ∼40 Ma by performing time series analysis on the Caijia section, which covers the Qijiachuan and Honggou Formations.

5.5.1 Cyclicity

The Honggou Formation is dominated by massive brick-red mudrocks, similar to the overlying Mahalagou Formation and interpreted as a dry mudflat (Chapter 3). The red mudrocks are alternated with meter-scale intervals of brown to green mudrocks with fine horizontal laminations interbedded with cm-scale beds of carbonate and gypsum. These laminated mudrocks are interpreted as lacustrine and reflect wetter atmospheric conditions (Chapter 3). The alternations between the red

and lacustrine mudrocks are regular, but with a long period of 10-12 meters compared to the meter-scale cycles in the Mahalagou Formation. Thirteen of these low frequency cycles can be identified in the Caijia section (Fig. 5.4). No lacustrine deposits are identified in cycle 4, but a meter-scale channel body of very fine sandstone is observed here instead. The channel body contains trough cross-bedding and grades laterally into cm-scale beds of very fine sandstone with ripple laminations interpreted as fluvial deposits (Chapter 3). Two of the cycles contain gypsum beds instead of lacustrine mudrocks (cycle 5 and 8) indicating more saline conditions (Chapter 3). Gypsum beds are more common in the upper part of the Honggou Formation and the cyclicity is less obvious. Two groups of meter-scale gypsum beds with a lacustrine interval in between may represent three more cycles (cycle 11-13). Afterwards, no more cycles are observed in the upper part of the section. No cyclicity is observed as well in the Qijiachuan Formation at the base.

5.5.2 Spectral analysis

Spectral analysis (Fig. 5.4) of the color records reveals a >95% confidence peak at a period of 12 meters in a^* (red over green) and b^* (yellow over blue). L^* (lightness) shows a >99% confidence peak at 19.6 meters. The bandpass filter of L^* shows that this period follows the occurrence of gypsum and carbonate beds, but fails to identify some of the lacustrine mudrocks which have a similar lightness as the red mudrocks. Therefore, the 19.6 meters period may represent a double cycle of the 12-meters cyclicity. The XRF proxies are dominated by higher frequency cycles with periods of 1-3 meters, which reflect the individual gypsum and carbonate beds that occur in the lacustrine intervals. The lower frequency cycles are represented in the Ca/S record which shows a >95% confidence peak at 10.6 meters (Fig. 5.4). No cyclicity is observed in the grain-size record, which is discussed below.

5.5.3 Correlations

The cycles in the 50-45 Ma interval of the Caijia section can be correlated bed-to-bed with the East Xining section located ∼9 km to the west (Fig. C.8). Similar cycles are observed as well in the Xiejia section, located ∼14 km to the south. However, these cycles consist of sandstone beds in the lower part instead of lacustrine mudrocks (Fig. C.8). The Xiejia section is located in a more proximal setting towards the southern margin of the basin which may explain the occurrence of fluvial sandstones during the wet phase of the cycles. Similar orbital cycles are observed in the mudflat deposits of the Teruel Basin in Spain with distal lacustrine deposits correlating with proximal fluvial beds during the wetter phases (Ventra et al., 2018). The correlations in the Xining Basin suggest that the cycles are basin-wide and possibly orbitally-forced. The accumulation rates are relatively constant at 3 cm/kyrs for the Honggou Formation (Chapter 3), which suggests that the cycles of 10-12 meters have a duration of 333-400 kyrs and may be forced by the long eccentricity cycle of 405 kyrs. The cycles are dated using the magnetostratigraphy of (Chapter 3) and various age models for the chron boundaries (Fig. C.9; Gradstein et al., 2012; Westerhold et al., 2015; Westerhold et al., 2017). The most recently tuned age model (Westerhold et al., 2017) reveals that the wet phases of the cycles correlate with the 405-kyrs eccentricity minima in the astronomical solution (Laskar et al., 2011).

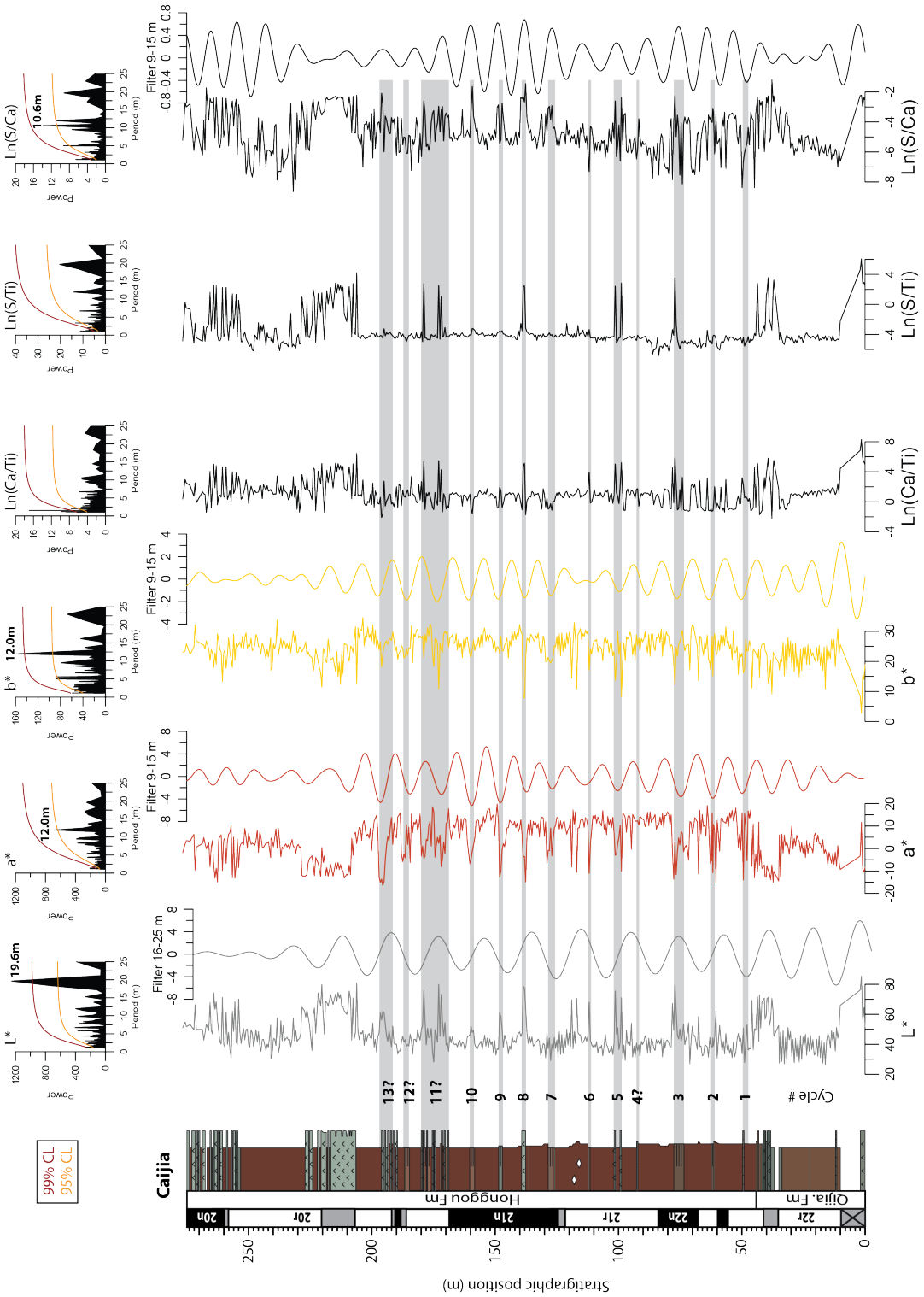

FIGURE 5.4: Time series of the Caijia section showing the color records: L^* (lightness), a^* (red over green) and b^* (yellow over blue) and XRF record of log-ratios: Ca/Ti, S/Ti and Ca/S. Filters and Redfit spectral analyses with confidence limits (CL) are shown as well. The cycles are numbered and the wet phases represented by lacustrine mudrocks, gypsum beds and fluvial sandstones are marked in grey. Litho- and magnetostratigraphy is from Chapter 3.

Interpretations

In the following, we explore the occurrence of the ~400-kyr cycles in terms of orbital forcing. Climate models suggest that both the summer monsoons and wintertime

westerlies are driven directly by orbital forcing through northern hemisphere insolation, although the phase is opposite (Bosmans et al., 2018; Shi et al., 2011; Zhang et al., 2016c). At the midlatitudes, this insolation is dominated by the precession cycle and, to a minor extent, by the obliquity cycle. The 405-kyr eccentricity cycle is only a modulation of the shorter precession and 100-kyr eccentricity cycles and therefore, the lack of these higher frequency cycles in our record is puzzling. Other studies have identified similar low frequency cyclicities in the absence of higher frequency cycles and ascribed this to limitations of the paleoenvironmental record (Abels et al., 2010) or to a clipped insolation response resulting in only the most extreme amplitudes being recorded (Nie et al., 2008). Alternatively, the paleoenvironmental response to orbital forcing may be modulated by other mechanisms. Marine records show that the lower frequency cycles such as the 405-kyr eccentricity cycle are preferentially amplified in the carbon cycle during the Cenozoic (Kocken et al., 2019) and therefore may have affected the Xining Basin via CO2 forcing. Additionally, teleconnections with the Antarctic ice sheets are proposed for the occurrence of 100-kyr eccentricity cycles in various Miocene records across the northeastern Tibetan Plateau (Wang et al., 2019c) and the incipient Eocene ice sheets may have similarly modulated the paleoenvironment in the Xining Basin. Regardless of the explanation for the 400-kyr cycles, our cyclostratigraphic analysis reveals no high frequency cyclities in the record before 40 Ma. This is in stark contrast to the obliquity cycles observed after 40 Ma by previous studies (Abels et al., 2011; Bosboom et al., 2014a; Dupont-Nivet et al., 2007; Xiao et al., 2010; Huang and Hinnov, 2019) suggesting a major paleoenvironmental shift at this time.

5.6 Grain-size analysis

5.6.1 Grain-size distributions

The GSDs of the studied sections are dominated by fine silt with a median grain-size of 4-6 µm (Fig. 5.5A). The GSDs measured in this study differ from the late Eocene grain-size record from the Xining Basin reported in (Licht et al., 2014), which is characterized by bimodal distributions with modes at 16-31 µm and at 1.6-2.8 µm. The samples in both studies were prepared using similar pre-treatments, but measured using a different laser diffraction device. Comparison studies have shown that although laser diffraction measurements are precise and highly reproducible (Goossens, 2008), the accuracy is limited and using different devices may result in different GSDs (Varga et al., 2019b). Therefore, care should be taken when comparing GSDs between studies and we exclude the results of (Licht et al., 2014) in this study. The comparison with the GSD of Quaternary loess (Fig. 5.5B) is made with samples measured using the same pre-treatment, laser diffraction device and optical settings.

5.6.2 End-member analysis

End-member analysis of the dataset reveals four end-members (Fig. 5.5A) based on the best correlation (R^2) per grain-size class. Three of these end-members have modes at 2.6 µm (EM1), 5.1 µm (EM2) and 10.1 µm (EM3). A fourth end-member is fine skewed with a mode at 51.5 µm (EM4). The composite record (Fig. 5.6) shows that the lower part of the stratigraphy (50.5-40 Ma) is dominated by EM1, EM2 and EM3, while the abundance of EM4 is low (5% on average). The upper part of the record (40-36 Ma) is dominated by EM3 and EM4, while the abundance of EM1 and

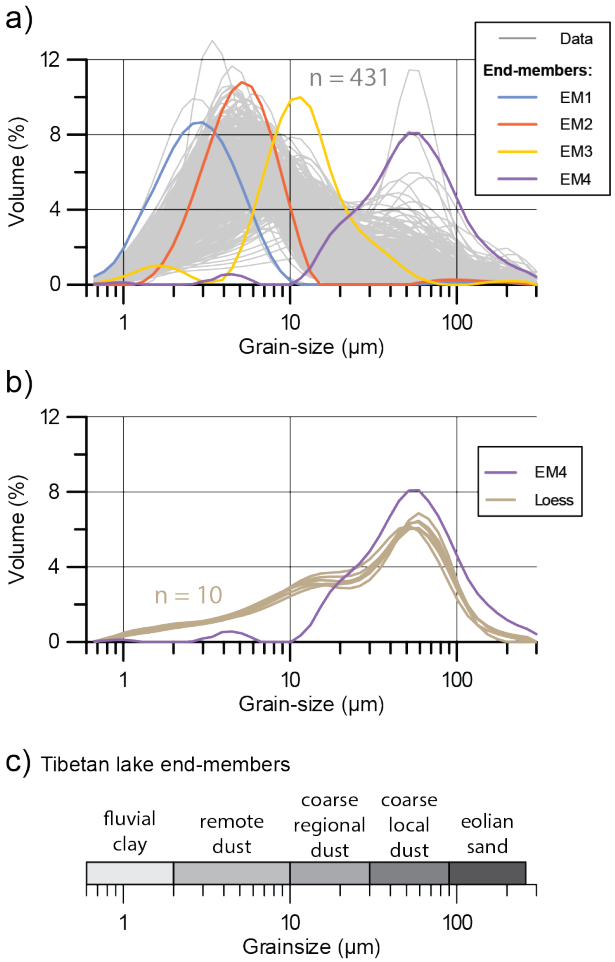

FIGURE 5.5: (A) Frequency curves of the total measured GSDs and of the end-members. (B) Comparison of EM4 with the GSD of local Quaternary loess in the Xining Basin. (C) Size ranges of end-members in Tibetan lake records (Dietze et al., 2014).

especially of EM2 are reduced. At 40 Ma, the abundance of EM4 increases abruptly to an average of 19% in different sections (Tiefo and Xiejia) at the same stratigraphic level suggesting a laterally continuous shift (Fig. C.3), coeval with the onset of obliquity cycles in the basin. Samples from the Oligocene mudrocks show similar end-member abundances as in the upper part of the Eocene record (Fig. C.3).

5.6.3 End-member interpretations

The GSD of EM4 is remarkably similar to the Quaternary loess in the Xining Basin (Fig. 5.5B), which corresponds to the coarse local dust component (Fig. 5.5C) observed in global loess populations (Dietze et al., 2014). However, similar GSDs are observed on mudflats formed by fluvial transport (van Toorenenburg et al., 2018) and therefore the GSD alone is not a diagnostic feature for eolian transport. Additional evidence is provided by previous surface morphology analyses of the >20 µm quartz grains, which suggests an eolian origin for these grains (Licht et al., 2014). Furthermore, the abrupt laterally continuous appearance of EM4 suggests an eolian rather than a fluvial origin. Cross-bedded silt- and sandstone beds indicating fluvial transport are observed as well, but decrease upwards (Chapter 3). Such channels only reappear during the Miocene related to the uplift of the surrounding mountain

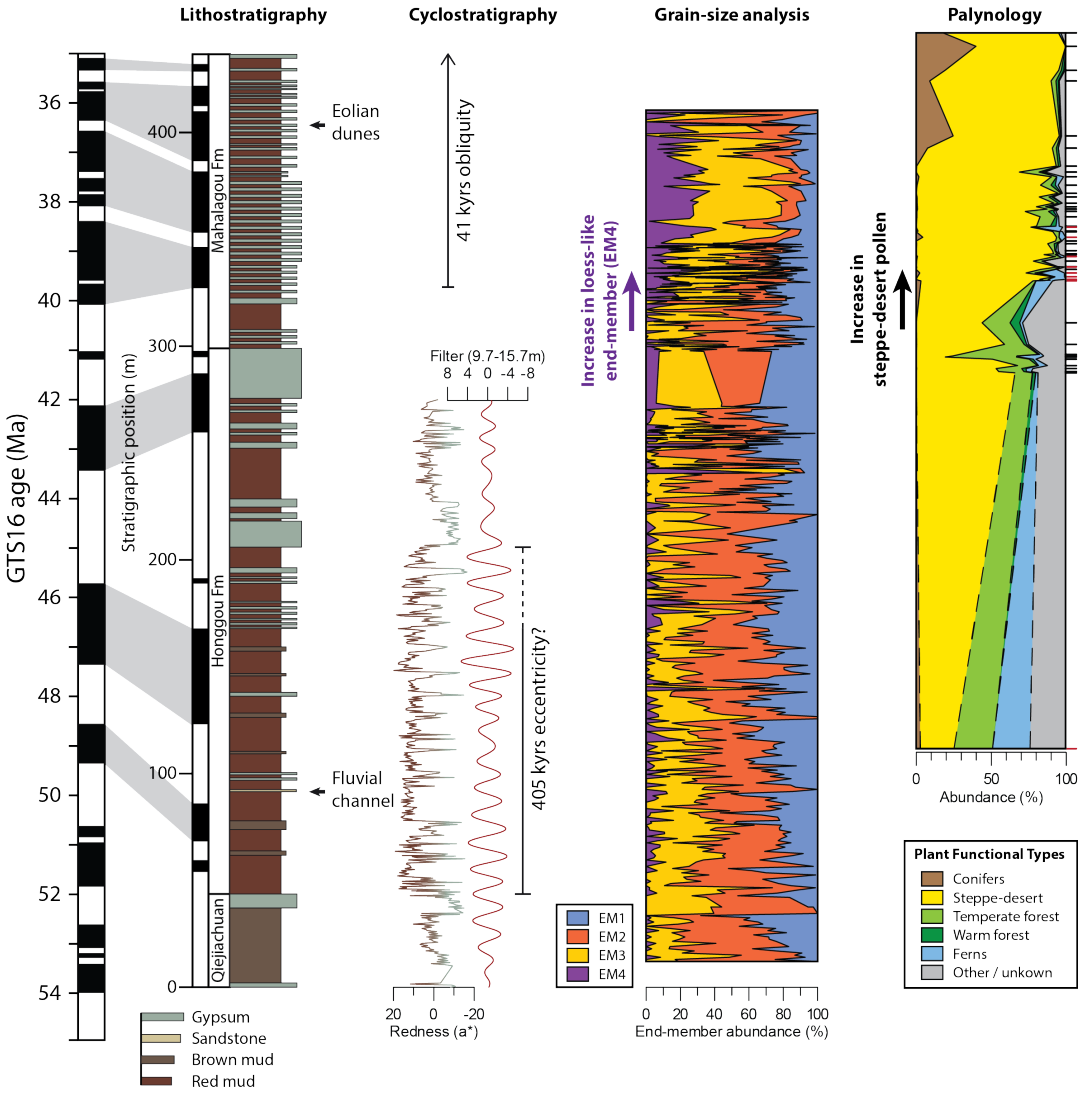

FIGURE 5.6: Composite of the early-late Eocene record of the Xining Basin based on magnetostratigraphic correlations between the studied sections. The composite shows the lithostratigraphy, cyclostratigraphy, end-member abundances of the grain-size record and Plant Functional Type abundances of the palynological record with new samples from this study indicated in red. The magnetostratigraphy is correlated with the GTS16 (Ogg et al., 2016).

ranges (Xiao et al., 2012; Yang et al., 2017). This suggests a reduction in fluvial activity rather than an increase at 40 Ma as observed in EM4. We therefore interpret the appearance of EM4 as a loess-like dust component.

The origin of the finer-grained end-members is more difficult to assess because these grains are too small for quartz surface morphology analysis and the GSDs may occur in several sedimentological settings. In terms of eolian dust, these include long-term suspension transport, possibly by upper-level westerlies (Pye, 1995; Sun, 2002), or as aggregates in short-term suspension as observed in modern-day dust storms (Qiang et al., 2010). We also note that EM3 might reflect the fine-grained dust component commonly observed in the Mio-Pliocene records of the Red Clay Formation (Shang et al., 2016). Alternatively, a fluvio-lacustrine origin may be inferred either in suspended load or as mud aggregates transported in bedload (Wright and Marriott, 2007). Because of these difficulties, we refrain from deriving any sedimentological and paleoclimatic information using these end-members and focus on EM4 instead.

Note, that because we only interpret EM4 with an average abundance of 19% as being eolian in origin, the Xining deposits are not predominantly composed of wind-blown silt. Therefore, these deposits are not classified as a lithified loess (Pye, 1995), but rather interpreted as a diverse depositional environment containing a loess-like component as well as other fluvio-lacustrine and/or dust components (Fig. 5.7). This interpretation is in line with recent depositional models for the Miocene Red Clay (Alonso-Zarza et al., 2009; Liu et al., 2019).

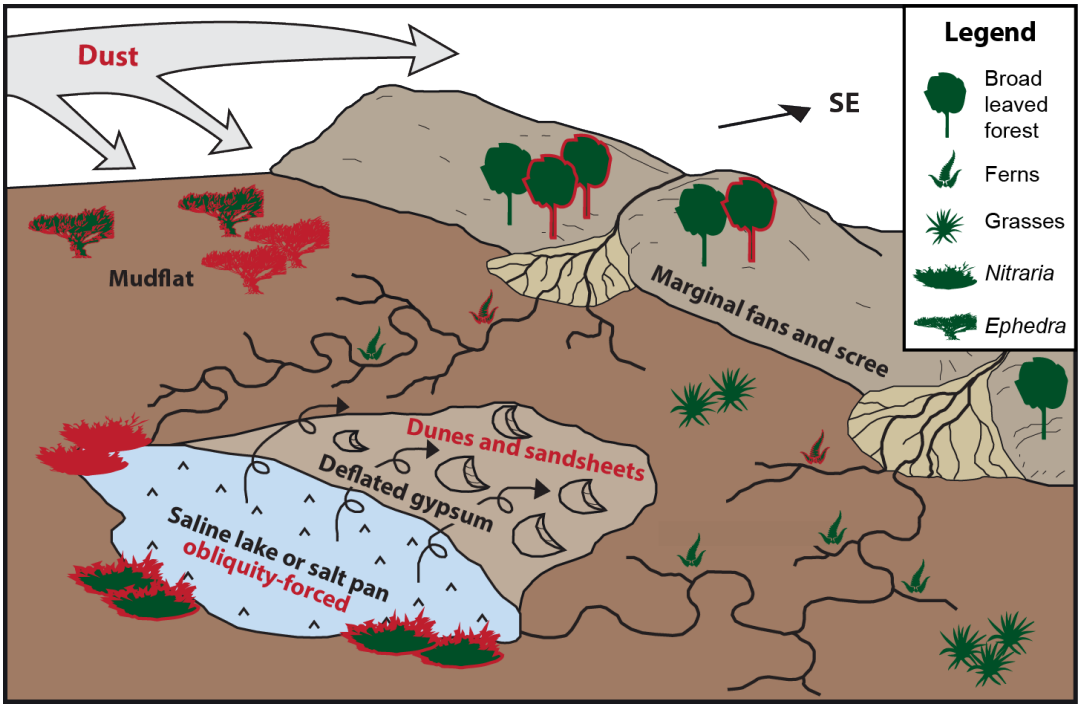

FIGURE 5.7: Depositional environment and paleovegetation of the Xining Basin during the Eocene (modified from Talbot et al., 1994). Dominant vegetation before 40 Ma is indicated in green, and after 40 Ma, in red (vegetation present throughout is colored in green with red outline). Sedimentary features appearing after 40 Ma are indicated in red as well.

5.7 Palynology

To study the vegetation response to the 40 Ma event, we complement the existing palynological record of the Xining Basin with new samples from the early and middle Eocene (Fig. 5.6). Only one sample from the early Eocene was productive and reveals a semi-arid steppe-forest ecosystem occupied by xerophytic grasses and halophytic shrubs (*Graminidites* and *Nitraria* respectively), that also hosted considerable areas of temperate woodland and ferns surrounding watercourses (Fig. 5.7). The middle Eocene is represented by multiple samples indicating a more arid steppe-desert environment than the early Eocene, with a now-subordinate component of temperate broad leaved forest. This is followed by a major increase in both the abundance and diversity of the xerophytic and halophytic desert and steppe shrubs, *Ephedra* and *Nitraria*, and a concurrent decrease in temperate broad-leaved forest diversity. After this shift, steppe-desert vegetation (alternating between *Ephedra* and *Nitraria* being dominant) comprises around three quarters or more of the palynological assemblage, with many samples including 80–95% steppe-desert pollen. This reflects a significant drying event previously recognized (Bosboom et al., 2014a) and now better constrained by our new pollen samples to occur between 40.7 and 39.9

Ma. This shift is again coeval with the onset of obliquity cycles (Bosboom et al., 2014a) as well as the appearance of the loess-like end-member observed in our grain-size analyses (Fig. 5.6). The late Eocene record is characterized by the appearance of conifers at ~37 Ma, as recognized in previous studies, and linked to cooling and aridification (Abels et al., 2011; Dupont-Nivet et al., 2008a; Page et al., 2019).

5.8 Discussion

Our study shows an abrupt shift occurring in the Xining Basin at 40 Ma with the appearance of eolian dust (EM4), the onset of obliquity-forced moisture cycles and a large increase in the proportion of steppe-desert pollen in the palynological record (Fig. 5.6). Although the latter indicates a marked expansion of low-growing, bushy shrubs that would have acted as efficient local dust traps (Pye, 1995), the vegetation shift alone cannot explain the onset of dust in the basin because these taxa were also relatively abundant at intervals prior to 40 Ma. Furthermore, these sudden changes are unlikely to be related to the slow local tectonics occurring in the basin at this time (Fan et al., 2019), but rather imply a regional reconfiguration of the atmospheric circulation.

5.8.1 Onset of the Siberian High

Modern-day observations show that the northwesterly winter monsoons are driven by the Siberian High resulting in dust storms due to the break-up of this high-pressure system during spring (Roe, 2009). Therefore, the appearance of both the dust in the grain-size record and the prevailing northwesterly winds evidenced in the Baimasi section indicate the establishment of a similar atmospheric configuration at 40 Ma. This is corroborated by provenance data showing that the source of the Xining dust was identical to the Quaternary loess suggesting that the Asian atmospheric circulation has been a resilient feature since the late Eocene (Licht et al., 2016b). The establishment of the Siberian High also explains the cyclicity appearing at 40 Ma, because this high-latitude pressure system is primarily driven by obliquity at orbital timescales (Shi et al., 2011) and interacts with atmospheric moisture from the monsoons and westerlies. A stronger Siberian High during high obliquity deflects more atmospheric moisture, whereas low obliquity results in a weaker high-pressure system and more moisture transported inland. During the Eocene, the Xining Basin is proposed to be dominated by moisture derived from the wintertime westerlies (Chapter 3) and therefore would have been especially susceptible to the Siberian High. Overall, the presence of the Siberian High would have enhanced the aridification of the region and driven the shift to widespread steppe-desert vegetation. We thus propose that the changes observed at 40 Ma mark the onset of atmospheric circulation associated with the establishment of a high-pressure system developing over Siberia. Climate models show that the strengthening of the Siberian High is primarily driven by atmospheric cooling, Tibetan Plateau uplift and proto-Paratethys Sea retreat all occurring at this time. In the following, we consider the respective contributions of these proposed driving mechanisms.

5.8.2 Driving mechanisms

Atmospheric cooling is proposed to drive aridification (Dupont-Nivet et al., 2007; Lu et al., 2010) and expand Arctic sea ice strengthening the Siberian High (Roe, 2009). Global temperatures dropped during the Eocene starting at 50 Ma (Cramwinckel

et al., 2018) and ephemeral sea ice in the Barents Sea is recorded since at least 45 Ma (Tripati and Darby, 2018), both predating the 40 Ma event in the Xining Basin. The long-term Eocene cooling is punctuated by the Middle Eocene Climatic Optimum (MECO), a warming event lasting ∼100 kyrs and followed by a cooling step (Cramwinckel et al., 2018). This step has been proposed to drive the onset of obliquity cycles and the shift in the pollen record of the Xining Basin at 40 Ma (Bosboom et al., 2014a). However a recent study using clumped isotopes found no such cooling event in the Xining Basin, but rather a two-tiered cooling at 37 Ma and at the Eocene-Oligocene Transition (EOT), 33.5 Ma (Page et al., 2019). Both cooling steps are interpreted to correlate with aridification events identified as a decrease in gypsum beds (Abels et al., 2011; Dupont-Nivet et al., 2007). However, we do not observe an increase in the loess-like end-member at 37 Ma (Fig. 5.6), nor in the Oligocene deposits after 34 Ma (Fig. C.3). This suggests that atmospheric cooling was not a major driver of the mineral dust.

Climate model sensitivity simulations suggest that the winter monsoons and Siberian High are sensitive to uplift of the Tibetan and the Mongolian Plateau (Sha et al., 2015; Yu et al., 2018; Zhu et al., 2019). Uplift of the latter is poorly constrained to be late Cenozoic (Vassallo et al., 2007) and therefore postdates the onset of dust in the Xining Basin. In contrast, numerous studies report that the Tibetan Plateau has expanded northwards since 40 Ma (Rohrmann et al., 2012; Wang et al., 2014b) and may have intensified the Siberian High and dust transport (Zhu et al., 2019). However, this long-term tectonic process would have resulted in a gradual increase of dust over time rather than the sudden appearance observed in the Xining Basin at 40 Ma.

Finally, we consider the sea incursions of the inland proto-Paratethys Sea (Fig. 5.8). Recent studies constrained the extent and timing of these sea incursions and dated a major sea retreat at ∼41-40 Ma (Kaya et al., 2019), coeval with the shifts in the Xining Basin. Sensitivity climate model simulations using various paleogeographies of the proto-Paratethys Sea show that the Asian climate is especially sensitive to this particular sea retreat from the Tarim and Siberian Sea (Zhang et al., 2007). According to these simulations, this regression acts as a tipping point resulting in both the strengthening of a high-pressure system over Siberia due to increased continentality as well as the aridification of northwestern China by removing a major moisture source for this region (Fig. 5.8). Therefore, we propose that the sea retreat is the most plausible mechanism to drive the appearance of the Siberian High and explain the shifts observed in the Xining Basin. Other mechanisms such as atmospheric cooling and Tibetan Plateau uplift may have played a role in setting-up the long-term boundary conditions, but the sea retreat acted as the critical trigger at 40 Ma. Hereafter, the proto-Paratethys Sea experienced another sea incursion between 39.7 and 36.7 Ma (Kaya et al., 2019). However, this highstand was less extensive and did not affect the loess-like end-member (Fig. 5.6).

5.8.3 Regional aridification and dust records

The onset of dust in the Xining Basin precedes the eolian deposits observed in most other regions of Central Asia, except for a poorly dated record at ∼51 Ma in the Xorkol Basin (Li et al., 2018a), which is located outside of the East Asian winter monsoonal region and likely driven by a different atmospheric configuration. Dust is observed to significantly increase in the grain-size record of the neighboring Lanzhou Basin at ∼26 Ma (Zhang et al., 2014). But a recent reanalysis of this magnetostratigraphic record suggests a dust increase at ∼40 Ma (Wang et al., 2016a), coeval with

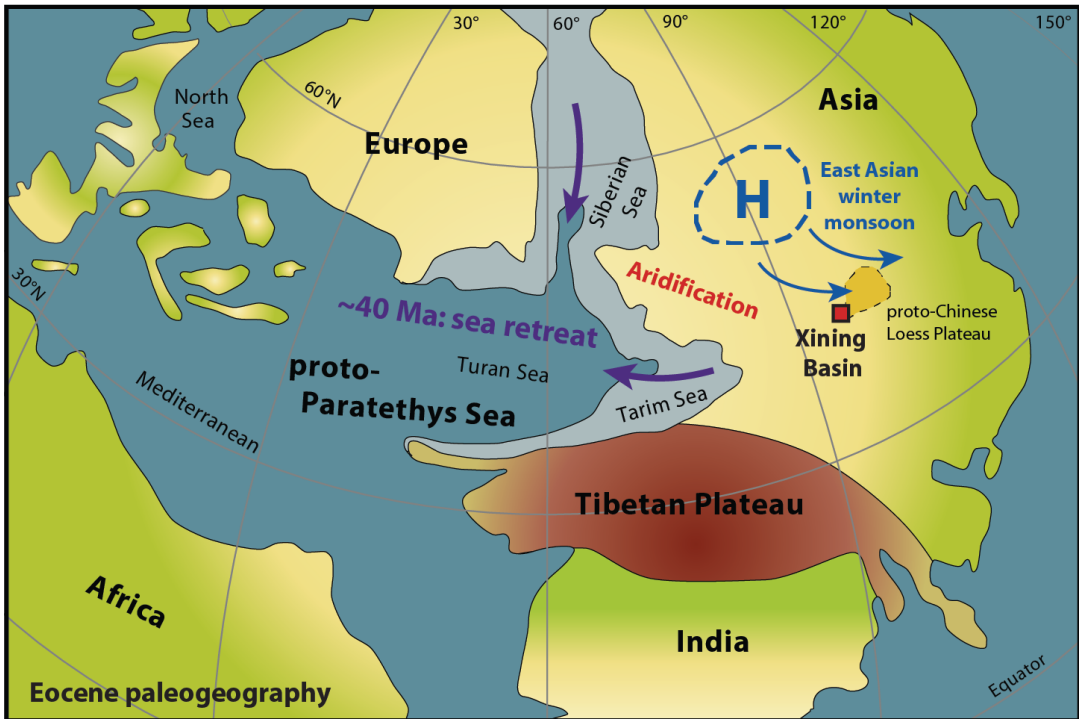

FIGURE 5.8: Eocene paleogeography of Eurasia (modified from Bosboom et al., 2011) showing the retreat of the proto-Paratethys Sea resulting in aridification and the onset of a high-pressure system over Siberia driving the East Asian winter monsoon and dust storms in the Xining Basin.

the Xining Basin and therefore suggesting a regional signal. Sedimentary records from Tajikistan show eolian dunes and loess shortly after the third Paleogene regression of the proto-Paratethys Sea (Carrapa et al., 2015), dated at 36.7 Ma (Kaya et al., 2019). The onset of loess in Mongolia as well as eolian dunes in the Tarim Basin are observed at 34 Ma and are linked to the final retreat of the proto-Paratethys Sea at the EOT (Blayney et al., 2019; Sun and Windley, 2015). These records suggest that the continued retreat of the proto-Paratethys Sea resulted in the desertification of western Central Asia. Subsequent aridification due to atmospheric cooling and uplift during the Miocene may have progressively enhanced dust accumulation on the Chinese Loess Plateau as observed by the onset of dust at 26-20 Ma in the western part (Garzione et al., 2005; Guo et al., 2002; Jiang and Ding, 2010; Wang et al., 2011; Qiang et al., 2011) and at 11-8 Ma in the eastern part (Ao et al., 2016; Sun et al., 1998a; Wang et al., 2014a). Alternatively, these basal ages may reflect a tectonic control on the accommodation and preservation of loess rather than an atmospheric shift (Wang et al., 2018).

A poorly dated record from the eastern Pacific Ocean reveals the appearance of a detrital dust component between 50 and 40 Ma, followed by an increase of this component at 20 Ma (Ziegler et al., 2007). Provenance data shows that the northern Pacific Ocean is dominated by Asian dust since 40 Ma (Pettke et al., 2002). Dust accumulation rates of this record are low during the Cenozoic followed by a doubling at 25 Ma and an even larger increase in accumulation rate at 3-4 Ma (Janecek and Rea, 1983). However, a recent study with improved age constraints suggests that the accumulation rates increased continuously since at least 25 Ma rather than stepwise (Zhang et al., 2016b). These records corroborate our findings for the onset of dust at 40 Ma followed by a progressive aridification of the Asian interior resulting in increased dust accumulation.

5.9 Conclusion

We identified the appearance of a loess-like dust component coeval with the onset of obliquity cycles and a shift to dominance of steppe-desert pollen in the terrestrial record of the Xining Basin at 40 Ma. We propose that the retreat of the proto-Paratethys Sea, superimposed on the long-term Tibetan Plateau uplift and global cooling, is the trigger for setting up the Siberian High resulting in winter monsoonal circulation and associated dust storms. This obliquity-driven high-pressure system would have deflected westerly moisture and driven the cyclicity observed in the Xining Basin as well as regional aridification and corresponding biotic shifts. Furthermore, the Siberian High may have driven cold surges over eastern Asia since 40 Ma and should be taken into account when reconstructing temperatures in this region (Tang et al., 2015). The Asian dust may have played a critical role in the global cooling and set-up of the greenhouse to icehouse transition by scattering incoming radiation, promoting the formation of clouds and affecting the carbon cycle by fertilizing phytoplankton production in the Pacific Ocean (Jickells et al., 2005; Martin, 1990; Shaffer and Lambert, 2018). The role of this Eocene dust as well as the atmospheric circulation associated with the Siberian High should be tested in future proxy records and climate modelling studies.

Chapter 6

Discussion and conclusions

The aim of this thesis was to identify the key geological mechanisms that have shaped the climate in Asia. This climate is characterized by the East Asian summer monsoon bringing southeasterly moisture and a dry continental interior including northwesterly winter monsoons, dust storms and the low-level westerlies. These features are hypothesized to be driven by uplift of the Tibetan Plateau, global cooling and retreat of the inland proto-Paratethys Sea from the Eurasian continent, all occurring during the Eocene period (56-34 Ma) and well-constrained in time by recent studies, as shown in Figure 6.1.

To assess the role of these various driving mechanisms, Eocene paleoenvironments have been reconstructed using detailed stratigraphic records from the Xining Basin in central China. In the following, I will summarize these findings by first considering dust records as a proxy for aridification and winter monsoons. Then, I will present the age model constructed for the Xining Basin and subsequently summarize the paleoenvironmental evolution recorded here. Finally, the role of the various driving mechanisms will be discussed and future research prospects and conclusions are presented.

6.1 Windblown dust in the geological record

Over the past millions of years, windblown dust has accumulated on the Chinese Loess Plateau located in central China. These dust storms are linked dynamically to the East Asian winter monsoons via the Siberian High: an atmospheric high pressure system developing over Asia during winter and driving strong northwesterly winds and dust storms during the springtime break-up of this system (Roe, 2009). Consequently, geological records of these dust storms have been used to track the evolution of the East Asian monsoons, which I review in Chapter 2. The archetypical dust deposits are found in the Quaternary period as loess (Pye, 1995), but older siltstones were subsequently interpreted as windblown deposits extending the earliest evidence for monsoons first to the Miocene (An et al., 2001; Guo et al., 2002) and later to the Eocene period (Licht et al., 2014; Li et al., 2018a). In Chapter 2, these pre-Quaternary records are shown to reflect a mix of both alluvial and eolian deposits, based on recent provenance and sedimentological evidence and are therefore different from the exclusively windblown loess. Yet the dust contribution can be tracked in these records by using a combination of quartz surface morphology, provenance and grain-size-shape end-member analysis. Applying these methods will aid in recognizing windblown dust in various depositional settings and therefore enables recording aridification and dust fluxes in the past.

6.2 Dating the Eocene deposits of the Xining Basin

Detailed age models are crucial for understanding the paleoenvironmental evolution and linking these to possible driving mechanisms. Previous studies in the Xining Basin have used magnetostratigraphy to construct an accurate age model extending from the Pliocene down to the Eocene period (Abels et al., 2011; Bosboom et al., 2014a; Dai et al., 2006; Dupont-Nivet et al., 2007; Horton et al., 2004; Yang et al., 2017; Yang et al., 2019; Xiao et al., 2010; Xiao et al., 2012; Zhang et al., 2017). However, the early to middle Eocene remained poorly constrained and the onset of Cenozoic deposition has been inconsistently reported between 54 and 52 Ma (Dai et al., 2006; Fang et al., 2019a; Yang et al., 2019).

These issues are resolved in Chapters 3 and 4 of this thesis. Chapter 3 presents a high-resolution magnetostratigraphy of three laterally equivalent sections covering the early to middle Eocene. The identified polarity zones can be correlated across the sections resulting in a reliable correlation with the geological timescale and supported by the radiometric age of a tuff layer identified in one of the sections. This is the first tuff layer recognized in the region and provides a crucial tie point for the age model. Chapter 4 extends the magnetostratigraphy down to ∼50.9 Ma using a section located towards the margin of the basin (and therefore not hampered by the thick diamagnetic evaporites found elsewhere). Furthermore, a previously unknown unconformity was identified by an abrupt shift in rock magnetic properties at the stratigraphic level of ∼50.9 Ma.

6.3 Eocene paleoenvironments in the Xining Basin

The major paleoenvironmental shifts in the Xining Basin (Fig. 6.1) were recorded by the lithostratigraphy (Chapter 3, 4 and 5), palynology (compilation in Chapters 4 and 5) and dust records (Chapter 5) and will be discussed in the following. In addition, a compilation of $\delta^{13}C$ values of pedogenic carbonate (Chapter 4) and Licht et al. (2020) is used as a crude estimate of soil respiration rates following Caves Rugenstein and Chamberlain (2018), with enriched $\delta^{13}C$ values indicating aridity.

6.3.1 Early Eocene

The early Eocene is characterized by low $\delta^{13}C$ values in pedogenic carbonates (-10 to -8‰) and a low abundance of windblown dust (∼5%) suggesting a relatively humid environment (Fig. 6.1; Chapter 4). This is corroborated by the few productive pollen samples in this interval revealing a semi-arid steppe-forest ecosystem occupied by grasses, shrubs and considerable amounts of temperate woodland and ferns (Fig. 6.1). In addition, a transient interval between ∼50.4 and 49.8 Ma is characterized by pedogenic $\delta^{18}O$ values suggesting reduced evaporation of soil water, high sediment accumulation rates and increased bulk organic carbon preservation (Fig. 6.1), all interpreted as an intensified hydrological cycle in Chapter 4 and linked to the peak greenhouse warmth of the EECO. Furthermore, these strata are underlain by an interval of massive evaporites alternated with organic-rich beds between 50.9 and 50.4 Ma. These are suggested to correspond to an unstable and highly variable climate recorded in marine records (Westerhold et al., 2018). At 49.8 Ma, the depositional environment shifts abruptly to a dry subaerial mudflat punctuated by lacustrine intervals every ∼400 kyrs up to ∼45 Ma. These lakes are interpreted to be driven by the 405-kyr eccentricity cycle (Chapter 5).

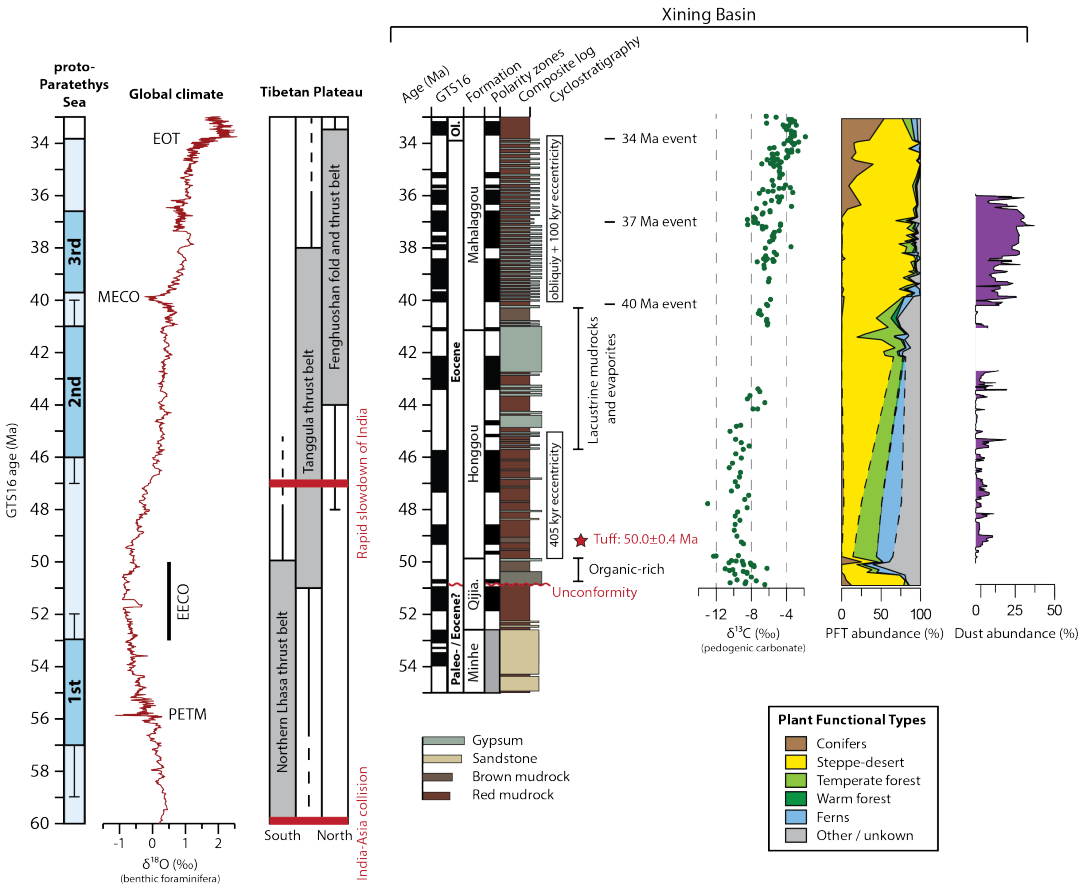

FIGURE 6.1: Eocene compilation showing the proto-Paratethys Sea incursions (Kaya et al., 2019); the global climate reflected by a 9-point moving average through the benthic foraminifera $\delta^{18}O$ compilation of Cramer et al. (2009); the northward growth of the Tibetan Plateau indicated by periods of deformation in various thrust belts (North Lhasa and Tanggula thust belts are from Kapp and DeCelles, 2019 and references therein; Fenghuoshan fold and thrust belt is from Staisch et al., 2016. Composite litho- and magnetostratigraphy of the Ledu, Caijia, Tiefo and Shuiwan sections in the Xining Basin (Chapters 3 and 4; Abels et al., 2011; Bosboom et al., 2014a). paleoenvironmental proxies are shown as well including $\delta^{13}C$ of pedogenic carbonate (compiled from Chapter 4 and Licht et al., 2020), Plant Functional Types in the palynological record (using the compilation of Chapters 4 and 5) and the abundance of dust in the grain-size record (5-point moving median of end-member 4 from Chapter 5).

6.3.2 Middle to late Eocene

The middle to late Eocene record reveals a long-term aridification trend indicated by the increase in evaporites, shift in rock magnetic properties (Fang et al., 2015), decrease in chemical weathering (Fang et al., 2019b) and higher $\delta^{13}C$ values of pedogenic carbonates (Fig. 6.1; Licht et al., 2020). This trend corresponds to both the long-term global cooling and northward growth of the Tibetan Plateau, but is punctuated by several steps. Between 46 and 40 Ma an increase in lacustrine strata and evaporites suggests an increase in atmospheric moisture (Fig. 6.1). This interval correlates with the second Paleogene highstand of the proto-Paratethys Sea (Kaya et al., 2019), which is proposed to provide additional atmospheric moisture for the low-level westerlies (Chapter 3).

At ~40 Ma, the lacustrine mudrocks and carbonates disappear abruptly and are replaced by beds of evaporites and subaerial mudflat deposits showing obliquity

cycles (Fig. 6.1; Abels et al., 2011; Bosboom et al., 2014a; Xiao et al., 2010). In addition, steppe-desert pollen increase, northwesterly wind directions are observed in reworked evaporites and a windblown mineral dust component is identified in the grain-size record (Fig. 6.1). This dust remains a minor contribution to the predominantly alluvial deposits, but together with the onset of high-latitude obliquity cycles, northwesterly wind directions and aridification, it is interpreted as the onset of a high atmospheric pressure system similar to the modern-day Siberian High driving winter monsoons and dust storms in the region. The onset of this high atmospheric pressure system is linked to the proto-Paratethys Sea retreat from Siberia (Chapter 5).

Subsequent aridification steps are recognized as a decrease in saline lakes due to a drop in groundwater level at 37 Ma, followed by the ultimate disappearance of evaporites at the EOT, 34 Ma (Fig. 6.1; Abels et al., 2011; Dupont-Nivet et al., 2007). Both of these events correspond to an increase in conifers and dramatic temperature drops of > 9°C identified in clumped isotopes of pedogenic carbonates (Fig. 6.1; Dupont-Nivet et al., 2008a; Hoorn et al., 2012; Page et al., 2019). In addition, these events correlate with further regressions of the proto-Paratethys Sea (Kaya et al., 2019).

6.4 Driving mechanisms of Asian paleoenvironments

The results of this thesis reveal a marked shift between the relatively humid early Eocene and the more arid middle to late Eocene. Regional compilations of pedogenic carbonate $\delta^{13}C$ show a gradient during the Eocene from the arid continental interior with higher $\delta^{13}C$ values to monsoonal southeastern China with lower $\delta^{13}C$ values (Caves Rugenstein and Chamberlain, 2018). The latter suggests that the Xining Basin was part of the humid summer monsoonal domain at this time (Fig. 6.2A). This is supported by some climate model studies (Farnsworth et al., 2019; Licht et al., 2014; Roe et al., 2016), but others argue that the East Asian moisture during the Eocene is derived from both westerly Indian winds and weak Pacific easterlies, rather than a summer monsoon (Tardif et al., 2019). Regardless of the exact dynamics of the East Asian moisture, the intensified hydrological cycle observed in the Xining Basin during the EECO suggests that global climate and in particular atmospheric CO_2 levels were the dominant driver of the Asian climate at this time. In addition, the carbon cycle preferentially amplifies low frequency orbital cycles (Kocken et al., 2019) and therefore may explain the occurrence of the 405-kyrs eccentricity cycles in the lacustrine strata between $\sim$50 and 45 Ma.

The subsequent aridification during the middle-late Eocene may be driven by either the long-term global cooling or northward growth of the Tibetan Plateau or a combination of both (Fig. 6.1). This aridification is also observed in other regional records (Caves Rugenstein and Chamberlain, 2018) but not in climate model simulations which show an increase in monsoonal precipitation throughout the Eocene (Farnsworth et al., 2019). The reason for this mismatch between proxies and climate model simulations remains unclear. The enriched pedogenic $\delta^{13}C$ values suggest that the Xining Basin is part of the arid continental interior during the middle to late Eocene and dominated by westerly moisture during proto-Paratethys highstands (Fig. 6.2B). In addition, the proto-Paratethys Sea plays a major role in triggering the East Asian winter monsoons as revealed by the onset of windblown dust at 40 Ma.

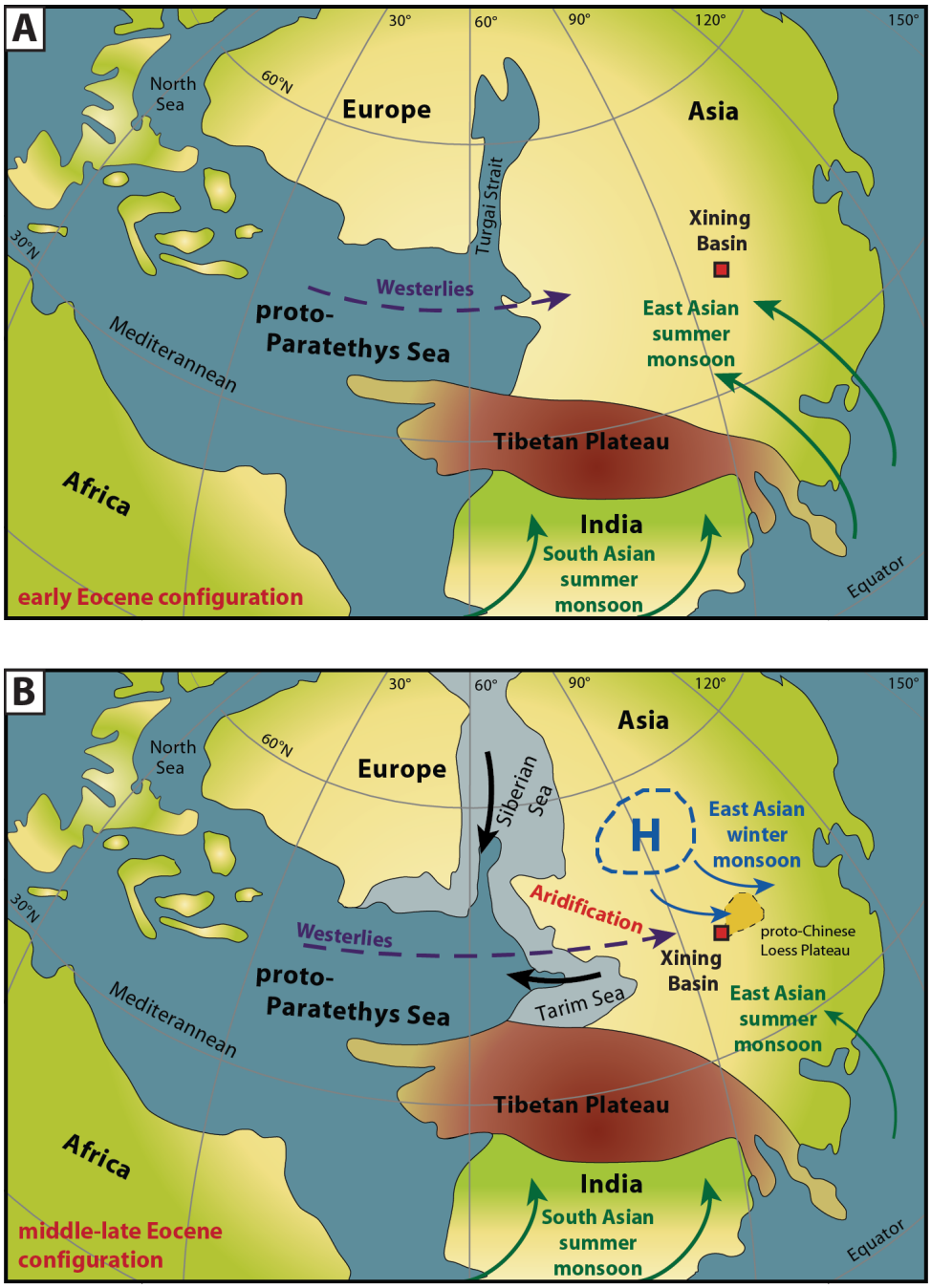

FIGURE 6.2: Paleogeographic setting and atmospheric circulation in Asia during: (A) the early Eocene showing an intensified hydrological cycle possibly due to the East Asian summer monsoon (green arrows). (B) The middle to late Eocene showing the proto-Paratethys highstand (in light blue) and corresponding westerly moisture (purple arrow), followed by the ~40 Ma sea retreat (black arrows) and resulting aridification and East Asian winter monsoons. Map is redrawn from Bosboom et al. (2011) and proto-Paratethys paleogeographies are derived from Kaya et al. (2019).

Beside the long-term effects of Tibetan Plateau uplift and global cooling, the previously unrecognized proto-Paratethys Sea is revealed to be a major driver of Asian paleoenvironments during the middle to late Eocene. These marine incursions have a direct effect by acting as a source of moisture for the low-level westerlies and by affecting atmospheric circulation through land-sea contrasts. Kaya et al. (2019) show

that these marine incursions are ultimately driven by regional tectonics but also eustatic sea-level. Because eustasy is strongly affected by the formation of ice sheets and therefore global cooling, the respective roles of the decreasing atmospheric CO_2 concentrations and proto-Paratethys Sea retreat in driving the 37 Ma and 34 Ma cooling events remain unclear. Nevertheless, the sea retreat at 40 Ma is shown to be crucial in triggering the aridification and dust storms in central China and can be considered as the first step in setting up the modern-day atmospheric configuration (Fig. 6.2B).

6.5 Directions for future research

The records presented in this thesis have been used for lithostratigraphy, cyclostratigraphy, rock magnetism, pedogenic and organic stable isotopes, sedimentology, grain-size distributions and palynology to study the paleoenvironmental evolution. However, key climate metrics such as temperature and precipitation remain poorly quantified and possible interactions between biotic and paleoenvironmental shifts remain unexplored. In the middle to upper Eocene strata, carbonate growth temperatures have been constrained using clumped isotopes (Page et al., 2019), cooling and aridification inferred from leaf waxes (Long et al., 2011) and soil respiration rates estimated using pedogenic and organic stable isotopes (Licht et al., 2020). Such studies can now be extended to cover the early to middle Eocene using the records presented here. Future stratigraphic studies may also extend these records further downwards and better constrain the age of the underlying Paleo- to Eocene strata to enable additional paleoenvironmental reconstructions and to derive the tectonic origin of the Xining Basin (e.g. Fan et al., 2019). In addition, more well-dated Eocene records from Central and East Asia are needed to assess whether the trends observed in the Xining Basin are only local features or reflect a regional response.

The climatic interpretations and conclusions presented throughout this thesis are based predominantly on correlations between paleoenvironmental shifts and presumed driving mechanisms. However, it should be stressed that these correlations do not necessarily indicate a causal relation. Future studies should therefore focus on testing these interpretations by using climate models to simulate the Eocene period and perform sensitivity experiments. These models may aid in identifying the mechanisms responsible for the intensified hydrological cycle during the EECO and better assess the impact of the proto-Paratethys Sea retreat.

Finally, the methods presented in Chapter 2 of this thesis enable future studies to better constrain dust fluxes not only from the Cenozoic and in Asia, but throughout the geological history and across the globe. This will aid in reconstructing aridification and help to assess the role of dust as a driver of the climate system. In particular the role of dust-derived iron in fertilizing marine biota has been suggested to partly explain the glacial-interglacial atmospheric CO_2 variations (Martin, 1990), but its possible role in the pre-Quaternary periods remains to be explored.

6.6 Conclusions

- Massive terrestrial siltstones in the pre-Quaternary geological record are not exclusive to windblown loessites but may reflect a mix of alluvial and eolian deposition. These various components can be unmixed by using a combination of quartz surface morphology, provenance and grain-size-shape end-member analysis. These methods enable tracking of dust and aridification throughout the geological record.
- The early Eocene in central China is characterized by a relatively humid and possibly monsoonal climate driven by atmospheric CO_2 levels as shown by the intensified hydrological cycle during peak greenhouse warmth of the EECO
- Long-term aridification of the middle to late Eocene records in central China resulted in an atmospheric configuration predominantly driven by the proto-Paratethys Sea by supplying moisture to the westerlies during highstands and triggering winter monsoons as well as dust storms due to the sea retreat at $\sim$40 Ma.

Appendix A

Supplementary Information for Chapter 3

A.1 Analytical procedure for U-Pb geochronology

U-Pb geochronology was conducted by in-situ laser ablation inductively coupled plasma mass spectrometry (LA-ICPMS) at Géosciences Rennes using an ESI NWR193 UC excimer laser coupled to a quadripole Agilent 7700x ICP-MS equipped with a dual pumping system to enhance sensitivity (Paquette et al., 2014). The instrumental conditions are reported in Table A.2.

The ablated material is carried into helium, and then mixed with nitrogen and argon, before being injected into the plasma source. The alignment of the instrument and mass calibration was performed before the analytical session using the NIST SRM 612 reference glass, by inspecting the ^{238}U signal and by minimizing the ThO+/Th+ ratio (<0.5%). During the course of an analysis, the signals of ^{204}(Pb+Hg), ^{206}Pb, ^{207}Pb, ^{208}Pb and ^{238}U masses are acquired. The ^{235}U signal is calculated from ^{238}U on the basis of the ratio ^{238}U /^{235}U =137.88.

Single analyses consisted of 20 seconds of background integration followed by 60 seconds integration with the laser firing and then a 15 seconds delay to wash out the previous sample. The ESI NWR193UC laser is equipped with a rotational XY shutter, which allows rectangular ablations while ensuring an even "dosage" of the laser energy to the sample during the analyses. Because the zircon grains of the tuff sample are very elongated and narrow, we defined a rectangle of 70x20 mm that was suitable for most of the grains in this sample. This ablation rectangle, which can rotate freely around its center, was then used for all the standards and the zircon crystals in order to use the same analytical conditions during the analyses.

The data were corrected for U–Pb fractionation and for mass bias by repeated measurements of the Gj1 zircon standard (Jackson et al., 2004). The six Plešovice zircon standard (Sláma et al., 2008) measurements were treated as unknowns and were used to control the reproducibility and accuracy of the corrections. During the course of the analyses, they provided a Concordia age of 337.7 ± 3.1 Ma (MSWD=0.15, probability=0.999). Data reduction was carried out with the Glitter Software (Van Achterbergh et al., 2001). Concordia ages and diagrams were generated using Isoplot/Ex (Ludwig, 2001). All errors given in the data tables are listed at one sigma, but where data are combined for regression analysis, the final results are provided with 95% confidence limits. Further information on the protocol can be found in Ballouard et al. (2015).

A.2 Supplementary Tables

Additional data files with the U-Pb Pleso standards and ChRM directions can be found online at `https://doi.org/10.1016/j.epsl.2018.12.031`.

TABLE A.1: Geochemical analyses of major (%) and minor (ppm) elements of the three layers within the tuff bed (A, B and C).

Sample #	SiO2 (%)	TiO2 (%)	Al2O3 (%)	Fe2O3 (%)	MnO (%)	MgO (%)	CaO (%)	Na2O (%)	K2O (%)	P2O5 (%)	LOI (%)	Sum (%)
XJTUFF C	58.47	0.35	18.51	1.19	0.06	0.87	2.37	8.87	0.74	0.10	8.14	99.67
XJTUFF B	56.88	0.33	18.37	0.90	0.09	0.76	3.37	9.10	0.62	0.09	9.28	99.79
XJTUFF A	58.80	0.37	18.88	1.31	0.05	0.96	1.67	8.75	0.86	0.10	8.15	99.90
Sample #	Ba (ppm)	Cr (ppm)	Ga (ppm)	Nb (ppm)	Ni (ppm)	Rb (ppm)	Sr (ppm)	V (ppm)	Y (ppm)	Zn (ppm)	Zr (ppm)	Sum (ppm)
XJTUFF C	338	35	14	25	19	51	185	102	20	15	106	910
XJTUFF B	325	17	16	26	13	41	277	44	24	24	89	896
XJTUFF A	338	37	15	25	18	49	206	64	21	30	100	903

TABLE A.2: Operating conditions for the LA-ICP-MS equipment.

Laboratory & Sample Preparation	
Laboratory name	Géosciences Rennes, UMR CNRS 6118, Rennes, France
Sample type/mineral	Detrital and magmatic zircon grains
Sample preparation	Conventional mineral separation, 1 inch resin mount, 1mm polish to finish
Imaging	CL: RELION CL instrument, Olympus Microscope BX51WI, Leica Color Camera DFC 420C
Laser ablation system	
Make, Model & type	ESI NWR193UC, Excimer
Ablation cell	ESI NWR TwoVol2
Laser wavelength	193 nm
Pulse width	<5 ns
Fluence	8.0 J/cm^2
Repetition rate	3 Hz
Spot size	20x70 µm (rotational XY shutter)
Sampling mode / pattern	Single spot
Carrier gas	100% He, Ar make-up gas and N2 (3 ml/mn) combined using in-house smoothing device
Background collection	20 seconds
Ablation duration	60 seconds
Wash-out delay	15 seconds
Cell carrier gas flow (He)	0.72 l/min
ICP-MS Instrument	
Make, Model & type	Agilent 7700x, Q-ICP-MS
Sample introduction	Via conventional tubing
RF power	1350W
Sampler, skimmer cones	Ni
Extraction lenses	X type
Make-up gas flow (Ar)	0.81 l/min
Detection system	Single collector secondary electron multiplier
Data acquisition protocol	Time-resolved analysis
Scanning mode	Peak hopping, one point per peak
Detector mode	Pulse counting, dead time correction applied, and analog mode when signal intensity >∼10^6 cps
Masses measured	^{204}(Hg + Pb), ^{206}Pb, ^{207}Pb, ^{208}Pb, ^{232}Th, ^{238}U
Integration time per peak	10-30 ms
Sensitivity / Efficiency	24000 cps/ppm Pb (50µm, 10Hz)
Data Processing	
Gas blank	20 seconds on-peak
Calibration strategy	GJ1 zircon standard used as primary reference material, Plešovice used as secondary reference material (quality control)
Reference Material info	GJ1 (Jackson et al., 2004) Plešovice (Sláma et al., 2008)
Data processing package used	GLITTER ® (Van Achterbergh et al., 2001)
Quality control / Validation	Plešovice: concordia age = 337.7 ± 3.1 Ma (N=6; MSWD=0.15; probability=0.999)

TABLE A.3: U-Pb data for the 31 analyzed zircon grains. All errors are listed at 1σ. Data in bold were used for the tuff age calculation (%conc. = Percentage of concordance).

					Isotopic ratios				Apparent Ages				
Grain number	Pb (ppm)	U (ppm)	Th (ppm)	Th/U	238U/206Pb	Error (%)	207Pb/206Pb	Error (%)	206Pb/238U	Abs.Err	207Pb/235U	Abs.Err	% Conc.
Zr1	95	1559	343	0.2	17.33	1.16	0.1053	1.02	362	4	618	5	59
Zr3	97	163	145	0.9	2.111	1.17	0.1753	1.01	2500	24	2560	11	98
Zr5	**9**	**986**	**823**	**0.8**	**128.4**	**1.16**	**0.0486**	**1.28**	**50.0**	**0.6**	**51.6**	**0.7**	**97**
Zr7	128	1093	283	0.3	9.04	1.17	0.1057	1.01	676	8	975	7	69
Zr9	32	219	120	0.5	7.363	1.17	0.0670	1.03	821	9	825	7	99
Zr10	**3**	**346**	**195**	**0.6**	**127.6**	**1.15**	**0.0506**	**1.62**	**50.3**	**0.6**	**54**	**0.9**	**93**
Zr11	**4**	**503**	**387**	**0.8**	**127.2**	**1.15**	**0.0496**	**1.53**	**50.5**	**0.6**	**53.1**	**0.84**	**95**
Zr13	**7**	**744**	**687**	**0.9**	**129.5**	**1.17**	**0.0489**	**1.60**	**49.6**	**0.6**	**51.5**	**0.84**	**96**
Zr14	**7**	**832**	**802**	**1.0**	**131.8**	**1.19**	**0.0512**	**1.23**	**48.7**	**0.6**	**53**	**0.7**	**92**
Zr16	**9**	**999**	**797**	**0.8**	**128.0**	**1.15**	**0.0482**	**1.39**	**50.1**	**0.6**	**51.3**	**0.75**	**98**
Zr17	**4**	**433**	**310**	**0.7**	**127.9**	**1.15**	**0.0476**	**1.57**	**50.2**	**0.6**	**50.9**	**0.83**	**99**
Zr18	**4**	**492**	**278**	**0.6**	**125.8**	**1.26**	**0.0501**	**1.46**	**51.1**	**0.6**	**54.4**	**0.83**	**94**
Zr20	**5**	**550**	**457**	**0.8**	**128.4**	**1.16**	**0.0501**	**1.34**	**50.0**	**0.6**	**53.2**	**0.76**	**94**
Zr21	11	228	108	0.5	21.03	1.18	0.0633	1.12	300	3	352	4	85
Zr22	9	146	148	1.0	20.46	1.19	0.0595	1.18	308	4	342	4	90
Zr27	**6**	**632**	**471**	**0.7**	**128.9**	**1.16**	**0.0540**	**1.32**	**49.8**	**0.6**	**57**	**0.79**	**87**
zr28	**4**	**465**	**197**	**0.4**	**125.0**	**1.25**	**0.0502**	**2.95**	**51.4**	**0.7**	**54.7**	**1.57**	**94**
Zr29	**7**	**818**	**646**	**0.8**	**129.4**	**1.16**	**0.0524**	**1.35**	**49.6**	**0.6**	**55.2**	**0.78**	**90**
Zr31	**6**	**607**	**527**	**0.9**	**123.9**	**1.24**	**0.0491**	**1.53**	**51.8**	**0.6**	**54.1**	**0.84**	**96**
Zr34	**5**	**525**	**365**	**0.7**	**129.4**	**1.16**	**0.0502**	**1.75**	**49.6**	**0.6**	**52.9**	**0.94**	**94**
Zr36	**5**	**502**	**373**	**0.7**	**129.2**	**1.16**	**0.0535**	**1.53**	**49.7**	**0.6**	**56.4**	**0.89**	**88**
Zr38	**9**	**904**	**850**	**0.9**	**124.8**	**1.12**	**0.0474**	**1.24**	**51.5**	**0.6**	**51.8**	**0.69**	**99**
Zr39	**6**	**706**	**544**	**0.8**	**130.9**	**1.18**	**0.0487**	**1.58**	**49.1**	**0.6**	**50.8**	**0.83**	**97**
Zr40	11	98	88	0.9	10.35	1.16	0.0608	1.10	595	7	602	6	99
Zr41	**4**	**371**	**438**	**1.2**	**126.4**	**1.14**	**0.0512**	**1.76**	**50.8**	**0.6**	**55.2**	**0.97**	**92**
Zr42	50	326	91	0.3	6.576	1.16	0.0696	1.05	913	10	914	7	100
Zr43	**9**	**895**	**787**	**0.9**	**126.4**	**1.14**	**0.0621**	**1.22**	**50.8**	**0.6**	**66.5**	**0.86**	**76**
Zr44	18	435	226	0.5	26.69	1.15	0.0653	1.07	237	3	295	3	80
Zr45	11	161	122	0.8	17.30	1.16	0.0593	1.11	362	4	393	4	92
Zr47	21	348	152	0.4	17.11	1.16	0.0614	1.11	366	4	408	4	90
Zr48	43	342	114	0.3	7.988	1.16	0.0654	1.05	760	8	767	6	99

A.3 Supplementary Figures

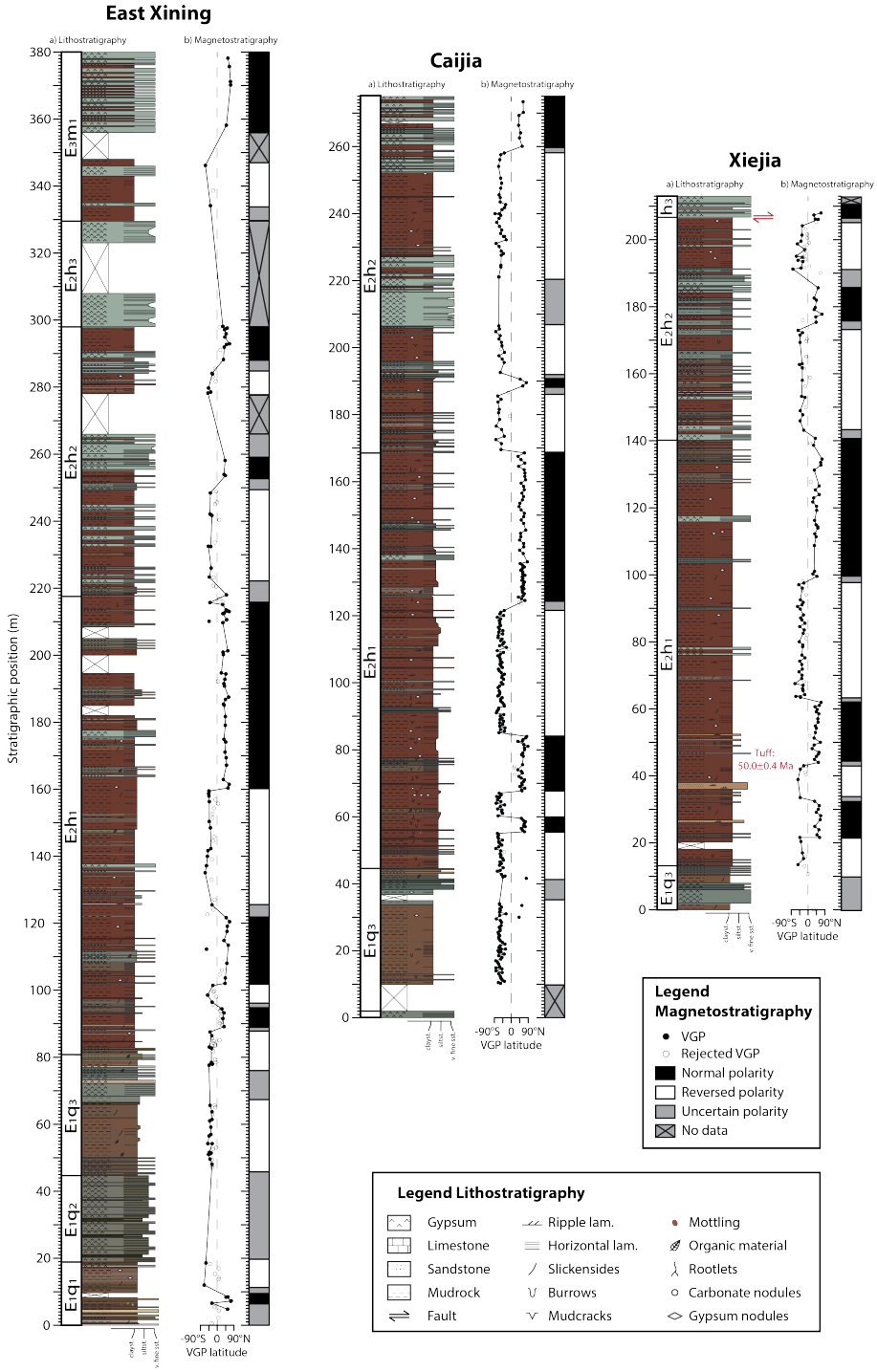

FIGURE A.1: Studied sections showing: (A) detailed lithological logs of the studied sections. (B) Virtual Geomagnetic Pole (VGP) latitudes and corresponding polarity zones. A higher resolution version of this figure can be found online at `https://doi.org/10.1016/j.epsl.2018.12.031`.

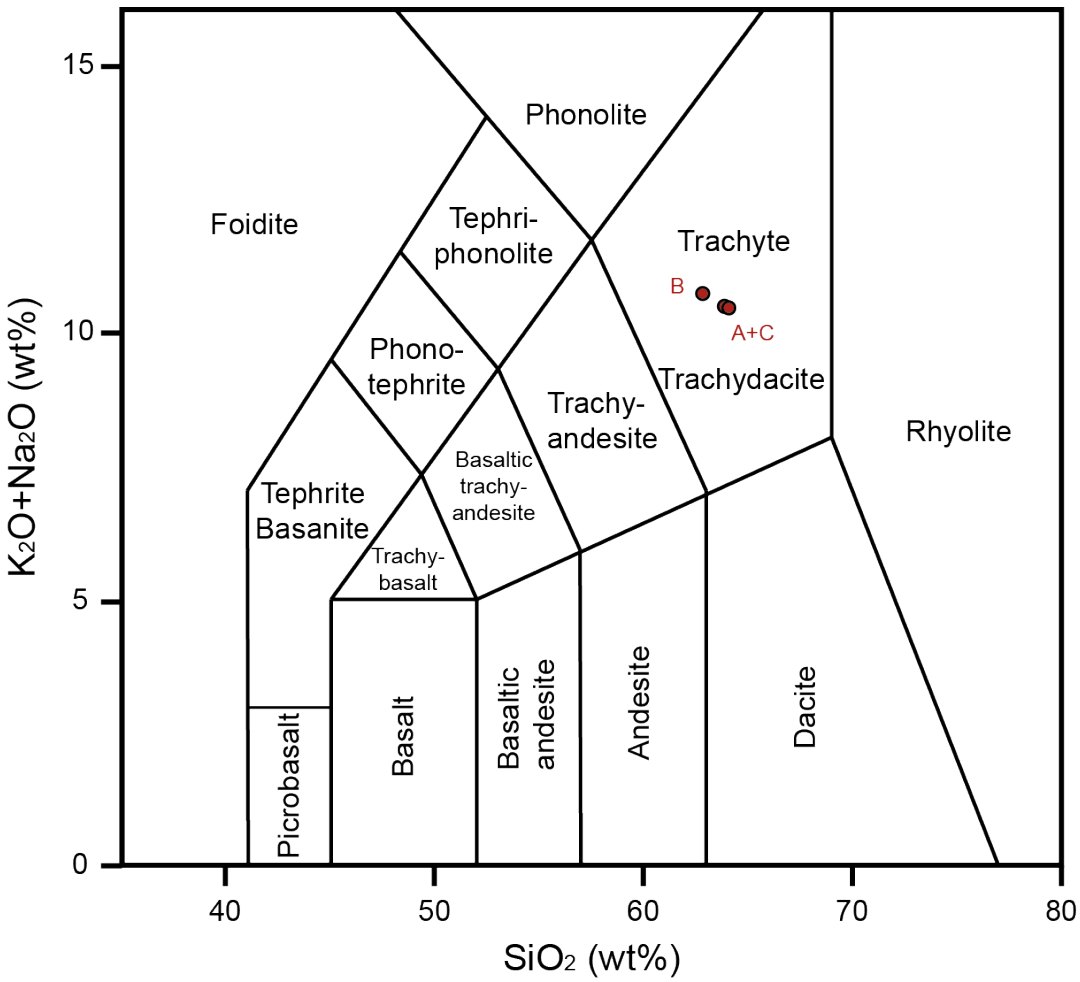

FIGURE A.2: Total alkali-silica (TAS) diagram (Le Maitre et al., 1989) of the tuff layers (A, B and C in Fig. 3.3G) classifying the tuff as trachyte.

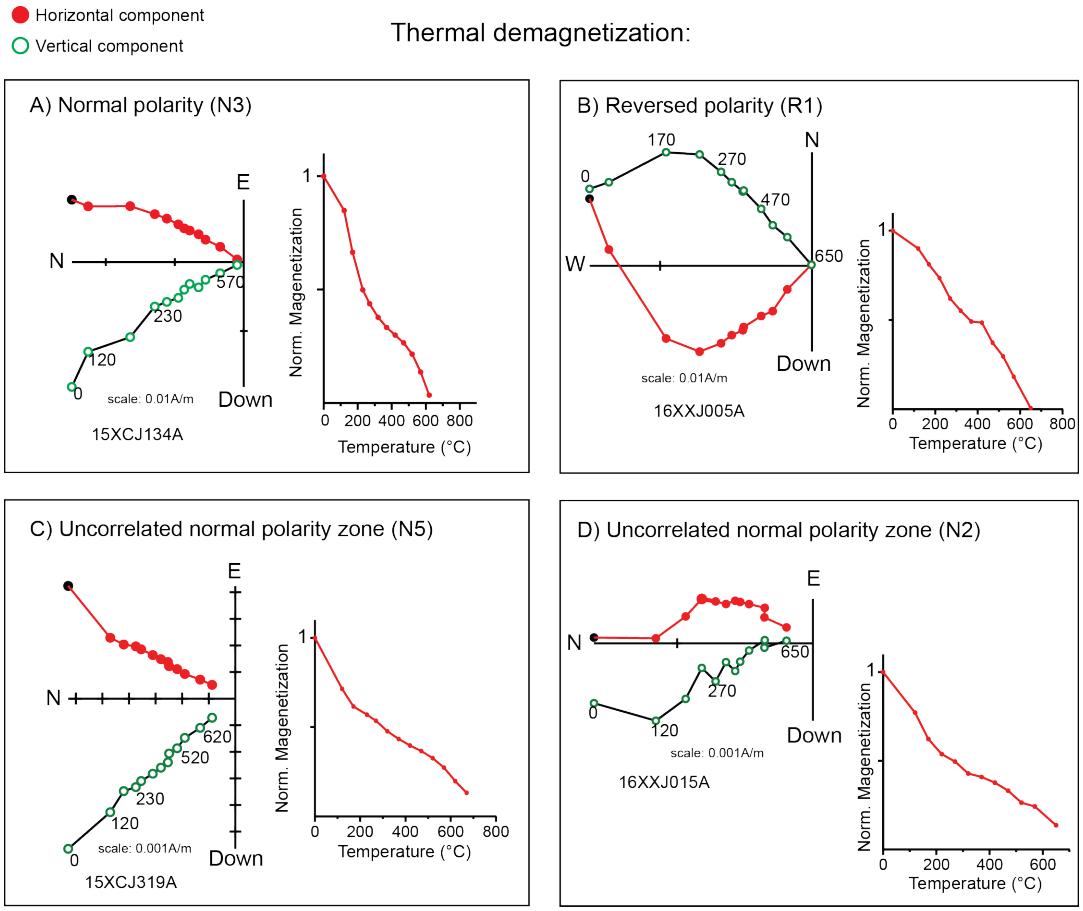

FIGURE A.3: Thermal demagnetization of representative samples shown in vector end point diagrams on the left (numbers indicate temperature steps) and remanent magnetization on the right. (A) Normal polarity in N3 (Caija, 71.5 meter). (B) Reversed polarity in R1 (Xiejia, 15.3 meter). (C) Normal polarity in N5 (Caijia, 188.5 meter). (D) Normal polarity in N2 (Xiejia, 29.1 meter). The samples shown in (C) and (D) are from normal polarity zones that were not correlated to the GTS.

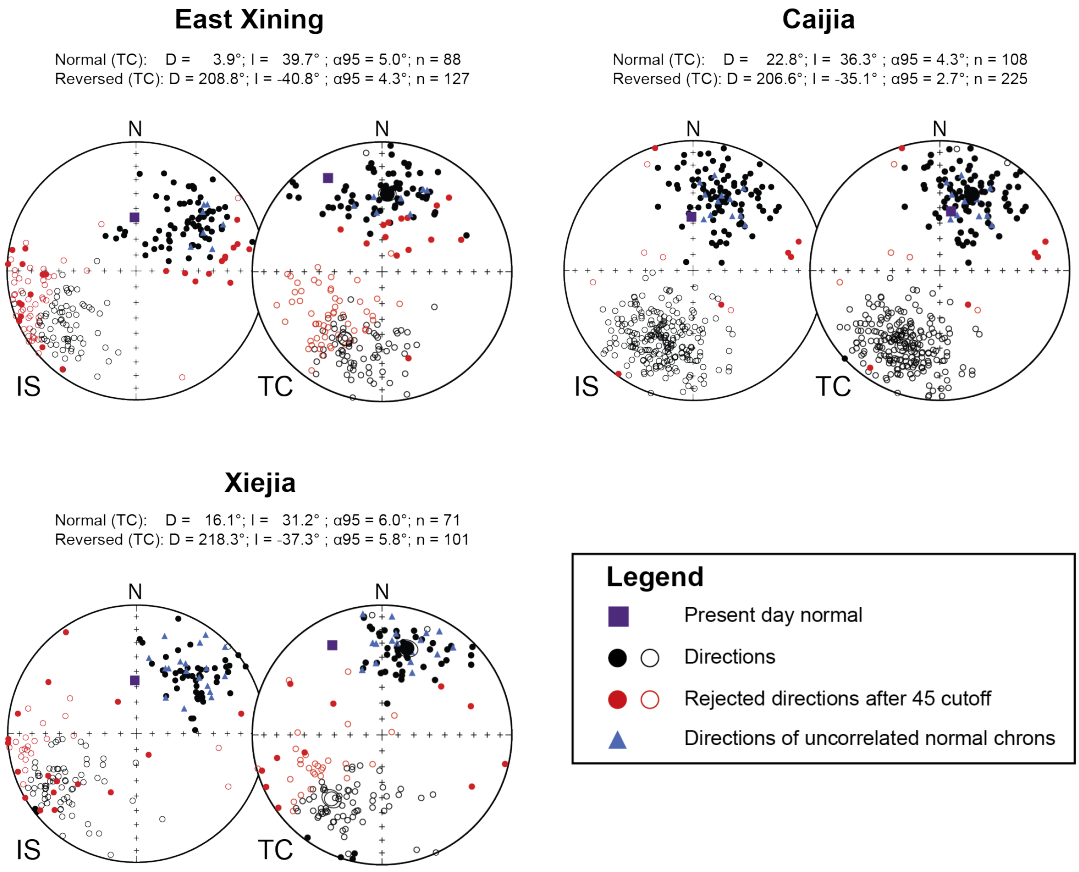

FIGURE A.4: Equal-area stereographic projections in the lower hemisphere of the ChRMs calculated in the different sections. The ChRMs are shown both in situ (IS) and tilt-corrected (TC). Samples removed after 45° cutoff are indicated in red and samples from normal polarity zones that are not correlated to the GTS are indicated in blue.

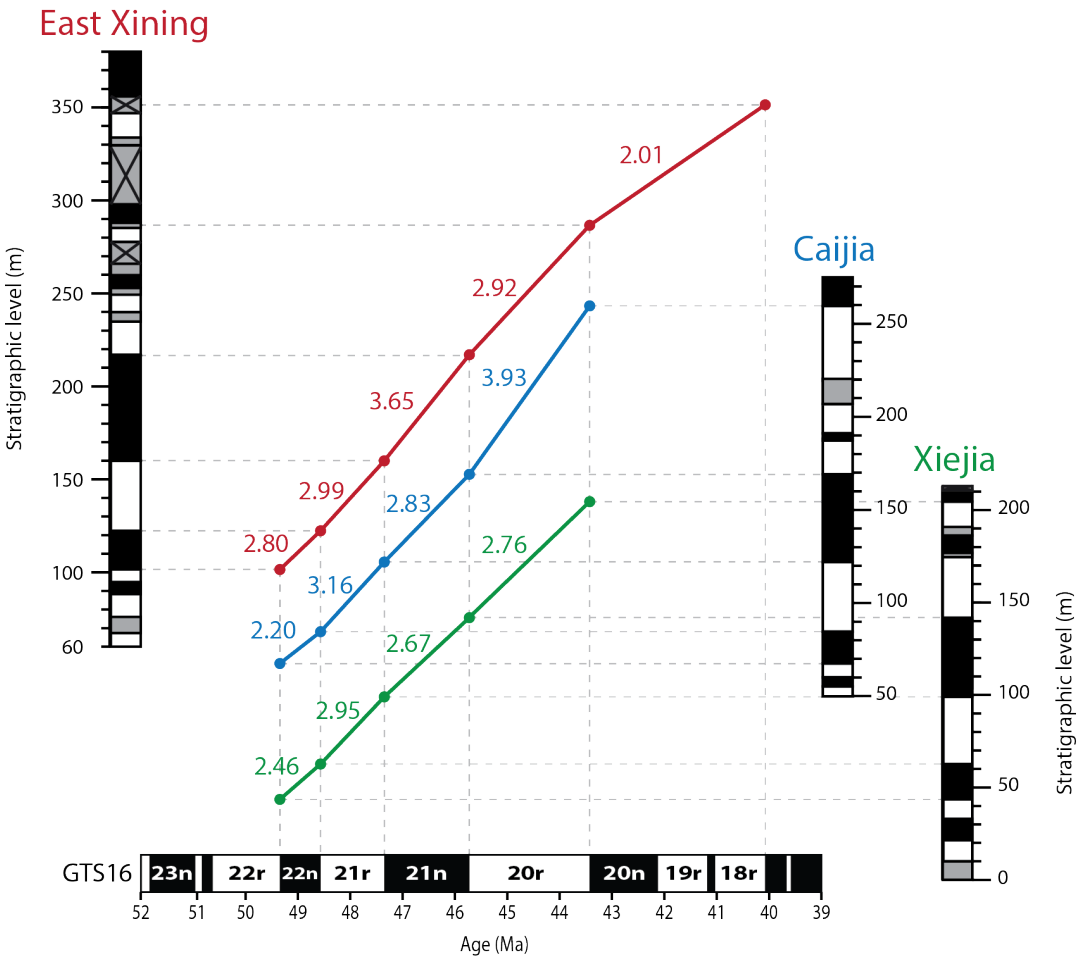

FIGURE A.5: Sediment accumulation rates for the different magnetostratigraphic sections correlated to the GTS16 (Ogg et al., 2016). Rates are shown in cm/kyr.

Appendix B

Supplementary Information for Chapter 4

B.1 Supplementary Tables

TABLE B.1: U-Pb data of carbonate sample CJC07 and calcite standard WC-1

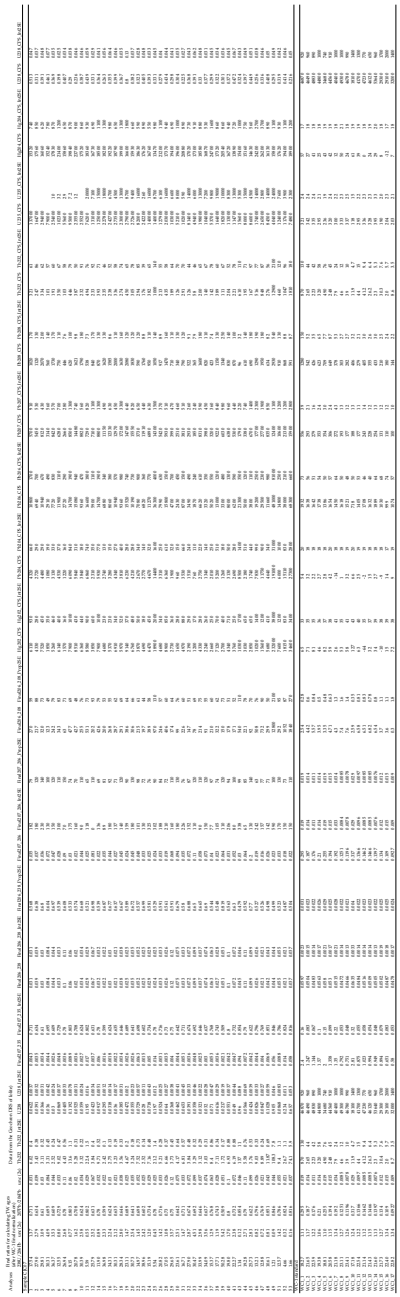

TABLE B.2: Stable isotope data

Sample	Section	Stratigraphic Position (m)	Composite Stratigraphic Position (m)	Carbonate d13C (in ‰ V-PDB)	Carbonate d18O (in ‰ V-PDB)	Organic Matter d13C (in ‰ V-PDB)
15CJ_L10.25	Caijia	10.25	-34.25	-6.22	-7.60	-27.92
15CJ_L15		15.00	-29.50	-7.69	-7.43	-28.04
15CJ_L19.5		19.50	-25.00	-8.88	-7.82	-27.07
15CJ_0.5		20.00	-24.50	-8.02	-7.48	-27.08
15CJ_5		24.50	-20.00	-8.10	-8.00	-27.34
15CJ_10		29.50	-15.00	-9.03	-7.52	-26.02
15CJ_15		34.50	-10.00			-23.68
15CJ_22		41.50	-3.00			-22.07
15CJ_24.5		44.00	-0.50			-23.53
15CJ_30.25		49.75	5.25			-24.33
15CJ_35		54.50	10.00			-22.33
15CJ_40		59.50	15.00			-21.94
15CJ_45		64.50	20.00			-22.07
15CJ_48.5		68.00	23.50	-8.90	0.14	-23.34
15CJ_50		69.50	25.00	-9.14	-0.58	-22.87
15CJ_55		74.50	30.00	-9.65	-2.49	-24.02
15CJ_60		79.50	35.00	-9.95	-1.46	-24.17
15CJ_65		84.50	40.00	-9.85	-6.36	-20.99
15CJ_70		89.50	45.00	-9.30	-6.09	-22.36
15CJ_75		94.50	50.00	-9.84	-0.80	-24.70
15CJ_80		99.50	55.00	-9.57	-5.34	-21.85
15CJ_85		104.50	60.00	-8.49	-1.48	-23.98
15CJ_90		109.50	65.00	-12.97	-6.39	-23.05
15CJ_95		114.50	70.00	-8.76	-3.58	-24.85
15CJ_100		119.50	75.00	-8.30	-1.85	-24.55
15CJ_105		124.50	80.00	-10.26	-4.89	-24.15
15CJ_110		129.50	85.00	-9.58	0.20	-25.35
15CJ_115		134.50	90.00	-9.84	-1.45	-24.22
15CJ_120		139.50	95.00	-9.36	-1.23	-24.44
15CJ_125		144.50	100.00	-9.24	-5.77	-24.34
15CJ_130		149.50	105.00	-10.52	-6.93	-24.17
15CJ_135		154.50	110.00	-10.15	-4.31	-24.94
15CJ_140.5		160.00	115.50	-9.15	-5.50	-24.39
15CJ_145		164.50	120.00	-9.78	-4.79	-24.37
15CJ_150		169.50	125.00	-8.93	0.77	-24.43
15CJ_155		174.50	130.00	-8.26	-1.18	-23.40
15CJ_160		179.50	135.00	-9.16	0.56	-24.06
15CJ_165		184.50	140.00	-9.79	-4.86	-22.26
15CJ_170.5		190.00	145.50			-24.10
15CJ_170.9		190.40	145.90			
15CJ_175		194.50	150.00			-24.14
15CJ_180		199.50	155.00			-24.30
15CJ_184.5		204.00	159.50	-9.71	-3.94	-23.38
16CJ_217.5		217.50	173.00			
16CJ_221		221.00	176.50			
16CJ_223.5		223.50	179.00	-7.59	-0.38	
16CJ_230		230.00	185.50	-7.33	-1.25	
16CJ_235		235.00	190.50	-7.81	-5.66	
16CJ_239.5		239.50	195.00	-6.48	-5.58	
16CJ_245		245.00	200.50	-7.44	-1.27	
16CJ_250		250.00	205.50	-7.25	0.12	
16CJ_256		256.00	211.50	-6.89	-0.99	
16CJ_260		260.00	215.50			
16CJ_265		265.00	220.50			
16CJ_269		269.00	224.50	-6.45	-2.06	
16SH_1	Sanhe	75.00	-73.00			-18.96
16SH_6		70.00	-78.00	-1.36	-4.81	-19.55
16SH_10.9		65.10	-82.90	-2.20	-3.41	-21.27
16SH_15.05		60.95	-87.05	1.95	-3.75	-23.41
16SH_20.2		55.80	-92.20	1.51	-3.63	-24.07
16SH_25.5		50.50	-97.50	-1.00	-2.52	-23.33
16SH_29.25		46.75	-101.25	-1.94	-1.74	-21.81
16SH_36		40.00	-108.00			-21.81
16SH_60.5		15.50	-132.50	-1.49	-1.09	
18Ld-104	Ledu	-104.00	-119.00			-22.38
18Ld-102		-102.00	-117.00	-4.05	-6.32	-22.34
18Ld-100		-100.00	-115.00			-22.32
18Ld-98		-98.00	-113.00	-4.58	-6.72	-23.74
18Ld-96		-96.00	-111.00	-4.88	-5.02	-21.73
18Ld-94		-94.00	-109.00	-4.97	-6.64	-24.24
18Ld-92		-92.00	-107.00	-5.11	-5.77	-22.40
18Ld-90		-90.00	-105.00	-5.33	-6.93	
18Ld-88		-88.00	-103.00	-5.45	-6.46	-23.36
18Ld-86		-86.00	-101.00	-5.88	-6.14	
18Ld-82		-82.00	-97.00	-6.04	-6.75	
18LD-80		-80.00	-95.00	-6.68	-7.57	-23.94
18LD-80		-80.00	-95.00			-23.23
18Ld-79		-79.00	-94.00	-6.53	-6.16	-23.39
18Ld-78		-78.00	-93.00	-6.45	-7.60	-23.37
18Ld-76		-76.00	-91.00			-23.14
18Ld-72		-72.00	-87.00			-23.48
18Ld-70		-70.00	-85.00	-6.18	-6.83	-20.46
18Ld-68		-68.00	-83.00			-23.54
18Ld-56		-56.00	-71.00	-4.16	-5.52	-19.76
18Ld-54		-54.00	-69.00	-6.09	-7.48	-20.82
18Ld-52		-52.00	-67.00	-6.05	-8.68	
18Ld-50		-50.00	-65.00	-6.47	-10.45	-19.69
18Ld-48		-48.00	-63.00	-8.72	-6.92	-19.06
18Ld-46		-46.00	-61.00	-10.42	-7.04	-19.23
18Ld-44		-44.00	-59.00	-8.63	-8.11	-19.52
18Ld-42		-42.00	-57.00	-7.45	-9.08	-18.94
18Ld-40		-40.00	-55.00	-9.63	-8.85	-16.97
18Ld-38		-38.00	-53.00			-20.47
18Ld-34		-34.00	-49.00	-8.00	-11.75	-21.34
18Ld-30		-30.00	-45.00			-21.45
18Ld-30		-30.00	-45.00			-21.39
18Ld-28		-28.00	-43.00	-9.88	-11.88	-21.47
18Ld-26		-26.00	-41.00	-8.50	-7.45	-21.49
18Ld-24		-24.00	-39.00	-8.49	-7.58	
18Ld-22		-22.00	-37.00	-8.92	-6.88	
18Ld-20		-20.00	-35.00	-10.48	-7.80	
18Ld-18		-18.00	-33.00	-10.11	-8.12	-27.66
18Ld-16		-16.00	-31.00	-10.98	-7.32	
18Ld-10		-10.00	-25.00	-7.70	-8.35	-24.83
18Ld-8		-8.00	-23.00	-7.73	-7.81	
18Ld-4		-4.00	-19.00	-8.94	-8.81	
18Ld-2		-2.00	-17.00	-10.55	-8.88	
18Ld+2		2.00	-13.00	-9.74	-7.67	-27.01
18Ld+3		3.00	-12.00	-10.27	-9.29	-27.56
18Ld+13.3		13.30	-1.70	-12.30	-7.24	-25.72
18Ld+13.8		13.80	-1.20	-12.02	-9.12	-22.22
18Ld+14.8		14.80	-0.20	-9.48	-9.13	-22.81
SA 6	Bingling Shan	6.00	-72.00			-19.13
SA 7.5		7.50	-70.50			-21.83
SA 8.5		8.50	-69.50			-20.48
SA 10.4		10.40	-67.60			-19.34
SA 11		11.00	-67.00			-21.00
SA 11.5		11.50	-66.50			-19.56
SA 11.8		11.80	-66.20			-19.34
SA 12.5		12.50	-65.50			-19.30
SA 14.25		14.25	-63.75			-20.13
SA 15		15.00	-63.00			-20.29
SA 16.75		16.75	-61.25			-20.23
SA 18.5		18.50	-59.50			-20.44
SA 18.75		18.75	-59.25			-20.05
SA 19.40		19.40	-58.60			-20.15
SA 20A		20.00	-58.00			-20.66
SA 20.4		20.40	-57.60			-20.97
SA 21		21.00	-57.00			-22.06
SA 23		23.00	-55.00			-20.08
SA 25		25.00	-53.00			-20.40
SA 26		26.00	-52.00			-20.01
SA 28		28.00	-50.00			-21.43
SA 29		29.00	-49.00			-20.97
SA 33.25		33.25	-44.75			-22.54
SA 33.5		33.50	-44.50			-20.37
SA 34		34.00	-44.00			-20.58
SA 34.5		34.50	-43.50			-22.40
SA 37.5		37.50	-40.50			-21.20
SA 39.5		39.50	-38.50			-21.13
SA 40.5		40.50	-37.50			-21.32
SA 41		41.00	-37.00			-22.73
SA 41.5		41.50	-36.50			-21.28

TABLE B.3: Palynological data

						NLR Veg Groups Abundance (%)						
Section	Sample #	Reference	Section strat. pos. (m)	Composite stratigraphic position (m)	Age (GTS12)	Conifers	Steppe/desert	Temperate broad leaved forest	Warm broad leaved forest	Pteridophytes	Other / Unknown
East Xining	PEX-12	*This study*	20	-61.4	50.9	13	66	6	0	0	14
East Xining	PEX-15	*This study*	32.5	-48.9	50.7	6	74	1	0	1	18
East Xining	PEX-17	*This study*	36.8	-44.6	50.6	0	32	12	0	26	30
East Xining	PGP1	*This study*	0.5	-36	50.5	3	70	0	0	7	20
Caija	17CJ-L1.5	*This study*	1.5	-35	50.5	0	38	9	0	13	40
Dazhai	Liver	*This study*	~20	-30	~50.1	0	19	7	1	13	60
Caijia	17CJ-L18.5	*This study*	18.5	-26	49.9	25	21	6	0	8	40
Xiejia	17XJ-11b	*This study*	11	-1.8	49.8	0	14	30	0	21	35
Xiejia	17XJ-NB-88	*Chapter 5*	88	75.2	47.7	3	23	26	0	25	24

B.2 Supplementary Figures

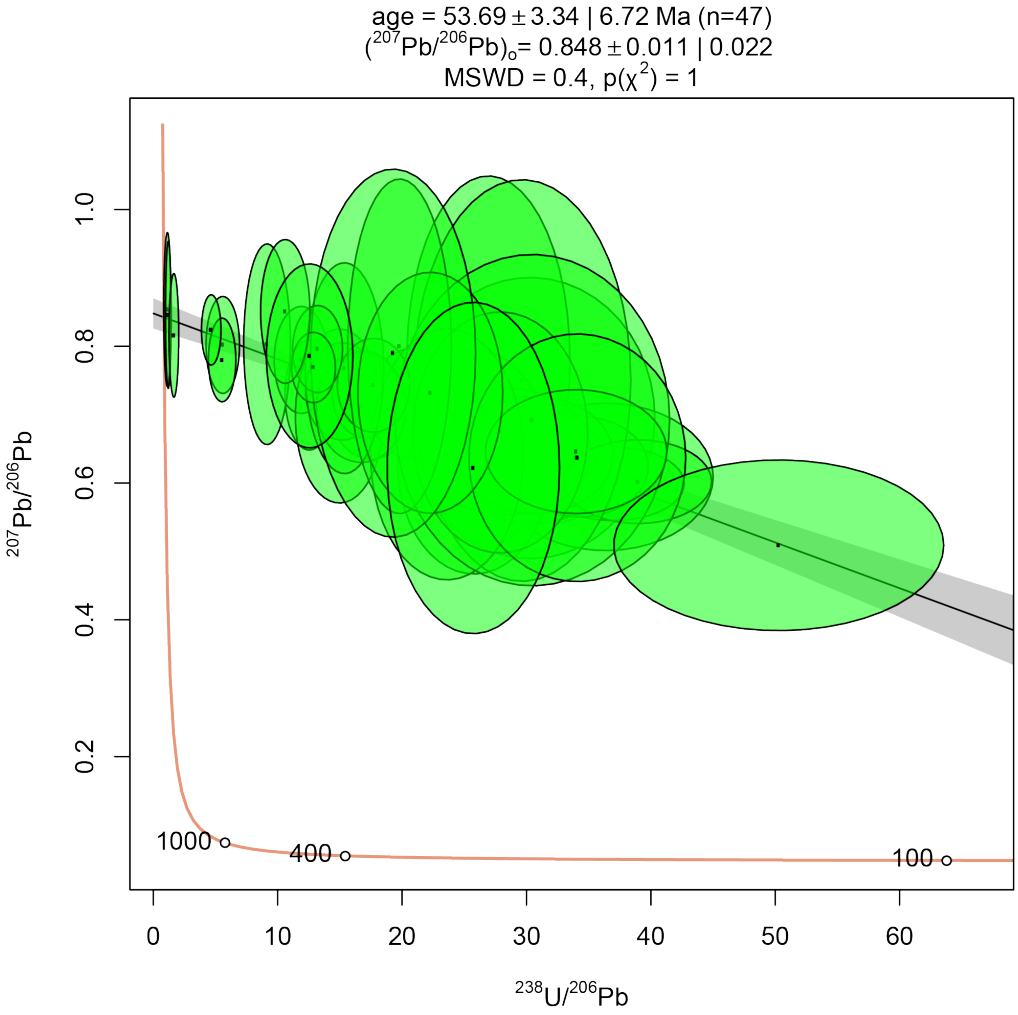

FIGURE B.1: Tera-Wasserburg diagram of the lacustrine carbonate sample CJC07.

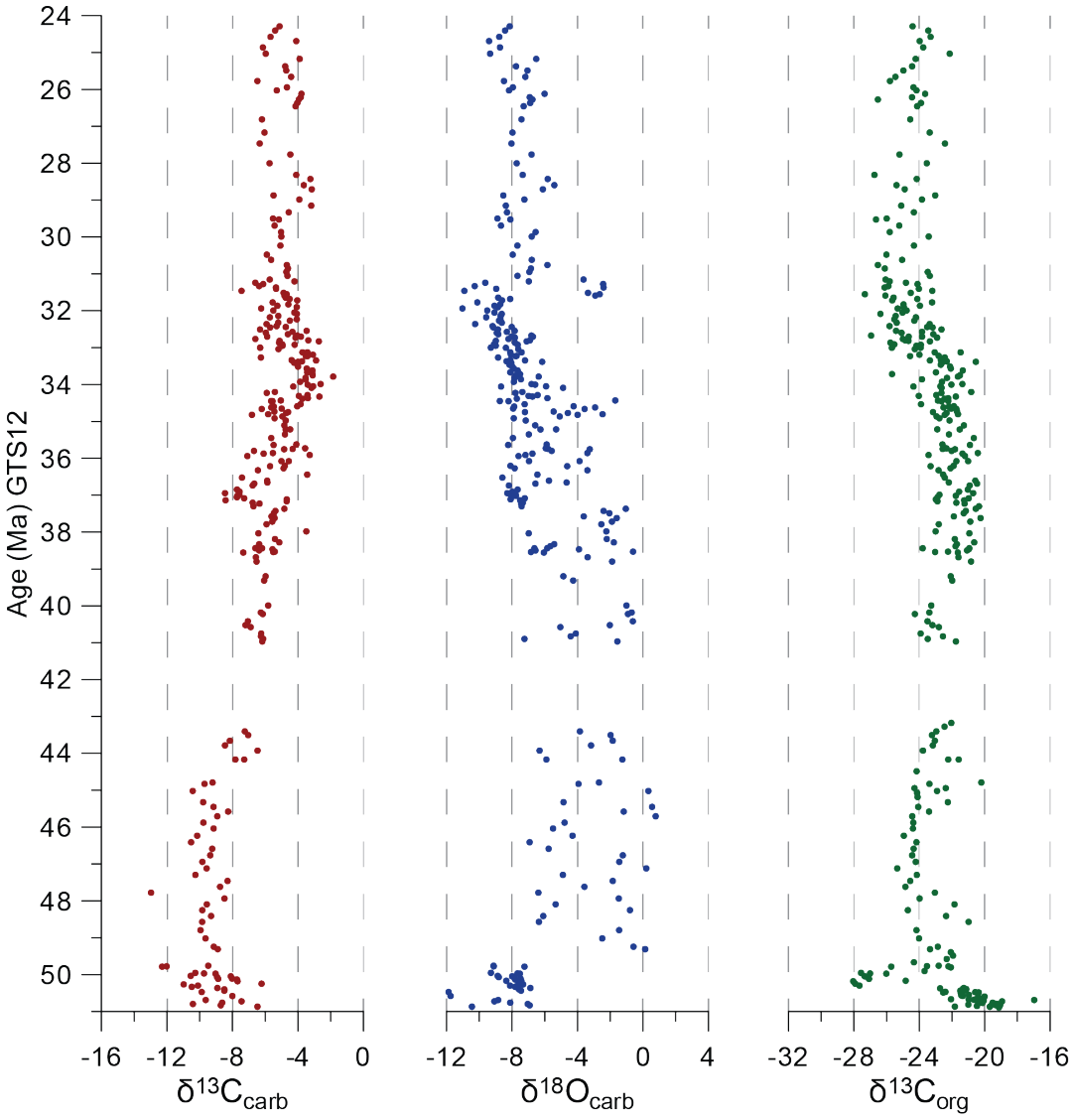

FIGURE B.2: Compilation of pedogenic and bulk organic stable isotope data from Licht et al. (2020) and this study.

Appendix C

Supplementary Information for Chapter 5

Data files are available online at `https://doi.pangaea.de/10.1594/PANGAEA.923996`.

C.1 Supplementary Figures

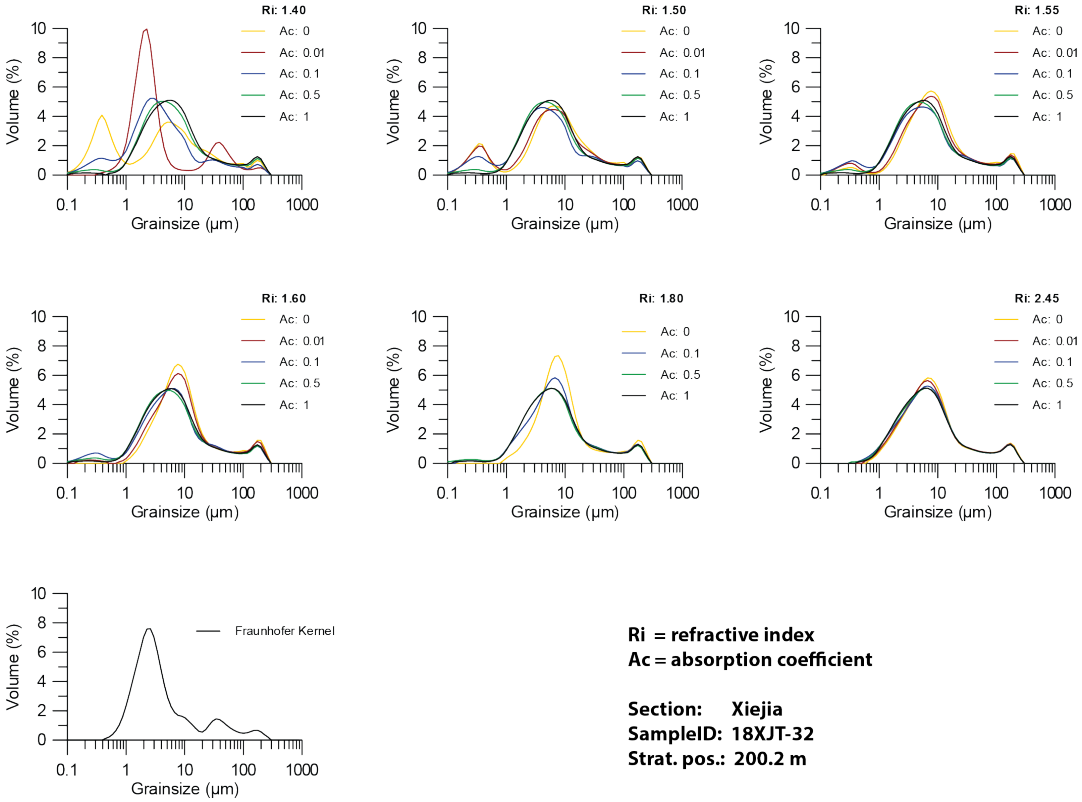

FIGURE C.1: Grain-size distributions of sample 18XJT-32 calculated using the Mie optical model with different refractive indices (Ri) and absorption coefficients (Ac) and the Fraunhofer optical model.

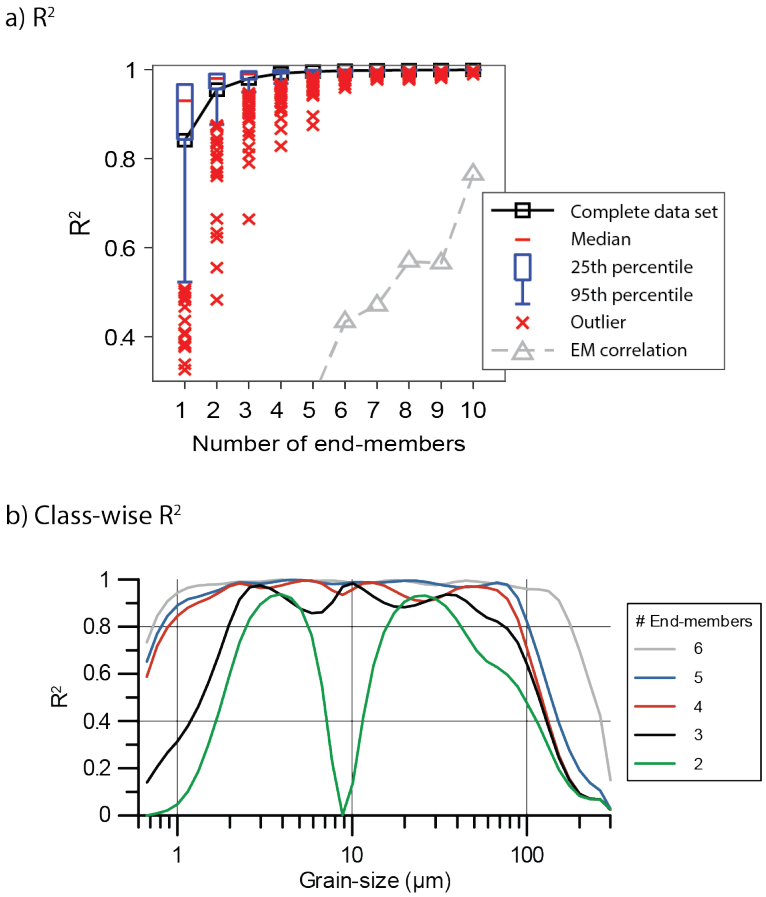

FIGURE C.2: (A) Quality of fit (R^2) of the end-member models with varying numbers of end-members (1-10), showing that using four end-members results in R^2 of 0.984 (Paterson and Heslop, 2015). (B) Class-wise R^2 (van Hateren et al., 2018) of the end-member models with varying numbers of end-members (1-6) shows that using four end-members results in R^2 of >0.95 for particle sizes ranging between 2 and 70 µm.

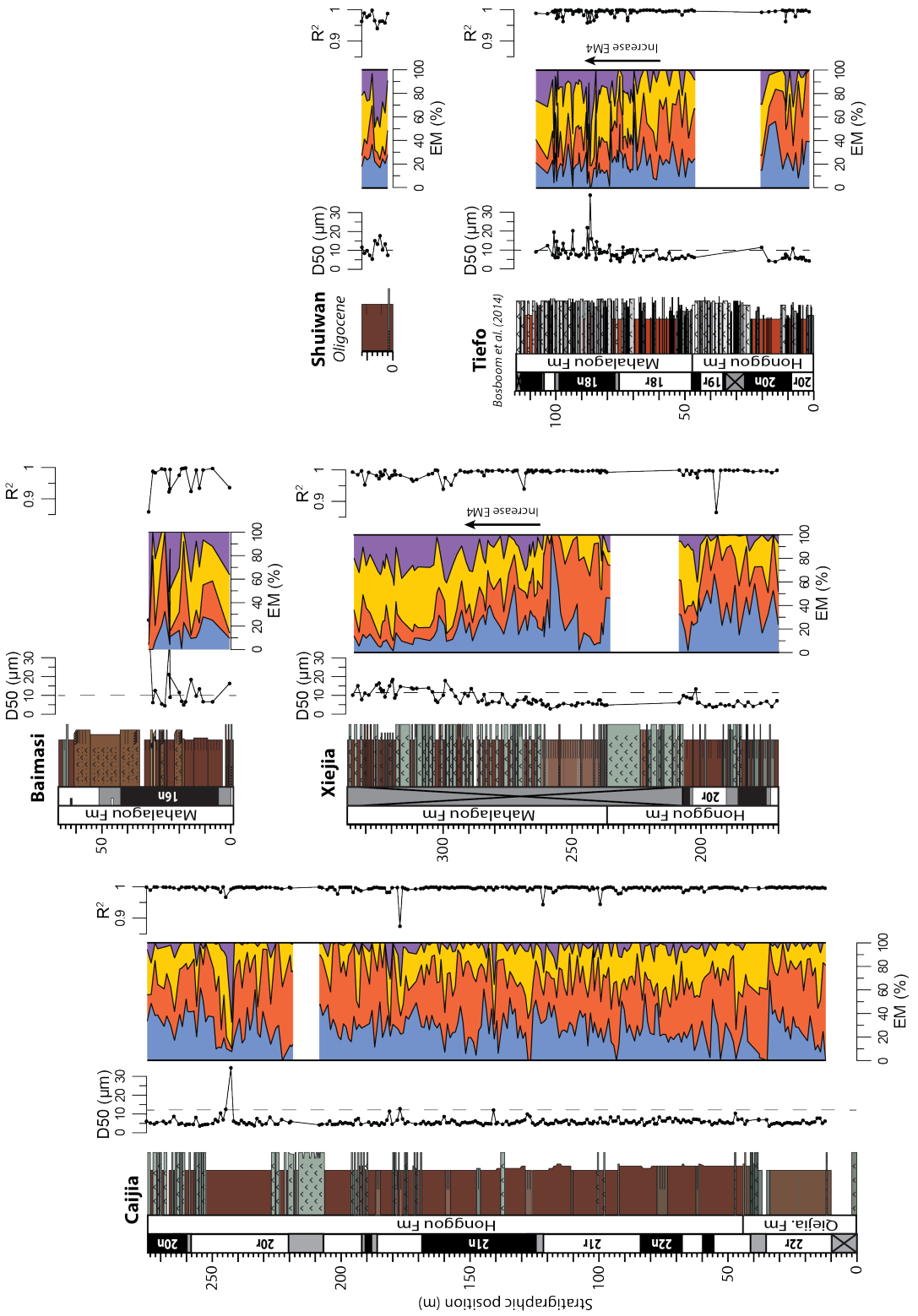

FIGURE C.3: (A) Grain-size records of the studied sections in the Xining Basin showing median grain-size (D50), end-member abundances (EM) and sample-wise quality of fit (R^2) of the end-member model. GSDs of the end-members are shown in Fig. 5.5. Litho- and magnetostratigraphy from Bosboom et al. (2014a) and Chapter 3.

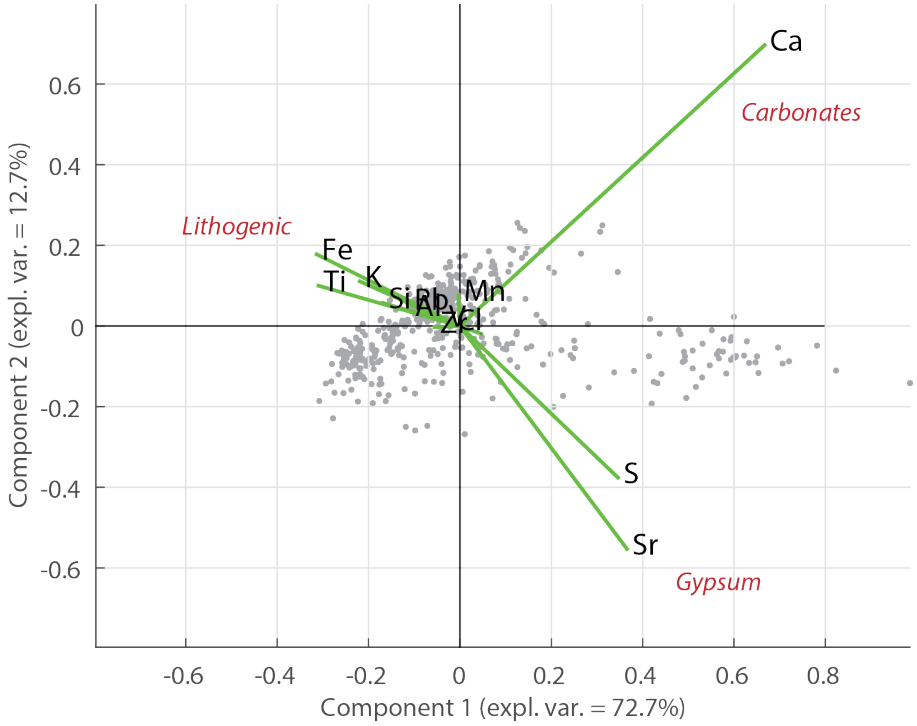

FIGURE C.4: Biplot of the XRF scanning data of the Caijia section after principal component analysis using ItraXelerate (Weltje et al., 2015).

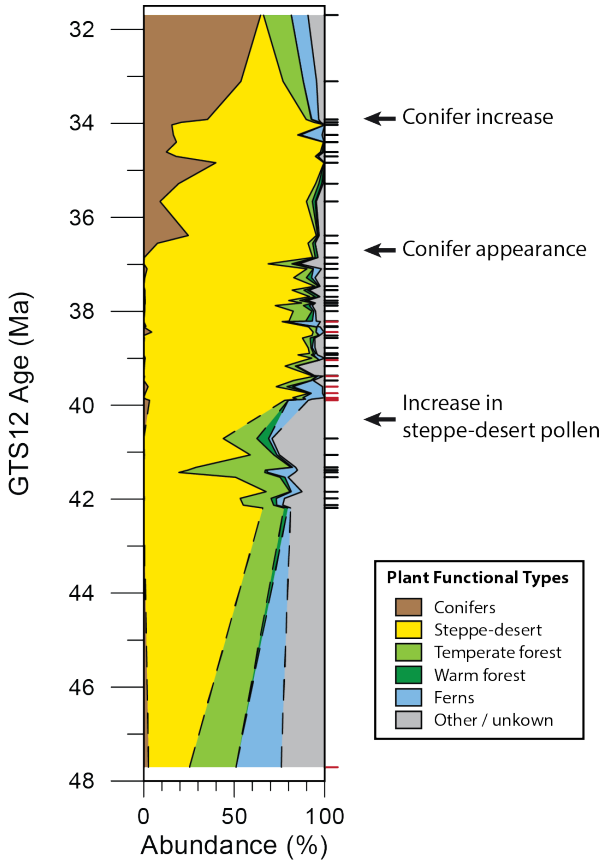

FIGURE C.5: Xining palynological record (Bosboom et al., 2014a; Dupont-Nivet et al., 2008a; Hoorn et al., 2012; Page et al., 2019). Newly added sample from this study are indicated in red.

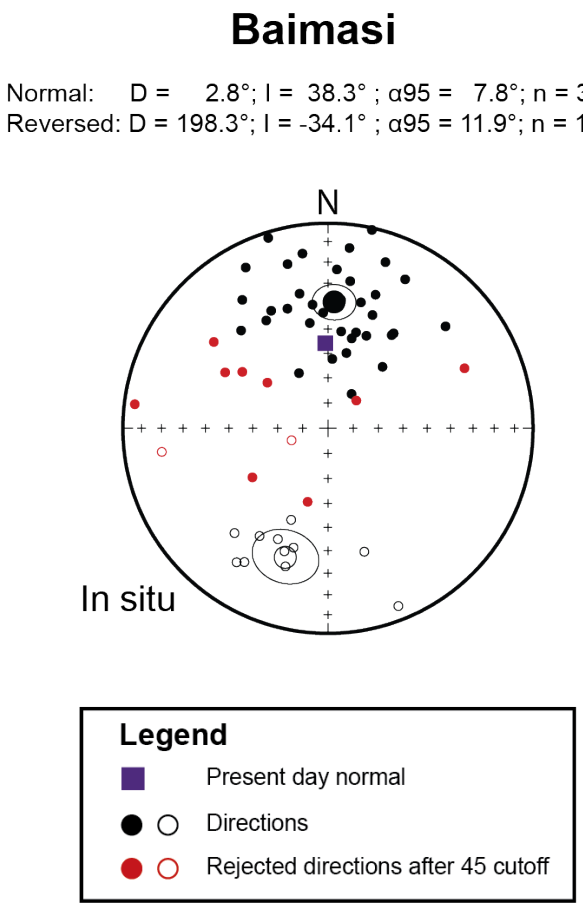

FIGURE C.6: Equal-area stereographic projection of the ChRM directions of the Baimasi section.

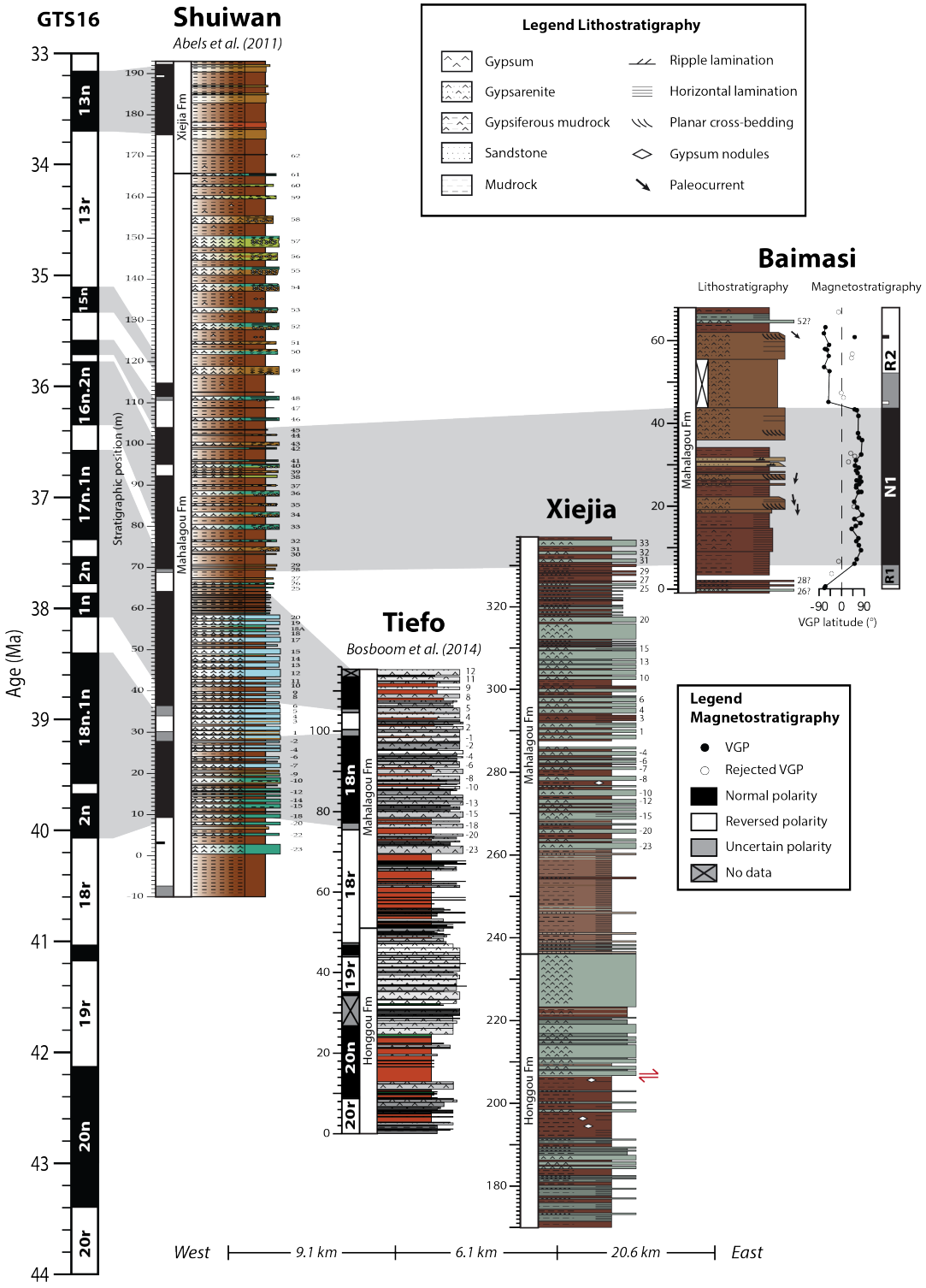

FIGURE C.7: Lithostratigraphic and magnetostratigraphic correlations between the Shuiwan (Abels et al., 2011), Tiefo (Bosboom et al., 2014a), Xiejia (Chapter 3) and Baimasi sections and the GTS16 (Ogg et al., 2016).

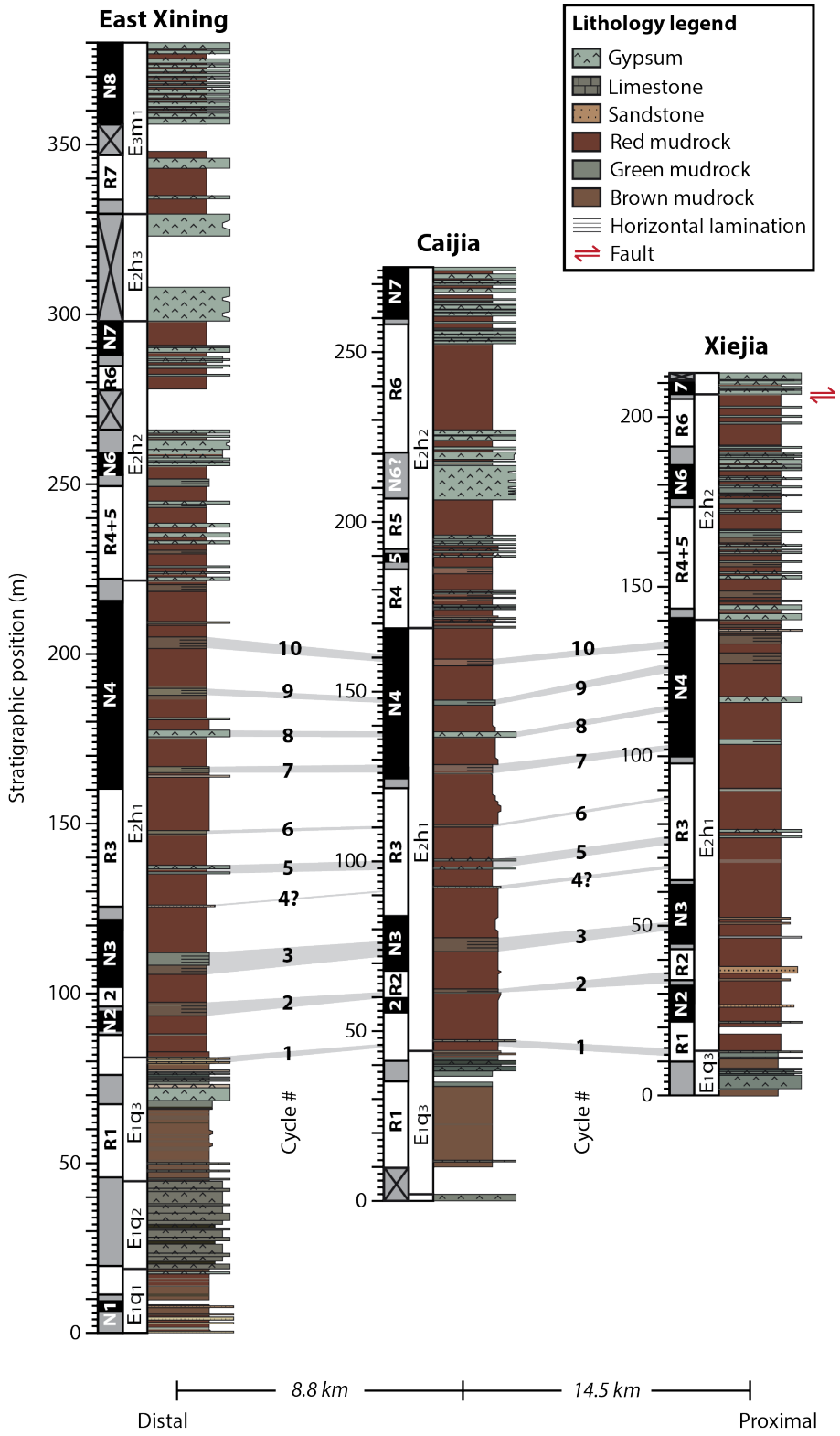

FIGURE C.8: Lithostratigraphic correlations of the cyclicity in the Honggou Formation between the East Xining, Caijia and Xiejia sections. Litho- and magnetostratigraphy are from Chapter 3.

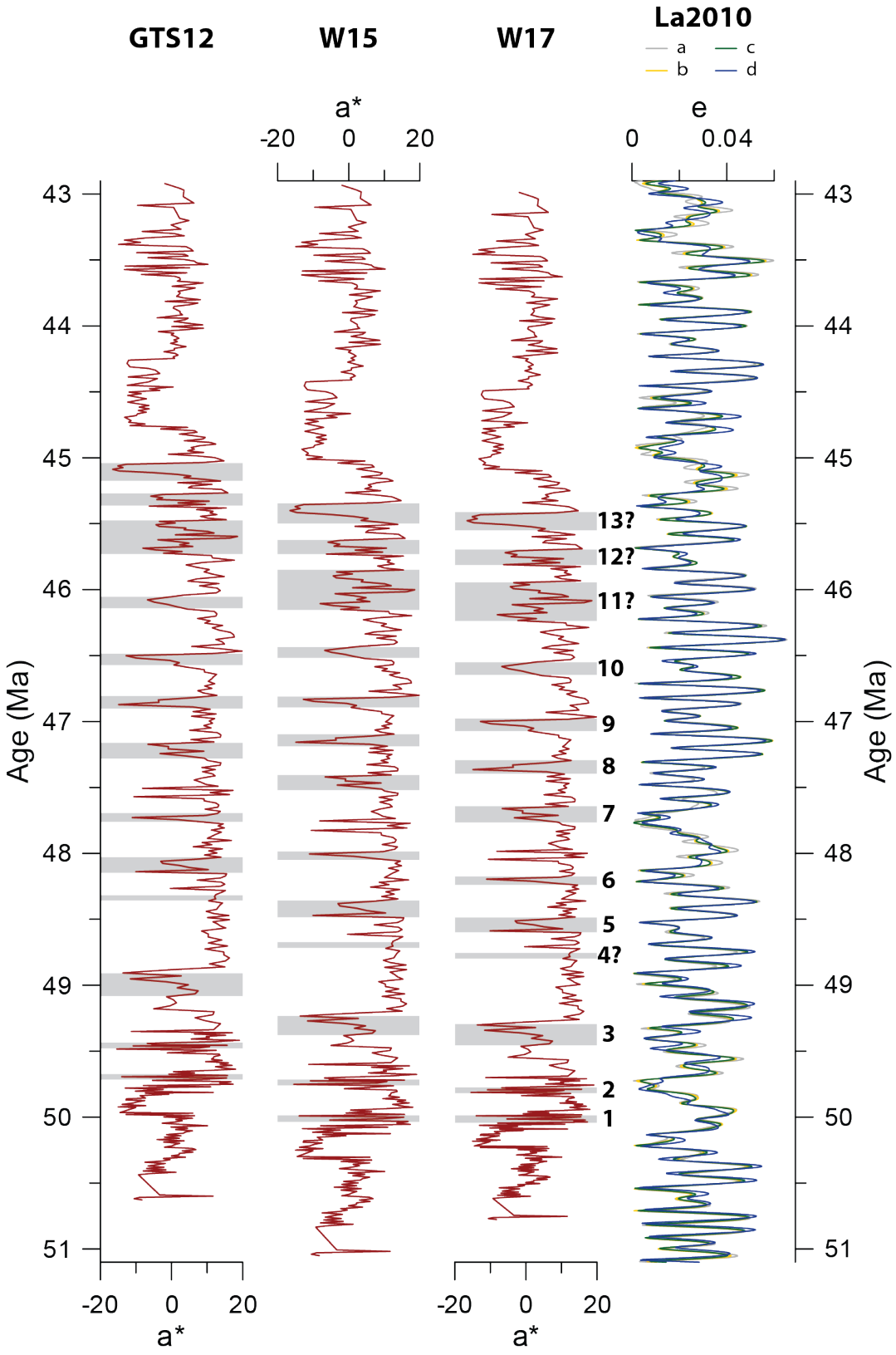

FIGURE C.9: Color record a^* (red over green) of the Caijia section correlated to the astronomical solutions (a-d) of eccentricity, e (Laskar et al., 2011). The ages of the Caijia section are calculated by linear interpolation between chron boundaries identified by (Chapter 3). The base of the Caijia section is correlated to the top of C23n. Chron ages of the following timescales are used: GTS12 (Gradstein et al., 2012), W15 (Westerhold et al., 2015) and W17 (Westerhold et al., 2017). The latter shows wet phases of cycle 1 to 13 during 405-kyr eccentricity minima.

Bibliography

Abels, H. A. et al. (2010). "Long-period eccentricity control on sedimentary sequences in the continental Madrid Basin (middle Miocene, Spain)". In: *Earth and Planetary Science Letters* 289.1-2, pp. 220–231. DOI: 10.1016/j.epsl.2009.11.011.

Abels, H. A. et al. (2011). "Step-wise change of Asian interior climate preceding the Eocene-Oligocene Transition (EOT)". In: *Palaeogeography, Palaeoclimatology, Palaeoecology* 299.3-4, pp. 399–412. DOI: 10.1016/j.palaeo.2010.11.028.

Ahmed, I. A. M. and B.A. Maher (2018). "Identification and paleoclimatic significance of magnetite nanoparticles in soils". In: *Proceedings of the National Academy of Sciences of the United States of America* 115.8, pp. 1736–1741. DOI: 10.1073/pnas.1719186115.

Alonso-Zarza, A. M. et al. (2009). "Mudflat/distal fan and shallow lake sedimentation (upper Vallesian-Turolian) in the Tianshui Basin, Central China: Evidence against the late Miocene eolian loess". In: *Sedimentary Geology* 222.1-2, pp. 42–51. DOI: 10.1016/j.sedgeo.2009.03.010.

Alonso-Zarza, A. M. et al. (2010). "Reply to the comment on "Mudflat/distal fan and shallow lake sedimentation (upper Vallesian–Turolian) in the Tianshui Basin, Central China: Evidence against the late Miocene eolian loess" by A. M. Alonso-Zarza, Z. Zhao, C. H. Song, J. J. Li, J. Zhang, A. Martín-Pérez, R. Martín-García, X. X. Wang, Y. Zhang and M. H. Zhang [Sedimentary Geology 222 (2009) 42–51]". In: *Sedimentary Geology* 230.1-2, pp. 90–93. DOI: 10.1016/j.sedgeo.2010.06.018.

An, Z. et al. (1990). "The long-term paleomonsoon variation recorded by the loess-paleosol sequence in Central China". In: *Quaternary International* 7-8.C, pp. 91–95. DOI: 10.1016/1040-6182(90)90042-3.

An, Z. et al. (1999). "Eolian evidence from the Chinese Loess Plateau: The onset of the Late Cenozoic Great Glaciation in the Northern Hemisphere and Qinghai-Xizang Plateau uplift forcing". In: *Science in China, Series D: Earth Sciences* 42.3, pp. 258–271. DOI: 10.1007/BF02878963.

An, Z. et al. (2001). "Evolution of Asian monsoons and phased uplift of the Himalaya - Tibetan plateau since Late Miocene times". In: *Nature* 411.6833, pp. 62–66. DOI: 10.1038/35075035.

An, Z. et al. (2015). "Global Monsoon Dynamics and Climate Change". In: *Annual Review of Earth and Planetary Sciences* 43.1, pp. 29–77. DOI: 10.1146/annurev-earth-060313-054623.

An, Z. (Ed.) (2014). *Late Cenozoic climate change in Asia: loess, monsoon and monsoon-arid environment evolution*. Vol. 16. Springer Netherlands. DOI: 10.1007/978-94-007-7817-7.

Anagnostou, E. et al. (2016). "Changing atmospheric CO2 concentration was the primary driver of early Cenozoic climate". In: *Nature* 533.7603, pp. 380–384. DOI: 10.1038/nature17423.

Ao, H. et al. (2016). "Late Miocene-Pliocene Asian monsoon intensification linked to Antarctic ice-sheet growth". In: *Earth and Planetary Science Letters* 444, pp. 75–87. DOI: 10.1016/j.epsl.2016.03.028.

Assallay, AM et al. (1998). "Silt: 2–62 μm, 9–4φ". In: *Earth-Science Reviews* 45.1-2, pp. 61–88. DOI: 10.1016/S0012-8252(98)00035-X.

Ballouard, C. et al. (2015). "Tectonic record, magmatic history and hydrothermal alteration in the Hercynian Guérande leucogranite, Armorican Massif, France". In: *Lithos* 220-223, pp. 1–22. DOI: 10.1016/j.lithos.2015.01.027.

Begét, J. E. et al. (1993). "Mineral particles from Asia found in volcanic loess on the island of Hawaii". In: *Sedimentary Geology* 84.1-4, pp. 189–197. DOI: 10.1016/0037-0738(93)90055-A.

Bellosi, E. S. (2010). "Physical stratigraphy of the Sarmiento formation (middle Eocene-lower Miocene) at Gran Barranca, central Patagonia". In: *Madden, R., et al., eds., The paleontology of Gran Barranca: evolution and environmental change through the middle Cenozoic of Patagonia: Cambridge University Press, New York* June, pp. 19–31.

Bijl, P. K. et al. (2013). "Eocene cooling linked to early flow across the Tasmanian Gateway". In: *Proceedings of the National Academy of Sciences of the United States of America* 110.24, pp. 9645–9650. DOI: 10.1073/pnas.1220872110.

Bird, A. et al. (2015). "Quaternary dust source variation across the Chinese Loess Plateau". In: *Palaeogeography, Palaeoclimatology, Palaeoecology* 435, pp. 254–264. DOI: 10.1016/j.palaeo.2015.06.024.

Bird, A. et al. (2020). "A constant Chinese Loess Plateau dust source since the late Miocene". In: *Quaternary Science Reviews* 227, p. 106042. DOI: 10.1016/j.quascirev.2019.106042.

Blayney, T. et al. (2019). "Tectonic Evolution of the Pamir Recorded in the Western Tarim Basin (China): Sedimentologic and Magnetostratigraphic Analyses of the Aertashi Section". In: *Tectonics* 38.2, pp. 492–515. DOI: 10.1029/2018TC005146.

Bloemendal, J. et al. (1995). "Correlation of the magnetic susceptibility stratigraphy of Chinese loess and the marine oxygen isotope record: chronological and palaeoclimatic implications". In: *Earth and Planetary Science Letters* 131.3-4, pp. 371–380. DOI: 10.1016/0012-821X(95)00016-6.

Blott, S. J. and K. Pye (2001). "Gradistat: A grain size distribution and statistics package for the analysis of unconsolidated sediments". In: *Earth Surface Processes and Landforms* 26.11, pp. 1237–1248. DOI: 10.1002/esp.261.

Boos, W. R. and Z. Kuang (2010). "Dominant control of the South Asian monsoon by orographic insulation versus plateau heating". In: *Nature* 463.7278, pp. 218–222. DOI: 10.1038/nature08707.

Borradaile, G. J. and B. Henry (1997). "Tectonic applications of magnetic susceptibility and its anisotropy". In: *Earth-Science Reviews* 42.1-2, pp. 49–93. DOI: 10.1016/S0012-8252(96)00044-X.

Bosboom, R. et al. (2011). "Late Eocene sea retreat from the Tarim Basin (west China) and concomitant Asian paleoenvironmental change". In: *Palaeogeography, Palaeoclimatology, Palaeoecology* 299.3-4, pp. 385–398. DOI: 10.1016/j.palaeo.2010.11.019.

Bosboom, R. et al. (2014a). "Aridification in continental Asia after the Middle Eocene Climatic Optimum (MECO)". In: *Earth and Planetary Science Letters* 389, pp. 34–42. DOI: 10.1016/j.epsl.2013.12.014.

Bosboom, R. et al. (2014b). "Linking Tarim Basin sea retreat (west China) and Asian aridification in the late Eocene". In: *Basin Research* 26.5, pp. 621–640. DOI: 10.1111/bre.12054.

Bosboom, R. et al. (2014c). "Timing, cause and impact of the late Eocene stepwise sea retreat from the Tarim Basin (west China)". In: *Palaeogeography, Palaeoclimatology, Palaeoecology* 403, pp. 101–118. DOI: 10.1016/j.palaeo.2014.03.035.

Bosboom, R. et al. (2017). "Late Eocene palaeogeography of the proto-Paratethys Sea in Central Asia (NW China, southern Kyrgyzstan and SW Tajikistan)". In: *Geological Society Special Publication* 427.1, pp. 565–588. DOI: 10.1144/SP427.11.

Bosmans, J. H. C. et al. (2018). "Response of the Asian summer monsoons to idealized precession and obliquity forcing in a set of GCMs". In: *Quaternary Science Reviews* 188, pp. 121–135. DOI: 10.1016/j.quascirev.2018.03.025.

Botsyun, S. et al. (2019). "Revised paleoaltimetry data show low Tibetan Plateau elevation during the Eocene". In: *Science* 363.6430. DOI: 10.1126/science.aaq1436.

Bougeois, L. et al. (2014). "A high resolution study of trace elements and stable isotopes in oyster shells to estimate central asian middle eocene seasonality". In: *Chemical Geology* 363, pp. 200–212. DOI: 10.1016/j.chemgeo.2013.10.037.

Bougeois, L. et al. (2018). "Asian monsoons and aridification response to Paleogene sea retreat and Neogene westerly shielding indicated by seasonality in Paratethys oysters". In: *Earth and Planetary Science Letters* 485, pp. 99–110. DOI: 10.1016/j.epsl.2017.12.036.

Bouligand, C. et al. (2006). "Geomagnetic field variations between chrons 33r and 19r (83-41 Ma) from sea-surface magnetic anomaly profiles". In: *Earth and Planetary Science Letters* 250.3-4, pp. 541–560. DOI: 10.1016/j.epsl.2006.06.051.

Bronger, A. and T. Heinkele (1989). "Micromorphology and genesis of paleosols in the Luochuan loess section, China: Pedostratigraphic and environmental implications". In: *Geoderma* 45.2, pp. 123–143. DOI: 10.1016/0016-7061(89)90046-3.

Brune, S. et al. (2017). "Potential links between continental rifting, CO2 degassing and climate change through time". In: *Nature Geoscience* 10.12, pp. 941–946. DOI: 10.1038/s41561-017-0003-6.

Bureau of Geological and Mineral Resources of Qinghai Province (BGMRQP) (1965). *Regional geological survey reports of Ledu sheet (1:200000), Qinghai Province, P.R. China (in Chinese)*. Geological Publishing House Beijing.

Burke, K. D. et al. (2018). "Pliocene and Eocene provide best analogs for near-future climates". In: *Proceedings of the National Academy of Sciences of the United States of America* 115.52, pp. 13288–13293. DOI: 10.1073/pnas.1809600115.

Carrapa, B. et al. (2015). "Tectono-climatic implications of Eocene Paratethys regression in the Tajik basin of central Asia". In: *Earth and Planetary Science Letters* 424, pp. 168–178. DOI: 10.1016/j.epsl.2015.05.034.

Carroll, A. R. and K. M. Bohacs (1999). "Stratigraphic classification of ancient lakes: Balancing tectonic and climatic controls". In: *Geology* 27.2, pp. 99–102. DOI: 10.1130/0091-7613(1999)027<0099:SCOALB>2.3.CO;2.

Carroll, A. R. et al. (2010). "Walled sedimentary basins of China". In: *Basin Research* 22.1, pp. 17–32. DOI: 10.1111/j.1365-2117.2009.00458.x.

Carter, A. et al. (2017). "Widespread Antarctic glaciation during the Late Eocene". In: *Earth and Planetary Science Letters* 458, pp. 49–57. DOI: 10.1016/j.epsl.2016.10.045.

Caves, J. K. et al. (2015). "Role of the westerlies in Central Asia climate over the Cenozoic". In: *Earth and Planetary Science Letters* 428.August, pp. 33–43. DOI: 10.1016/j.epsl.2015.07.023.

Caves, J. K. et al. (2016). "Cenozoic carbon cycle imbalances and a variable weathering feedback". In: *Earth and Planetary Science Letters* 450, pp. 152–163. DOI: 10.1016/j.epsl.2016.06.035.

Caves Rugenstein, J. K. and C. P. Chamberlain (2018). "The evolution of hydroclimate in Asia over the Cenozoic: A stable-isotope perspective". In: *Earth-Science Reviews* 185.September, pp. 1129–1156. DOI: 10.1016/j.earscirev.2018.09.003.

Cerling, T. E. (1984). "The stable isotopic composition of modern soil carbonate and its relationship to climate". In: *Earth and Planetary science letters* 71.2, pp. 229–240. DOI: 10.1016/0012-821X(84)90089-X.

Chang, C.-P. et al. (2006). "The Asian winter monsoon". In: *The Asian Monsoon*. Springer, pp. 89–127. DOI: 10.1007/3-540-37722-0_3.

Chapman, J. B. and P. Kapp (2017). "Tibetan Magmatism Database". In: *Geochemistry, Geophysics, Geosystems* 18.11, pp. 4229–4234. DOI: 10.1002/2017GC007217.

Chapman, J. B. et al. (2019). "The Tajik Basin: A composite record of sedimentary basin evolution in response to tectonics in the Pamir". In: *Basin Research* September 2018, pp. 1–21. DOI: 10.1111/bre.12381.

Chen, J. et al. (2019). "Sedimentary dynamics and climatic implications of Cretaceous loess-like red beds in the Lanzhou basin, Northwest China". In: *Journal of Asian Earth Sciences* 180.October 2017, p. 103865. DOI: 10.1016/j.jseaes.2019.05.010.

Chen, T. et al. (2010). "Characteristics and formation mechanism of pedogenic hematite in Quaternary Chinese loess and paleosols". In: *Catena* 81.3, pp. 217–225. DOI: 10.1016/j.catena.2010.04.001.

Cheng, F. et al. (2018). "Geochemical and detrital zircon U-Pb geochronological constraints on provenance of the Xiaomei red earth sediments (Bose Basin, Guangxi Province, southern China)". In: *Palaeogeography, Palaeoclimatology, Palaeoecology* 510, pp. 49–62. DOI: 10.1016/j.palaeo.2017.08.040.

Chiang, J. C.H. et al. (2015). "Role of seasonal transitions and westerly jets in East Asian paleoclimate". In: *Quaternary Science Reviews* 108, pp. 111–129. DOI: 10.1016/j.quascirev.2014.11.009.

Chou, C. et al. (2009). "Evaluating the "rich-get-richer" mechanism in tropical precipitation change under global warming". In: *Journal of Climate* 22.8, pp. 1982–2005. DOI: 10.1175/2008JCLI2471.1.

Clark, M. K. et al. (2010). "Early Cenozoic faulting of the northern Tibetan Plateau margin from apatite (U-Th)/He ages". In: *Earth and Planetary Science Letters* 296.1-2, pp. 78–88. DOI: 10.1016/j.epsl.2010.04.051.

Cong, F. et al. (in preparation). "A thermal pulse induced by a Permian mantle plume in the Tarim Basin, Southwest China: Constraints from clumped isotope thermometry and in-situ calcite U-Pb dating". In: *Geochimica and Cosmochimica Acta*.

Costa, P. J.M. et al. (2013). "Aeolian microtextures in silica spheres induced in a wind tunnel experiment: Comparison with aeolian quartz". In: *Geomorphology* 180-181, pp. 120–129. DOI: 10.1016/j.geomorph.2012.09.011.

Coxall, H. K. et al. (2005). "Rapid stepwise onset of Antarctic glaciation and deeper calcite compensation in the Pacific Ocean". In: *Nature* 433.7021, pp. 53–57. DOI: 10.1038/nature03135.

Cramer, B. S. et al. (2003). "Orbital climate forcing of δ13C excursions in the late Paleocene-early Eocene (chrons C24n-C25n)". In: *Paleoceanography* 18.4, pp. 1–25. DOI: 10.1029/2003PA000909.

Cramer, B. S. et al. (2009). "Ocean overturning since the late cretaceous: Inferences from a new benthic foraminiferal isotope compilation". In: *Paleoceanography* 24.4, pp. 1–14. DOI: 10.1029/2008PA001683.

Cramwinckel, M. J. et al. (2018). "Synchronous tropical and polar temperature evolution in the Eocene letter". In: *Nature* 559.7714, pp. 382–386. DOI: 10.1038/s41586-018-0272-2.

Crouvi, O. et al. (2010). "Active sand seas and the formation of desert loess". In: *Quaternary Science Reviews* 29.17-18, pp. 2087–2098. DOI: 10.1016/j.quascirev.2010.04.026.

Dai, S. et al. (2006). "Magnetostratigraphy of Cenozoic sediments from the Xining Basin: Tectonic implications for the northeastern Tibetan Plateau". In: *Journal of Geophysical Research: Solid Earth* 111.11, pp. 1–19. DOI: 10.1029/2005JB004187.

DeConto, R. M. and D. Pollard (2003). "Rapid Cenozoic glaciation of Antarctica induced by declining atmospheric CO2". In: *Nature* 421.6920, pp. 245–249. DOI: 10.1038/nature01290.

Derbyshire, E. et al. (1998). "Provenance, transport and characteristics of modern aeolian dust in western Gansu Province, China, and interpretation of the Quaternary loess record". In: *Journal of Arid Environments* 39.3, pp. 497–516. DOI: 10.1006/jare.1997.0369.

Dickens, G. R. (2001). "Carbon addition and removal during the late Palaeocene thermal maximum: Basic theory with a preliminary treatment of the isotopic record at ODP Site 1051, Blake Nose". In: *Geological Society Special Publication* 183, pp. 293–305. DOI: 10.1144/GSL.SP.2001.183.01.14.

Dietze, E. and M. Dietze (2019). "Grain-size distribution unmixing using the R package EMMAgeo". In: *E&G Quaternary Science Journal* 68.1, pp. 29–46. DOI: 10.5194/egqsj-68-29-2019.

Dietze, E. et al. (2014). "Sediment transport processes across the Tibetan Plateau inferred from robust grain-size end members in lake sediments". In: *Climate of the Past* 10.1, pp. 91–106. DOI: 10.5194/cp-10-91-2014.

Ding, Z. L. et al. (1994). "Towards an orbital time scale for Chinese loess deposits". In: *Quaternary Science Reviews* 13.1, pp. 39–70. DOI: 10.1016/0277-3791(94)90124-4.

Ding, Z. L. et al. (1995). "Ice-volume forcing of east asian winter monsoon variations in the past 800,000 years". In: *Quaternary Research* 44.2, pp. 149–159. DOI: 10.1006/qres.1995.1059.

Ding, Z. L. et al. (1997). "The Onset of Extensive Loess Deposition Around the G/M Boundary in China and Its Palaeoclimatic Implications". In: *Quaternary International* 40.1, pp. 53–60. DOI: 10.1016/s1040-6182(96)00061-4.

Ding, Z. L. et al. (1998a). "Preliminary magnetostratigraphy of a thick eolian red clay-loess sequence at Lingtai, the Chinese Loess Plateau". In: *Geophysical Research Letters* 25.8, pp. 1225–1228. DOI: 10.1029/98GL00836.

Ding, Z. L. et al. (1998b). "Wind-blown origin of the Pliocene red clay formation in the central Loess Plateau, China". In: *Earth and Planetary Science Letters* 161.1-4, pp. 135–143. DOI: 10.1016/S0012-821X(98)00145-9.

Ding, Z. L. et al. (1999a). "Changes in sand content of loess deposits along a north–south transect of the Chinese Loess Plateau and the implications for desert variations". In: *Quaternary Research* 52.1, pp. 56–62. DOI: 10.1006/qres.1999.2045.

Ding, Z. L. et al. (1999b). "Pedostratigraphy and paleomagnetism of a ˜7.0 Ma eolian loess-red clay sequence at Lingtai, Loess Plateau, north-central China and the implications for paleomonsoon evolution". In: *Palaeogeography, Palaeoclimatology, Palaeoecology* 152.1-2, pp. 49–66. DOI: 10.1016/S0031-0182(99)00034-6.

Ding, Z. L. et al. (2000). "Re-arrangement of atmospheric circulation at about 2.6 Ma over northern China: Evidence from grain size records of loess-palaeosol and red clay sequences". In: *Quaternary Science Reviews* 19.6, pp. 547–558. DOI: 10.1016/S0277-3791(99)00017-7.

Ding, Z. L. et al. (2001). "Magnetostratigraphy and sedimentology of the Jingchuan red clay section and correlation of the Tertiary eolian red clay sediments of the Chinese Loess Plateau". In: *Journal of Geophysical Research: Solid Earth* 106.B4, pp. 6399–6407. DOI: 10.1029/2000jb900445.

Ding, Z. L. et al. (2002). " Stacked 2.6-Ma grain size record from the Chinese loess based on five sections and correlation with the deep-sea δ 18 O record ". In: *Paleoceanography* 17.3, pp. 5–1–5–21. DOI: 10.1029/2001pa000725.

Ding, Z. L. et al. (2005). "Stepwise expansion of desert environment across northern China in the past 3.5 Ma and implications for monsoon evolution". In: *Earth and Planetary Science Letters* 237.1-2, pp. 45–55. DOI: 10.1016/j.epsl.2005.06.036.

D'Odorico, P. et al. (2013). "Global desertification: Drivers and feedbacks". In: *Advances in Water Resources* 51, pp. 326–344. DOI: 10.1016/j.advwatres.2012.01.013.

Donselaar, M. E. et al. (2013). "Avulsion processes at the terminus of low-gradient semi-arid fluvial systems: Lessons from the Río Colorado, Altiplano endorheic basin, Bolivia". In: *Sedimentary Geology* 283, pp. 1–14. DOI: 10.1016/j.sedgeo.2012.10.007.

Drost, K. et al. (2018). "An Image Mapping Approach to U-Pb LA-ICP-MS Carbonate Dating and Applications to Direct Dating of Carbonate Sedimentation". In: *Geochemistry, Geophysics, Geosystems* 19.12, pp. 4631–4648. DOI: 10.1029/2018GC007850.

Dupont-Nivet, G. et al. (2004). "Paleogene clockwise tectonic rotation of the Xining-Lanzhou region, northeastern Tibetan Plateau". In: *Journal of Geophysical Research: Solid Earth* 109.4, pp. 1–13. DOI: 10.1029/2003JB002620.

Dupont-Nivet, G. et al. (2007). "Tibetan plateau aridification linked to global cooling at the Eocene-Oligocene transition". In: *Nature* 445.7128, pp. 635–638. DOI: 10.1038/nature05516.

Dupont-Nivet, G. et al. (2008a). "Tibetan uplift prior to the Eocene-Oligocene climate transition: Evidence from pollen analysis of the Xining Basin". In: *Geology* 36.12, pp. 987–990. DOI: 10.1130/G25063A.1.

Dupont-Nivet, G. et al. (2008b). "Timing and distribution of tectonic rotations in the northeastern Tibetan Plateau". In: *Special Paper of the Geological Society of America* 444.05, pp. 73–87. DOI: 10.1130/2008.2444(05).

Durand, M. and S. Bourquin (2013). "Criteria for the identification of ventifacts in the geological record: A review and new insights". In: *Comptes Rendus - Geoscience* 345.3, pp. 111–125. DOI: 10.1016/j.crte.2013.02.004.

Duvall, A. R. et al. (2011). "Direct dating of Eocene reverse faulting in northeastern Tibet using Ar-dating of fault clays and low-temperature thermochronometry". In: *Earth and Planetary Science Letters* 304.3-4, pp. 520–526. DOI: 10.1016/j.epsl.2011.02.028.

Edwards, M. B. (1979). "Late Precambrian Glacial Loessites from North Norway and Svalbard". In: *SEPM Journal of Sedimentary Research* Vol. 49.1, pp. 85–91. DOI: 10.1306/212f76c6-2b24-11d7-8648000102c1865d.

Elsworth, G. et al. (2017). "Enhanced weathering and CO 2 drawdown caused by latest Eocene strengthening of the Atlantic meridional overturning circulation". In: *Nature Geoscience* 10.3, pp. 213–216. DOI: 10.1038/ngeo2888.

Evans, M. E. et al. (1991). "Preliminary magnetostratigraphy of the red clay underlying the loess sequence at Baoji, China". In: *Geophysical Research Letters* 18.8, pp. 1409–1412. DOI: 10.1029/91GL01800.

Fan, L. G. et al. (2019). "Paleogene crustal extension in the eastern segment of the NE Tibetan plateau". In: *Earth and Planetary Science Letters* 514, pp. 62–74. DOI: 10.1016/j.epsl.2019.02.036.

Fan, M. et al. (2018). "Terrestrial cooling and changes in hydroclimate in the continental interior of the United States across the Eocene-Oligocene boundary". In: *Bulletin of the Geological Society of America* 130.7-8, pp. 1073–1084. DOI: 10.1130/B31732.1.

Fan, M. et al. (2020). "Late Paleogene emergence of a North American loess plateau". In: *Geology* 48.3, pp. 273–277. DOI: 10.1130/G47102.1.

Fang, X. et al. (2003). "Flexural subsidence by 29 Ma on the NE edge of Tibet from the magnetostratigraphy of Linxia Basin, China". In: *Earth and Planetary Science Letters* 210.3-4, pp. 545–560. DOI: 10.1016/S0012-821X(03)00142-0.

Fang, X. et al. (2015). "An Eocene-Miocene continuous rock magnetic record from the sediments in the Xining Basin, NW China: Indication for Cenozoic persistent drying driven by global cooling and Tibetan Plateau uplift". In: *Geophysical Journal International* 201.1, pp. 78–89. DOI: 10.1093/gji/ggv002.

Fang, X. et al. (2016). "Tectonosedimentary evolution model of an intracontinental flexural (foreland) basin for paleoclimatic research". In: *Global and Planetary Change* 145, pp. 78–97. DOI: 10.1016/j.gloplacha.2016.08.015.

Fang, X. et al. (2019a). "Cenozoic magnetostratigraphy of the Xining Basin, NE Tibetan Plateau, and its constraints on paleontological, sedimentological and tectonomorphological evolution". In: *Earth-Science Reviews* 190, pp. 460–485. DOI: 10.1016/j.earscirev.2019.01.021.

Fang, X. et al. (2019b). "Paleogene global cooling-induced temperature feedback on chemical weathering, as recorded in the northern Tibetan Plateau". In: *Geology* 47.10, pp. 992–996. DOI: 10.1130/G46422.1.

Farnsworth, A. et al. (2019). "Past East Asian monsoon evolution controlled by paleogeography, not CO2". In: *Science Advances* 5.10. DOI: 10.1126/sciadv.aax1697.

Favre, A. et al. (2015). "The role of the uplift of the Qinghai-Tibetan Plateau for the evolution of Tibetan biotas". In: *Biological reviews of the Cambridge Philosophical Society* 90.1, pp. 236–253. DOI: 10.1111/brv.12107.

Fisher, R. A. (1953). "Dispersion on a sphere". In: *Proceedings of the Royal Society of London. Series A. Mathematical and Physical Sciences* 217.1130, pp. 295–305. DOI: 10.1098/rspa.1953.0064.

Fluteau, F. et al. (1999). "Simulating the evolution of the Asian and African monsoons during the past 30 Myr using an atmospheric general circulation model". In: *Journal of Geophysical Research Atmospheres* 104.D10, pp. 11995–12018. DOI: 10.1029/1999JD900048.

Flynn, L. J. et al. (2011). "Observations on the Hipparion red clays of the Loess Plateau". In: *Vertebrata PalAsiatica* 49.July, pp. 275–284.

France-Lanord, C. and L. A. Derry (1997). "Organic carbon burial forcing of the carbon cycle from Himalayan erosion". In: *Nature* 390.6655, pp. 65–67. DOI: 10.1038/36324.

Gadgil, S. (2018). "The monsoon system: Land–sea breeze or the ITCZ?" In: *Journal of Earth System Science* 127.1, pp. 1–29. DOI: 10.1007/s12040-017-0916-x.

Gallet, S. et al. (1998). "Loess geochemistry and its implications for particle origin and composition of the upper continental crust". In: *Earth and Planetary Science Letters* 156.3-4, pp. 157–172. DOI: 10.1016/s0012-821x(97)00218-5.

Garzione, C. N. et al. (2005). "Source of Oligocene to Pliocene sedimentary rocks in the Linxia basin in northeastern Tibet from Nd isotopes: Implications for tectonic forcing of climate". In: *Bulletin of the Geological Society of America* 117.9-10, pp. 1156–1166. DOI: 10.1130/B25743.1.

Goossens, D. (2008). "Techniques to measure grain-size distributions of loamy sediments: A comparative study of ten instruments for wet analysis". In: *Sedimentology* 55.1, pp. 65–96. DOI: 10.1111/j.1365-3091.2007.00893.x.

Gradstein, F. M. et al. (2012). *The geologic time scale 2012*. Elsevier. DOI: 10.1016/C2011-1-08249-8.

Grise, K. M. and L. M. Polvani (2014). "Is climate sensitivity related to dynamical sensitivity? A Southern Hemisphere perspective". In: *Geophysical Research Letters* 41.2, pp. 534–540. DOI: 10.1002/2013GL058466.

Gulick, S. P.S. et al. (2017). "Initiation and long-term instability of the East Antarctic Ice Sheet". In: *Nature* 552.7684, pp. 225–229. DOI: 10.1038/nature25026.

Guo, B. et al. (2020). "Magnetostratigraphy and Palaeoclimatic Significance of the Late Pliocene Red Clay-Quaternary Loess Sequence in the Lanzhou Basin, Western Chinese Loess Plateau". In: *Geophysical Research Letters* 47.3, pp. 1–10. DOI: 10.1029/2019GL086556.

Guo, Z. T. et al. (2001). "Origin of the miocene - Pliocene Red-Earth formation at Xifeng in northern China and implications for paleoenvironments". In: *Palaeogeography, Palaeoclimatology, Palaeoecology* 170.1-2, pp. 11–26. DOI: 10.1016/S0031-0182(01)00235-8.

Guo, Z. T. et al. (2002). "Onset of Asian desertification by 22 Myr ago inferred from loess deposits in China". In: *Nature* 416.6877, pp. 159–163. DOI: 10.1038/416159a.

Guo, Z. T. et al. (2004). "Late Miocene-Pliocene development of Asian aridification as recorded in the Red-Earth Formation in northern China". In: *Global and Planetary Change* 41.3-4, pp. 135–145. DOI: 10.1016/j.gloplacha.2004.01.002.

Guo, Z. T. et al. (2008). "A major reorganization of Asian climate by the early Miocene". In: *Climate of the Past* 4.3, pp. 153–174. DOI: 10.5194/cp-4-153-2008.

Guo, Z. T. et al. (2010). "Comment on "Mudflat/distal fan and shallow lake sedimentation (upper Vallesian–Turolian) in the Tianshui Basin, Central China: Evidence against the late Miocene eolian loess" by A. M. Alonso-Zarza, Z. Zhao, C. H. Song, J. J. Li, J. Zhang, A. Martín-Pérez, R. Martín-García, X. X. Wang, Y. Zhang and M. H. Zhang [Sedimentary Geology 222 (2009) 42–51]". In: *Sedimentary Geology* 230.1-2, pp. 86–89. DOI: 10.1016/j.sedgeo.2010.06.019.

Hajek, E. A. and K. M. Straub (2017). "Autogenic Sedimentation in Clastic Stratigraphy". In: *Annual Review of Earth and Planetary Sciences* 45.1, pp. 681–709. DOI: 10.1146/annurev-earth-063016-015935.

Halley, E. (1686). "An historical account of the trade winds, and monsoons, observable in the seas between and near the Tropicks, with an attempt to assign the physical cause of the said winds". In: *Philosophical Transactions of the Royal Society of London* 16.183, pp. 153–168. DOI: 10.1098/rstl.1686.0026.

Hammer, Ø. et al. (2001). "PAST: Paleontological statistics software package for education and data analysis". In: *Palaeontologia electronica* 4.1, p. 9.

Han, J. et al. (2002). "Assessment of the palaeoclimate during 3.0-2.6 Ma registered by transition of Red Clay to loess-palaeosol sequence in central North China". In: *Palaeogeography, Palaeoclimatology, Palaeoecology* 185.3-4, pp. 355–368. DOI: 10.1016/S0031-0182(02)00382-6.

Hao, Q. and Z. Guo (2004). "Magnetostratigraphy of a Late Miocene-Pliocene loess-soil sequence in the western Loess Plateau in China". In: *Geophysical Research Letters* 31.9, pp. 14–17. DOI: 10.1029/2003GL019392.

Hao, Q. et al. (2008). "The magnetic properties of loess and paleosol samples from the Chinese Loess Plateau spanning the last 22 million years". In: *Palaeogeography, Palaeoclimatology, Palaeoecology* 260.3-4, pp. 389–404. DOI: 10.1016/j.palaeo.2007.11.010.

Hardie, Lawrence A et al. (1978). "Saline lakes and their deposits: a sedimentological approach". In: *Modern and ancient lake sediments*. Vol. 2. Blackwell Oxford, pp. 7–41. DOI: 10.1002/9781444303698.ch2.

Hasegawa, H. et al. (2012). "Drastic shrinking of the Hadley circulation during the mid-Cretaceous Supergreenhouse". In: *Climate of the Past* 8.4, pp. 1323–1337. DOI: 10.5194/cp-8-1323-2012.

Hays, J. D. et al. (1976). "Variations in the earth's orbit: Pacemaker of the ice ages". In: *Science* 194.4270, pp. 1121–1132. DOI: 10.1126/science.194.4270.1121.

He, P. et al. (2018). "Cenozoic deformation history of the Qilian Shan (northeastern Tibetan Plateau) constrained by detrital apatite fission-track thermochronology in the northeastern Qaidam Basin". In: *Tectonophysics* 749, pp. 1–11. DOI: 10.1016/j.tecto.2018.10.017.

Heavens, N. G. et al. (2012). "A paleogeographic approach to aerosol prescription in simulations of deep time climate". In: *Journal of Advances in Modeling Earth Systems* 4.11, pp. 1–13. DOI: 10.1029/2012MS000166.

Heermance, R. V. et al. (2018). "Erg deposition and development of the ancestral Taklimakan Desert (western China) between 12.2 and 7.0 Ma". In: *Geology* 46.10, pp. 919–922. DOI: 10.1130/G45085.1.

Held, I. M. and B. J. Soden (2006). "Robust responses of the hydrological cycle to global warming". In: *Journal of climate* 19.21, pp. 5686–5699. DOI: 10.1175/JCLI3990.1.

Heller, F. and T Liu (1984). "Magnetism of Chinese loess deposits". In: *Geophysical Journal International* 77.1, pp. 125–141. DOI: 10.1111/j.1365-246X.1984.tb01928.x.

Henehan, M. J. et al. (2020). " Revisiting the Middle Eocene Climatic Optimum 'Carbon Cycle Conundrum' with new estimates of atmospheric pCO 2 from boron isotopes ". In: *Paleoceanography and Paleoclimatology* 35.6. DOI: 10.1029/2019pa003713.

Herman, A. B. et al. (2017). "Eocene–early Oligocene climate and vegetation change in southern China: Evidence from the Maoming Basin". In: *Palaeogeography, Palaeoclimatology, Palaeoecology* 479, pp. 126–137. DOI: 10.1016/j.palaeo.2017.04.023.

Hollis, C. J. et al. (2019). "The DeepMIP contribution to PMIP4: Methodologies for selection, compilation and analysis of latest Paleocene and early Eocene climate proxy data, incorporating version 0.1 of the DeepMIP database". In: *Geoscientific Model Development* 12.7, pp. 3149–3206. DOI: 10.5194/gmd-12-3149-2019.

Hoorn, C. et al. (2012). "A late Eocene palynological record of climate change and Tibetan Plateau uplift (Xining Basin, China)". In: *Palaeogeography, Palaeoclimatology, Palaeoecology* 344-345, pp. 16–38. DOI: 10.1016/j.palaeo.2012.05.011.

Horowitz, A. (1992). *Palynology of Arid Lands*. Elsevier, p. 546.

Horton, B. K. et al. (2004). "Mesozoic-Cenozoic evolution of the Xining-Minhe and Dangchang basins, northeastern Tibetan Plateau: Magnetostratigraphic and biostratigraphic results". In: *Journal of Geophysical Research: Solid Earth* 109.B4, pp. 1–15. DOI: 10.1029/2003jb002913.

Horton, T. W. et al. (2016). "Evaporation induced $\delta^{18}O$ and $\delta^{13}C$ enrichment in lake systems: a global perspective on hydrologic balance effects". In: *Quaternary Science Reviews* 131, pp. 365–379. DOI: 10.1016/j.quascirev.2015.06.030.

Hough, B. G. et al. (2014). "Timing and spatial patterns of basin segmentation and climate change in northeastern Tibet". In: *Special Paper of the Geological Society of America* 507.07, pp. 129–153. DOI: 10.1130/2014.2507(07).

Huang, C. and L. Hinnov (2019). "Astronomically forced climate evolution in a saline lake record of the middle Eocene to Oligocene, Jianghan Basin, China". In: *Earth and Planetary Science Letters* 528, p. 115846. DOI: 10.1016/j.epsl.2019.115846.

Huber, M. and A. Goldner (2012). "Eocene monsoons". In: *Journal of Asian Earth Sciences* 44, pp. 3–23. DOI: 10.1016/j.jseaes.2011.09.014.

Hunter, R. E. (1977). "Basic types of stratification in small eolian dunes". In: *Sedimentology* 24.3, pp. 361–387. DOI: 10.1111/j.1365-3091.1977.tb00128.x.

Hyland, E. G. and N. D. Sheldon (2013). "Coupled CO2-climate response during the Early Eocene Climatic Optimum". In: *Palaeogeography, Palaeoclimatology, Palaeoecology* 369, pp. 125–135. DOI: 10.1016/j.palaeo.2012.10.011.

Hyland, E. G. et al. (2017). "Constraining the early Eocene climatic optimum: A terrestrial interhemispheric comparison". In: *Bulletin of the Geological Society of America* 129.1-2, pp. 244–252. DOI: 10.1130/B31493.1.

Jackson, S. E. et al. (2004). "The application of laser ablation-inductively coupled plasma-mass spectrometry to in situ U–Pb zircon geochronology". In: *Chemical Geology* 211, pp. 47–69. DOI: 10.1016/j.chemgeo.2004.06.017.

Janecek, T. R. and D. K. Rea (1983). "Eolian deposition in the northeast Pacific Ocean: Cenozoic history of atmospheric circulation." In: *Geological Society of America Bulletin* 94.6, pp. 730–738. DOI: 10.1130/0016-7606(1983)94<730:EDITNP>2.0.CO;2.

Jansonius, J. and L. V. Hills (1976). "Genera file of fossil spores and pollen. Supplement". In: *Special Publication, Department of Geology, University of Calgary, Canada*.

Jefferson, I. et al. (2002). "Mercia Mudstone as a Triassic aeolian desert sediment". In: *Mercian Geologist* 15.3, pp. 157–162.

Jeong, G. Y. et al. (2011). "Changes in mineralogy of loess-paleosol sections across the Chinese Loess Plateau". In: *Quaternary Research* 75.1, pp. 245–255. DOI: 10.1016/j.yqres.2010.09.001.

Jiang, H. and Z. Ding (2010). "Eolian grain-size signature of the Sikouzi lacustrine sediments (Chinese Loess Plateau): Implications for Neogene evolution of the East Asian winter monsoon". In: *Bulletin of the Geological Society of America* 122.5-6, pp. 843–854. DOI: 10.1130/B26583.1.

Jickells, T. D. et al. (2005). "Global iron connections between desert dust, ocean biogeochemistry, and climate". In: *Science* 308.5718, pp. 67–71. DOI: 10.1126/science.1105959.

Johnson, S. Y. (1989). "Significance of loessite in the Maroon Formation (Middle Pennsylvanian to Lower Permian), Eagle Basin, northwest Colorado". In: *Journal of Sedimentary Petrology* 59.5, pp. 782–791. DOI: 10.1306/212F9070-2B24-11D7-8648000102C1865D.

Kaakinen, A. and J. P. Lunkka (2003). "Sedimentation of the Late Miocene Bahe Formation and its implications for stable environments adjacent to Qinling mountains in Shaanxi, China". In: *Journal of Asian Earth Sciences* 22.1, pp. 67–78. DOI: 10.1016/S1367-9120(03)00044-0.

Kaakinen, A. et al. (2013). "Stratigraphy and paleoecology of the classical dragon bone localities of Baode County, Shanxi Province". In: *Fossil Mammals of Asia: Neogene Biostratigraphy and Chronology. Columbia University Press, New York*, pp. 203–217.

Kapp, P. and P. G. DeCelles (2019). "Mesozoic–Cenozoic geological evolution of the Himalayan-Tibetan orogen and working tectonic hypotheses". In: *American Journal of Science* 319.3, pp. 159–254. DOI: 10.2475/03.2019.01.

Kapp, P. et al. (2011). "Wind erosion in the Qaidam basin, central Asia: Implications for tectonics, paleoclimate, and the source of the Loess Plateau". In: *GSA Today* 21.4-5, pp. 4–10. DOI: 10.1130/GSATG99A.1.

Kapp, P. et al. (2015). "From dust to dust: Quaternary wind erosion of the Mu Us Desert and Loess Plateau, China". In: *Geology* 43.9, pp. 835–838. DOI: 10.1130/G36724.1.

Kaya, M. Y. et al. (2019). "Paleogene evolution and demise of the proto-Paratethys Sea in Central Asia (Tarim and Tajik basins): Role of intensified tectonic activity at ca. 41 Ma". In: *Basin Research* 31.3, pp. 461–486. DOI: 10.1111/bre.12330.

Kaya, M. Y. et al. (2020). "Cretaceous evolution of the Central Asian proto-Paratethys Sea: tectonic, eustatic and climatic controls". In: *Tectonics* 39.9. DOI: 10.1029/2019TC005983.

Keiser, L. J. et al. (2015). "Use of Quartz Microtextural Analysis To Assess Possible Proglacial Deposition For the Pennsylvanian–Permian Cutler Formation (Colorado, U.S.A.)" In: *Journal of Sedimentary Research* 85.11, pp. 1310–1322. DOI: 10.2110/jsr.2015.81.

Kennett, J. P. (1977). "Cenozoic evolution of Antarctic glaciation, the circum-Antarctic Ocean, and their impact on global paleoceanography". In: *Journal of geophysical research* 82.27, pp. 3843–3860. DOI: 10.1029/JC082i027p03843.

Kennett, J. P. and L. D. Stott (1991). "Abrupt deep-sea warming, palaeoceanographic changes and benthic extinctions at the end of the Palaeocene". In: *Nature* 353.6341, pp. 225–229. DOI: 10.1038/353225a0.

Kirschvink, J. L. (1980). "The least-squares line and plane and the analysis of palaeomagnetic data". In: *Geophysical Journal of the Royal Astronomical Society* 62.3, pp. 699–718. DOI: 10.1111/j.1365-246X.1980.tb02601.x.

Kirtland-Turner, S. et al. (2014). "Persistence of carbon release events through the peak of early Eocene global warmth". In: *Nature Geoscience* 7.10, pp. 748–751. DOI: 10.1038/NGEO2240.

Knippertz, P. and J.-B. W Stuut (2014). *Mineral dust*. Vol. 10. Springer, pp. 978–994. DOI: 10.1007/978-94-017-8978-3.

Kocken, I. J. et al. (2019). "The 405-kyr and 2.4-Myr eccentricity components in Cenozoic carbon isotope records". In: *Climate of the Past* 15.1, pp. 91–104. DOI: 10.5194/cp-15-91-2019.

Kohn, M. J. (2010). "Carbon isotope compositions of terrestrial C3 plants as indicators of (paleo)ecology and (paleo)climate". In: *Proceedings of the National Academy of Sciences of the United States of America* 107.46, pp. 19691–19695. DOI: 10.1073/pnas.1004933107.

Krinsley, D. H. and F. W. McCoy (1977). "Significance and origin of surface textures on broken sand grains in deep-sea sediments". In: *Sedimentology* 24.6, pp. 857–862. DOI: 10.1111/j.1365-3091.1977.tb01920.x.

Krinsley, D. H. and I. J. Smalley (1973). "Shape and Nature of Small Sedimentary Quartz Particles". In: *Science* 180.4092, pp. 1277–1279. DOI: 10.1126/science.180.4092.1277.

Krinsley, D. H. and T. Takahashi (1962). "Applications of electron microscopy to geology". In: *Transactions of the New York Academy of Sciences* 25.1 Series II, pp. 3–22. DOI: 10.1111/j.2164-0947.1962.tb03509.x.

Krinsley, D. H. and P. Trusty (1985). "Environmental Interpretation of Quartz Grain Surface Textures". In: *Provenance of Arenites*, pp. 213–229. DOI: 10.1007/978-94-017-2809-6_10.

Kukla, G. (1987). "Loess stratigraphy in central China". In: *Quaternary Science Reviews* 6.3-4, pp. 203–225. DOI: 10.1016/0277-3791(87)90004-7.

Kukla, G. et al. (1988). "Pleistocene climates in China dated by magnetic susceptibility". In: *Geology* 16.9, pp. 811–814. DOI: 10.1130/0091-7613(1988)016<0811:PCICDB>2.3.CO;2.

Ladant, J. B. et al. (2014). "The respective role of atmospheric carbon dioxide and orbital parameters on ice sheet evolution at the Eocene-Oligocene transition". In: *Paleoceanography* 29.8, pp. 810–823. DOI: 10.1002/2013PA002593.

Large, D. J. and C. Marshall (2015). "Use of carbon accumulation rates to estimate the duration of coal seams and the influence of atmospheric dust deposition on coal composition". In: *Geological Society Special Publication* 404, pp. 303–315. DOI: 10.1144/SP404.15.

Laskar, J. et al. (2011). "Milankovitch Orbital Data Viewer". In: *Astronomy Astrophysics* 89, pp. 1–15. DOI: 10.1051/0004-6361/201116836.

Lauretano, V. et al. (2018). "Orbitally Paced Carbon and Deep-Sea Temperature Changes at the Peak of the Early Eocene Climatic Optimum". In: *Paleoceanography and Paleoclimatology* 33.10, pp. 1050–1065. DOI: 10.1029/2018PA003422.

Le Maitre, R. W. et al. (1989). *Igneous rocks: a classification and glossary of terms: recommendations of the International Union of Geological Sciences Subcommission on the Systematics of Igneous Rocks*. Cambridge University Press.

Lease, R. O. (2014). "Cenozoic mountain building on the northeastern Tibetan Plateau". In: *Special Paper of the Geological Society of America* 507.06, pp. 115–127. DOI: 10.1130/2014.2507(06).

Lease, R. O. et al. (2011). "Middle Miocene reorganization of deformation along the northeastern Tibetan Plateau". In: *Geology* 39.4, pp. 359–362. DOI: 10.1130/G31356.1.

Lease, R. O. et al. (2012). "Pulsed Miocene range growth in northeastern Tibet: Insights from Xunhua Basin magnetostratigraphy and provenance". In: *Bulletin of the Geological Society of America* 124.5-6, pp. 657–677. DOI: 10.1130/B30524.1.

Lee, L. A. et al. (2016). "On the relationship between aerosol model uncertainty and radiative forcing uncertainty". In: *Proceedings of the National Academy of Sciences of the United States of America* 113.21, pp. 5820–5827. DOI: 10.1073/pnas.1507050113.

Li, F. et al. (2006a). "Wind-blown origin of Dongwan late Miocene-Pliocene dust sequence documented by land snail record in western Chinese Loess Plateau". In: *Geology* 34.5, pp. 405–408. DOI: 10.1130/G22232.1.

Li, J. et al. (2006b). "Miocene Bahean stratigraphy in the Longzhong Basin, northern central China and its implications in environmental change". In: *Science in China Series D: Earth Sciences* 49.12, pp. 1270–1279. DOI: 10.1007/s11430-006-2057-y.

Li, J. X. et al. (2018a). "Global cooling and enhanced Eocene Asian mid-latitude interior aridity". In: *Nature Communications* 9.1, pp. 1–32. DOI: 10.1038/s41467-018-05415-x.

Li, X. et al. (2018b). "Do climate simulations support the existence of East Asian monsoon climate in the Late Eocene?" In: *Palaeogeography, Palaeoclimatology, Palaeoecology* 509.December 2016, pp. 47–57. DOI: 10.1016/j.palaeo.2017.12.037.

– (2018c). "What enhanced the aridity in Eocene Asian inland: Global cooling or early Tibetan Plateau uplift?" In: *Palaeogeography, Palaeoclimatology, Palaeoecology* 510.November, pp. 6–14. DOI: 10.1016/j.palaeo.2017.10.029.

Li, Y. et al. (2020). "Loess genesis and worldwide distribution". In: *Earth-Science Reviews* 201.March, p. 102947. DOI: 10.1016/j.earscirev.2019.102947.

Licht, A. et al. (2014). "Asian monsoons in a late Eocene greenhouse world". In: *Nature* 513.7519, pp. 501–506. DOI: 10.1038/nature13704.

Licht, A. et al. (2016a). "Eolian cannibalism: Reworked loess and fluvial sediment as the main sources of the Chinese Loess Plateau". In: *Bulletin of the Geological Society of America* 128.5-6, pp. 944–956. DOI: 10.1130/B31375.1.

Licht, A. et al. (2016b). "Resilience of the Asian atmospheric circulation shown by Paleogene dust provenance". In: *Nature Communications* 7, pp. 1–6. DOI: 10.1038/ncomms12390.

Licht, A. et al. (2019). "Paleogene evolution of the Burmese forearc basin and implications for the history of India-Asia convergence". In: *Bulletin of the Geological Society of America* 131.5-6, pp. 730–748. DOI: 10.1130/B35002.1.

Licht, A. et al. (2020). "Synchronous cooling and decline in monsoonal rainfall in northeastern Tibet during the fall into the Oligocene icehouse". In: *Palaeogeography, Palaeoclimatology, Palaeoecology* 560. DOI: 10.1130/G45480.1.

Lisiecki, L. E. and M. E. Raymo (2005). "A Pliocene-Pleistocene stack of 57 globally distributed benthic δ18O records". In: *Paleoceanography* 20.1. DOI: 10.1029/2004PA001071.

Littler, K. et al. (2014). "A high-resolution benthic stable-isotope record for the South Atlantic: Implications for orbital-scale changes in Late Paleocene-Early Eocene climate and carbon cycling". In: *Earth and Planetary Science Letters* 401, pp. 18–30. DOI: 10.1016/j.epsl.2014.05.054.

Liu, J. et al. (2006). "Eolian origin of the Miocene loess-soil sequence at Qin'an, China: Evidence of quartz morphology and quartz grain-size". In: *Chinese Science Bulletin* 51.1, pp. 117–120. DOI: 10.1007/s11434-005-0811-8.

Liu, S. et al. (2013). "Timing of Xunhua and Guide basin development and growth of the northeastern Tibetan Plateau, China". In: *Basin Research* 25.1, pp. 74–96. DOI: 10.1111/j.1365-2117.2012.00548.x.

Liu, S. et al. (2019). "Reappraisal of Miocene eolian deposition in Tianshui Basin, China, based on an investigation of stratigraphy and provenance". In: *Bulletin of the Geological Society of America* 131.7-8, pp. 1312–1332. DOI: 10.1130/B32056.1.

Liu, S. F. et al. (2007). "Cenozoic basin development and its indication of plateau growth in the Xunhua-Guide district". In: *Science in China, Series D: Earth Sciences* 50.SUPPL. 2, pp. 277–291. DOI: 10.1007/s11430-007-6012-3.

Liu, T. and Z. Ding (1998). "Chinese Loess and the Paleomonsoon". In: *Annual Review of Earth and Planetary Sciences* 26.1, pp. 111–145. DOI: 10.1146/annurev.earth.26.1.111.

Liu, X. et al. (1988). "The Chinese loess in Xifeng, II. A study of anisotropy of magnetic susceptibility of loess from Xifeng". In: *Geophysical Journal* 92.2, pp. 349–353. DOI: 10.1111/j.1365-246X.1988.tb01147.x.

Liu, X. M. et al. (2003). "Paleoclimatic significance of magnetic properties on the Red Clay underlying the loess and paleosols in China". In: *Palaeogeography, Palaeoclimatology, Palaeoecology* 199.1-2, pp. 153–166. DOI: 10.1016/S0031-0182(03)00504-2.

Long, L. Q. et al. (2011). "Northern Tibetan Plateau cooling and aridification linked to Cenozoic global cooling: Evidence from n-alkane distributions of Paleogene sedimentary sequences in the Xining Basin". In: *Chinese Science Bulletin* 56.15, pp. 1569–1578. DOI: 10.1007/s11434-011-4469-0.

Lu, H. et al. (2001). "Aeolian origin and palaeoclimatic implications of the 'Red Clay' (north China) as evidenced by grain-size distribution". In: *Journal of Quaternary Science* 16.1, pp. 89–97. DOI: 10.1002/1099-1417(200101)16:1<89::AID-JQS578>3.0.CO;2-8.

Lu, H. et al. (2010). "Aeolian sediment evidence that global cooling has driven late Cenozoic stepwise aridification in central Asia". In: *Geological Society Special Publication* 342, pp. 29–44. DOI: 10.1144/SP342.4.

Ludwig, K. R (2001). "Isoplot/Ex version 2.49: A geochronology toolkit for Microsoft Excel". In: *Berkeley Geochronology Center Special Publication* 55.

Ludwig, K. R. and R. Mundil (2002). "Extracting reliable U-Pb ages and errors from complex populations of zircons from Phanerozoic tuffs". In: *Geochimica et Cosmochimica Acta*. Vol. 66. 15 A. Elsevier, A463–A463.

Lunt, D. et al. (2020). "DeepMIP: Model intercomparison of early Eocene climatic optimum (EECO) large-scale climate features and comparison with proxy data". In: *Climate of the Past Discussions* January, pp. 1–27. DOI: 10.5194/cp-2019-149.

Macdonald, F. A. et al. (2019). "Arc-continent collisions in the tropics set Earth's climate state". In: *Science* 364.6436, pp. 181–184.

Maher, B. A. (2016). "Palaeoclimatic records of the loess/palaeosol sequences of the Chinese Loess Plateau". In: *Quaternary Science Reviews* 154, pp. 23–84. DOI: 10.1016/j.quascirev.2016.08.004.

Maher, B. A. and R. Thompson (1991). "Mineral magnetic record of the Chinese loess and paleosols". In: *Geology* 19.1, pp. 3–6. DOI: 10.1130/0091-7613(1991)019<0003:MMROTC>2.3.CO;2.

Manabe, S. and A. J. Broccoli (1990). "Mountains and arid climates of middle latitudes". In: *Science* 247.4939, pp. 192–195. DOI: 10.1126/science.247.4939.192.

Marshall, C. et al. (2016). "Coal-derived rates of atmospheric dust deposition during the Permian". In: *Gondwana Research* 31, pp. 20–29. DOI: 10.1016/j.gr.2015.10.002.

Martin, J. H. (1990). "Glacial-interglacial CO2 change: The iron hypothesis". In: *Paleoceanography* 5.1, pp. 1–13. DOI: 10.1029/PA005i001p00001.

McFadden, P. L. and M. W. McElhinny (1990). "Classification of the reversal test in palaeomagnetism". In: *Geophysical Journal International* 103.3, pp. 725–729. DOI: 10.1111/j.1365-246X.1990.tb05683.x.

McInerney, F. A. and S. L. Wing (2011). "The Paleocene-Eocene Thermal Maximum: A Perturbation of Carbon Cycle, Climate, and Biosphere with Implications for the Future". In: *Annual Review of Earth and Planetary Sciences* 39.1, pp. 489–516. DOI: 10.1146/annurev-earth-040610-133431.

McKee, E. D. (1966). "Structures of sand dunes at white sands national monument, New Mexico (and a comparison with structures of dunes from other selected areas". In: *Palaeogeography, Palaeoclimatology, Palaeoecology* 4.3, pp. 229–230. DOI: 10.1016/0031-0182(68)90052-7.

Miao, X. et al. (2004). "Spatial pattern of grain size in the Late Pliocene 'Red Clay' deposits (North China) indicates transport by low-level northerly winds". In: *Palaeogeography, Palaeoclimatology, Palaeoecology* 206.1-2, pp. 149–155. DOI: 10.1016/j.palaeo.2004.01.018.

Miao, Y. et al. (2012). "What controlled Mid-Late Miocene long-term aridification in Central Asia? - Global cooling or Tibetan Plateau uplift: A review". In: *Earth-Science Reviews* 112.3-4, pp. 155–172. DOI: 10.1016/j.earscirev.2012.02.003.

Mo, D. and E. Derbyshire (1991). "The depositional environment of the late Pliocene "red clay", Jing-Le Basin, Shanxi Province, China". In: *Sedimentary Geology* 70.1, pp. 33–40. DOI: 10.1016/0037-0738(91)90064-K.

Molnar, P. et al. (1993). "Mantle dynamics, uplift of the Tibetan Plateau, and the Indian Monsoon". In: *Reviews of Geophysics* 31.4, pp. 357–396. DOI: 10.1029/93RG02030.

Molnar, P. et al. (2010). "Orographic Controls on Climate and Paleoclimate of Asia: Thermal and Mechanical Roles for the Tibetan Plateau". In: *Annual Review of Earth and Planetary Sciences* 38.1, pp. 77–102. DOI: 10.1146/annurev-earth-040809-152456.

Mudelsee, M. et al. (2014). "Cenozoic climate changes: A review based on time series analysis of marine benthic δ18O records". In: *Reviews of Geophysics* 52.3, pp. 333–374. DOI: 10.1002/2013RG000440.

Muhs, D. R. (2013). "The geologic records of dust in the Quaternary". In: *Aeolian Research* 9, pp. 3–48. DOI: 10.1016/j.aeolia.2012.08.001.

Muhs, D. R. and E. A. Bettis (2003). "Quaternary loess-paleosol sequences as examples of climate-driven sedimentary extremes". In: *Special Paper of the Geological Society of America* 370.August 2015, pp. 53–74. DOI: 10.1130/0-8137-2370-1.53.

Nie, J. et al. (2008). "Tibetan uplift intensified the 400 k.y. signal in paleoclimate records at 4 Ma". In: *Bulletin of the Geological Society of America* 120.9-10, pp. 1338–1344. DOI: 10.1130/B26349.1.

Nie, J. et al. (2014). "Provenance of the upper Miocene-Pliocene Red Clay deposits of the Chinese loess plateau". In: *Earth and Planetary Science Letters* 407, pp. 35–47. DOI: 10.1016/j.epsl.2014.09.026.

Nie, J. et al. (2015). "Loess plateau storage of northeastern Tibetan plateau-derived yellow river sediment". In: *Nature Communications* 6. DOI: 10.1038/ncomms9511.

Nie, J. et al. (2016). "A review of recent advances in red-clay environmental magnetism and paleoclimate history on the Chinese Loess Plateau". In: *Frontiers in Earth Science* 4. DOI: 10.3389/feart.2016.00027.

Nie, J. et al. (2018). "Pre-Quaternary decoupling between Asian aridification and high dust accumulation rates". In: *Science Advances* 4.2. DOI: 10.1126/sciadv.aao6977.

Nieter, W. M. and D. H. Krinsley (1976). "The production and recognition of aeolian features on sand grains by silt abrasion". In: *Sedimentology* 23.5, pp. 713–720. DOI: 10.1111/j.1365-3091.1976.tb00104.x.

North, C. P. and S. K. Davidson (2012). "Unconfined alluvial flow processes: Recognition and interpretation of their deposits, and the significance for palaeogeographic reconstruction". In: *Earth-Science Reviews* 111.1-2, pp. 199–223. DOI: 10.1016/j.earscirev.2011.11.008.

Nottebaum, V. et al. (2015). "Unmixed loess grain size populations along the northern Qilian Shan (China): Relationships between geomorphologic, sedimentologic and climatic controls". In: *Quaternary International* 372, pp. 151–166. DOI: 10.1016/j.quaint.2014.12.071.

Obrist-Farner, J. and W. Yang (2016). "Implications of loess and fluvial deposits on paleoclimatic conditions during an icehouse-hothouse transition, Capitanian upper Quanzijie low-order cycle, Bogda Mountains, NW China". In: *Palaeogeography, Palaeoclimatology, Palaeoecology* 441, pp. 959–981. DOI: 10.1016/j.palaeo.2015.10.041.

Ogg, J. G. et al. (2016). *A concise geologic time scale: 2016*. Elsevier. DOI: 10.1016/C2009-0-64442-1.

Page, M. et al. (2019). "Synchronous cooling and decline in monsoonal rainfall in northeastern Tibet during the fall into the Oligocene icehouse". In: *Geology* 47.3, pp. 203–206. DOI: 10.1130/G45480.1.

Paillard, D. et al. (1996). "Macintosh program performs time-series analysis". In: *Eos, Transactions American Geophysical Union* 77.39, p. 379. DOI: 10.1029/96EO00259.

Paquette, J.-L. et al. (2014). "Sensitivity enhancement in LA-ICP-MS by N2 addition to carrier gas: application to radiometric dating of U-Th-bearing minerals". In: *Agilent ICP-MS Journal* 58, pp. 4–5.

Parrish, R. R. et al. (2018). "Vein calcite dating reveals Pyrenean orogen as cause of Paleogene deformation in southern England". In: *Journal of the Geological Society* 175.3, pp. 425–442. DOI: 10.1144/jgs2017-107.

Paterson, G. A. and D. Heslop (2015). "New methods for unmixing sediment grain size data". In: *Geochemistry, Geophysics, Geosystems* 16.12, pp. 4494–4506. DOI: 10.1002/2015GC006070.

Paton, C. et al. (2010). "Improved laser ablation U-Pb zircon geochronology through robust downhole fractionation correction". In: *Geochemistry, Geophysics, Geosystems* 11.3. DOI: 10.1029/2009GC002618.

Pearson, P. N. et al. (2009). "Atmospheric carbon dioxide through the Eocene-Oligocene climate transition". In: *Nature* 461.7267, pp. 1110–1113. DOI: 10.1038/nature08447.

Pécsi, M. (1990). "Loess is not just the accumulation of dust". In: *Quaternary International* 7, pp. 1–21. DOI: 10.1016/1040-6182(90)90034-2.

Peng, W. et al. (2016). "A comparison of heavy mineral assemblage between the loess and the Red Clay sequences on the Chinese Loess Plateau". In: *Aeolian Research* 21, pp. 87–91. DOI: 10.1016/j.aeolia.2016.02.004.

Pettke, T. et al. (2002). "Cenozoic evolution of Asian climate and sources of Pacific seawater Pb and Nd derived from eolian dust of sediment core LL44-GPC3". In: *Paleoceanography* 17.3, pp. 3–1–3–13. DOI: 10.1029/2001pa000673.

Popov, S. V. et al. (2004). *Lithological-paleogeographic maps of Paratethys-10 maps late Eocene to Pliocene*. Schweizerbart'sche Verlagsbuchhandlung.

Porter, S. C. (2001). "Chinese loess record of monsoon climate during the last glacial-interglacial cycle". In: *Earth-Science Reviews* 54.1-3, pp. 115–128. DOI: 10.1016/S0012-8252(01)00043-5.

Potter, P. E. et al. (2005). *Mud and mudstones: Introduction and overview*. Springer Science & Business Media. DOI: 10.1007/b138571.

Prell, W. L. and J. E. Kutzbach (1992). "Sensitivity of the Indian monsoon to forcing parameters and implications for its evolution". In: *Nature* 360.6405, pp. 647–652. DOI: 10.1038/360647a0.

Prins, M. A. et al. (2007). "Late Quaternary aeolian dust input variability on the Chinese Loess Plateau: inferences from unmixing of loess grain-size records". In: *Quaternary Science Reviews* 26.1-2, pp. 230–242. DOI: 10.1016/j.quascirev.2006.07.002.

Pullen, A. et al. (2011). "Qaidam Basin and northern Tibetan Plateau as dust sources for the Chinese Loess Plateau and paleoclimatic implications". In: *Geology* 39.11, pp. 1031–1034. DOI: 10.1130/G32296.1.

Pye, K. (1987). *Aeolian Dust and Dust Deposits*. Academic Press. DOI: 10.1016/C2013-0-05007-4.

– (1995). "The nature, origin and accumulation of loess". In: *Quaternary Science Reviews* 14.7-8, pp. 653–667. DOI: 10.1016/0277-3791(95)00047-X.

Pye, K. and L. P. Zhou (1989). "Late Pleistocene and Holocene aeolian dust deposition in North China and the Northwest Pacific Ocean". In: *Palaeogeography, Palaeoclimatology, Palaeoecology* 73.1-2, pp. 11–23. DOI: 10.1016/0031-0182(89)90041-2.

Qi, B. et al. (2016). "Apatite fission track evidence for the Cretaceous-Cenozoic cooling history of the Qilian Shan (NW China) and for stepwise northeastward growth of the northeastern Tibetan Plateau since early Eocene". In: *Journal of Asian Earth Sciences* 124, pp. 28–41. DOI: 10.1016/j.jseaes.2016.04.009.

Qiang, M. et al. (2010). "Do fine-grained components of loess indicate westerlies: Insights from observations of dust storm deposits at Lenghu (Qaidam Basin, China)". In: *Journal of Arid Environments* 74.10, pp. 1232–1239. DOI: 10.1016/j.jaridenv.2010.06.002.

Qiang, X. K. et al. (2011). "New eolian red clay sequence on the western Chinese Loess Plateau linked to onset of Asian desertification about 25 Ma ago". In: *Science China Earth Sciences* 54.1, pp. 136–144. DOI: 10.1007/s11430-010-4126-5.

Qiang, X.K. et al. (2001). "Magnetostratigraphic record of the Late Miocene onset of the East Asian monsoon, and Pliocene uplift of northern Tibet". In: *Earth and Planetary Science Letters* 187.1-2, pp. 83–93. DOI: 10.1016/S0012-821X(01)00281-3.

Qiao, Y. et al. (2006). "Grain-size features of a Miocene loess-soil sequence at Qinan: Implications on its origin". In: *Science in China, Series D: Earth Sciences* 49.7, pp. 731–738. DOI: 10.1007/s11430-006-0731-8.

Qinghai Bureau of Geology and Mineral Resources (QBGMR) (1985). *Geologic maps of the Duoba, Gaodian, Tianjiazai, and Xining regions (4 sheets), with regional geologic report (1: 50,000 scale)*. Geological Publishing House Beijing.

Quade, J. and L. J. Roe (1999). "The stable-isotope composition of early ground-water cements from sandstone in paleoecological reconstruction". In: *Journal of Sedimentary Research* 69.3, pp. 667–674. DOI: 10.2110/jsr.69.667.

Quan, C. et al. (2012). "Eocene monsoon prevalence over China: A paleobotanical perspective". In: *Palaeogeography, Palaeoclimatology, Palaeoecology* 365-366, pp. 302–311. DOI: 10.1016/j.palaeo.2012.09.035.

Quan, C. et al. (2014). "Revisiting the Paleogene climate pattern of East Asia: A synthetic review". In: *Earth-Science Reviews* 139, pp. 213–230. DOI: 10.1016/j.earscirev.2014.09.005.

Ramstein, G. et al. (1997). "Effect of orogeny, plate motion and land-sea distribution on Eurasian climate change over the past 30 million years". In: *Nature* 386.6627, pp. 788–795. DOI: 10.1038/386788a0.

Raymo, M. E. and W. F. Ruddiman (1992). "Tectonic forcing of late Cenozoic climate". In: *Nature* 359.6391, pp. 117–122. DOI: 10.1038/359117a0.

Rea, D. K. et al. (2000). "Atmospheric and oceanic circulation dynamics in the equatorial Pacific of the Paleogene world". In: *Gff* 122.1, pp. 135–136. DOI: 10.1080/11035890001221135.

Richthofen, B. F. (1882). "On the Mode of the Origin of the Loess". In: *Geological Magazine* 9.7, pp. 293–305.

Rits, D. S. et al. (2016). "Facies analysis of the Middle and Late Quaternary sediment infill of the northern Weihe Basin, Central China". In: *Journal of Quaternary Science* 31.2, pp. 152–165. DOI: 10.1002/jqs.2853.

Roberts, N. M. W. et al. (2017). "A calcite reference material for LA-ICP-MS U-Pb geochronology". In: *Geochemistry, Geophysics, Geosystems* 18.7, pp. 2807–2814. DOI: 10.1002/2016GC006784.

Roe, G. (2009). "On the interpretation of Chinese loess as a paleoclimate indicator". In: *Quaternary Research* 71.2, pp. 150–161. DOI: 10.1016/j.yqres.2008.09.004.

Roe, G. H. et al. (2016). "A modeling study of the response of Asian summertime climate to the largest geologic forcings of the past 50 Ma". In: *Journal of Geophysical Research* 121.10, pp. 5453–5470. DOI: 10.1002/2015JD024370.

Rohrmann, A. et al. (2012). "Thermochronologic evidence for plateau formation in central Tibet: By 45 Ma". In: *Geology* 40.2, pp. 187–190. DOI: 10.1130/G32530.1.

Rosen, M. R. (1994). "The importance of groundwater in playas: A review of playa classifications and the sedimentology and hydrology of playas". In: *Special Paper of the Geological Society of America* 289.January 1994, pp. 1–18. DOI: 10.1130/SPE289-p1.

Rust, B. R. and G. C. Nanson (1989). "Bedload transport of mud as pedogenic aggregates in modern and ancient rivers". In: *Sedimentology* 36.2, pp. 291–306. DOI: 10.1111/j.1365-3091.1989.tb00608.x.

Rutter, N. and Z. Ding (1993). "Paleoclimates and monsoon variations interpreted from micromorphogenic features of the Baoji paleosols, China". In: *Quaternary Science Reviews* 12.10, pp. 853–862. DOI: 10.1016/0277-3791(93)90024-G.

Rutter, N. et al. (1991). "Baoji-type pedostratigraphic section, Loess Plateau, north-central China". In: *Quaternary Science Reviews* 10.1, pp. 1–22. DOI: 10.1016/0277-3791(91)90028-S.

Sampe, T. and S. P. Xie (2010). "Large-scale dynamics of the meiyu-baiu rainband: Environmental forcing by the westerly jet". In: *Journal of Climate* 23.1, pp. 113–134. DOI: 10.1175/2009JCLI3128.1.

Scher, H. D. et al. (2014). "Isotopic interrogation of a suspected late Eocene glaciation". In: *Paleoceanography* 29.6, pp. 628–644. DOI: 10.1002/2014PA002648.

Schiemann, R. et al. (2009). "Seasonality and interannual variability of the westerley jet in the Tibetan Plateau region". In: *Journal of Climate* 22.11, pp. 2940–2957. DOI: 10.1175/2008JCLI2625.1.

Schlanser, K. et al. (2020). "On geologic timescales, plant carbon isotope fractionation responds to precipitation similarly to modern plants and has a small negative correlation with pCO2". In: *Geochimica et Cosmochimica Acta* 270, pp. 264–281. DOI: 10.1016/j.gca.2019.11.023.

Schneider, T. et al. (2014). "Migrations and dynamics of the intertropical convergence zone." In: *Nature* 513.7516, pp. 45–53. DOI: 10.1038/nature13636.

Schulz, M. and M. Mudelsee (2002). "REDFIT: Estimating red-noise spectra directly from unevenly spaced paleoclimatic time series". In: *Computers and Geosciences* 28.3, pp. 421–426. DOI: 10.1016/S0098-3004(01)00044-9.

Schwartz, S. E. and M. O. Andreae (1996). "Uncertainty in Climate Change Caused by Aerosols". In: *Science* 272.5265, pp. 1121–0. DOI: 10.1126/science.272.5265.1121.

Selkin, P. A. et al. (2015). "Climate, dust, and fire across the Eocene-Oligocene transition, Patagonia". In: *Geology* 43.7, pp. 567–570. DOI: 10.1130/G36664.1.

Sexton, P. F. et al. (2011). "Eocene global warming events driven by ventilation of oceanic dissolved organic carbon". In: *Nature* 471.7338, pp. 349–353. DOI: 10.1038/nature09826.

Sha, Y. et al. (2015). "Distinct impacts of the Mongolian and Tibetan Plateaus on the evolution of the East Asian monsoon". In: *Journal of Geophysical Research: Atmospheres* 120.10, pp. 4764–4782. DOI: 10.1002/2014JD022880.

Shaffer, G. and F. Lambert (2018). "In and out of glacial extremes by way of dust-climate feedbacks". In: *Proceedings of the National Academy of Sciences of the United States of America* 115.9, pp. 2026–2031. DOI: 10.1073/pnas.1708174115.

Shang, Y. et al. (2016). "Variations in the provenance of the late Neogene Red Clay deposits in northern China". In: *Earth and Planetary Science Letters* 439, pp. 88–100. DOI: 10.1016/j.epsl.2016.01.031.

Shang, Y. et al. (2018). "Aeolian silt transport processes as fingerprinted by dynamic image analysis of the grain size and shape characteristics of Chinese loess and Red Clay deposits". In: *Sedimentary Geology* 375, pp. 36–48. DOI: 10.1016/j.sedgeo.2017.12.001.

Shi, Z. G. et al. (2011). "Distinct responses of East Asian summer and winter monsoons to astronomical forcing". In: *Climate of the Past* 7.4, pp. 1363–1370. DOI: 10.5194/cp-7-1363-2011.

Sláma, J. et al. (2008). "Plešovice zircon - A new natural reference material for U-Pb and Hf isotopic microanalysis". In: *Chemical Geology* 249.1-2, pp. 1–35. DOI: 10.1016/j.chemgeo.2007.11.005.

Sluijs, A. et al. (2013). "A middle Eocene carbon cycle conundrum". In: *Nature Geoscience* 6.6, pp. 429–434. DOI: 10.1038/ngeo1807.

Smalley, I. J. (1966a). "Formation of quartz sand". In: *Nature* 211.5048, pp. 476–479. DOI: 10.1038/211476a0.

– (1966b). "The Properties of Glacial Loess and the Formation of Loess Deposits". In: *SEPM Journal of Sedimentary Research* Vol. 36.3, pp. 669–676. DOI: 10.1306/74d7153c-2b21-11d7-8648000102c1865d.

– (1972). "The interaction of great rivers and large deposits of primary loess". In: *Transactions of the New York Academy of Sciences* 34.6, pp. 534–542. DOI: 10.1002/2014JD022880.

– (1995). "Making the material: The formation of silt sized primary mineral particles for loess deposits". In: *Quaternary Science Reviews* 14.7-8, pp. 645–651. DOI: 10.1016/0277-3791(95)00046-1.

Smalley, I. J. and D. H. Krinsley (1978). "Loess deposits associated with deserts". In: *Catena* 5.1, pp. 53–66. DOI: 10.1016/S0341-8162(78)80006-X.

Smalley, I. J. and C. Vita-Finzi (1968). "The Formation of Fine Particles in Sandy Deserts and the Nature Of 'Desert' Loess". In: *SEPM Journal of Sedimentary Research* Vol. 38.3. DOI: 10.1306/74d71a69-2b21-11d7-8648000102c1865d.

Smalley, I. J. et al. (2001). "Some major events in the development of the scientific study of loess". In: *Earth-Science Reviews* 54.1-3, pp. 5–18. DOI: 10.1016/S0012-8252(01)00038-1.

Smalley, I. J. et al. (2009). "Rivers and loess: The significance of long river transportation in the complex event-sequence approach to loess deposit formation". In: *Quaternary International* 198.1-2, pp. 7–18. DOI: 10.1016/j.quaint.2008.06.009.

Smoot, J. P. and T. K. Lowenstein (1991). "Chapter 3 Depositional Environments of Non-Marine Evaporites". In: *Developments in Sedimentology* 50.C, pp. 189–347. DOI: 10.1016/S0070-4571(08)70261-9.

Smoot, J. P. and P. E. Olsen (1988). "Massive mudstones in basin analysis and paleoclimatic interpretation of the Newark Supergroup". In: *Developments in Geotectonics* 22.C, pp. 249–274. DOI: 10.1016/B978-0-444-42903-2.50015-4.

Son, J. H. et al. (2019). "Dynamical Control of the Tibetan Plateau on the East Asian Summer Monsoon". In: *Geophysical Research Letters* 46.13, pp. 7672–7679. DOI: 10.1029/2019GL083104.

Song, B. et al. (2018). "Qaidam Basin paleosols reflect climate and weathering intensity on the northeastern Tibetan Plateau during the Early Eocene Climatic Optimum". In: *Palaeogeography, Palaeoclimatology, Palaeoecology* 512, pp. 6–22. DOI: 10.1016/j.palaeo.2018.03.027.

Song, Y. et al. (2001). "Magnetostratigraphy of Late Tertiary sediments from the Chinese Loess Plateau and its paleoclimatic significance". In: *Chinese Science Bulletin* 46.SUPPL. Pp. 16–22. DOI: 10.1007/bf03187230.

Song, Z. C. et al. (1999). "Fossil spores and pollen of China. Vol. 1. The Late Cretaceous and Tertiary spores and pollen". In: *Science Press, Beijing* 17.910, p. 207.

Soreghan, G. S. et al. (2008). "Origin and significance of loess in late Paleozoic western Pangaea: A record of tropical cold?" In: *Palaeogeography, Palaeoclimatology, Palaeoecology* 268.3-4, pp. 234–259. DOI: 10.1016/j.palaeo.2008.03.050.

Soreghan, M. J. et al. (2002). "Paleowinds inferred from detrital-zircon geochronology of upper Paleozoic loessite, western equatorial Pangea". In: *Geology* 30.8, pp. 695–698. DOI: 10.1130/0091-7613(2002)030<0695:PIFDZG>2.0.CO;2.

Soreghan, M. J. et al. (2014). "Abrupt and high-magnitude changes in atmospheric circulation recorded in the Permian Maroon formation, tropical Pangaea". In: *Bulletin of the Geological Society of America* 126.3-4, pp. 569–584. DOI: 10.1130/B30840.1.

Sperazza, M. et al. (2004). "High-Resolution Particle Size Analysis of Naturally Occurring Very Fine-Grained Sediment Through Laser Diffractometry". In: *Journal of Sedimentary Research* 74.5, pp. 736–743. DOI: 10.1306/031104740736.

Spicer, R. A. et al. (2016). "Asian Eocene monsoons as revealed by leaf architectural signatures". In: *Earth and Planetary Science Letters* 449, pp. 61–68. DOI: 10.1016/j.epsl.2016.05.036.

Spicer, R. A. et al. (2017). "Paleogene monsoons across India and South China: Drivers of biotic change". In: *Gondwana Research* 49, pp. 350–363. DOI: 10.1016/j.gr.2017.06.006.

Spicer, R. A. et al. (2020). "Why the 'Uplift of the Tibetan Plateau' is a myth". In: *National Science Review*. DOI: 10.1093/nsr/nwaa091.

Stacey, J. S. and J. D. Kramers (1975). "Approximation of terrestrial lead isotope evolution by a two-stage model". In: *Earth and Planetary Science Letters* 26.2, pp. 207–221. DOI: 10.1016/0012-821X(75)90088-6.

Staisch, L. M. et al. (2016). "Eocene to late Oligocene history of crustal shortening within the Hoh Xil Basin and implications for the uplift history of the northern Tibetan Plateau history of the northern Tibetan Plateau". In: *Tectonics* 35.4, pp. 862–895. DOI: 10.1002/2015TC003972.Received.

Stevens, T. et al. (2013). "Genetic linkage between the Yellow River, the Mu Us desert and the Chinese Loess Plateau". In: *Quaternary Science Reviews* 78, pp. 355–368. DOI: 10.1016/j.quascirev.2012.11.032.

Sun, D. et al. (1997). "Magnetostratigraphy and palaeoclimate of Red Clay sequences from Chinese Loess Plateau". In: *Science in China, Series D* 40.4, pp. 337–343. DOI: 10.1007/BF02877564.

Sun, D. et al. (1998a). "Magnetostratigraphy and palaeoclimatic significance of late Tertiary aeolian sequences in the Chinese Loess Plateau". In: *Geophysical Journal International* 134.1, pp. 207–212. DOI: 10.1046/j.1365-246X.1998.00553.x.

Sun, D. et al. (1998b). "Magnetostratigraphy and paleoclimatic interpretation of a continuous 7.2Ma Late Cenozoic eolian sediments from the Chinese Loess Plateau". In: *Geophysical Research Letters* 25.1, pp. 85–88. DOI: 10.1029/97GL03353.

Sun, D. et al. (2002). "Grain-size distribution function of polymodal sediments in hydraulic and aeolian environments, and numerical partitioning of the sedimentary components". In: *Sedimentary Geology* 152.3-4, pp. 263–277. DOI: 10.1016/S0037-0738(02)00082-9.

Sun, D. et al. (2004). "Bimodal grain-size distribution of Chinese loess, and its palaeoclimatic implications". In: *Catena* 55.3, pp. 325–340. DOI: 10.1016/S0341-8162(03)00109-7.

Sun, J. (2002). "Provenance of loess material and formation of loess deposits on the Chinese Loess Plateau". In: *Earth and Planetary Science Letters* 203, pp. 845–859. DOI: 10.1016/S0012-821X(02)00921-4.

– (2005). "Nd and Sr isotopic variations in Chinese eolian deposits during the past 8 Ma: Implications for provenance change". In: *Earth and Planetary Science Letters* 240.2, pp. 454–466. DOI: 10.1016/j.epsl.2005.09.019.

Sun, J. and B. F. Windley (2015). "Onset of aridification by 34 Ma across the Eocene-Oligocene transition in Central Asia". In: *Geology* 43.11, pp. 1015–1018. DOI: 10.1130/G37165.1.

Sun, J. and X. Zhu (2010). "Temporal variations in Pb isotopes and trace element concentrations within Chinese eolian deposits during the past 8 Ma: Implications for provenance change". In: *Earth and Planetary Science Letters* 290.3-4, pp. 438–447. DOI: 10.1016/j.epsl.2010.01.001.

Sun, J. et al. (2001). "Spatial and temporal characteristics of dust storms in China and its surrounding regions, 1960-1999: Relations to source area and climate". In: *Journal of Geophysical Research Atmospheres* 106.D10, pp. 10325–10333. DOI: 10.1029/2000JD900665.

Sun, J. et al. (2010). "Late Oligocene-Miocene mid-latitude aridification and wind patterns in the Asian interior". In: *Geology* 38.6, pp. 515–518. DOI: 10.1130/G30776.1.

Sun, X. and P. Wang (2005). "How old is the Asian monsoon system? - Palaeobotanical records from China". In: *Palaeogeography, Palaeoclimatology, Palaeoecology* 222.3-4, pp. 181–222. DOI: 10.1016/j.palaeo.2005.03.005.

Sun, Y. et al. (2006). "Grain size of loess, palaeosol and Red Clay deposits on the Chinese Loess Plateau: Significance for understanding pedogenic alteration and palaeomonsoon evolution". In: *Palaeogeography, Palaeoclimatology, Palaeoecology* 241.1, pp. 129–138. DOI: 10.1016/j.palaeo.2006.06.018.

Sun, Y. et al. (2012). "Influence of Atlantic meridional overturning circulation on the East Asian winter monsoon". In: *Nature Geoscience* 5.1, pp. 46–49. DOI: 10.1038/ngeo1326.

Sun, Y. et al. (2020). "Source-to-sink fluctuations of Asian aeolian deposits since the late Oligocene". In: *Earth-Science Reviews* 200.October 2019, p. 102963. DOI: 10.1016/j.earscirev.2019.102963.

Szalai, Z. et al. (2019). "Application of Raman spectroscopy combined automated 2D image analysis for geosciences." In: *Geophysical Research Abstracts*. Vol. 21.

Talbot, M. R. et al. (1994). "Sedimentation in low-gradient desert margin systems: A comparison of the Late Triassic of northwest Somerset". In: *Paleoclimate and basin evolution of playa systems* 289, p. 97.

Tang, H. et al. (2015). "Strong winter monsoon wind causes surface cooling over India and China in the Late Miocene". In: *Climate of the Past Discussions* 11.1, pp. 63–93. DOI: 10.5194/cpd-11-63-2015.

Tardif, D. et al. (2019). "The onset of Asian Monsoons: a modelling perspective". In: *Climate of the Past Discussions* 16, pp. 847–865. DOI: 10.5194/cp-2019-144.

Teng, X. et al. (2019). "Sedimentological and mineralogical records from drill core SKD1 in the Jianghan Basin, Central China, and their implications for late Cretaceous–early Eocene climate change". In: *Journal of Asian Earth Sciences* 182, p. 103936. DOI: 10.1016/j.jseaes.2019.103936.

Tripati, A. and D. Darby (2018). "Evidence for ephemeral middle Eocene to early Oligocene Greenland glacial ice and pan-Arctic sea ice". In: *Nature Communications* 9.1, pp. 1–11. DOI: 10.1038/s41467-018-03180-5.

Tsoar, H. and K. Pye (1987). "Dust transport and the question of desert loess formation". In: *Sedimentology* 34.1, pp. 139–153. DOI: 10.1111/j.1365-3091.1987.tb00566.x.

Turtù, A. et al. (2017). "Integrated stratigraphy of the Smirra Core (Umbria-Marche Basin, Apennines, Italy): A new early Paleogene reference section and implications for the geologic time scale". In: *Palaeogeography, Palaeoclimatology, Palaeoecology* 487, pp. 158–174. DOI: 10.1016/j.palaeo.2017.08.031.

Újvári, G. et al. (2016). "The physics of wind-blown loess: Implications for grain size proxy interpretations in Quaternary paleoclimate studies". In: *Earth-Science Reviews* 154, pp. 247–278. DOI: 10.1016/j.earscirev.2016.01.006.

Valdes, P. J. et al. (2019). "Comment on "Revised paleoaltimetry data show low Tibetan Plateau elevation during the Eocene"". In: *Science* 365.6459, eaax8474. DOI: 10.1126/science.aax8474.

Van Achterbergh, E. et al. (2001). "Data reduction software for LA-ICP-MS". In: *Laser Ablation-ICP-mass spectrometry in the earth sciences: principles and applications*, pp. 239–243.

van der Does, M. et al. (2018). "The mysterious long-range transport of giant mineral dust particles". In: *Science advances* 4.12, eaau2768. DOI: 10.1126/sciadv.aau2768.

van der Ploeg, R. et al. (2018). "Middle Eocene greenhouse warming facilitated by diminished weathering feedback". In: *Nature Communications* 9.1, pp. 1–10. DOI: 10.1038/s41467-018-05104-9.

van Hateren, J. A. et al. (2018). "On the genetically meaningful decomposition of grain-size distributions: A comparison of different end-member modelling algorithms". In: *Sedimentary Geology* 375, pp. 49–71. DOI: 10.1016/j.sedgeo.2017.12.003.

van Hateren, J. A. et al. (2020). "Identifying sediment transport mechanisms from grain size-shape distributions". In: *Earth Surface Dynamics* 8.2, pp. 527–553. DOI: 10.5194/esurf-8-527-2020.

van Toorenenburg, K. A. et al. (2018). "The life cycle of crevasse splays as a key mechanism in the aggradation of alluvial ridges and river avulsion". In: *Earth Surface Processes and Landforms* 43.11, pp. 2409–2420. DOI: 10.1002/esp.4404.

Vandenberghe, J. (2013). "Grain size of fine-grained windblown sediment: A powerful proxy for process identification". In: *Earth-Science Reviews* 121, pp. 18–30. DOI: 10.1016/j.earscirev.2013.03.001.

Vandenberghe, J. et al. (2006). "Penetration of Atlantic westerly winds into Central and East Asia". In: *Quaternary Science Reviews* 25.17-18, pp. 2380–2389. DOI: 10.1016/j.quascirev.2006.02.017.

Vandenberghe, J. et al. (2018). "Grain-size characterization of reworked fine-grained aeolian deposits". In: *Earth-Science Reviews* 177.November 2017, pp. 43–52. DOI: 10.1016/j.earscirev.2017.11.005.

Varga, G. et al. (2018). "Granulometric characterization of paleosols in loess series by automated static image analysis". In: *Sedimentary Geology* 370, pp. 1–14. DOI: 10.1016/j.sedgeo.2018.04.001.

Varga, G. et al. (2019a). "Interpretation of sedimentary (sub) populations extracted from grain size distributions of Central European loess-paleosol series". In: *Quaternary International* 502, pp. 60–70. DOI: 10.1016/j.quaint.2017.09.021.

Varga, G. et al. (2019b). "On the reliability and comparability of laser diffraction grain size measurements of paleosols in loess records". In: *Sedimentary Geology* 389, pp. 42–53. DOI: 10.1016/j.sedgeo.2019.05.011.

Vassallo, R. et al. (2007). "Uplift age and rates of the Gurvan Bogd system (Gobi-Altay) by apatite fission track analysis". In: *Earth and Planetary Science Letters* 259.3-4, pp. 333–346. DOI: 10.1016/j.epsl.2007.04.047.

Ventra, D. et al. (2018). "Orbital-climate control of mass-flow sedimentation in a Miocene alluvial-fan succession (Teruel Basin, Spain)". In: *Geological Society Special Publication* 440.1, pp. 129–157. DOI: 10.1144/SP440.14.

Vermeesch, P. (2018). "IsoplotR: A free and open toolbox for geochronology". In: *Geoscience Frontiers* 9.5, pp. 1479–1493. DOI: 10.1016/j.gsf.2018.04.001.

Vos, K. et al. (2014). "Surface textural analysis of quartz grains by scanning electron microscopy (SEM): From sample preparation to environmental interpretation". In: *Earth-Science Reviews* 128, pp. 93–104. DOI: 10.1016/j.earscirev.2013.10.013.

Wang, B. et al. (2014a). "Middle Miocene eolian sediments on the southern Chinese Loess Plateau dated by magnetostratigraphy". In: *Palaeogeography, Palaeoclimatology, Palaeoecology* 411, pp. 257–266. DOI: 10.1016/j.palaeo.2014.07.007.

Wang, B. et al. (2018). "Tectonic controls of the onset of aeolian deposits in Chinese Loess Plateau–a preliminary hypothesis". In: *International Geology Review* 60.8, pp. 945–955. DOI: 10.1080/00206814.2017.1362362.

Wang, Bin et al. (2020a). "Understanding future change of global monsoons projected by CMIP6 models". In: *Journal of Climate* 33.15, pp. 6471–6489. DOI: 10.1175/JCLI-D-19-0993.1.

Wang, C. et al. (2014b). "Outward-growth of the Tibetan Plateau during the Cenozoic: A review". In: *Tectonophysics* 621.September, pp. 1–43. DOI: 10.1016/j.tecto.2014.01.036.

Wang, D. et al. (2013a). "Eocene prevalence of monsoon-like climate over eastern China reflected by hydrological dynamics". In: *Journal of Asian Earth Sciences* 62, pp. 776–787. DOI: 10.1016/j.jseaes.2012.11.032.

Wang, P. (1990). "The ice-age China sea-research results and problems." In: *Proc. 1st Intern. Conf. Asian Marine Geology.* China Ocean Press, pp. 181–197.

Wang, Q. et al. (2019a). "Clay mineralogy of the upper Miocene-Pliocene red clay from the central Chinese Loess Plateau and its paleoclimate implications". In: *Quaternary International*. DOI: 10.1016/j.quaint.2019.11.039.

Wang, W. et al. (2011). "A revised chronology for Tertiary sedimentation in the Sikouzi basin: Implications for the tectonic evolution of the northeastern corner of the Tibetan Plateau". In: *Tectonophysics* 505.1-4, pp. 100–114. DOI: 10.1016/j.tecto.2011.04.006.

Wang, W. et al. (2013b). "Tertiary basin evolution along the northeastern margin of the Tibetan Plateau: Evidence for basin formation during Oligocene transtension". In: *Bulletin of the Geological Society of America* 125.3-4, pp. 377–400. DOI: 10.1130/B30611.1.

Wang, W. et al. (2016a). "Pulsed growth of the West Qinling at ˜30 Ma in northeastern Tibet: Evidence from Lanzhou Basin magnetostratigraphy and provenance". In: *Journal of Geophysical Research: Solid Earth* 121.11, pp. 7754–7774. DOI: 10.1002/2016JB013279.

Wang, W. et al. (2017). "Expansion of the Tibetan Plateau during the Neogene". In: *Nature Communications* 8.May, pp. 1–12. DOI: 10.1038/ncomms15887.

Wang, X. et al. (2016b). "Central Asian aridification during the late Eocene to early Miocene inferred from preliminary study of shallow marine-eolian sedimentary rocks from northeastern Tajik Basin". In: *Science China Earth Sciences* 59.6, pp. 1242–1257. DOI: 10.1007/s11430-016-5282-z.

Wang, X. et al. (2019b). "Parathethys Last Gasp in Central Asia and Late Oligocene Accelerated Uplift of the Pamirs". In: *Geophysical Research Letters* 46.21, pp. 11773–11781. DOI: 10.1029/2019GL084838.

Wang, X. et al. (2020b). "The role of the westerlies and orography in Asian hydroclimate since the late Oligocene". In: *Geology* 48.7, pp. 1–5. DOI: 10.1130/g47400.1.

Wang, Y. X. et al. (2007). "The Sr and Nd isotopic variations of the Chinese Loess Plateau during the past 7 Ma: Implications for the East Asian winter monsoon and source areas of loess". In: *Palaeogeography, Palaeoclimatology, Palaeoecology* 249.3-4, pp. 351–361. DOI: 10.1016/j.palaeo.2007.02.010.

Wang, Z. et al. (2019c). "Middle to Late Miocene Eccentricity Forcing on Lake Expansion in NE Tibet". In: *Geophysical Research Letters* 46.12, pp. 6926–6935. DOI: 10.1029/2019GL082283.

Wasiljeff, J. et al. (2020). "Magnetostratigraphic constraints on the fossiliferous Ulantatal sequence in Inner Mongolia, China: Implications for Asian aridification and faunal turnover before the Eocene-Oligocene boundary". In: *Earth and Planetary Science Letters* 535, p. 116125. DOI: 10.1016/j.epsl.2020.116125.

Weltje, G. J. and M. A. Prins (2003). "Muddled or mixed? Inferring palaeoclimate from size distributions of deep-sea clastics". In: *Sedimentary Geology* 162.1-2, pp. 39–62. DOI: 10.1016/S0037-0738(03)00235-5.

– (2007). "Genetically meaningful decomposition of grain-size distributions". In: *Sedimentary Geology* 202.3, pp. 409–424. DOI: 10.1016/j.sedgeo.2007.03.007.

Weltje, G. J. and R. Tjallingii (2008). "Calibration of XRF core scanners for quantitative geochemical logging of sediment cores: Theory and application". In: *Earth and Planetary Science Letters* 274.3-4, pp. 423–438. DOI: 10.1016/j.epsl.2008.07.054.

Weltje, G. J. et al. (2015). "Prediction of geochemical composition from XRF core scanner data: a new multivariate approach including automatic selection of calibration samples and quantification of uncertainties". In: *Micro-XRF Studies of Sediment Cores*. Springer, pp. 507–534. DOI: 10.1007/978-94-017-9849-5_21.

Westerhold, T. and U. Röhl (2013). "Orbital pacing of Eocene climate during the Middle Eocene Climate Optimum and the chron C19r event: Missing link found in the tropical western Atlantic". In: *Geochemistry, Geophysics, Geosystems* 14.11, pp. 4811–4825. DOI: 10.1002/ggge.20293.

Westerhold, T. et al. (2015). "Astronomical calibration of the geological timescale: Closing the middle Eocene gap". In: *Climate of the Past* 11.9, pp. 1181–1195. DOI: 10.5194/cp-11-1181-2015.

Westerhold, T. et al. (2017). "Astronomical calibration of the Ypresian timescale: Implications for seafloor spreading rates and the chaotic behavior of the solar system?" In: *Climate of the Past* 13.9, pp. 1129–1152. DOI: 10.5194/cp-13-1129-2017.

Westerhold, T. et al. (2018). "Global Extent of Early Eocene Hyperthermal Events: A New Pacific Benthic Foraminiferal Isotope Record From Shatsky Rise (ODP Site 1209)". In: *Paleoceanography and Paleoclimatology* 33.6, pp. 626–642. DOI: 10.1029/2017PA003306.

Whalley, W. B. et al. (1982). "Origin of desert loess from some experimental observations". In: *Nature* 300.5891, pp. 433–435. DOI: 10.1038/300433a0.

Wilkins, A. D. et al. (2018). "Palaeo-environment in an ancient low-latitude, arid lacustrine basin with loessite: The Smith Bank Formation (Early Triassic) in the Central North Sea, UK Continental Shelf". In: *Sedimentology* 65.2, pp. 335–359. DOI: 10.1111/sed.12382.

Wilson, M. J. et al. (2020). "Mineralogical evidence for multiple dust sources in an early Triassic loessite". In: *Sedimentology* 67.1, pp. 239–260. DOI: 10.1111/sed.12641.

Wright, J. S. (2001a). "Desert loess versus glacial loess: Quartz silt formation, source areas and sediment pathways in the formation of loess deposits". In: *Geomorphology* 36.3-4, pp. 231–256. DOI: 10.1016/S0169-555X(00)00060-X.

– (2001b). "Making loess-sized quartz silt: Data from laboratory simulations and implications for sediment transport pathways and theformation of 'desert' loess deposits associated with the Sahara". In: *Quaternary International* 76-77, pp. 7–19. DOI: 10.1016/S1040-6182(00)00085-9.

– (2007). "An overview of the role of weathering in the production of quartz silt". In: *Sedimentary Geology* 202.3, pp. 337–351. DOI: 10.1016/j.sedgeo.2007.03.024.

Wright, V. P. and S. B. Marriott (2007). "The dangers of taking mud for granted: Lessons from Lower Old Red Sandstone dryland river systems of South Wales". In: *Sedimentary Geology* 195.1-2, pp. 91–100. DOI: 10.1016/j.sedgeo.2006.03.028.

Wu, L. et al. (2020). "CFLab: A MATLAB GUI program for decomposing sediment grain size distribution using Weibull functions". In: *Sedimentary Geology* 398. DOI: 10.1016/j.sedgeo.2020.105590.

Wynn, J. G. (2007). "Carbon isotope fractionation during decomposition of organic matter in soils and paleosols: Implications for paleoecological interpretations of paleosols". In: *Palaeogeography, Palaeoclimatology, Palaeoecology* 251.3-4, pp. 437–448. DOI: 10.1016/j.palaeo.2007.04.009.

Xiao, G. et al. (2012). "Evidence for northeastern Tibetan Plateau uplift between 25 and 20Ma in the sedimentary archive of the Xining Basin, Northwestern China". In: *Earth and Planetary Science Letters* 317-318, pp. 185–195. DOI: 10.1016/j.epsl.2011.11.008.

Xiao, G. Q. et al. (2010). "Asian aridification linked to the first step of the Eocene-Oligocene climate Transition (EOT) in obliquity-dominated terrestrial records (Xining Basin, China)". In: *Climate of the Past* 6.4, pp. 501–513. DOI: 10.5194/cp-6-501-2010.

Xiao, J. et al. (1997). "Eolian Quartz Flux to Lake Biwa, Central Japan, over the Past 145,000 Years". In: *Quaternary Research* 48.1, pp. 48–57. DOI: 10.1006/qres.1997.1893.

Xie, Y. et al. (2019). "Middle Eocene East Asian monsoon prevalence over southern China: Evidence from palynological records". In: *Global and Planetary Change* 175, pp. 13–26. DOI: 10.1016/j.gloplacha.2019.01.019.

– (2020). "A major environmental shift by the middle Eocene in southern China: Evidence from palynological records". In: *Review of Palaeobotany and Palynology* 278, p. 104226. DOI: 10.1016/j.revpalbo.2020.104226.

Xu, Y. et al. (2009). "An 11-Ma-old red clay sequence on the Eastern Chinese Loess Plateau". In: *Palaeogeography, Palaeoclimatology, Palaeoecology* 284.3-4, pp. 383–391. DOI: 10.1016/j.palaeo.2009.10.023.

Xu, Y. et al. (2018). "Late Neogene aridification and wind patterns in the Asian interior: Insight from the grain-size of eolian deposits in Altun Shan, northern Tibetan Plateau". In: *Palaeogeography, Palaeoclimatology, Palaeoecology* 511.September 2018, pp. 532–540. DOI: 10.1016/j.palaeo.2018.09.017.

Yan, Y. et al. (2017). "Tectonic and climatic controls on provenance changes of fine-grained dust on the Chinese Loess Plateau since the late Oligocene". In: *Geochimica et Cosmochimica Acta* 200, pp. 110–122. DOI: 10.1016/j.gca.2016.12.009.

Yang, F. et al. (2019). "High-Resolution Eocene Magnetostratigraphy of the Xijigou Section: Implications for the Infilling Process of Xining Basin, Northeastern Tibetan Plateau". In: *Journal of Geophysical Research: Solid Earth* 124.8, pp. 7588–7603. DOI: 10.1029/2019JB017624.

Yang, R. et al. (2017). "Paleomagnetic Constraints on the Middle Miocene-Early Pliocene Stratigraphy in the Xining Basin, NE Tibetan Plateau, and the Geologic Implications". In: *Geochemistry, Geophysics, Geosystems* 18.11, pp. 3741–3757. DOI: 10.1002/2017GC006945.

Yang, S. and Z. Ding (2010). "Drastic climatic shift at 2.8Ma as recorded in eolian deposits of China and its implications for redefining the Pliocene-Pleistocene boundary". In: *Quaternary International* 219.1-2, pp. 37–44. DOI: 10.1016/j.quaint.2009.10.029.

Yang, S. L. and Z. L. Ding (2004). "Comparison of particle size characteristics of the Tertiary 'red clay' and Pleistocene loess in the Chinese Loess Plateau: Implications for origin and sources of the 'red clay'". In: *Sedimentology* 51.1, pp. 77–93. DOI: 10.1046/j.1365-3091.2003.00612.x.

Yu, E. et al. (2018). "High-resolution simulation of Asian monsoon response to regional uplift of the Tibetan Plateau with regional climate model nested with global climate model". In: *Global and Planetary Change* 169, pp. 34–47. DOI: 10.1016/j.gloplacha.2018.07.002.

Zachos, J. et al. (2001). "Trends, rhythms, and aberrations in global climate 65 Ma to present". In: *Science* 292.5517, pp. 686–693. DOI: 10.1126/science.1059412.

Zachos, J. C. et al. (2008). "An early Cenozoic perspective on greenhouse warming and carbon-cycle dynamics". In: *Nature* 451.7176, pp. 279–283. DOI: 10.1038/nature06588.

Zhai, Y. and T. Cai (1984). "The Tertiary System of Gansu Province". In: *People's Press of Gansu*, pp. 1–40.

Zhang, H. et al. (2018a). "Expansion of Dust Provenance and Aridification of Asia Since ~7.2 Ma Revealed by Detrital Zircon U-Pb Dating". In: *Geophysical Research Letters* 45.24, pp. 13,437–13,448. DOI: 10.1029/2018GL079888.

Zhang, J. et al. (2013). "Paleomagnetic ages of Miocene fluvio-lacustrine sediments in the Tianshui Basin, western China". In: *Journal of Asian Earth Sciences* 62, pp. 341–348. DOI: 10.1016/j.jseaes.2012.10.014.

Zhang, J. et al. (2015a). "Evolution of the NE Qinghai-Tibetan Plateau, constrained by the apatite fission track ages of the mountain ranges around the Xining Basin in NW China". In: *Journal of Asian Earth Sciences* 97.PA, pp. 10–23. DOI: 10.1016/j.jseaes.2014.10.002.

Zhang, J. et al. (2016a). "Tectonics of the Xining Basin in NW China and its implications for the evolution of the NE Qinghai-Tibetan Plateau". In: *Basin Research* 28.2, pp. 159–182. DOI: 10.1111/bre.12104.

Zhang, R. et al. (2015b). "The impact of regional uplift of the tibetan plateau on the asian monsoon climate". In: *Palaeogeography, Palaeoclimatology, Palaeoecology* 417, pp. 137–150. DOI: 10.1016/j.palaeo.2014.10.030.

Zhang, R. et al. (2018b). "Changes in Tibetan Plateau latitude as an important factor for understanding East Asian climate since the Eocene: A modeling study". In: *Earth and Planetary Science Letters* 484.February, pp. 295–308. DOI: 10.1016/j.epsl.2017.12.034.

Zhang, Ran et al. (2018c). "Global Cooling Contributed to the Establishment of a Modern-Like East Asian Monsoon Climate by the Early Miocene". In: *Geophysical Research Letters* 45.21, pp. 11–941. DOI: 10.1029/2018GL079930.

Zhang, W. et al. (2016b). "Evolving flux of Asian dust in the North Pacific Ocean since the late Oligocene". In: *Aeolian Research* 23, pp. 11–20. DOI: 10.1016/j.aeolia.2016.09.004.

Zhang, W. et al. (2017). "Termination of fluvial-alluvial sedimentation in the Xining Basin, NE Tibetan Plateau, and its subsequent geomorphic evolution". In: *Geomorphology* 297, pp. 86–99. DOI: 10.1016/j.geomorph.2017.09.008.

Zhang, X. et al. (2016c). "Forcing mechanisms of orbital-scale changes in winter rainfall over northwestern China during the Holocene". In: *Holocene* 26.4, pp. 549–555. DOI: 10.1177/0959683615612569.

Zhang, Y. et al. (2014). "Cenozoic record of aeolian sediment accumulation and aridification from Lanzhou, China, driven by Tibetan Plateau uplift and global climate". In: *Global and Planetary Change* 120.December, pp. 1–15. DOI: 10.1016/j.gloplacha.2014.05.009.

Zhang, Z. et al. (2007). "What triggers the transition of palaeoenvironmental patterns in China, the Tibetan Plateau uplift or the Paratethys Sea retreat?" In: *Palaeogeography, Palaeoclimatology, Palaeoecology* 245.3-4, pp. 317–331. DOI: 10.1016/j.palaeo.2006.08.003.

Zhang, Z. et al. (2012). "Early Eocene Asian climate dominated by desert and steppe with limited monsoons". In: *Journal of Asian Earth Sciences* 44, pp. 24–35. DOI: 10.1016/j.jseaes.2011.05.013.

Zheng, H. (2016). "Asia dust production ramped up since latest Oligocene driven by Tibetan Plateau uplift". In: *National Science Review* 3.3, pp. 271–274. DOI: 10.1093/nsr/nww028.

Zheng, H. et al. (1992). "New contributions to Chinese Plio-Pleistocene magnetostratigraphy". In: *Physics of the Earth and Planetary Interiors* 70.3-4, pp. 146–153. DOI: 10.1016/0031-9201(92)90177-W.

Zheng, H. et al. (2015). "Late Oligocene-early Miocene birth of the Taklimakan Desert". In: *Proceedings of the National Academy of Sciences of the United States of America* 112.25, pp. 7662–7667. DOI: 10.1073/pnas.1424487112.

Zhou, L. P. et al. (1990). "Partly pedogenic origin of magnetic variations in Chinese loess". In: *Nature* 346.6286, pp. 737–739. DOI: 10.1038/346737a0.

Zhu, C. et al. (2019). "East-Central Asian Climate Evolved With the Northward Migration of the High Proto-Tibetan Plateau". In: *Geophysical Research Letters* 46.14, pp. 8397–8406. DOI: 10.1029/2019GL082703.

Zhu, Y. et al. (2008). "A new magnetostratigraphic framework for late Neogene Hipparion Red Clay in the eastern Loess Plateau of China". In: *Palaeogeography, Palaeoclimatology, Palaeoecology* 268.1-2, pp. 47–57. DOI: 10.1016/j.palaeo.2008.08.001.

Ziegler, C. L. et al. (2007). "Resolving eolian, volcanogenic, and authigenic components in pelagic sediment from the Pacific Ocean". In: *Earth and Planetary Science Letters* 254.3-4, pp. 416–432. DOI: 10.1016/j.epsl.2006.11.049.

Zoura, D. et al. (2019). "Atmospheric carbon dioxide, ice sheet and topographic constraints on palaeo moisture availability in Asia". In: *Earth and Planetary Science Letters* 519, pp. 12–27. DOI: 10.1016/j.epsl.2019.04.035.

Zoura, D. et al. (2020). "The role of Central Asian uplift in East Asian Monsoon circulation and its palaeoclimate implication". In: *Global and Planetary Change* 184, p. 103073. DOI: 10.1016/j.gloplacha.2019.103073.

Říha, K. et al. (2019). "Image analysis applied to quartz grain microtextural provenance studies". In: *Computers and Geosciences* 125.January, pp. 98–108. DOI: 10.1016/j.cageo.2019.01.007.

Zusammenfassung

Asiatischer Staub, Monsune und Westwind während des Eozäns

Die ostasiatischen Monsune prägen das heutige asiatische Klima, doch ihr geologischer Ursprung und ihre Antriebsmechanismen sind nach wie vor umstritten. Der südöstliche Sommermonsun bringt Feuchtigkeit, während der nordwestliche Wintermonsun Staub aus dem trockenen asiatischen Inland aufwirbelt und das chinesische Lössplateau bildet. Der Ursprung dieses Lösses und damit des Monsuns wurde vor 8 Millionen Jahren vermutet (Ma). In den letzten Jahren sind diese Lößablagerungen jedoch weiter in das Eozän (56-34 Ma) zurückverlegt worden, einer Periode, die durch bedeutende Änderungen sowohl in der regionalen Geographie als auch im globalen Klima gekennzeichnet ist. Inwieweit diese Rekonfigurationen die atmosphärische Zirkulation antrieben und ob es sich bei den lößartigen Sedimenten um monsunartige Ablagerungen handelt, bleibt jedoch umstritten. In dieser Dissertation untersuche ich die terrestrischen Ablagerungen des Xining-Beckens, die zuvor als Löss aus dem Eozän identifiziert wurden, um die paläo-umweltbedingte Entwicklung der Region abzuleiten und die geologischen Prozesse zu identifizieren, die das asiatische Klima geprägt haben.

Ich überprüfe die Staubablagerungen im geologischen Archiv und komme zu dem Schluss, dass diese durch eine Mischung aus windgetriebenen und wassergelagerten Sedimenten dargestellt werden, im Gegensatz zu dem rein windgetriebenen Material, das als Löß bekannt ist. Doch durch die Verwendung einer Kombination der oberflächenmorphologien von Quartz, Herkunftsmerkmalen und unterscheidenden Korngrößenverteilungen kann windgetriebener Staub in einer Vielzahl von Umgebungen identifiziert und quantifiziert werden. Dies hat wichtige Auswirkungen auf die Nachverfolgung der Aridifizierung und der Staubflüsse in dem gesamten geologischen Archiv.

Frühere Umkehrungen des Erdmagnetfeldes werden in den Ablagerungen des Xining-Beckens aufgezeichnet und ich verwende diese zusammen mit einer datierten vulkanischen Ascheschicht, um das Alter genau auf die Eozän-Periode einzugrenzen. Eine Kombination aus Pollenansammlungen, geringen Staubhäufigkeiten und anderen geochemischen Daten deutet darauf hin, dass das frühe Eozän relativ feucht war, was auf einen verstärkten Sommermonsun aufgrund des wärmeren Treibhausklimas zu dieser Zeit hinweist. Eine anschließende Verschiebung von überwiegend Süßwasser zu Salzseen spiegelt einen langfristigen Aridifizierungstrend wider, der möglicherweise durch die globale Abkühlung und die kontinuierliche Hebung des Tibetischen Plateaus angetrieben wurde. Überlagert wird diese Aridifizierung von feuchteren Intervallen, die durch eine Zunahme in Seeablagerungen gekennzeichnet werden und mit den Hochständen des inländischen proto-Paratethys-Meeres korrelieren. Dieses Meer bedeckte den eurasischen Kontinent und versorgte dadurch die winterlichen Westwinde mit zusätzlicher Feuchtigkeit im mittleren bis späten Eozän.

Die kontinuierliche Aridifizierung gipfelte in einer abrupten Verschiebung bei 40 Ma, die sich in der Entstehung von windgetriebenen Staub, nordwestlichen Winden, einer Zunahme von Steppenwüstenpollen und dem Auftreten von Orbitalzyklen widerspiegelte. Zusammengenommen deuten diese Verschiebungen auf das Einsetzen eines sibirischen Hochdrucksystems hin, das den ostasiatischen Wintermonsun ebenso wie Staubstürme antreibt. Ausgelöst wurde dieses System durch einen großen Meeresrückzug aus dem asiatischen Landesinneren. Diese Ergebnisse zeigen daher, dass das Proto-Paratethys-Meer, obwohl weniger bekannt als die Tibetischen Plateaus und das Klima, eine wichtige Antriebkraft für die Entstehung des heutigen Klimas in Asien war.

Samenvatting

Aziatisch stof, moessons en westenwinden tijdens het Eoceen

De Oost-Aziatische moessons kenmerken het hedendaagse Aziatische klimaat, maar hun geologische oorsprong en drijfveren blijven controversieel. De zuidoostelijke zomermoesson zorgt voor vocht, terwijl de noordwestelijke wintermoesson stof uit het droge Aziatische binnenland opveegt en daarmee het Chineze lössplateau vormt. De oorsprong van dit löss, en dus van de moessons, zou 8 miljoen jaar geleden liggen (Ma). De laatste jaren zijn deze lössrecords echter verder terug in de tijd uitgebreid naar het Eoceen (56-34 Ma), een periode die wordt gekenmerkt door belangrijke veranderingen in zowel de regionale geografie als in het globale klimaat. Maar de mate waarin deze reorganisaties de atmosferische circulatie aandrijven en in hoeverre de lössachtige afzettingen een moesson aantonen, is nog steeds onderwerp van discussie. In dit proefschrift bestudeer ik de afzettingen van het Xining bekken, die eerder werden geïdentificeerd als Eoceen löss, om de paleomilieus in de regio te reconstrueren en de geologische processen te identificeren die het Aziatische klimaat hebben gevormd.

Ik bestudeer stofafzettingen in geologische opeenvolgingen en concludeer dat deze worden vertegenwoordigd door een mix van zowel wind- als watergedragen sedimenten, in tegenstelling tot het louter door de wind getransporteerde materiaal dat bekend staat als löss. Door gebruik te maken van een combinatie van oppervlaktemorfologieën van kwarts, herkomstkarakteristieken en onderscheidende korrelgrootteverdelingen, kan het opgewaaide stof worden geïdentificeerd en gekwantificeerd in een verscheidenheid aan omgevingen. Dit heeft belangrijke implicaties voor het reconstrueren van verdroging en stof fluxen in de geologische geschiedenis.

Vroegere omkeringen van het aardmagnetisch veld worden geregistreerd in de afzettingen van het Xining bekken en ik gebruik deze samen met een gedateerde vulkanische aslaag om de ouderdom nauwkeurig te begrenzen in het Eoceen. Een combinatie van pollensamenstellingen, lage stof concentraties en andere geochemische gegevens geeft aan dat het vroege Eoceen relatief vochtig was, wat duidt op een intensievere zomermoesson als gevolg van het warmere broeikasklimaat op dat moment. Een daaropvolgende verschuiving van overwegend zoetwater naar zoutmeren weerspiegelt een langdurige verdrogingstrend die mogelijk wordt aangedreven door de wereldwijde afkoeling en de toenemende groei van het Tibetaanse plateau. Bovenop deze verdroging vinden nattere intervallen plaats, weergegeven door meerafzettingen die correleren met hoogstanden in de binnenlandse proto-Paratethys Zee. Deze zee bedekte het Euraziatische continent en zorgde zo voor extra vocht voor de winterse westenwinden tijdens het midden- tot late Eoceen.

De voortdurende droogte resulteerde in een abrupte verschuiving op 40 Ma, die werd weerspiegeld door de opkomst van opgeblazen stof, noordwestelijke winden, een toename van steppe-woestijn pollen en het optreden van hoge-latitude orbitale cycli. Samen wijzen deze op het begin van een systeem van hoge atmosferisch druk

in Siberië dat de Oost-Aziatische wintermoesson en de stofstormen aandrijft. Dit systeem werd in gang gezet door een grote terugtrekking van de zee uit het Aziatische binnenland. Deze resultaten tonen daarom aan dat de proto-Paratethys Zee, hoewel minder erkend dan het Tibetaanse Plateau en het klimaat, een belangrijke drijfveer is geweest bij het ontstaan van het moderne klimaat in Azië.

Acknowledgements

It's been almost five years since I got on the plane in Amsterdam to fly to Xining and start my PhD. It ended up being an incredible experience including multiple field trips to China and Tajikistan, moving to Potsdam, visiting Rennes for lab work, excursions to the Harz and attending scientific conferences all over the world. I have had a truly amazing time and this is mostly thanks to all the fascinating and wonderful people I've met along the way. In the following, I'd like to thank you all for your support and friendship.

First and foremost, I want to thank my supervisor Guillaume Dupont-Nivet. I've always enjoyed our collaboration, our discussions and your great sense of humour. You have been a tremendous support at times that I needed it, but also let me pursue my own interests, for which I'm grateful. Your diligent work and unwavering optimism will be a continuous inspiration for me. I thank my second supervisor Hemmo Abels for guiding me into the world of terrestrial climate archives and for your support during this project. I'm very thankful for the many skills that you taught me, especially to dig deep and look for the details. I'm also incredibly grateful to Alexis Licht for providing me with so many great ideas and contributions to my thesis. Your guidance and feedback has been a great help during all these years and especially during the stressful weeks towards the end.

I'd like to thank everyone who joined me on the many field trips for their hard work but also for the fun times that we had. I'm especially grateful to the many Chinese colleagues who made our field work both very successful and enjoyable. In particular, I want to thank Meimei Xiao and Yang Zhang for introducing me to Chinese food, culture and KTVs. Furthermore, I'd like to thank Zhongping Lai, Xiang-Jun Liu, Aijun Sun, Tianyuan Chen, Zhipeng Wu, Shengcheng Lu, Xiaohui Wu, Fuyan An, Yuwen Li and Zhaojie Guo as well as the drivers Minggang Li, Yankui Zhang and Fuzhong Zhou for all their help.

I'm very thankful to Pierrick Roperch for his astute supervision at the paleomagnetic laboratory in Rennes which has prevented many mistakes and taught me a great deal. Also thanks for asking the 'difficult' questions and checking my thin sections in great detail. Other people in Rennes that I'd like to thank are Marc Poujol for dating the tuff layer that proofed to be so crucial for the age model and Sylvie Bourquin for providing many ideas on ancient dust. I also thank Olivier Bochet and Guillaume Baby for hosting me at their house and for the great time I had staying there along with Fernando, Regis, Nicolas, Stéphane, Marie, Barbara and others.

I thank Mustafa Kaya for being my PhD-buddy since the very beginning. I've truly enjoyed your band's gigs and our conversations on the Paratethys, politics and many other things. I'm especially thankful to you and your wife Sema for the delicious Turkish dinners (with Raki!). I thank Alexander Rohrmann for his contributions and for teaching me many things about stable isotopes and tectonics. Véronica Torres for being very supportive and organizing the nice meetings with the MAGIC team. I'm particularly grateful to Natasha Barbolini, Amber Woutersen and Carina Hoorn for providing me with their pollen data and interpretations, even during these busy last weeks. I also thank Delphine Tardif, Frédéric Fluteau, Yannick Donnadieu, Agathe Toumoulin and Guillaume Le Hir for trying to test my paleoclimate-fantasies (and bring them back to reality) with climate models.

I'd like to acknowledge the various people who have helped me acquiring the stable isotope data used in Chapter 5. These include Jens Fiebig and Andreas Mulch at Goethe University-Senckenberg in Frankfurt, Simon Anderson and Andrew Schauer at the University of Washington in Seattle and Hanno Meyer and Mikaela Weiner at the AWI in Potsdam. I thank Femke Saulus for the magnetostratigraphic data of the Pingan section (though I renamed it to the Dazhai section in Chapter 4). Koen van Toorenenburg and Yuan Shang for sharing their grain-size data. Hans van Hateren for sharing his MATLAB script for analyzing grain-size data. João Trabucho-Alexandre for helping me write about quartz surface morphologies and Hong Ao for sending the photograph of the Shilou section used in Chapter 2. I also thank Aki Sakuma and Ryuji Tada for measuring ESR and CI.

I want to thank the lab managers at the University of Potsdam: Antje Musiol for her help with XRF and TOC, Christina Günther for the SEM data and Christine Fischer for making beautiful thin sections of even the muddiest samples. I'm grateful to Martina Heidemann and Tanja Klaka-Tauscher for taking care of the many samples that I shipped and for dealing with my bureaucratic issues. I thank Maria Mutti and Sven Maerz for guiding me during my teaching project and for the very nice excursions to the Harz with Gerd Winterleitner, Xia Wang and Richard Arndt. In addition, I'd like to thank Sven for helping me with the 'Zusammenfassung' and Xia for translating Chinese geological maps. I also thank the many other people at the University of Potsdam that have made my time in Golm, Potsdam and Berlin so much more enjoyable. My office mates Leyla Rezaei and Maryam Ramezani for the much-needed coffee breaks. Lélia Libon for supporting me with delicious food during these past weeks. Also, Iris van der Veen, Stephanie Olen, Gamze Koc, Sebastian Zapata Henao, Alessia Borghini, Roberta Spallanzani, Fabiana Castino, Silvio Ferrero, Iris Wannhoff, Johannes Rembe, Martin Zeckra, Sara Figueroa Villegas, Asfaw Erbello Doelesso and many others! I thank you all for the drinks, parties and fun times.

I've also spent a great deal of time at the GFZ, mostly for measuring grain-sizes but also for the nice company and the strong coffee at the Geomorphology section. I thank Christoff Andermann, Micha Dietze, Stefan Liening and Caroline Zorn for their help in the SedLab. I'm very grateful to David Maas for being a great friend since the very start of my PhD and Luc Illien for inspiring me with his many passions, for being a dear friend and for your help with Overleaf these past days. I thank Camilla Brunello and Marisa Repasch for the fun times and sharing their office with me. Rik Tjallingii for his help with the XRF-data. Norbert Nowaczyk for his support in the paleomagnetism lab. Jiabo Liu and Roberts Blukis for their help with constructing and understanding FORC diagrams. In addition, I want to thank the Earth Surface Geochemistry section for the interesting scientific discussions but mostly for the amazing 'Bier nach Vier's. In particular, Renee van Dongen for organizing so many great activities and being a wonderful friend. Also, Michael Henehan for always taking the time to answer my paleoceanographic questions and for proofreading my thesis. Furthermore, I thank Patrick, Daniel, Rene, Nick, Donovan, Leif, Nestor, Emma, Kristen, Kai, Di, Charlotte, Katharina, Sophia, Chenyu and many others for all the great fun!

At the moment of writing this, it seems ages ago but I used to have a happy life thanks to all of you joining me with cycling tours, board game evenings (or days), running, volleyball, swimming in the lakes or even ice skating sometimes, dinners, drinks, city trips and movies. I'm especially thankful to Leila Coudray and Pelle

Hartmans for the delicious food, murder mysteries, board games, cinema trips and your friendship and support. Also, I want to thank Paula, Remco, Femke, Matthias, Barbara, Elodie, Didac, Maxime, Federica, Mia and many others for all the good times. I feel incredibly lucky and grateful for living with my flatmates, both current and former: Adrian, Marie, Ruben, Peter, Lotte, Lena, Alina, Pauline, Jan, Tabea and Jenny. I've very much enjoyed our games, 'Ausflüge', dinners, activities and your companionship. Thanks for providing these much-needed distractions.

I thank my friends in the Netherlands for visiting me and keeping in touch. In particular, I want thank to Bas van der Meulen; I've greatly enjoyed your support, our conversations and your friendship. Thanks for letting me stay at your place numerous times and also for proofreading my thesis. I'm grateful to Kevin Ike for being an amazing friend since many years. Above all, I thank my family, my parents Wim and Henriëtte and my brother Ruben for their unconditional support for whatever I'm doing.